EXPERIMENTAL INVESTIGATION OF NORMAL, SONIC INJECTION THROUGH A WEDGE-SHAPED NOZZLE INTO SUPERSONIC FLOW

by

Matthew James Barber

Thesis Submitted to the Faculty of the

Virginia Polytechnic Institute and State University

in partial fulfillment of the requirements for the degree of

Master of Science

in

Mechanical Engineering

APPROVED

Dr. L. A. Roe, Chairman

Dr. J. A. Schetz

Dr. W. F. Ng

January 1991

Blacksburg, Virginia

C.2

5655
V855
1991
B371
c.2

EXPERIMENTAL INVESTIGATION OF NORMAL, SONIC INJECTION THROUGH A WEDGE-SHAPED NOZZLE INTO SUPERSONIC FLOW

by

Matthew James Barber

Committee Chairman: Larry A. Roe

Mechanical Engineering

(ABSTRACT)

An experimental evaluation of normal, sonic, helium injection from a wedge-shaped nozzle and a circular nozzle into a Mach 3 free stream with a total pressure of 6.5 atm and a total temperature of 294 K was conducted. The expansion ratio and the mass rate of flow of both nozzles were matched in order to determine the effect of the geometric difference only. Decay rate, penetration, and jet area growth rate were used to compare the mixing performance of the nozzles. Oil flow photography was used to determine the size of the three-dimensional boundary layer separation zone in front of each nozzle, and nanoshadowgraph photography was used to visualize the system of shocks and the flow field of each nozzle. Mean flow quantity profiles at several lateral stations were made at three downstream locations. The profiles were used to calculate helium concentration, Mach number, static temperature, static pressure, density, flow velocity, local speed of sound, mass flux, and total pressure. The two nozzles were then compared on the basis of maximum helium concentration decay, core center and overall

penetration, and the growth rate and centroid penetration of a defined jet area. Although the decay rate of the jet from the circular nozzle was slightly higher than the decay rate of the jet from the wedge-shaped nozzle, the mixing performance of the wedge-shaped nozzle exceeded that of the circular nozzle in all other comparison parameters. The jet from the wedge-shaped nozzle penetrated further and its area grew more rapidly than the same parameters for the jet from the circular nozzle. The oil flow photography showed that the wedge-shaped nozzle also had no separation zone in front of it, whereas the circular nozzle had a large separation zone. A separation zone in front of a fuel injector in a scramjet engine can result in damage to the combustor from the extreme heat fluxes to the wall. Also, the total pressure loss in the combustor should be lower for fuel injection through a wedge-shaped nozzle due to the elimination of the normal shock. It was concluded that wedge-shaped fuel injectors should perform better than circular fuel injectors in supersonic combustors.

ACKNOWLEDGEMENTS

I would like to thank Dr. L. A. Roe for his guidance and support. I would also like to thank Dr. J. A. Schetz and Dr. R. H. Thomas for their advice and assistance. I also thank Dr. W. F. Ng for serving as a committee member.

Special appreciation goes to Charles Wood, Richard Mays, Ken Chadwick, John Mills, and Russ Thomas for making the long research hours entertaining and incredibly philosophical. Thanks also to Todd Ninneman, Eric Fuller, Gary Stafford, Fei Kwok, John Keady, and Rich Baker for their contributions.

I would also like to thank my parents for their love and guidance and my brothers for their constant help in building my character.

I would also like to express my appreciation for Leslie Barber, whose love, enduring patience, and support have made it all worthwhile.

TABLE OF CONTENTS

Introduction 1

Description of the Experiment 5

General Description 5

Facilities and Equipment 7

The Wind Tunnel 7

The Helium Supply System 8

The Models 8

The Traversing System 9

Instrumentation 10

The Data Acquisition System 10

Stagnation Properties 10

Flowmeter 11

Oil Flow Photography 12

Nanoshadowgraph Photography 12

Concentration Probe 12

Pressure and Temperature Probes 13

Position Measurement 15

Experimental Methods 16
Instrument Calibration 16
Expansion Ratio and Mass Flow Rate 18
Data Acquisition Procedures 19
Data Reduction 21
Nondimensionalization Method 24

Results 27
Oil Flow Photographs 27
Nanoshadowgraph Photographs 28
Concentration Data 30
Flowfield Structure 30
Jet Core Center Penetration 31
Maximum Helium Concentration Decay 32
Overall Penetration 34
Hydrogen-Air Lean Limit Area 34
Hydrogen-Air Lean Limit Centroid 35
Other Mean Flow Results 36
Data Profiles 36
Integrated Mass Flow Rate 37
Reliability of Results 38
Discussion 40

Conclusions and Recommendations 44

Bibliography 46

Figures 48

Appendices 157

Appendix A: Uncertainty Analysis 157

Appendix B: Computer Programs 160

Appendix C: Helium Mass Fraction Profiles 186

LIST OF FIGURES

Figure 1. Mach 3 Test Section. 49

Figure 2. Nozzle Insert 50

Figure 3. Wedge-shaped Nozzle Dimensions. 51

Figure 4. Instrumentation Positions. 52

Figure 5. Nanoshadowgraph Configuration. 53

Figure 6. Concentration Probe. 54

Figure 7. Cross-section of Concentration Probe. 55

Figure 8. Pitot Probe. 56

Figure 9. Cone-Static Probe. 57

Figure 10. Total Temperature Probe. 58

Figure 11. Concentration Probe Calibration Curves. 59

Figure 12. Oil Flow Photographs. 60

Figure 13. Nanoshadowgraph Composite, Circular Nozzle. 61

Figure 14. Nanoshadowgraph Composite, Wedge-shaped Nozzle. 62

Figure 15. Helium Concentration for the Circular Nozzle, $x/R_b=56$. 63

Figure 16. Helium Concentration for the Circular Nozzle, $x/R_b=97$. 64

Figure 17. Helium Concentration for the Circular Nozzle, $x/R_b=201$. 65

Figure 18. Contour Stack, Circular Nozzle. 66

Figure 19. Helium Concentration for the Wedge-shaped Nozzle, $x/R_b=56$. . . . 67

Figure 20. Helium Concentration for the Wedge-shaped Nozzle, $x/R_b=97$. . . . 68

Figure 21. Helium Concentration for the Wedge-shaped Nozzle, $x/R_b=201$. . . 69

Figure 22. Contour Stack, Wedge-shaped Nozzle. 70

Figure 23. Core Center Penetration. 71

Figure 24. Decay of Maximum Helium Concentration. 72

Figure 25. Overall Penetration. 73

Figure 26. Area Bounded by Lean-Limit Contour. 74

Figure 27. Centroid Penetration. 75

Figure 28. Total Pressure Profile, $y/R_b = +8$. 76

Figure 29. Total Pressure Profiles, $y/R_b = +6$. 77

Figure 30. Total Pressure Profiles, $y/R_b = +4$. 78

Figure 31. Total Pressure Profiles, $y/R_b = +2$. 79

Figure 32. Total Pressure Profiles, $y/R_b = 0$. 80

Figure 33. Total Pressure Profiles, $y/R_b = -2$. 81

Figure 34. Total Pressure Profiles, $y/R_b = -4$. 82

Figure 35. Total Pressure Profiles, $y/R_b = -6$. 83

Figure 36. Total Pressure Profiles, $y/R_b = -8$. 84

Figure 37. Static Pressure Profiles, $y/R_b = +8$. 85

Figure 38. Static Pressure Profiles, $y/R_b = +6$. 86

Figure 39. Static Pressure Profiles, $y/R_b = +4$. 87

Figure 40. Static Pressure Profiles, $y/R_b = +2$. 88

Figure 41. Static Pressure Profiles, $y/R_b = 0$. 89

Figure 42. Static Pressure Profiles, $y/R_b = -2$. 90

Figure 43. Static Pressure Profiles, $y/R_b = -4$. 91

Figure 44. Static Pressure Profiles, $y/R_b=-6$. 92

Figure 45. Static Pressure Profiles, $y/R_b=-8$. 93

Figure 46. Total Temperature Profiles, $y/R_b=+8$. 94

Figure 47. Total Temperature Profiles, $y/R_b=+6$. 95

Figure 48. Total Temperature Profiles, $y/R_b=+4$. 96

Figure 49. Total Temperature Profiles, $y/R_b=+2$. 97

Figure 50. Total Temperature Profiles, $y/R_b=0$. 98

Figure 51. Total Temperature Profiles, $y/R_b=-2$. 99

Figure 52. Total Temperature Profiles, $y/R_b=-4$. 100

Figure 53. Total Temperature Profiles, $y/R_b=-6$. 101

Figure 54. Total Temperature Profiles, $y/R_b=-8$. 102

Figure 55. Static Temperature Profiles, $y/R_b=+8$. 103

Figure 56. Static Temperature Profiles, $y/R_b=+6$. 104

Figure 57. Static Temperature Profiles, $y/R_b=+4$. 105

Figure 58. Static Temperature Profiles, $y/R_b=+2$. 106

Figure 59. Static Temperature Profiles, $y/R_b=0$. 107

Figure 60. Static Temperature Profiles, $y/R_b=-2$. 108

Figure 61. Static Temperature Profiles, $y/R_b=-4$. 109

Figure 62. Static Temperature Profiles, $y/R_b=-6$. 110

Figure 63. Static Temperature Profiles, $y/R_b=-8$. 111

Figure 64. Mach Number Profiles, $y/R_b=+8$. 112

Figure 65. Mach Number Profiles, $y/R_b=+6$. 113

Figure 66. Mach Number Profiles, $y/R_b = +4$. 114

Figure 67. Mach Number Profiles, $y/R_b = +2$. 115

Figure 68. Mach Number Profiles, $y/R_b = 0$. 116

Figure 69. Mach Number Profiles, $y/R_b = -2$. 117

Figure 70. Mach Number Profiles, $y/R_b = -4$. 118

Figure 71. Mach Number Profiles, $y/R_b = -6$. 119

Figure 72. Mach Number Profiles, $y/R_b = -8$. 120

Figure 73. Speed of Sound Profiles, $y/R_b = +8$. 121

Figure 74. Speed of Sound Profiles, $y/R_b = +6$. 122

Figure 75. Speed of Sound Profiles, $y/R_b = +4$. 123

Figure 76. Speed of Sound Profiles, $y/R_b = +2$. 124

Figure 77. Speed of Sound Profiles, $y/R_b = 0$. 125

Figure 78. Speed of Sound Profiles, $y/R_b = -2$. 126

Figure 79. Speed of Sound Profiles, $y/R_b = -4$. 127

Figure 80. Speed of Sound Profiles, $y/R_b = -6$. 128

Figure 81. Speed of Sound Profiles, $y/R_b = -8$. 129

Figure 82. Flow Speed Profiles, $y/R_b = +8$. 130

Figure 83. Flow Speed Profiles, $y/R_b = +6$. 131

Figure 84. Flow Speed Profiles, $y/R_b = +4$. 132

Figure 85. Flow Speed Profiles, $y/R_b = +2$. 133

Figure 86. Flow Speed Profiles, $y/R_b = 0$. 134

Figure 87. Flow Speed Profiles, $y/R_b = -2$. 135

Figure 88. Flow Speed Profiles, $y/R_b=-4$. 136

Figure 89. Flow Speed Profiles, $y/R_b=-6$. 137

Figure 90. Flow Speed Profiles, $y/R_b=-8$. 138

Figure 91. Density Profiles, $y/R_b=+8$. 139

Figure 92. Density Profiles, $y/R_b=+6$. 140

Figure 93. Density Profiles, $y/R_b=+4$. 141

Figure 94. Density Profiles, $y/R_b=+2$. 142

Figure 95. Density Profiles, $y/R_b=0$. 143

Figure 96. Density Profiles, $y/R_b=-2$. 144

Figure 97. Density Profiles, $y/R_b=-4$. 145

Figure 98. Density Profiles, $y/R_b=-6$. 146

Figure 99. Density Profiles, $y/R_b=-8$. 147

Figure 100. Mass Flux Profiles, $y/R_b=+8$. 148

Figure 101. Mass Flux Profiles, $y/R_b=+6$. 149

Figure 102. Mass Flux Profiles, $y/R_b=+4$. 150

Figure 103. Mass Flux Profiles, $y/R_b=+2$. 151

Figure 104. Mass Flux Profiles, $y/R_b=0$. 152

Figure 105. Mass Flux Profiles, $y/R_b=-2$. 153

Figure 106. Mass Flux Profiles, $y/R_b=-4$. 154

Figure 107. Mass Flux Profiles, $y/R_b=-6$. 155

Figure 108. Mass Flux Profiles, $y/R_b=-8$. 156

LIST OF SYMBOLS

α_{He} - helium mass fraction concentration

a - calibration constant of concentration probe

$ß_1$ - least squares fit constant

$ß_2$ - least squares fit constant

b - calibration constant of concentration probe

γ - specific heat ratio

l - active hot film sensor length

m - calibration constant of concentration probe

M - Mach number

MW_{He} - molecular weight of helium

MW_{mix}- molecular weight of helium-air mixture

η_1 - penetration and area growth rate of jet

η_2 - decay rate of helium mass fraction

P - static pressure

P_c - cone-static pressure

P_t - total pressure

q - dynamic pressure

ρ - density

R - gas constant of helium-air mixture

R_b - nondimensionalization parameter

R_e - free stream Reynolds number

T - static temperature

T_t - total temperature

u - flow velocity

V - hot film voltage

X_{He} - helium mole fraction concentration

x - axial distance downstream of nozzle

y - lateral distance from the nozzle centerline

z - vertical distance from wind tunnel floor

subscripts:

1 - local property

2 - post shock local property

j - jet property

∞ - free stream property

INTRODUCTION

The importance of air-breathing propulsion has been noted recently with its inclusion in the Defense Department's list of critical technologies[1] and its application to the National Aerospace Plane. A significant component of air-breathing propulsion research is the study of fuel and air mixing in the combustor of a supersonic combustion ramjet (scramjet). For a typical combustor, fuel must mix with air and combust in a millisecond or less to produce thrust. The performance of the combustor and the overall performance of the engine depend on how adequately mixing and combustion occur. Therefore, any improvement in mixing will result in a better engine with increased thrust.

Various fuel injection schemes for supersonic flow have been experimentally investigated. Typical methods include injection through transverse nozzles or wall slots. Transverse nozzles with a circular cross-section were studied by Rogers[2,3], McClinton[4], and Mays[5]. Rogers measured hydrogen concentration using a process gas chromatograph up to 200 diameters downstream of both a single sonic hydrogen jet[2] and a row of five sonic hydrogen jets, spaced either 6.25 diameters or 12.5 diameters apart[3], injected normal to a Mach 4 free stream. The penetration of the row of nozzles was found to be similar to the penetration of the single nozzle. Penetration is defined by Rogers to be the vertical height from the injector to the edge of the mixing region where the hydrogen volume fraction is 0.005. Likewise, the maximum concentration decay, which is a measure of the mixing rate of a jet, for the row of nozzles spaced 12.5 diameters apart

was similar to the single nozzle data. However, the closer spaced nozzles had a significantly lower decay rate, indicating a slower mixing rate. Rogers also noted a large region of very low total pressure downstream of both the single nozzle and the row of nozzles.

McClinton[4] studied the effect of injection angle on penetration, mixing rate, and total pressure recovery downstream of five sonic jets, spaced 6.25 diameters apart, injected into a Mach 4 free stream. The injection angle varied between 30° and 90°. He found that as the angle decreased, the penetration and mixing increased, and the total pressure loss decreased.

Mays[5] measured concentration up to 90 diameters downstream of a single sonic helium jet with injection angles of 15° and 30° injected into a Mach 3 free stream. A matched pressure and an underexpanded jet was studied for each injection angle. The investigation concluded that the best injector of the four studied was the 15°, underexpanded jet. This jet had the best combination of penetration, mixing, and low total pressure loss.

Fuel injection parallel to the free stream through wall slots has been studied by Yates[6], Kwok[7], and Smith[8]. The advantage of slot injection is that the momentum from the injected fuel contributes to the total thrust of the vehicle. However, mixing and penetration are much lower than in transverse injection.

Thomas, et al.[9] discuss other injection schemes and provide a review of the available high speed mixing database. The authors point out that the database is rather

sparse, and that more experimental data is needed to "provide... a basis against which computational fluid dynamics can be benchmarked."

Normal injection through a circular nozzle is one of the most analyzed injection schemes. Most analytical techniques use a solid body model to describe the behavior of the normal jet and its system of shock waves[10-12]. Schetz and Billig[10] extended subsonic solid body models to supersonic flows to describe the jet trajectory. They also introduced the concept of effective back pressure to make an analogy between underexpanded injection into a supersonic mainstream and underexpanded injection into a quiescent medium. Billig, Orth, and Lasky[11] developed correlations based on the effective back pressure that described the location of the Mach disk and "the size and shape of the initial portion of the jet." Several numerical techniques that attempt to describe jet behavior have also been developed[13-15].

The purpose of the present research, which was inspired by the work of Masyakin and Polyanskii[16], is to contribute to the high speed mixing database by investigating fuel injection through a wedge-shaped nozzle and to provide a set of initial conditions in order to improve analytical and numerical modeling techniques. The objective of the work done by Masyakin and Polyanskii was to determine a shape of the exit section of a nozzle such that no three-dimensional boundary layer separation zone occurred in front of the nozzle. A separation zone in front of a nozzle results in increased pressure and extreme heat fluxes to the wall in front of the nozzle. All normal circular nozzles have a relatively large separation zone. Masyakin and Polyanskii found that a normal, sonic triangular nozzle oriented with its apex toward the oncoming flow, and with apex half-

angle less than 12°, has no separation zone in front of it. Furthermore, it was found that the absence of the separation zone lead to a change in the system of shock waves in front of the jet. Based on these results, injecting fuel through a normal, sonic triangular nozzle could result in better fuel mixing than injecting fuel through a normal, sonic circular nozzle. Also, the total pressure loss in a combustor that utilizes triangular nozzles should be less than the total pressure loss in a combustor that utilizes circular nozzles since normal shocks are absent in front of the jets from the triangular nozzles. Large total pressure losses in a combustor reduce the fluid momentum available to a scramjet, resulting in lower engine performance.

The present research extends the work of Masyakin and Polyanskii by evaluating the mixing achieved when fuel is injected through a wedge-shaped nozzle with its apex oriented toward the oncoming flow. The wedge shape was used instead of a triangular shape because of fabrication considerations. Mixing studies of sonic helium injection through the wedge-shaped nozzle into a Mach 3 free stream are presented in this report. As a baseline for comparison, sonic helium injection through a circular nozzle was also studied. The mass rate of flow and the expansion ratio of both nozzles were matched so that any mixing differences would be a result of the geometric difference and not flow parameter differences.

DESCRIPTION OF THE EXPERIMENT

General Description

Tests were performed in the VPI&SU supersonic wind tunnel at the following free stream conditions:

$$M_\infty = 3.0$$

$$P_{t\infty} = 6.5\ atm$$

$$T_{t\infty} = 294\ K$$

Normal helium injection from a single, wedge-shaped, sonic nozzle was studied. To provide a baseline for comparison, tests were also performed on a single, circular, sonic nozzle. Both nozzles were flush to the wind tunnel floor. The total temperature of both jets was 299 K. Jet total pressure was 75.8 kPa for the wedge-shaped nozzle and 120 kPa for the circular nozzle. The expansion ratio, defined as the ratio of jet static pressure to the minimum static pressure required to choke the nozzle, was 1.45 for both nozzles. The mass flow rate of helium for both nozzles was 0.00089 kg/s. An effective radius, R_b, was defined for nondimensionalization purposes (see *Nondimensionalization Method*). R_b had a value of 1.56 mm.

The oil flow method was used to determine the size of the three-dimensional boundary-layer separation zone in front of each nozzle (see *Oil Flow Photography*). The

total pressure of the wedge-shaped nozzle was also selected based on observations of the oil flow (see *Expansion Ratio and Mass Flow Rate*).

The nanoshadowgraph method was used to photograph the flow fields of both jets. A series of photographs was made that extended from slightly upstream of the nozzle to slightly downstream of the third data acquisition location.

Continuous vertical profiles of helium concentration, Pitot pressure, cone-static pressure, and total temperature were obtained at three axial locations downstream of the jet. Profiles were taken at the tunnel centerline and at three lateral stations on each side of the centerline. At the third axial location, profiles were also taken at a fourth lateral station on each side of the centerline. Helium concentration, total pressure, static pressure, total temperature, static temperature, Mach number, local speed of sound, density, flow velocity, and mass flux were calculated from the acquired data.

Facilities and Equipment

The Wind Tunnel

The present research was conducted in the VPI&SU Supersonic Wind Tunnel. The tunnel is a blowdown type that can be run at total pressures up to 20 atm. Interchangeable test sections provide for runs at Mach numbers from 2.4 to 4.0. Air is compressed by an Ingersoll-Rand Type 40 water-cooled, reciprocating compressor and is piped through a dryer that removes moisture and a prefilter that removes oil. An after-filter removes dirt and dust in the air before the air is placed in storage tanks.

A run is initiated when the system control computer (an IBM-PC) opens a pneumatic butterfly valve that releases the air from the storage tanks into the settling chamber. The settling chamber pressure is maintained for the duration of the run by a hydraulic valve. The position of the valve is controlled by a feedback servo control circuit that receives a control signal from the computer and a settling chamber total pressure signal from a pressure transducer. The feedback system maintains the tunnel total pressure within five percent of the desired pressure. After the air passes through a transition cone and a set of five screens in the settling chamber to reduce flow angularity and turbulence, the air enters the test section.

The test section for the present case, which is shown in Figure 1, contained a two-dimensional, converging-diverging Mach 3 half-nozzle with a throat area of 61.5 cm^2. The nozzle accelerates the air through an 11.4 cm x 23.0 cm rectangular cross-section, constant area duct in which the experimental model and instrumentation were located.

Hinged windows on both sides of the duct provided access to the model and instrumentation and permitted production of oil flow photographs and nanoshadowgraphs. The air, or air and injectant mixture, then enters a step diffuser and exhausts into the atmosphere through a shrouded exit duct. Each run lasted approximately 13 seconds.

The Helium Supply System

Compressed helium was supplied by a bank of twelve, standard, commercial helium bottles that fed into a common manifold at a pressure of 27 to 170 atm. Flow from the manifold entered a Grove RBX 204-015 dome pressure regulator which reduced the pressure to 20 atm. A regulated air bottle provided a reference pressure for the dome pressure regulator. The output pressure was monitored with an oil-filled pressure gage. Further pressure reduction and fine tuning were accomplished with a manually operated needle valve which maintained jet total pressure within three percent of the desired value. Helium entered a plenum chamber, which had an internal volume of 4900 cm^3, through two straight copper tubes in the bottom of the plenum chamber.

The Models

The experimental models consisted of a nozzle block with two interchangeable nozzle inserts. The wedge-shaped nozzle insert is shown in Figure 2. This nozzle was situated so that its apex was oriented toward the Mach 3 free stream. An expanded view of the wedge-shaped nozzle can be seen in Figure 3. The circular nozzle was simply a 3.45 mm diameter hole in a nozzle insert drilled at the location of the centroid of the

wedge-shaped nozzle. Both nozzles were sonic and were designed for normal helium injection. The nozzle block with a nozzle insert was mounted on top of the plenum chamber.

A test plate downstream of the nozzle and flush with the top of the nozzle block contained slots which allowed lateral and vertical movement of mean flow probes. The plate is illustrated in Figure 4. The slots were located $107R_b$, $148R_b$, and $252R_b$ downstream of the jet. Since probe sensors extended $51R_b$ upstream of the slots, measurements were taken at axial stations $56R_b$, $97R_b$, and $201R_b$ downstream of the jet. The slots allowed lateral movement up to $24R_b$ off either side of the tunnel centerline. The slots were plugged flush to the top of the test plate with brass inserts and sealed with vacuum grease when not in use.

The Traversing System

The traversing system consisted of a rack geared to a software driven Computer Devices 4D-9200A stepper motor, with a net vertical probe motion of 0.013 cm per step. The stepper motor was run by an American Precision Industries DMA-64 controller that received instructions from a UAI 3071 Stepper command processor board. An IBM PC control computer communicated with the board through a standard RS-232C serial port. Stepper motor speed, traversing distance, and direction were specified by the computer operator.

Instrumentation

The Data Acquisition System

A Metrabyte DAS-20, High Speed, Analog to Digital (A/D) conversion board installed in an IBM PC data acquisition computer read conditioned voltages from the mean flow measurement transducers. The DAS-20 had 20 channels, each of which converted a 0 to 10 volt analog signal to a 12 bit binary number. A data acquisition software package, Labtech Notebook, converted the binary numbers to real data and stored the information on floppy diskette.

A Metrabyte DAS-16F, High Speed, Analog to Digital (A/D) conversion board that also had two digital to analog (D/A) conversion channels was installed in the system control computer. One of the D/A channels was used to supply a control voltage to the wind tunnel total pressure control circuit mentioned earlier. Digital outputs on the DAS-16 were used to activate a relay that opened the pneumatic butterfly valve on the wind tunnel to initiate a run. The digital outputs were also used to open a control valve in the helium supply line, which released compressed helium into the plenum chamber.

Stagnation Properties

Tunnel stagnation pressure was measured by a Pitot tube in the wind tunnel settling chamber and converted to a voltage signal by a Setra Systems 0 to 100 psia, 50 mV/psia pressure transducer. A circuit within the transducer housing filtered the signal

before it was read by the DAS-20 A/D system. The signal was also used by the wind tunnel servo-controller circuit as mentioned earlier.

An Omega Type K (Chromel-Alumel) thermocouple with a 0.13 mm bead measured tunnel stagnation temperature. The thermocouple was connected to a Metrabyte EXP-20 electronic icepoint and amplifier. The voltage was read directly by the DAS-20 A/D system.

A Pitot tube in the plenum chamber measured the helium jet total pressure. The pressure was converted to a voltage signal by a Statham PA822-100, 0 to 100 psia pressure transducer. The voltage was amplified by an Ectron Differential D.C. Amplifier Model 562 and was low pass filtered by a four pole Bessel filter with a cutoff frequency of 340 Hz. An Ectron Model 516-5SG Excitation Power Supply provided an excitation voltage to the pressure transducer. Jet total pressure was also monitored using a Heise C-53332 Analog Pressure Gage.

Flowmeter

A Brooks Instrument Division Model 1307DO8E1A1A rotameter was placed in the helium supply line just before the plenum chamber to measure the volumetric flow rate of helium through the nozzle. The rotameter scale was corrected for density using the measured supply pressure and temperature.

Oil Flow Photography

Flow visualization was accomplished using the oil flow method. Drops of orange and green Day-Glo 500 cs oil were placed on the surface of the nozzle block upstream and downstream of the nozzle. When the tunnel was run, the oil highlighted the separation zones upstream and downstream of the nozzles. A Minolta X-700 camera with a 100 mm zoom lens and +4 diopter at F11 loaded with Kodak 1000 ASA 35 mm film was used to photograph the oil flow field. Two ultraviolet floodlights enhanced the appearance of the oil.

Nanoshadowgraph Photography

Figure 5 shows the nanoshadowgraph system used for the present research. A 30 nanosecond light pulse from a Xenon Novatron 739-B Nanopulse Lamp that was powered by a Xenon Model 437A Nanopulser was reflected by a parabolic mirror through the wind tunnel test section into a modified Burke and James View Camera fitted with a Polaroid Model 545 film holder. The image was recorded on Polaroid Type 57 High Speed Instant Film. The parabolic mirror had a focal length of 1.8 m.

Concentration Probe

An aspirating, hot film probe described by Ng, et al.[17] and illustrated in Figures 6 and 7 was used to measure helium concentration. The probe was under development while this investigation was being conducted. The sensor in the probe was a Thermo Systems, Incorporated 101212 Hot Film Sensor with a diameter of 0.051 mm and an

active sensor length of 1.0 mm. The sensor was made of platinum on a cylindrical quartz substrate. To insure that the hot film was exposed to a gas sample that was undisturbed by the probe's presence, the probe was designed to pull its bow shock into the hot film chamber. A choked orifice downstream of the sensor fixed the Mach number at the hot film.

Pressures were measured near the sensor plane and downstream of the choked orifice. The ratio of these pressures was checked to verify that the orifice was choked. The pressure at the sensor plane, P_1, was measured with a Statham PA285TC-50036, 0 to 50 psia pressure transducer. The transducer voltage was read by the DAS-20 A/D system after being amplified by an Ectron amplifier and filtered by a Bessel filter. The downstream pressure, P_2, was visually monitored using a Heise CMM-11112C Analog Pressure Gage.

The hot film sensor was connected to a Dantec Model 55M10 Standard CTA Bridge attached to a Dantec Model 55M10 Main Unit. The signal from the constant temperature anemometer was low-pass filtered and offset by a Thermo Systems, Incorporated IFA-100 signal conditioner. The filter cutoff frequency was 300 Hz. The output of the IFA-100 was read by the DAS-20 A/D system.

Pressure and Temperature Probes

Total pressure was measured using the Pitot probe shown in Figure 8. The probe had a capture area of 0.0052 cm^2. A 0.64 cm stainless steel sleeve was soldered to the probe to prevent excessive probe deflections during use. The probe's time response was

approximately 0.015 seconds[18]. A Statham PA 285TC-50036 0 to 50 psia pressure transducer read total pressure. The transducer signal was amplified by an Ectron amplifier and filtered by a Bessel filter before being read by the DAS-20 A/D system.

The cone static probe, shown in Figure 9, was a 10° half angle brass cone soldered to 0.16 cm diameter stainless steel tubing. Four 0.33 mm diameter pressure taps drilled 90° apart around the cone circumference were located 2.7 cm from its vertex. In order to reduce yaw sensitivity, the pressure taps emptied into a common chamber so that an average pressure was measured. Excessive deflection during tests was prevented by soldering the probe into a 0.64 diameter stainless steel sleeve. The capture area of the probe was 0.012 cm^2, and its time response was 0.08 seconds[18]. An MB Electronics 151-EPAB-236, 0 to 10 psia pressure transducer read the static pressure. The DAS-20 A/D system read the transducer signal after it was amplified by an Ectron amplifier and filtered by a Bessel filter.

Figure 10 shows the total temperature probe. A cylindrical, ceramic cap, which reduced radiation losses, was attached to the end of a 0.32 cm diameter stainless steel probe housing. Flow entered the probe and stagnated inside the cap where an Omega Type K (Chromel-Alumel) thermocouple with a bead diameter of 0.38 mm was located. Two 0.11 cm vent holes behind the thermocouple bead provided an exit for the flow. The thermocouple was connected to the EXP-20 thermocouple amplifier and electronic icepoint. Voltage output was read by the DAS-20 A/D system.

Position Measurement

Vertical position of the probes was measured by a Trans-Tek Model 0246-0000 G-6 Linear Voltage Displacement Transducer (LVDT). The transducer housing was attached to an immobile part of the traverse, but the LVDT core was fixed to the traverse rack to enable it to move with the probe. Probe displacements up to 15 cm could be measured with an accuracy of 0.5 percent[19]. A 12 volt DC power supply was used to provide an excitation voltage to the LVDT. The IFA-100 amplified and low pass filtered the LVDT voltage at a cutoff frequency of 50 Hz before the DAS-20 system read the voltage.

Lines etched on the surface of the test plate in front of each slot provided the lateral probe locations. The tunnel centerline and four lateral positions to each side of the centerline were marked. Spacing between each line was $2.0R_b$. The centerline of a probe was lined up with the marks on the test plate in order to position a probe at a specific lateral station.

Experimental Methods

Instrument Calibration

All pressure data was obtained using electronic pressure transducers. Each transducer was calibrated by exposing it to several known pressures and recording its output voltage. Transducer voltage was related to pressure using a least squares linear fit. The pressure transducers were accurate to one percent. An Ametek Mk100 pneumatic pressure tester connected to a commercial air bottle provided a range of pressures from 101 kPa to 709 kPa in 71 kPa increments. The transducer was exposed to the tester pressure. For pressures below 101 kPa, the transducer and a Heise C-53332 Analog Pressure Gage were connected to a pressure vessel. A vacuum pump connected to the pressure vessel through an on/off valve was used to evacuate the pressure vessel in 20 kPa increments. Voltages were amplified, filtered, and read by the same methods used when obtaining actual data.

Total temperature data was obtained by connecting each thermocouple to the EXP-20 thermocouple amplifier and electronic icepoint. The software used for data acquisition, Labtech Notebook, automatically converted the voltage obtained from an Omega Type K (Chromel-Alumel) thermocouple to a temperature reading. Therefore, a separate calibration was unnecessary.

The concentration probe was calibrated by placing it in a small pressure vessel filled with a known concentration of air/helium mixture at 2 atm[17]. A vacuum pump pulled the gas in the pressure vessel through the probe. Measurements of P_1, P_2, hot film

voltage, and total temperature were made at specific vessel pressures as the vessel pressure decreased. Vessel pressure and P_2 were measured with Heise pressure gages, and vessel temperature was measured with a thermocouple connected to the EXP-20. P_1 was measured with the same electronic pressure transducer used during data acquisition. This procedure was repeated at five different air/helium compositions.

Hot film voltage is related to Reynolds number by the following equation:

$$V^2 = \frac{(R_s + R_w)^2}{R_w} \pi l k (aRe^m + b)(T_w - T_t)$$

where R_s, R_w, l, and T_w were known, k was a function of gas composition, and T_t was measured with a separate probe. Constants a, b, and m were derived from the calibration data obtained at each air/helium concentration. A logarithmic curve generated by a least squares computer program was fitted to the data for each concentration. The curve fits had a maximum error of 3.0 percent. Figure 11 shows a set of curves and data from a typical calibration.

The LVDT was calibrated after a probe was installed at an axial station. A PTI Catalog Number 2210 Cathetometer was used to measure probe displacement accurately to 0.001 cm. The cathetometer was leveled by adjusting cathetometer attitude until the top of both ends of a 1.3 cm square cross-section block were measured to be at the same height. The height of the top of the block was used to calculate the height of the wind tunnel floor. The cathetometer was then used to measure the height of the probe tip for four vertical probe positions. By taking repeated cathetometer measurements of a point,

the error introduced by the cathetometer was found to be 0.6 percent[5,8]. LVDT voltages for each probe position were read by the DAS-20 A/D system. The floor height was subtracted from the measured probe heights to obtain probe displacement. A least squares fit with an accuracy of 0.1 percent was calculated for a linear equation that related displacement to voltage.

Expansion Ratio and Mass Flow Rate

The jet total pressure used in the acquisition of mixing data for the wedge-shaped nozzle was selected based on oil flow observations. The pressure was increased in 6.9 kPa increments starting at 41.4 kPa until a separation zone was visible in front of the jet. The highest pressure at which no separation zone was visible was 75.8 kPa and was selected as the jet total pressure for the wedge-shaped nozzle.

The expansion ratio was defined as the ratio of jet static pressure to the minimum static pressure required to choke the nozzle, or P_j/P_{choke}. P_{choke} for the wedge-shaped nozzle was determined by varying the jet total pressure and recording a corresponding helium mass rate of flow measured by the flowmeter. The ratio of helium flow to jet total pressure becomes constant when a nozzle is choked. Therefore, this ratio was plotted against jet static pressure to determine P_{choke}. For the wedge-shaped nozzle, P_{choke} was 25.5 kPa, yielding an expansion ratio of 1.45 for the selected test pressure of 75.8 kPa.

The mass flow rate of helium for the wedge-shaped nozzle was simply calculated from the flowmeter reading when the jet total pressure was set at 75.8 kPa. The mass flow rate of helium through the wedge-shaped nozzle was 0.00089 kg/s.

The discharge coefficient for the wedge-shaped nozzle was calculated by dividing the actual helium mass flow rate through the nozzle by the theoretical mass flow rate through the nozzle. The discharge coefficient for the wedge-shaped nozzle was 0.90.

The expansion ratio and mass flow rate of the circular nozzle were matched to the same values for the wedge-shaped nozzle. The circular nozzle was drilled to a certain diameter and its P_{choke} was determined in the same manner that P_{choke} for the wedge-shaped nozzle was. P_{choke} for the circular nozzle was multiplied by the expansion ratio of 1.45 to calculate the required jet total pressure for the circular nozzle. The discharge coefficient for the circular nozzle was determined at the calculated jet total pressure, and a new diameter was calculated. The procedure was repeated until the helium mass flow rate through the circular nozzle was matched to the mass flow rate of helium through the wedge-shaped nozzle. The discharge coefficient of the circular nozzle was also 0.90.

Data Acquisition Procedures

Mean flow data was obtained by first installing the desired nozzle insert into the nozzle block. The compressor was started so that storage tank pressure would be high enough to run the tunnel. A probe was installed, and the LVDT was calibrated. A FORTRAN driver program listed as Program 1 in Appendix B was loaded into the system control computer. The program opened the valve that controlled helium flow into the

plenum chamber, operated the wind tunnel, ran the traverse, and sent a signal that told Labtech Notebook, which was loaded into the data acquisition computer, to start acquiring data. The program also controlled the timing of all events.

When a run was to be initiated, the tunnel operator turned on the servo control circuit and executed the computer program. The program opened the helium valve, waited five seconds, then opened the pneumatic butterfly valve to run the wind tunnel. Five seconds later, the program initiated data acquisition and raised the probe. About thirteen seconds later, the computer closed the helium valve and the butterfly valve, and the tunnel operator turned off the servo control circuit to end the tunnel run. The first five second delay allowed the plenum pressure to stabilize, and the second five second delay allowed the tunnel pressure to stabilize.

All probes were raised at a speed of 3.8 mm/s to a height of approximately $20R_b$. This speed was found by repeating probe traverses at sequentially lower speeds until the profile was repeated[5]. Probe data was obtained at a sampling rate of 100 Hz.

Wind tunnel runs used to produce oil flow or nanoshadowgraph photographs were controlled by a simple FORTRAN driver program. The program controlled only the helium valve and the wind tunnel butterfly valve. After the photography system was positioned, the tunnel operator started the tunnel run as described earlier. The photographer waited about five seconds after the butterfly valve opened before taking an oil flow or nanoshadowgraph photograph. Each photographic run lasted about ten seconds. A series of five nanoshadowgraph photographs was required to completely record the flow field of each jet.

Data Reduction

Helium concentration was calculated from data representing probe displacement, pressure P_1, hot film voltage, and total temperature. Since total temperature was obtained from a separate probe, a computer program calculated a value of total temperature for each concentration probe displacement by linear interpolation. The program assumed a total temperature value at the temperature profile extreme for concentration displacements not covered by the total temperature profile. Although this assumption was necessary because of minor differences in the probe displacements, it did not significantly affect the experimental results since the total temperature variation at both extremes of a profile was small. The FORTRAN program listed as Program 2 in Appendix B calculated helium concentration. For each probe displacement, the program sequentially searched for two calibration curves that bounded the hot film voltage at the appropriate P_1. A concentration value for the hot film voltage, P_1 data pair was then linearly interpolated from the two bounding curves.

Helium concentration, Pitot pressure, cone-static pressure, and total temperature profiles were used to calculate profiles of Mach number, static pressure, total pressure, static temperature, density, local speed of sound, flow velocity, and mass flux. After Pitot pressure and cone-static pressure profiles were aligned with concentration probe displacements as described earlier, a FORTRAN program listed as Program 3 in Appendix B performed the calculations under the assumption of calorically perfect, adiabatic flow. Values of γ and R were computed according to the helium concentration at each displacement point. Mach number was found with the cone-flow and Rayleigh-Pitot

equations. The cone-flow equation relates Mach number to the pressure on the surface of a cone:

$$\frac{P_c}{P_1} = 1 + \frac{\gamma M_1^2}{2} \frac{(P_c - P_1)}{q_1}$$

Static pressure dependence was eliminated by combining the cone-flow equation with the Rayleigh-Pitot equation:

$$\frac{P_1}{P_{t2}} = \frac{\left(\frac{2\gamma}{\gamma+1} M_1^2 - \frac{\gamma-1}{\gamma+1}\right)^{\frac{1}{\gamma-1}}}{\left(\frac{\gamma+1}{2} M_1^2\right)^{\frac{\gamma}{\gamma-1}}}$$

The derived relationship between Mach number, M_1, and the known quantities P_c, P_{t2}, and γ was used to generate a table of Mach numbers as a function of γ and the ratio P_c/P_{t2} for a 10° half angle cone. The program determined the Mach number by interpolation over γ and P_c/P_{t2} in the Mach number table. Static pressure, P_1, was then determined from the Rayleigh-Pitot equation. The derived relationship would have become invalid if the Mach number had dropped below 1.2 because the shock wave on the cone-static probe detaches. Although this did not occur, the program was written so that it could determine when the relationship became invalid and could calculate the Mach number using an appropriate method.

After complete profiles of Mach number and static pressure were computed, the program calculated profiles for the remaining flow quantities. Total pressure was calculated from Pitot pressure by the normal shock equation:

$$P_{t1} = P_{t2}\left[\frac{(\gamma-1)M_1^2+2}{(\gamma+1)M_1^2}\right]^{\frac{\gamma}{\gamma-1}}\left[\frac{2\gamma M_1^2-(\gamma-1)}{\gamma+1}\right]^{\frac{1}{\gamma-1}}$$

Since T_{t1} equals T_{t2} across a normal shock, static temperature was calculated from the isentropic relation:

$$T_1 = \frac{T_{t2}}{1+\frac{\gamma-1}{2}M_1^2}$$

The perfect gas law was used to calculate density:

$$\rho_1 = \frac{P_1}{RT_1}$$

The local speed of sound was determined from its perfect gas definition:

$$a_1 = \sqrt{\gamma RT_1}$$

Velocity was calculated from the Mach number definition:

$$u_1 = M_1 a_1$$

Total mass flux was found by multiplying density by velocity.

Each value was paired with its corresponding probe displacement to create complete profiles of flow quantities. A digital filter computer program was used to smooth the data. Also, every ten data pairs of mass fraction, probe displacement were averaged into a single data pair to decrease the amount of time required to create the contour plots.

Nondimensionalization Method

Since the shape of each nozzle rather than its size was to be used as the basis for comparison, the respective diameter (or equivalent diameter in the case of the wedge-shaped nozzle) of each nozzle could not be used as a nondimensionalization parameter. A nondimensionalization parameter that had the same value for both nozzles was required. Therefore, an effective radius (R_b) defined only in terms of flow parameters was used to reflect the matched flow conditions of the wedge-shaped nozzle and the circular nozzle. R_b is the approximate nose radius of a solid body used to represent the obstruction to the free stream created by the injected helium and is independent of nozzle size[20]. All distances were nondimensionalized by R_b, which was determined from the injected helium mass flow rate and free stream conditions:

$$R_b = \sqrt{\frac{\dot{m}_j}{\rho_\infty u_\infty}}$$

R_b had a value of 1.56 mm for both nozzles.

Helium concentration was converted from mole fraction to mass fraction according to:

$$\alpha_{He} = X_{He} \frac{MW_{He}}{MW_{mix}}$$

All other mean flow quantities were nondimensionalized by their free stream values. Free stream static pressure was calculated from the isentropic relation:

$$P_\infty = \frac{P_{t\infty}}{\left(1 + \frac{\gamma - 1}{2} M_\infty^2\right)^{\frac{\gamma}{\gamma - 1}}}$$

Free stream static temperature was found from the isentropic equation:

$$T_\infty = \frac{T_{t\infty}}{1 + \frac{\gamma - 1}{2} M_\infty^2}$$

Free stream density was calculated with the perfect gas law:

$$\rho_\infty = \frac{P_\infty}{R T_\infty}$$

The free stream speed of sound was found from:

$$a_\infty = \sqrt{\gamma R T_\infty}$$

The free stream velocity was computed from the Mach number definition:

$$u_\infty = M_\infty a_\infty$$

Finally, free stream mass flux was calculated by multiplying the free stream density by the free stream velocity.

RESULTS

Boundary layer separation zone photographs were obtained using the oil flow method. Composite nanoshadowgraph photographs of the flow field of both jets were assembled. Contour plots of concentration at each axial station were made for both jets. Plots of core center penetration, maximum concentration, overall penetration, hydrogen-air lean limit area, and hydrogen-air lean limit centroid were made. Vertical profiles of the other mean flow data were plotted for each lateral station.

Oil Flow Photographs

Figure 12 shows the oil flow photographs of both jets. The oil flow for the circular nozzle shows a well-defined three-dimensional boundary layer separation zone in front of the jet. However, the oil flow for the wedge-shaped nozzle shows that very little separation occurs in front of the jet. The recirculation zone immediately downstream of both jets was about the same size in each case.

Nanoshadowgraph Photographs

Figures 13 and 14 are nanoshadowgraphs of the injection flowfields from the circular and wedge-shaped nozzles, respectively. The jet entry point and axial stations are labeled. The Mach 3 free stream runs from left to right in the photographs.

Figure 13 shows the injection flowfield from the circular nozzle. The jet shock wave angle was 39° in the boundary layer and 27° in the free stream. The jet appears to penetrate the free stream slightly at approximately $x/R_b=51$; at $x/R_b=74$, the jet finally left the boundary layer and created a region of turbulence between the boundary layer and the free stream. By $x/R_b=97$, the turbulent region penetrated $8.3R_b$ into the free stream, and at $x/R_b=201$, penetration was $9.6R_b$. The turbulent region penetration increased 16 percent between $x/R_b=97$ and $x/R_b=201$.

The nanoshadowgraph for the wedge-shaped nozzle is shown in Figure 14. A weak secondary shock that branched off parallel to the main jet shock was present. The jet shock wave angle was 37° in the boundary layer and 26° in the free stream. The shock wave angles for the wedge-shaped nozzle were about the same as the shock wave angles for the circular nozzle since the flow conditions of the two jets were matched. The jet left the boundary layer at approximately $x/R_b=45$ and remained above it. By $x/R_b=56$, turbulent penetration into the free stream was $6.4R_b$; at $x/R_b=97$, penetration was $8.3R_b$; and by $x/R_b=201$, the turbulent region penetrated $12R_b$ into the free stream. The turbulent region grew 47 percent between $x/R_b=97$ and $x/R_b=201$. At the last

station, $x/R_b = 201$, the turbulent region of the wedge-shaped nozzle penetrated 27 percent more than the turbulent region of the circular nozzle.

Concentration Data

Flowfield Structure

Helium concentration data is presented in the form of contour plots at each axial station. The plots extend laterally $6R_b$ from each side of the nozzle centerline for the first two axial stations and $8R_b$ from each side of the nozzle centerline for the third axial station. Concentration data was acquired to an elevation of $21R_b$ above the wind tunnel floor, but a height of $16R_b$ for the contour plots adequately bounded the flow field of each jet. The contour plots show the maximum helium mass fraction and its location in the flow field. The first contour line represents the approximate lean limit mass fraction for homogeneous H_2-air deflagration at ambient conditions. The centroid of the area bounded by this lean-limit line is marked. After the first contour line, the contour lines proceed at regular intervals of 0.01 helium mass fraction for the first two axial stations and 0.005 helium mass fraction for the third axial station.

The circular nozzle contour plots are shown in Figures 15 - 17. At the first axial station ($x/R_b=56$), the core of the jet, defined as the region of maximum helium mass fraction, was located along the nozzle centerline at an elevation above the plate of $z/R_b=3.4$. By the second axial station ($x/R_b=97$), the core remained along the nozzle centerline but began dividing into two regions, a large one above the boundary layer at $z/R_b=5.2$ and a much smaller one within the boundary layer at $z/R_b=1.7$ as shown in Figure 16. At this position, the boundary layer height is approximately $3.2R_b$, as determined from the nanoshadowgraphs. The contour plot at $x/R_b=201$, Figure 17,

shows that the two core regions continued to divide and grow. The lateral position of the core region within the boundary layer drifted away from the nozzle centerline to y/R_b=-2.0 (indicating a slightly non-symmetric tunnel condition), while the core region above the boundary layer remained along the nozzle centerline. The vertical positions of the split core were z/R_b=1.2 and z/R_b=5.8. Figure 18 shows a stacked contour plot for the circular nozzle that illustrates the growth of the jet and the division of the core region.

Contour plots for the wedge-shaped nozzle can be seen in Figures 19 - 21. At the first station, x/R_b=56, the core of the jet was located at y/R_b=2.0 and z/R_b=5.2. By x/R_b=97, as shown in Figure 20, the core had moved toward the nozzle centerline and was centered at y/R_b=1.0 and z/R_b=6.7. Figure 21 shows that the core region at x/R_b=201 was along the nozzle centerline and at z/R_b=9.5. The core region did not bifurcate as rapidly as it did for the circular nozzle, but a smaller core region within the boundary layer began forming by the third axial station, as shown in Figure 21. If data had been acquired at another axial station further downstream, a better developed core region within the boundary layer would probably have been found. The growth of the area bounded by the lean-limit contour can be seen in the stacked contour plot of Figure 22.

Jet Core Center Penetration

Core center (region of maximum concentration) penetration as a function of axial distance is shown in Figure 23. The data fit a logarithmic equation of the form:

$$\frac{h_{core}}{R_b} = \eta_1 \log\left(\frac{x}{R_b}\right) + \beta_1$$

where η_1 and β_1 were determined by a curve fit. The rate of penetration of the core center is represented by η_1.

Two curves represent the core center penetration for the circular nozzle because the core divided. The curve labeled *Circle 1* is the core region that remained in the boundary layer, while the curve labeled *Circle 2* is the core region that penetrated into the free stream. The rate of core center penetration for *Circle 1* was $\eta_1 = -3.8$, and the rate of core center penetration for *Circle 2* was $\eta_1 = 4.1$.

The core center penetration for the wedge-shaped nozzle is also shown in Figure 23. The penetration rate of the core center for the wedge-shaped nozzle was $\eta_1 = 7.8$, which was 89 percent greater than the rate for the circular nozzle. The absolute value of the core center penetration for the wedge-shaped nozzle was 53 percent greater than the value for the circular nozzle at $x/R_b = 56$ and 64 percent greater at $x/R_b = 201$.

Maximum Helium Concentration Decay

Figure 24 shows the variation of maximum helium concentration with axial distance for both nozzles. Since the maximum helium concentration decayed exponentially, the following relation was used to compare the data:

$$\alpha_{max}=\beta_2(\frac{x}{R_b})^{-\eta_2}$$

where β_2 and η_2 were determined from a curve fit. The exponent, η_2, represents the decay rate of the jet. The decay rate indicates the mixing speed of the jet with the free stream. The higher the decay rate, the faster the jet mixed with the free stream. The hydrogen concentration necessary for complete combustion with air was marked on the decay plot for reference.

The decay rates and distances to stoichiometric H_2-air concentration were essentially the same for both nozzles. The rate of maximum helium concentration decay for the jet from the wedge-shaped nozzle was $\eta_2=0.86$, which was 6.6 percent less than the rate of maximum helium concentration decay for the jet from the circular nozzle, $\eta_2=0.92$. If the decay rates remained constant past $x/R_b=201$, the distance required for the jet from the circular nozzle to reach stoichiometric H_2-air concentration would be $260R_b$, whereas the distance for the jet from the wedge-shaped nozzle would be $262R_b$, or less than one percent more than for the jet from the circular nozzle.

The maximum helium concentration for injection from the wedge-shaped nozzle was 14 percent less than that for the circular nozzle at $x/R_b=56$. By $x/R_b=201$, the concentration for the wedge-shaped nozzle was only 5.6 percent less than the value for the circular nozzle.

Overall Penetration

The overall penetration at each axial station is displayed in Figure 25. The overall penetration is defined as the first point above the jet core center which has a helium mass fraction less than 0.0007[2]. The data again fit a logarithmic equation, where η_1 and β_1 were again determined by a curve fit. In this case, η_1 represents the rate of overall penetration of the jet.

The penetration rate for the jet from the circular nozzle was $\eta_1=6.5$. The penetration rate for the jet from the wedge-shaped nozzle was $\eta_1=9.2$, which is 42 percent greater than for the jet from the circular nozzle. The overall penetration of the jet from the wedge-shaped nozzle was 4.2 percent less than the overall penetration of the jet from the circular nozzle at $x/R_b=56$, but grew to be 9.4 percent greater at $x/R_b=201$.

Hydrogen-Air Lean Limit Area

The area of the region bounded within the homogeneous H_2-air deflagration lean limit contour is shown in Figure 26. The area was made dimensionless by dividing it by R_b^2. The data fit a logarithmic curve and the constants η_1 and β_1 were determined by a curve fit. The rate of H_2-air lean limit area growth is indicated by the coefficient η_1.

The rate of area growth is a good indication of how well a jet expands in both the lateral and vertical directions. The rate of area growth was $\eta_1=112$ for the circular case and $\eta_1=182$ for the wedge-shaped case, an increase of 63 percent above that of the circular case. At the first axial station, $x/R_b=56$, the lean limit area of the jet from the wedge-shaped nozzle was 24 percent less than the lean limit area of the jet from the

circular nozzle. However, by $x/R_b=201$, the lean limit area of the jet from the wedge-shaped nozzle had increased to be 14 percent greater than the lean limit area of the jet from the circular nozzle.

Hydrogen-Air Lean Limit Centroid

The location of the centroid of the region bounded by the H_2-air deflagration lean limit is shown in Figure 27. The data also fit a logarithmic form, but in this case η_1 represents the rate of penetration of the centroid of the jet.

The centroid penetration rate for the jet from the wedge-shaped nozzle was $\eta_1=3.2$. The jet from the circular nozzle had a rate of centroid penetration of $\eta_1=2.4$. Consequently, the wedge-shaped nozzle had a centroid penetration rate that was 31 percent greater than that of the circular nozzle. Also, the centroid of the jet from the wedge-shaped nozzle at each axial station was higher than the centroid of the jet from the circular nozzle. At $x/R_b=56$, the centroid of the jet from the wedge-shaped nozzle was 8.7 percent higher than the centroid of the jet from the circular nozzle. By $x/R_b=201$, the centroid of the jet from the wedge-shaped nozzle had increased to be 14 percent higher than the centroid of the jet from the circular nozzle.

Other Mean Flow Results

Data Profiles

Figures 28 - 108 show profiles of other flow parameters at each lateral and axial station. The profiles of each quantity reflect the mixing and penetration results described earlier.

Total pressure profiles are shown in Figures 28 - 36, and static pressure profiles are shown in Figures 37 - 45. The total pressure profiles near the nozzle centerline show that the total pressure of both jets decreased rapidly below a certain point. As axial distance increased, the rapid decrease occurred at a greater height, which showed the penetration of the jets. The static pressure profiles show that static pressure gradients tended to increase with increasing axial distance.

Total temperature and static temperature are shown in Figures 46 - 54 and Figures 55 - 63, respectively. The total temperature remained within two percent of its free stream value throughout all profiles. Near the wind tunnel floor, the static temperature was almost twice its free stream value. Both jets had static temperature gradients near the nozzle centerline that became smaller with increasing axial distance.

Mach number profiles are shown in Figures 64 - 72. Similar to the total pressure, the Mach number also decreased rapidly from its free stream value below a certain height. This height also increased with increasing axial distance.

Figures 73 - 81 show the local speed of sound at each station. Near the tunnel centerline and at the first station, high helium concentrations caused the local speed of

sound to increase rapidly over its value in the free stream. As the helium jet mixed with the free stream, the peak value decreased and its height increased.

Velocity profiles are shown in Figures 82 - 90. Although the profiles had small gradients near the nozzle centerline at all three axial stations, they mostly resembled the velocity profile of an undisturbed boundary layer.

Figures 91 - 99 and figures 100 - 108 show the density profiles and the mass flux profiles, respectively. Near the jet centerline, the density decreased rapidly from its free stream value because of the penetration of the lower density helium into the free stream air. The mass flux profiles followed the same trends as the density profiles.

Integrated Mass Flow Rate

The FORTRAN program listed as Program 4 in Appendix B was used to integrate the helium mass flow rate through each axial station from the mass flux profiles. The program calculated the helium mass flux for each lateral station by multiplying the mass fraction profile by the corresponding total mass flux profile. At each axial station, the vertical integration was accomplished by obtaining a Reimann sum of each helium mass flux profile, and the horizontal integration was accomplished by using Simpson's rule across the axial station. The integrated mass flow rates for the wedge-shaped nozzle were 0.0006 kg/s, 0.0013 kg/s, and 0.0013 kg/s for the first, second, and third axial stations, respectively. The integrated mass flow rates for the circular nozzle at the first, second, and third axial stations were 0.0010 kg/s, 0.0013 kg/s, and 0.0011 kg/s, respectively.

Reliability of Results

A comparison of the integrated mass flow rate results with the mass flow rates measured by the flowmeter show that for the worst case, the integrated results for both nozzles were about 46 percent greater than the measured results. To determine the source of this discrepancy, an uncertainty analysis (Appendix A) was performed using the methods of Kline and McClintock[21] and Moffat[22].

The mass rate of flow errors result from uncertainties in the measured flow quantities, the integration method, and the vertical probe location. The uncertainty analysis shows that the errors in flow quantities may result in an error as high as 15 percent for the total mass flux profiles. The mass flow rate integration method adds to the error because of the large increments between each data profile across an axial station. The uncertainty analysis shows that the maximum vertical location error is only about 2.1 percent of the full traverse height of 33 mm, but this 0.7 mm error results in larger accumulated flow quantity errors in the high shear regions of the flow. A 0.7 mm location error in a high shear region leads to a possible Mach number error of 11 percent. This Mach number error results in a total mass flux error greater than 30 percent. Therefore, the total possible error in the integrated mass rate of flow may be greater than 50 percent.

Although the mass rate of flow error is 46 percent, the maximum helium concentration error is only 5 percent. Since the same instrumentation and experimental procedures were used for both nozzles and the comparisons of the nozzles were based on

quantities derived directly from concentration data, the results of this investigation are valid.

DISCUSSION

Since the expansion ratio and the mass rate of flow of the wedge-shaped nozzle and the circular nozzle were matched, any advantages in the mixing performance of one nozzle over the other should be the result of the geometric difference only. The geometric difference causes changes in the system of shock waves in front of the nozzle, which lead to a change in the boundary layer separation zone in front of the nozzle[16]. Although nanoshadowgraphs showed that both jet shock waves were about the same strength, oil flow photographs showed that the wedge-shaped nozzle had no boundary layer separation zone in front of it. The absence of a separation zone indicates that the shock wave system for the wedge-shaped nozzle is probably different from the shock wave system for the circular nozzle, but the difference was not detected in the nanoshadowgraphs.

The contour plots show that at the first axial station, the core center of the jet from the wedge-shaped nozzle was located laterally at $y/R_b=2.0$. By the third axial station, the core center of the jet was located at $y/R_b=0.0$. Similarly, the core center of the jet from the circular nozzle drifted laterally from $y/R_b=0.0$ at the second axial station to $y/R_b=-2.0$ at the third axial station. The lateral drift of the jet from the wedge-shaped nozzle from the injection point to the first axial station may be a result of the instability of the thin jet structure. A slight asymmetry in the shock system could divert the jet away from the nozzle centerline. The drift towards the negative lateral stations exhibited

by both jets further downstream is a result of slight tunnel asymmetry, which has been previously observed[5]. All lateral deviations were small compared to the axial distances involved.

Both jets developed split cores -- one core that penetrated into the free stream and another core that remained within the boundary layer. The core of the jet from the circular nozzle began dividing by the second axial station, and the core of the jet from the wedge-shaped nozzle began dividing by the third axial station. The core division may have been a result of low velocity within the boundary layer minimizing mixing near the wall (see Figures 82 - 90).

In order to compare the nozzles, parameters describing mixing performance were calculated. Based on the degree of confidence in the data measurements, the primary comparison parameters included the maximum helium concentration decay rate, the core center penetration, and the growth of a defined jet area. The secondary comparison parameters included the overall penetration and the penetration of the centroid of the jet area.

The maximum concentration decay rate, the most widely used basis of comparison for gas mixing, is the rate at which the mass fraction of helium decays with axial distance. A high decay rate indicates a large amount of mixing of fuel and air. The decay rate for the wedge-shaped nozzle was 6.6 percent less than the decay rate for the circular nozzle.

A comparison method related to decay rate is the mixing distance. The mixing distance is the axial distance at which the concentration of fuel reaches the value required

for complete combustion with air. The mixing distances for both nozzles were essentially the same, indicating that the circular nozzles in a combustor could be replaced with matched wedge-shaped nozzles without increasing the length of the combustor.

Core center penetration and overall penetration provide alternative ways of comparing mixing performance. Jet penetration into the free stream is critical for large scale mixing because it allows more of the injected fuel to become entrained in the air. The core center is defined as the region of maximum fuel concentration within the jet. Core center penetration tells whether the main part of the jet is moving into the free stream or remaining in the boundary layer. The core of the jet from the circular nozzle split into two core center regions -- one that remained in the boundary layer and a second one that penetrated into the free stream. The jet from the wedge-shaped nozzle had only one core center which penetrated into the free stream 64 percent further than the main core of the jet from the circular nozzle. The rate of change of the core center penetration from the first axial station to the third axial station for the wedge-shaped nozzle was 89 percent greater than that of the circular nozzle.

Overall penetration is a measure of how far the outer regions of the fuel jet move into the free stream. Overall penetration is defined as the first point above the jet core center that has a fuel mass fraction less than 0.0007^2. The rate of overall penetration of the jet from the wedge-shaped nozzle was 42 percent greater than the rate of overall penetration of the jet from the circular nozzle. It should be noted that if other mass fraction contours (such as 0.003 or 0.010 instead of 0.0007) are used to define overall penetration, the same trend occurs.

Since a single, normal jet has a three-dimensional flow field, a measurement of the lateral spreading of the jet also provides a basis for mixing comparison. Expansion in the lateral direction provides a greater jet surface area that can lead to faster mixing with the free stream. The growth of a defined cross-sectional area of a jet indicates how well the jet expands in both the lateral and vertical directions. The cross-sectional area used in this research was defined to be the area of the jet within the lean limit for homogeneous hydrogen-air deflagration. The rate of growth of this area for the jet from the wedge-shaped nozzle was 63 percent greater than the rate of area growth for the jet from the circular nozzle.

Another type of penetration is the location of the centroid of the lean limit area defined above. As the centroid penetrates higher into the free stream, more fuel jet surface area is exposed to the supersonic free stream, which enhances mixing and combustion. The rate of penetration of the centroid for the jet from the wedge-shaped nozzle was 31 percent greater than the rate of centroid penetration for the jet from the circular nozzle. Also, the centroid for the jet from the wedge-shaped nozzle was higher than the centroid for the jet from the circular nozzle at all three axial stations.

Since the comparison parameters show that injection through the wedge-shaped nozzle results in better jet penetration and mixing with the free stream, the wedge-shaped nozzle is the better choice for a scramjet fuel injection system. The performance of a combustor utilizing circular nozzles could be improved without increasing its length by replacing the circular nozzles with matched wedge-shaped nozzles.

CONCLUSIONS AND RECOMMENDATIONS

The experimental investigation that was performed documented the flow fields of helium jets from a normal circular nozzle and a normal wedge-shaped nozzle. The expansion ratio and the mass rate of flow of the nozzles were matched in order to investigate the effect of their geometry on mixing. The jets were compared based on oil flow photographs, nanoshadowgraph photographs, and several mixing parameters calculated from helium concentration data.

The oil flow photographs showed that the wedge-shaped nozzle had no three-dimensional separation zone in front of it. The circular nozzle, however, had a very large separation zone in front of it. The absence of a separation zone in front of the wedge-shaped nozzle may have been caused by a difference in the jet's system of shock waves. Future investigations into the shock wave system of the wedge-shaped nozzle may lead to a better understanding of why the jet from the wedge-shaped nozzle mixes better than the jet from the circular nozzle.

The wedge-shaped nozzle performed better than the circular nozzle in all but one comparison parameter. The decay rate of the circular nozzle was slightly better than the decay rate of the wedge-shaped nozzle, but the core center penetration, overall penetration, cross-sectional area growth, and centroid penetration of the wedge-shaped nozzle were much better than the same parameters for the circular nozzle. Based on the comparison parameters, a combustor utilizing wedge-shaped nozzles would have a better

performance than a combustor utilizing circular nozzles. Also, a combustor using wedge-shaped nozzles would have a longer life span since no hot spots that could degrade the combustor exist in front of the nozzles.

Although it was not evaluated, the total pressure loss due to fuel injection through the wedge-shaped nozzle should be less than the total pressure loss due to fuel injection through the circular nozzle because a normal shock does not exist in front of the jet from the wedge-shaped nozzle. Therefore, a combustor utilizing wedge-shaped nozzles would perform better due to a smaller momentum loss.

Further investigations using the wedge-shaped nozzle should be performed to determine its heat transfer characteristics and to provide a more detailed aerodynamic analysis of its effects on mixing.

BIBLIOGRAPHY

1. "The 20 Most Wanted," *Electronics*, May 1990, p. 23.

2. Rogers, R. C., "A Study of the Mixing of Hydrogen Injected Normal to a Supersonic Airstream," NASA TN L-7386, Langley Research Center, September 1971.

3. Rogers, R. C., "Mixing of Hydrogen Injected from Multiple Injectors Normal to a Supersonic Airstream," NASA TN L-7896, Langley Research Center, September 1971.

4. McClinton, C. R., "The Effect of Injection Angle on the Interaction Between Sonic Secondary Jets and a Supersonic Free Stream," NASA TN-L 8125, Langley Research Center, February 1972.

5. Mays, R. B., "Experimental Investigation of Sonic Helium Injection at a Low Downstream Angle into Supersonic Flow," M. S. Thesis, Virginia Polytechnic Institute and State University, June 1990.

6. Yates, C. L., "Two-Dimensional, Supersonic Mixing of Hydrogen and Air Near a Wall," NASA CR-1793, The Johns Hopkins University, Applied Physics Laboratory, March 1971.

7. Kwok, F. T., Andrew, P. L., Ng, W. F., and Schetz, J. A., "Experimental Investigation of a Supersonic Shear Layer with Slot Injection of Helium," AIAA Technical Paper 90-0093, January 1990.

8. Smith, B. R., "Mean Flow Measurements of Heated Supersonic Slot Injection into a High Reynolds Number Supersonic Stream," M. S. Thesis, Virginia Polytechnic Institute and State University, February, 1989.

9. Thomas, R. H. and Schetz, J. A. and Billig, F. S., "Gaseous Injection in High Speed Flow," Paper presented at the Ninth International Symposium on Air Breathing Engines, Athens, Greece, Sept. 3-8, 1989.

10. Schetz, J. A. and Billig, F. S., "Penetration of Gaseous Jets Injected into a Supersonic Stream," *Journal of Spacecraft and Rockets*, Vol 3., No. 11, November 1966, pp. 1658-1664.

11. Billig, F. S., Orth, R. C., and Lasky, M., "A Unified Analysis of Gaseous Jet Penetration," AIAA Journal, Vol. 9, No. 6, June 1971, pp. 1048-1058.

12. Bussing, T. R. A., Lidstone, G. L., "A Model for 3-D Sonic/Supersonic Transverse Fuel Injection into a Supersonic Air Stream," AIAA-89-0460, January 1989.

13. Warfield, M. J., "Calculation of Supersonic Interacting Jet Flows," AIAA-89-0666, January 1989.

14. Yu, S., and Shuen, J., "Three-Dimensional Simulation of an Underexpanded Jet Interacting with a Supersonic Cross Flow," AIAA 88-3181, July 1988.

15. Heister, S., and Karagozian, A., "The Gaseous Jet in Supersonic Crossflow," AIAA 89-2547, July 1989.

16. Masyakin, N. E. and Polyanskii, M. N., "On the Possibility of Blowing a Gas Jet into a Supersonic Flow without Formation of a Three-Dimensional Boundary-Layer Separation Zone," *Izvestiya Akademii Nauk SSSR, Mekhanika Zhidkosti i Gaza*, No. 3, pp. 162-165, May-June 1979.

17. Ng, W. F., Kwok, F. T., and Ninnemann, T. A., "A Concentration Probe for the Study of Mixing in Supersonic Shear Flows," AIAA-89-2459, July 1989.

18. Campbell, R. L., "Experimental Study of Supersonic Slot Injection into a Supersonic Stream," M. S. Thesis, Virginia Polytechnic Institute and State University, 1987.

19. Trans-Tek, Incorporated, "Displacement Transducer DC-DC Series 240," Bulletin S012-0030-KHD, May 1989.

20. Schetz, J. A., "Interaction Shock Shape for Transverse Injection in Supersonic Flow," *Journal of Spacecraft and Rockets*, Vol. 7, No. 2, February 1970, pp. 143-148

21. Kline, S. J., and McClintock, F. A., "Describing Uncertainties in Single-Sample Experiments," *Mechanical Engineering*, January 1953, p. 3.

22. Moffat, R. J., "Contributions to the Theory of Single-Sample Uncertainty Analysis," *Journal of Fluids Engineering*, Vol. 104, June 1982, p. 250.

FIGURES

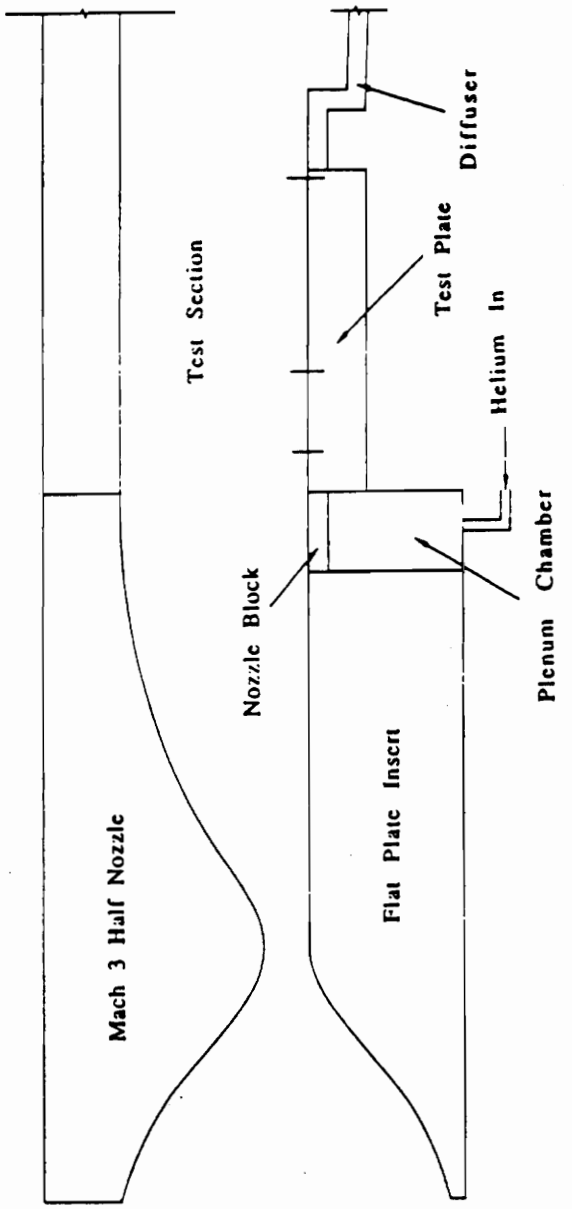

Figure 1. Mach 3 Test Section.

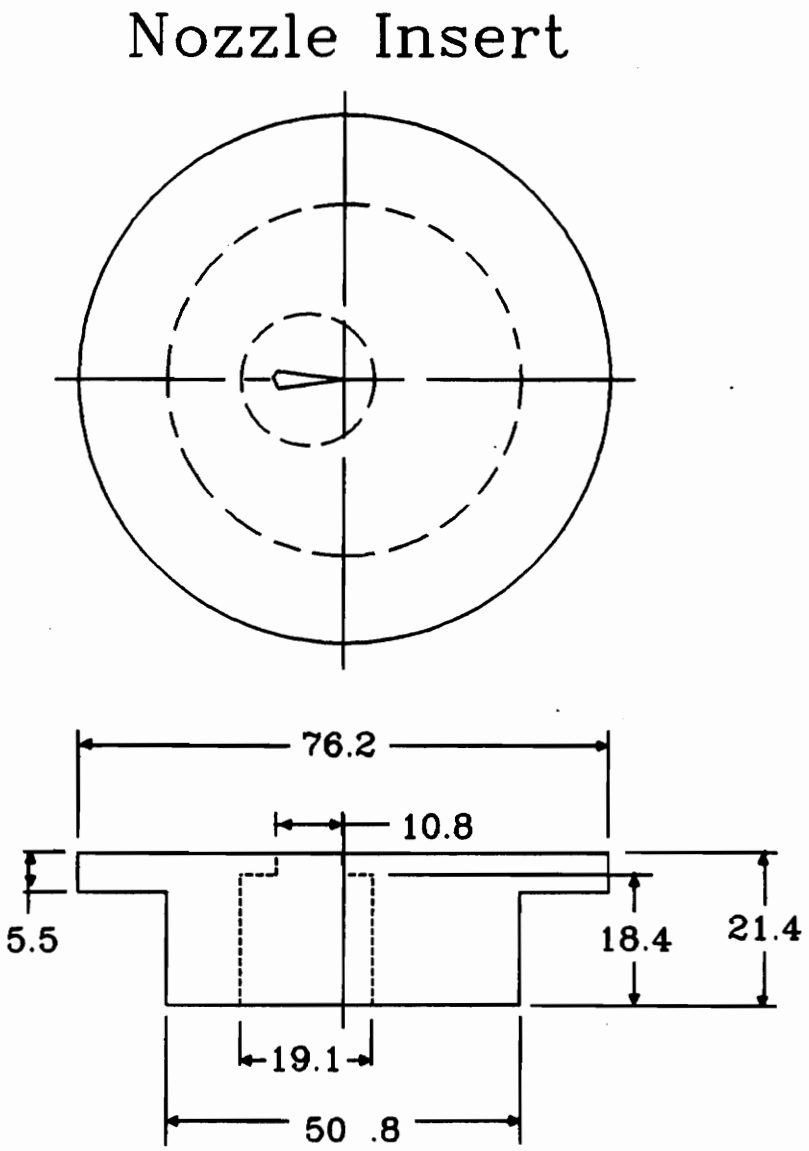

Figure 2. Nozzle Insert.

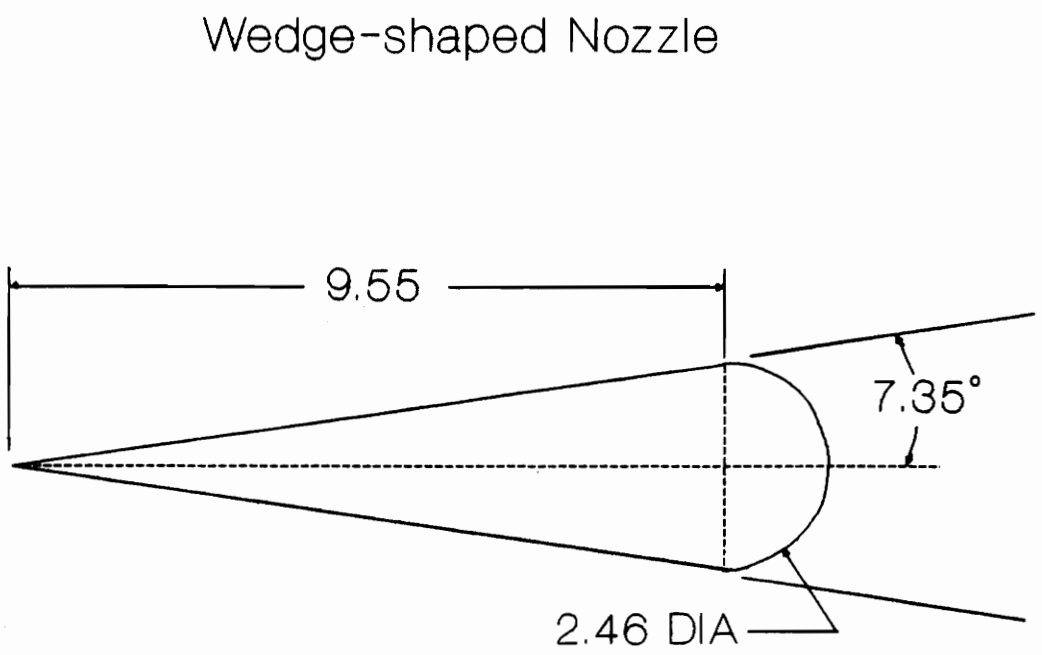

Figure 3. Wedge-shaped Nozzle Dimensions (mm).

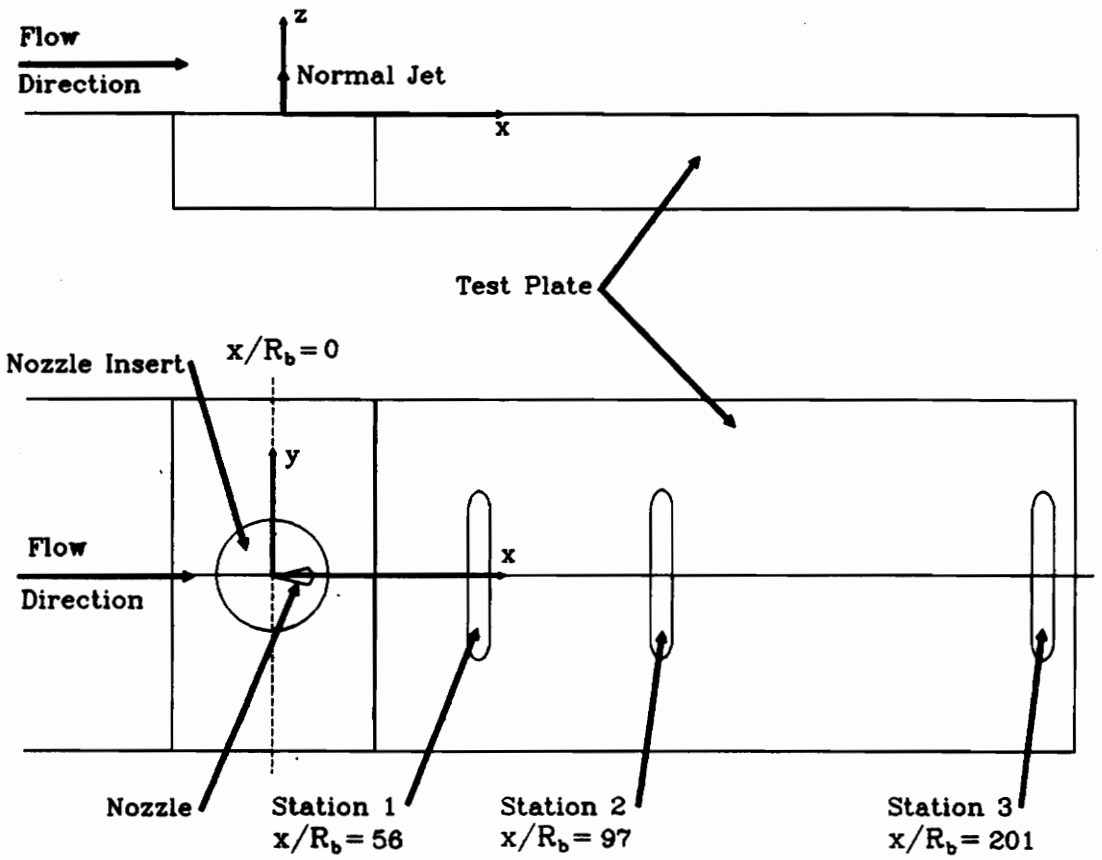

Figure 4. Instrumentation Positions.

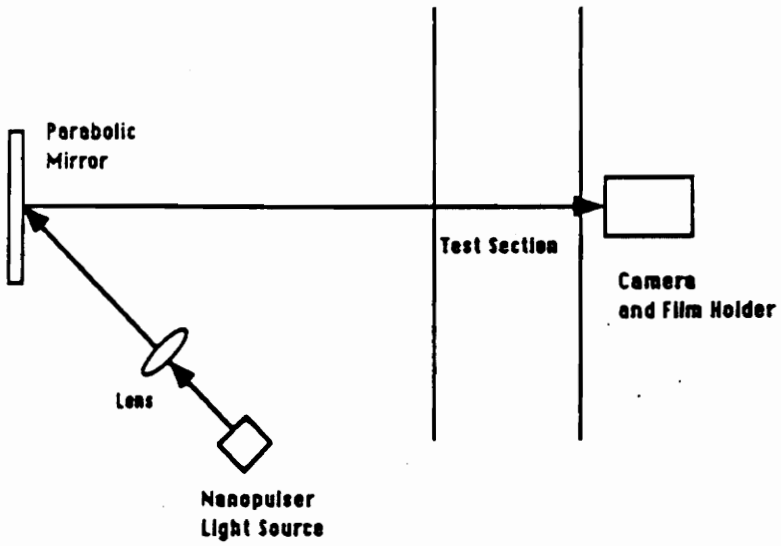

Figure 5. Nanoshadowgraph Configuration.

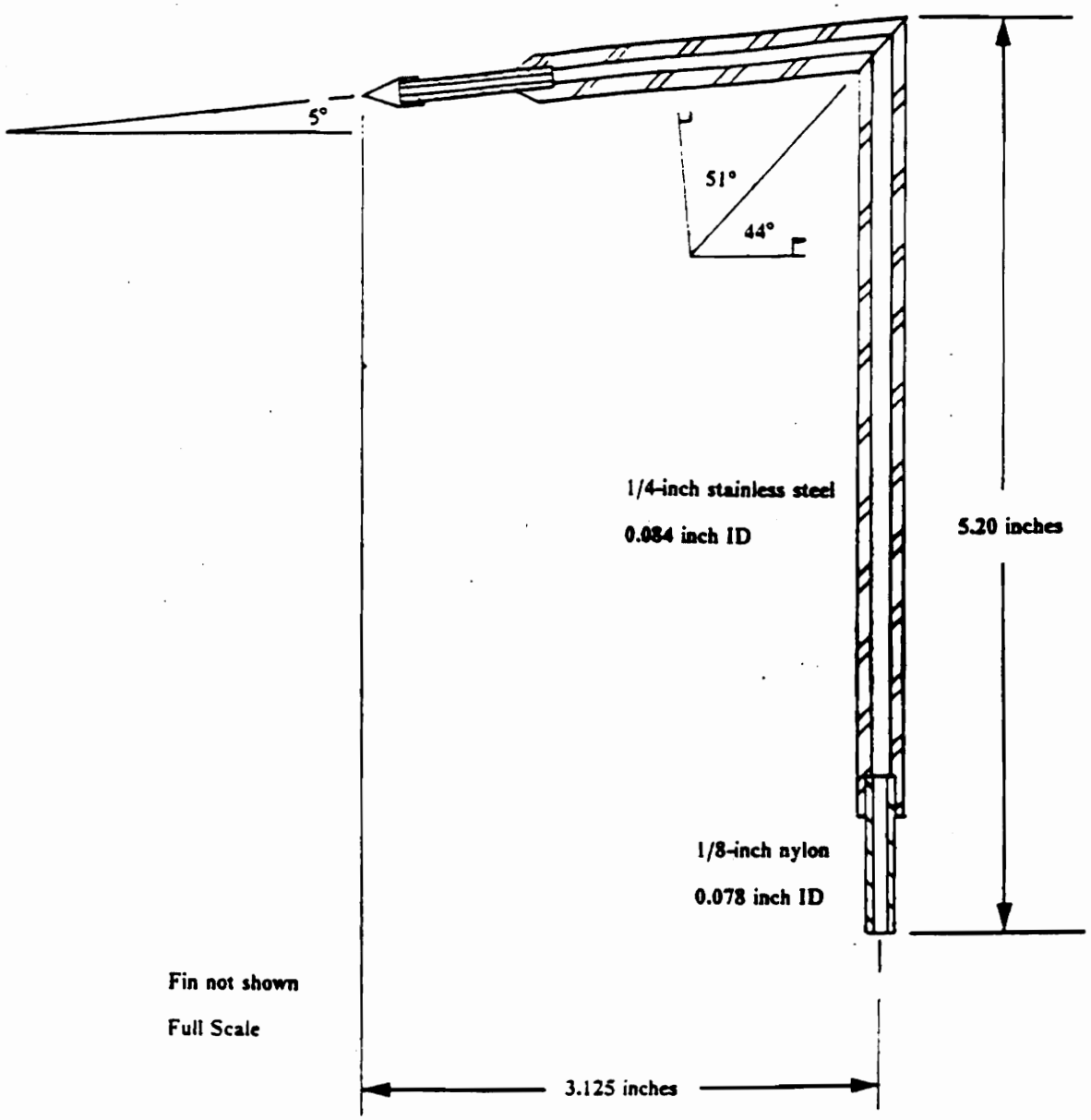

Figure 6. Concentration Probe.

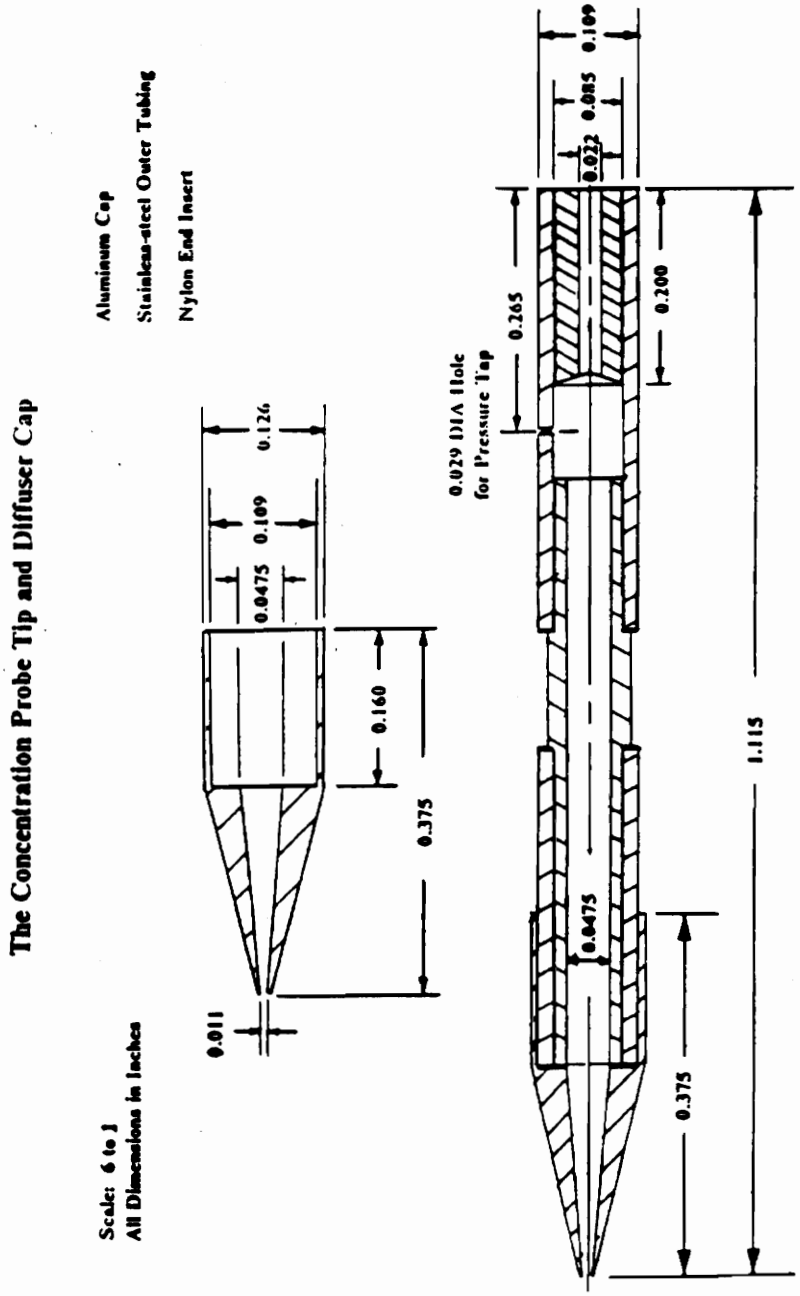

Figure 7. Cross-section of Concentration Probe.

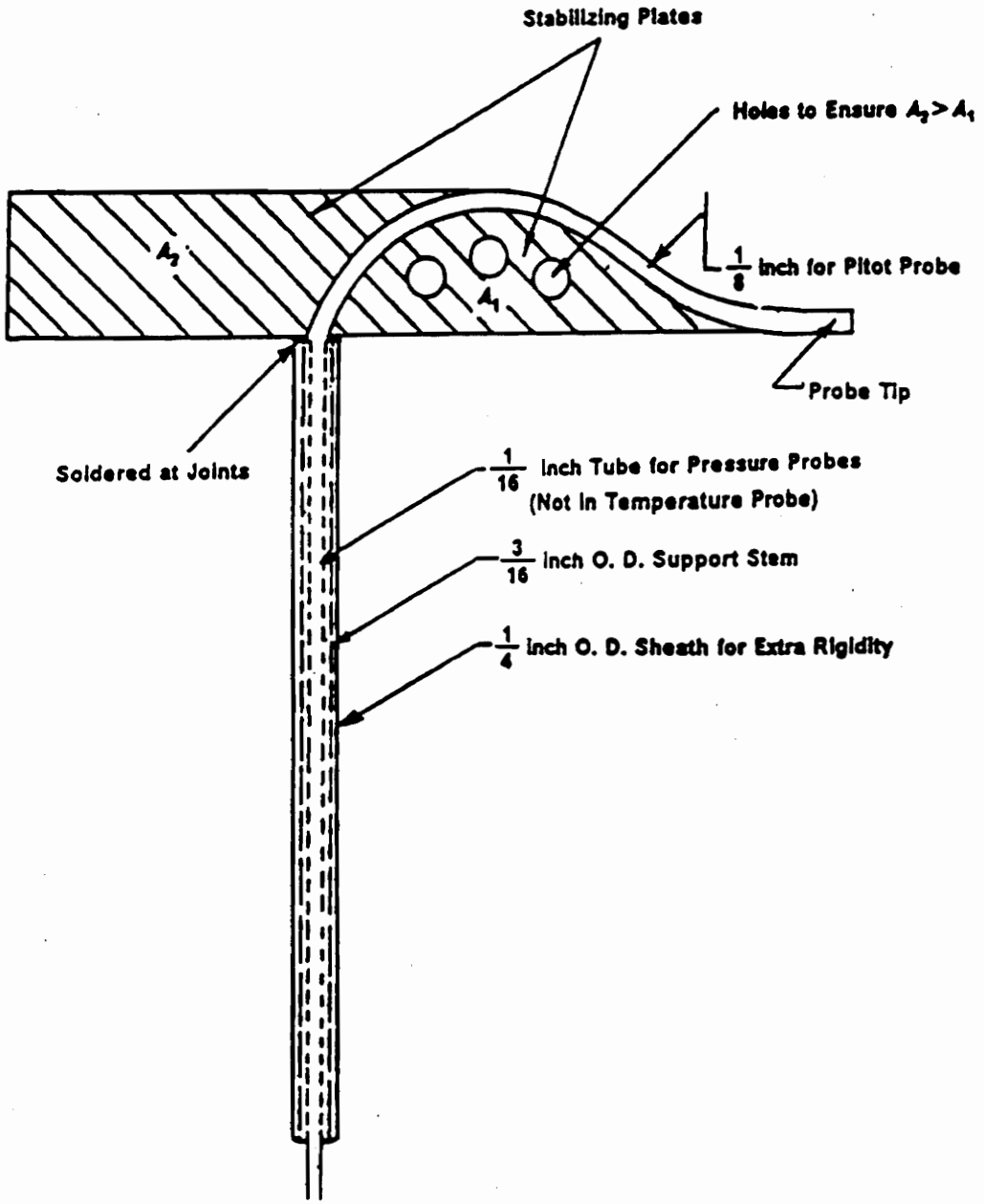

Figure 8. Pitot Probe.

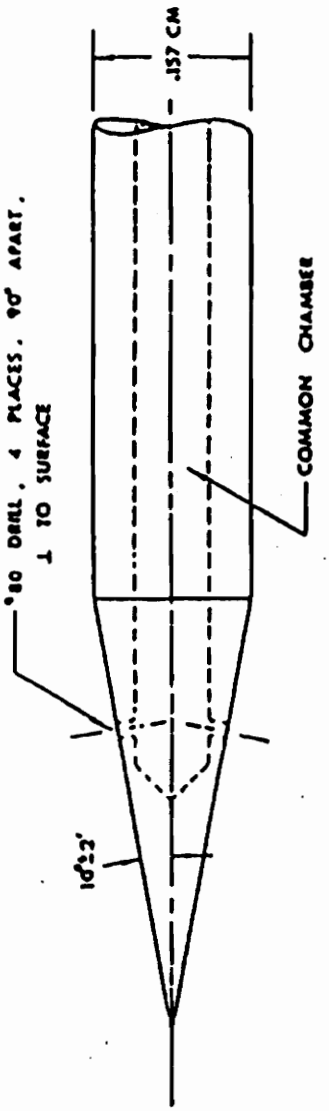

Figure 9. Cone-Static Probe.

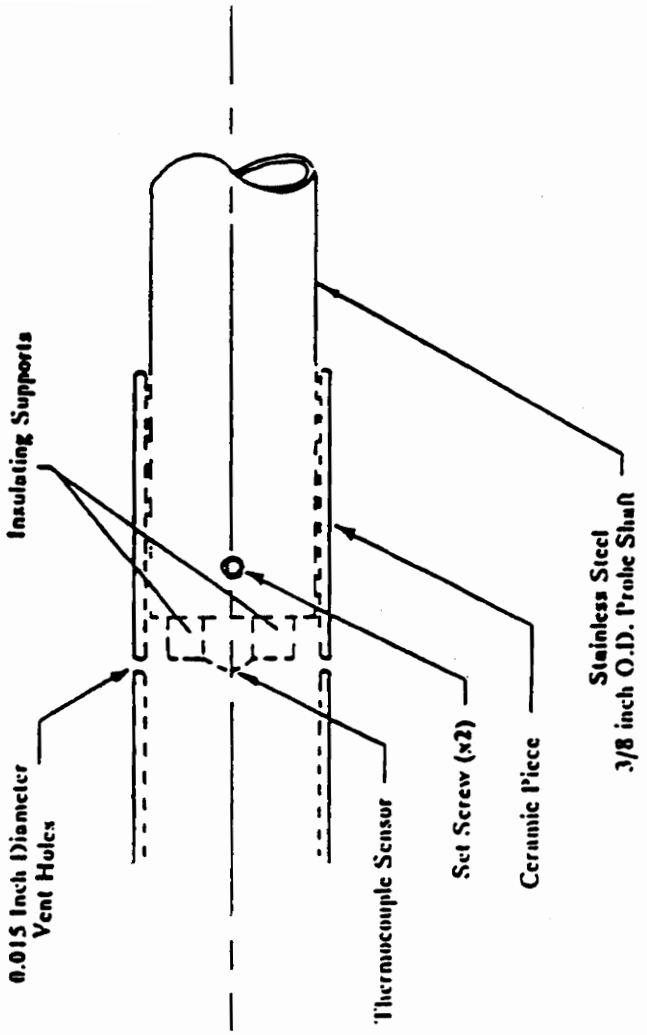

Figure 10. Total Temperature Probe.

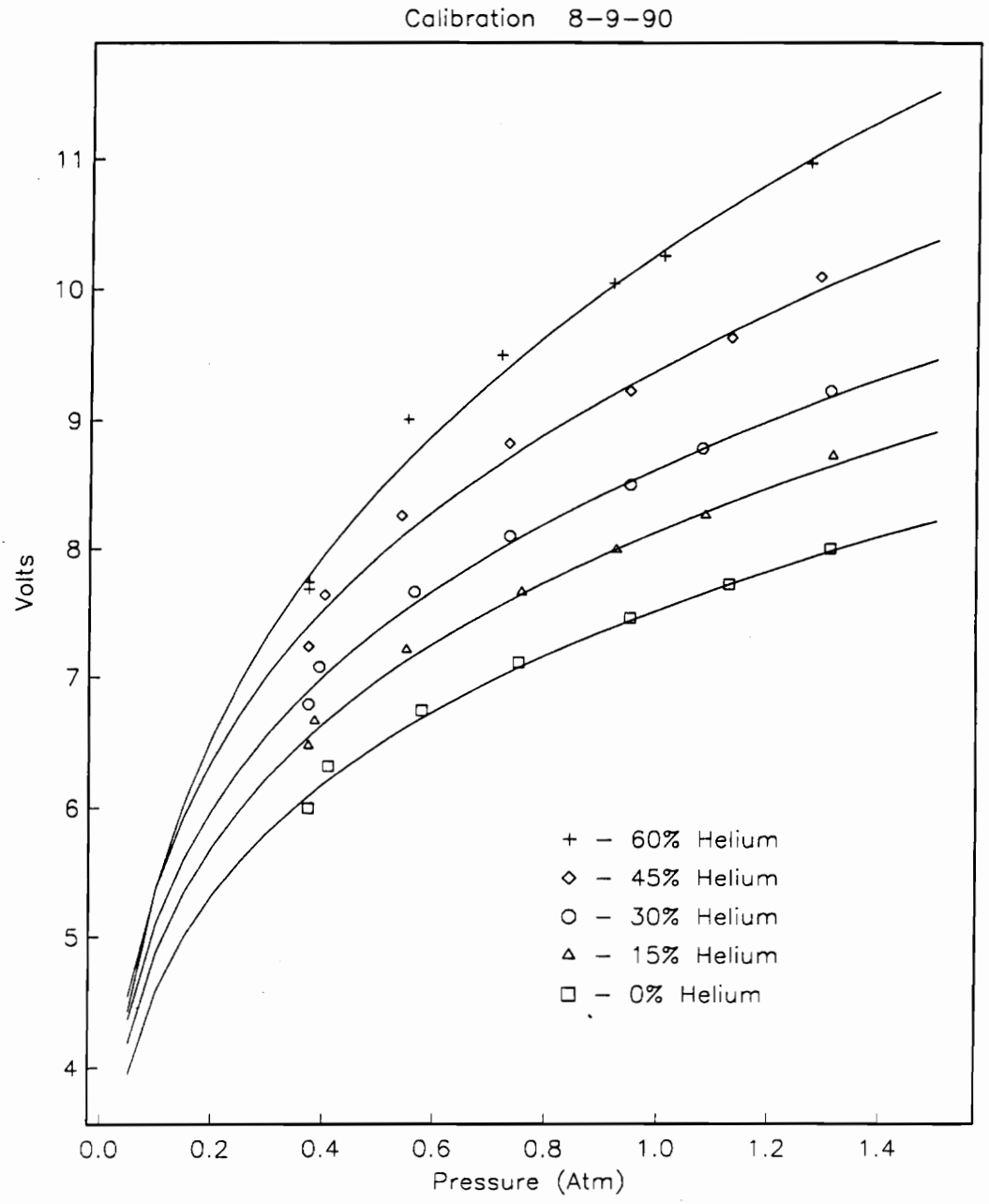

Figure 11. Concentration Probe Calibration Curves.

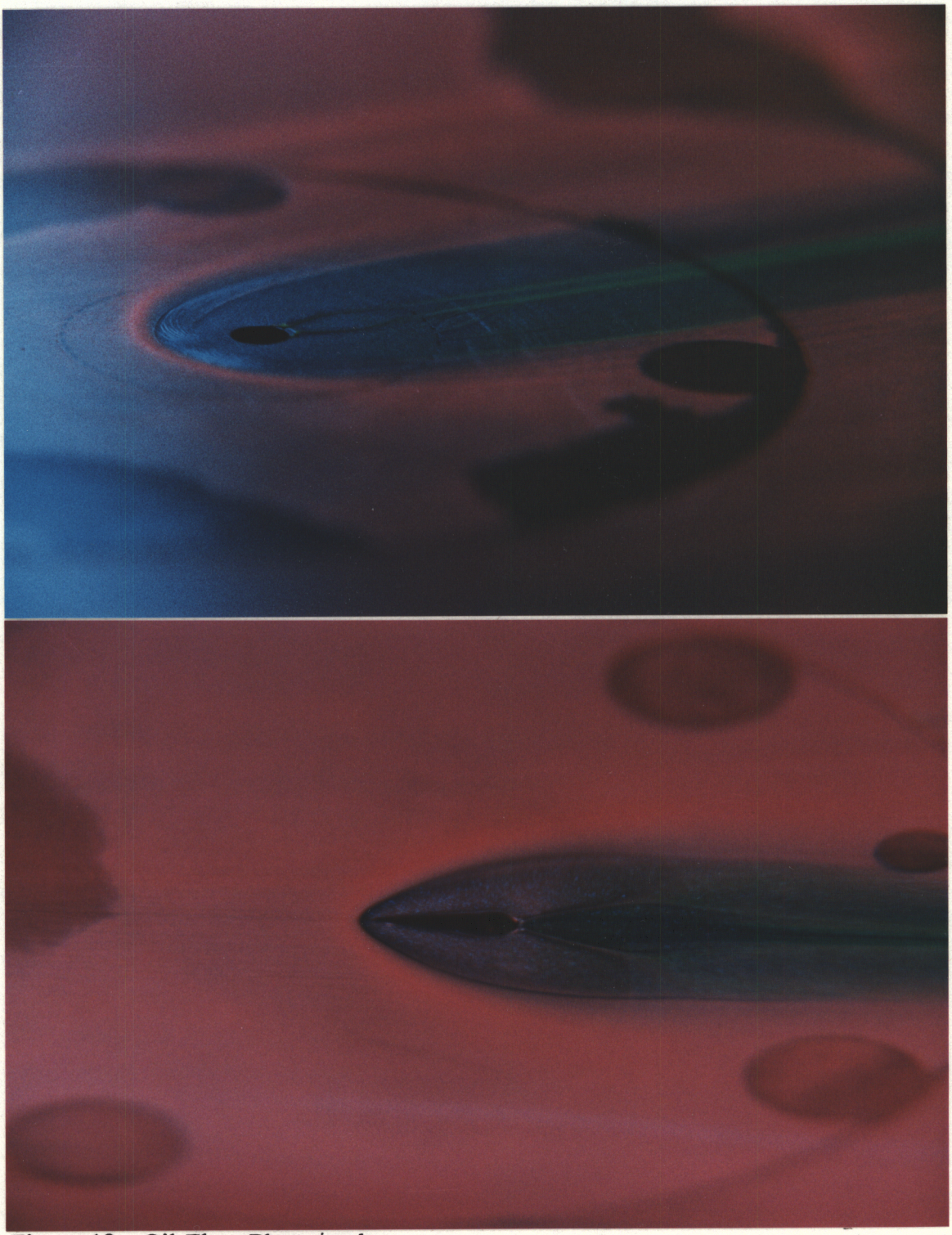

Figure 12. Oil Flow Photographs.

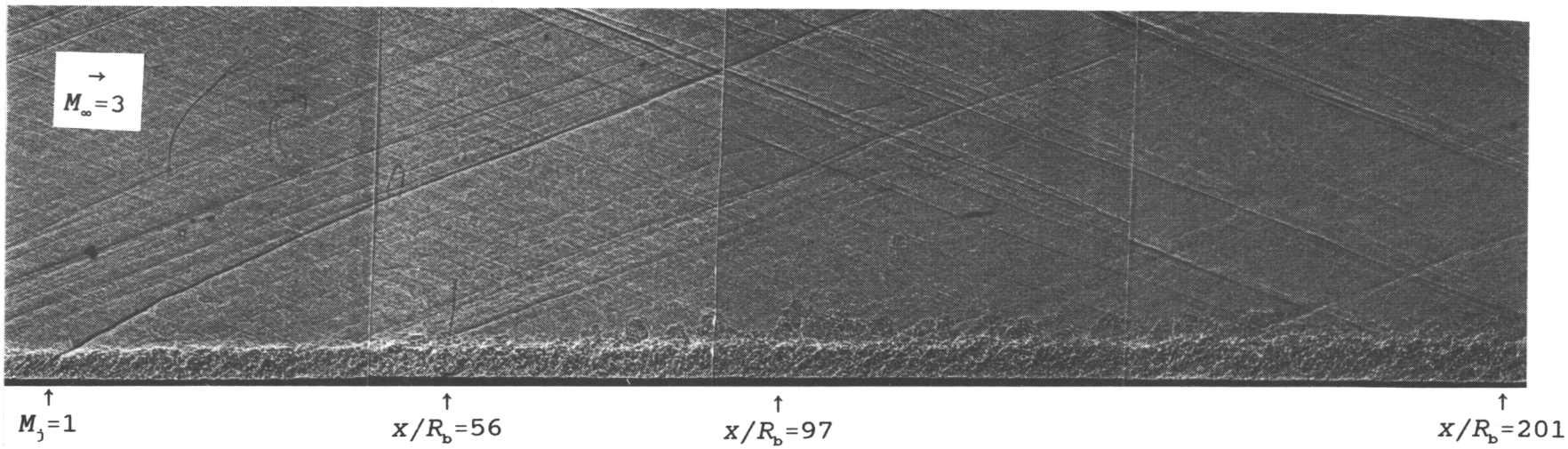

Figure 13. Nanoshadowgraph Composite, Circular Nozzle.

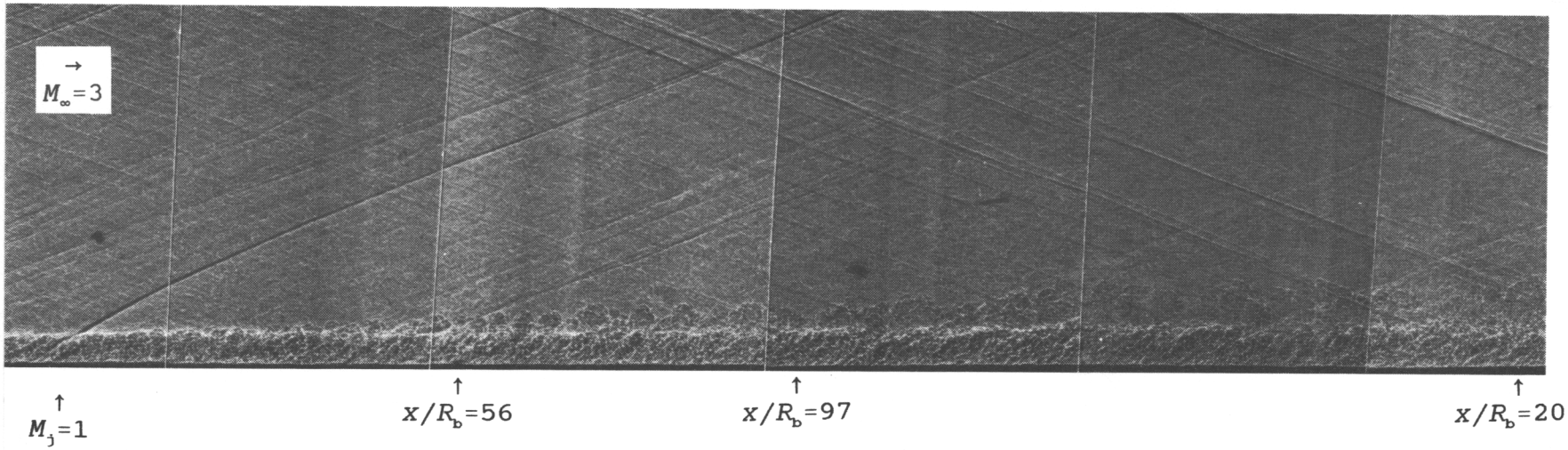

Figure 14. Nanoshadowgraph Composite, Wedge-shaped Nozzle.

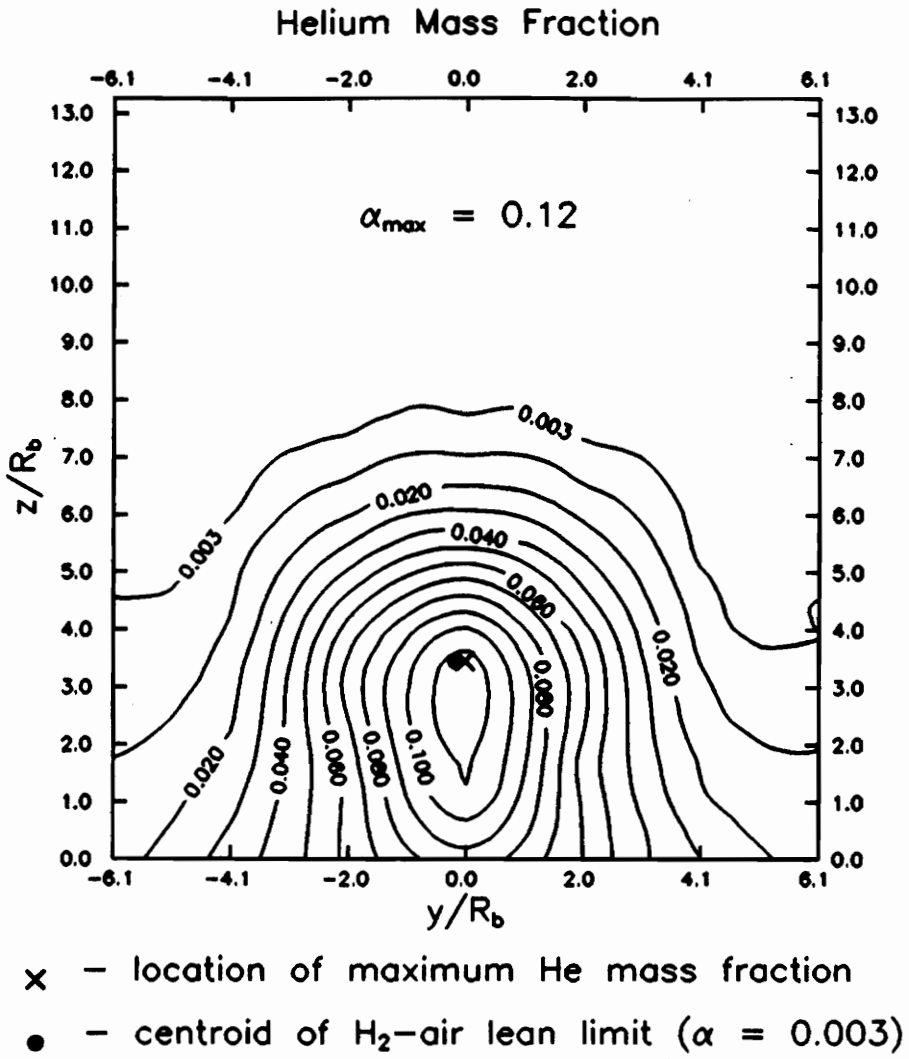

Figure 15. Helium Concentration for the Circular Nozzle, $x/R_b=56$.

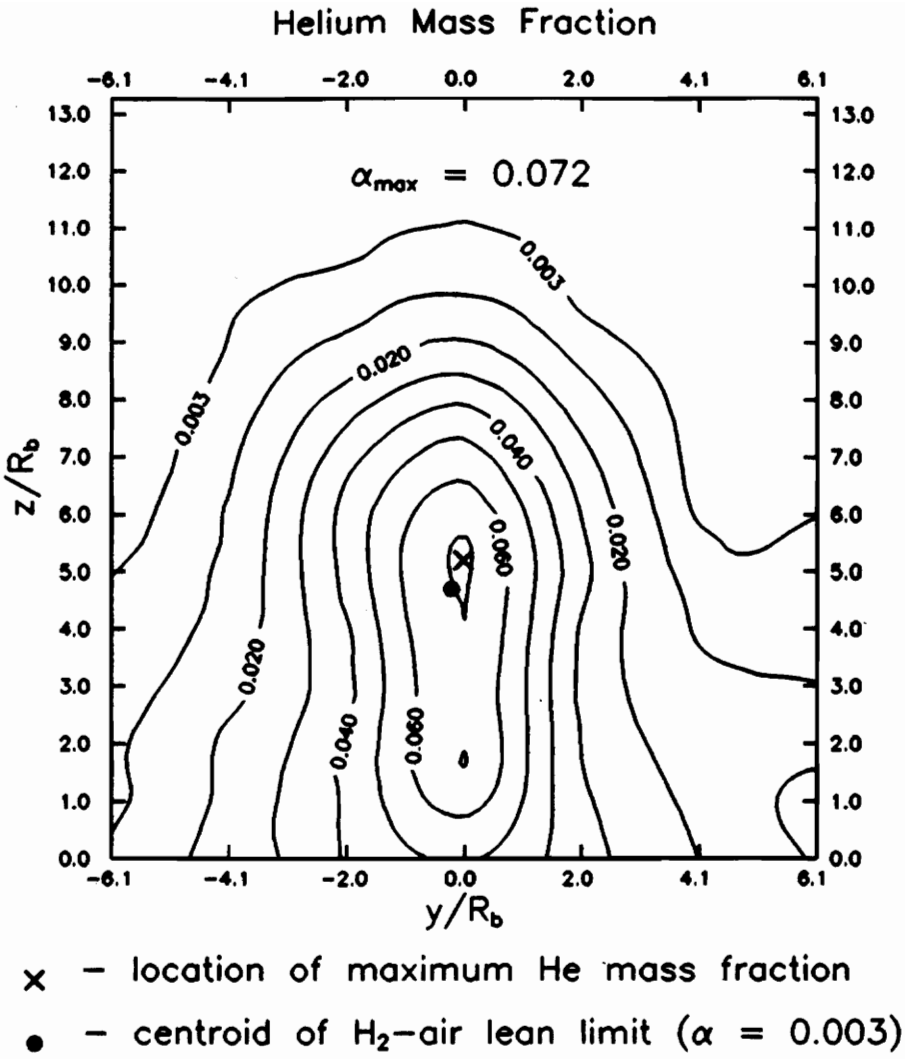

Figure 16. Helium Concentration for the Circular Nozzle, $x/R_b=97$.

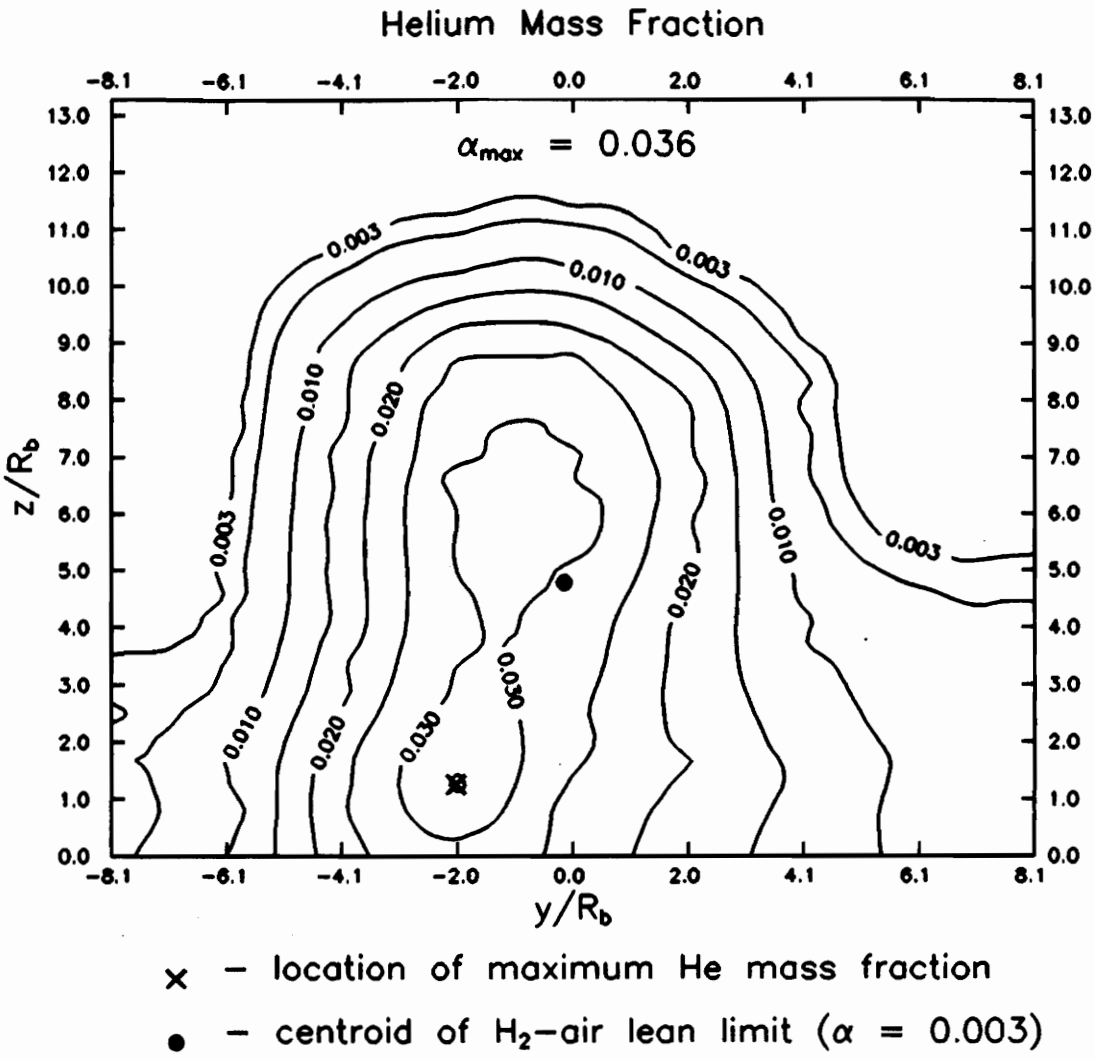

Figure 17. Helium Concentration for the Circular Nozzle, $x/R_b=201$.

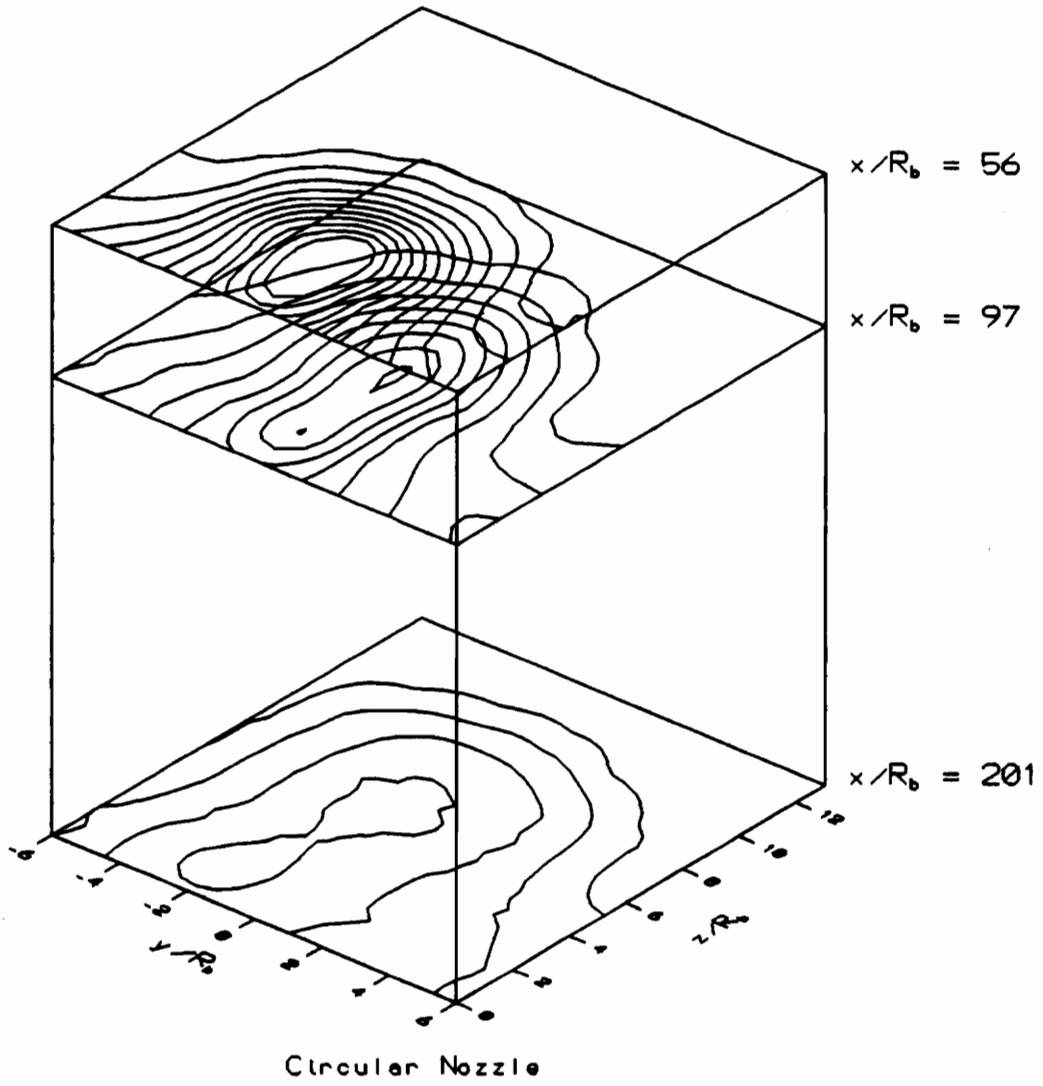

Figure 18. Contour Stack, Circular Nozzle.

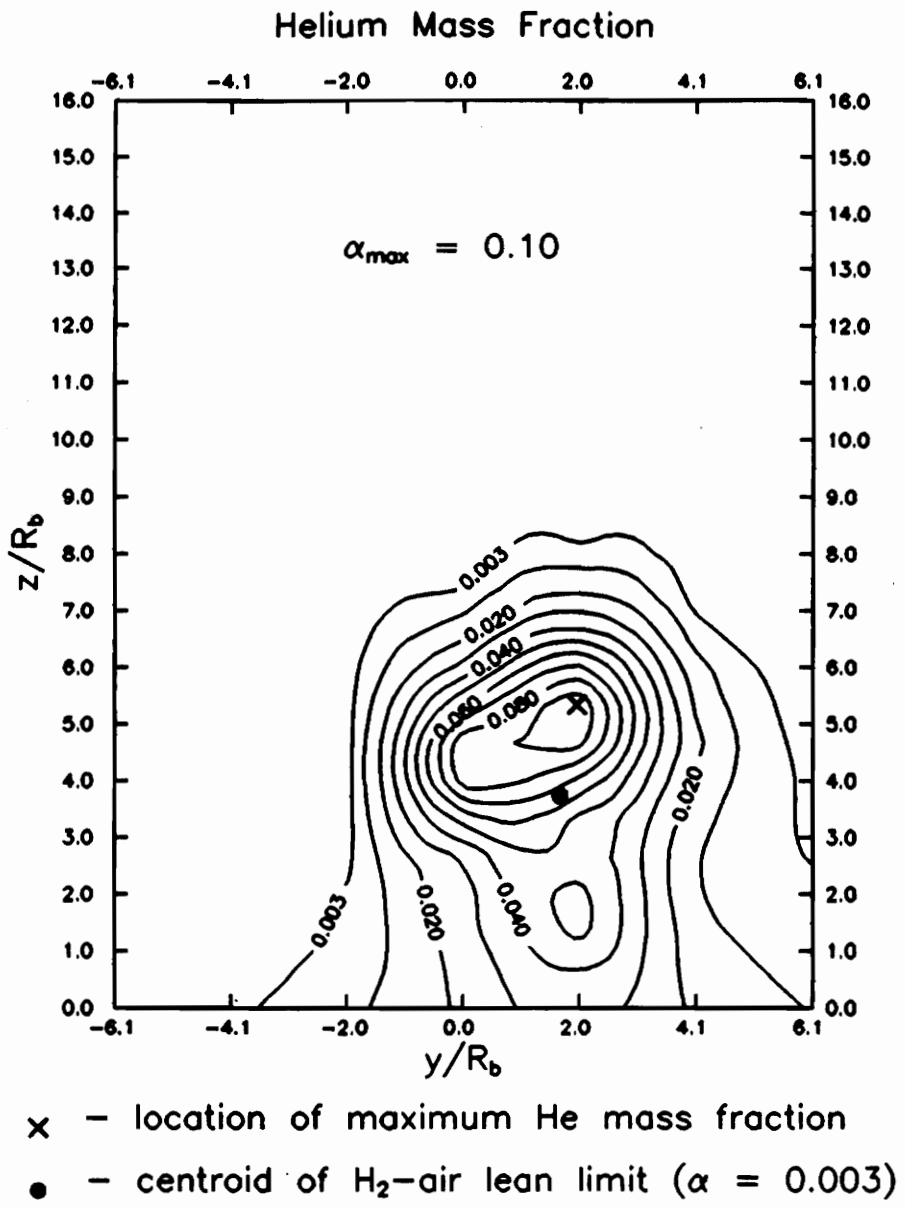

Figure 19. Helium Concentration for the Wedge-shaped Nozzle, $x/R_b=56$.

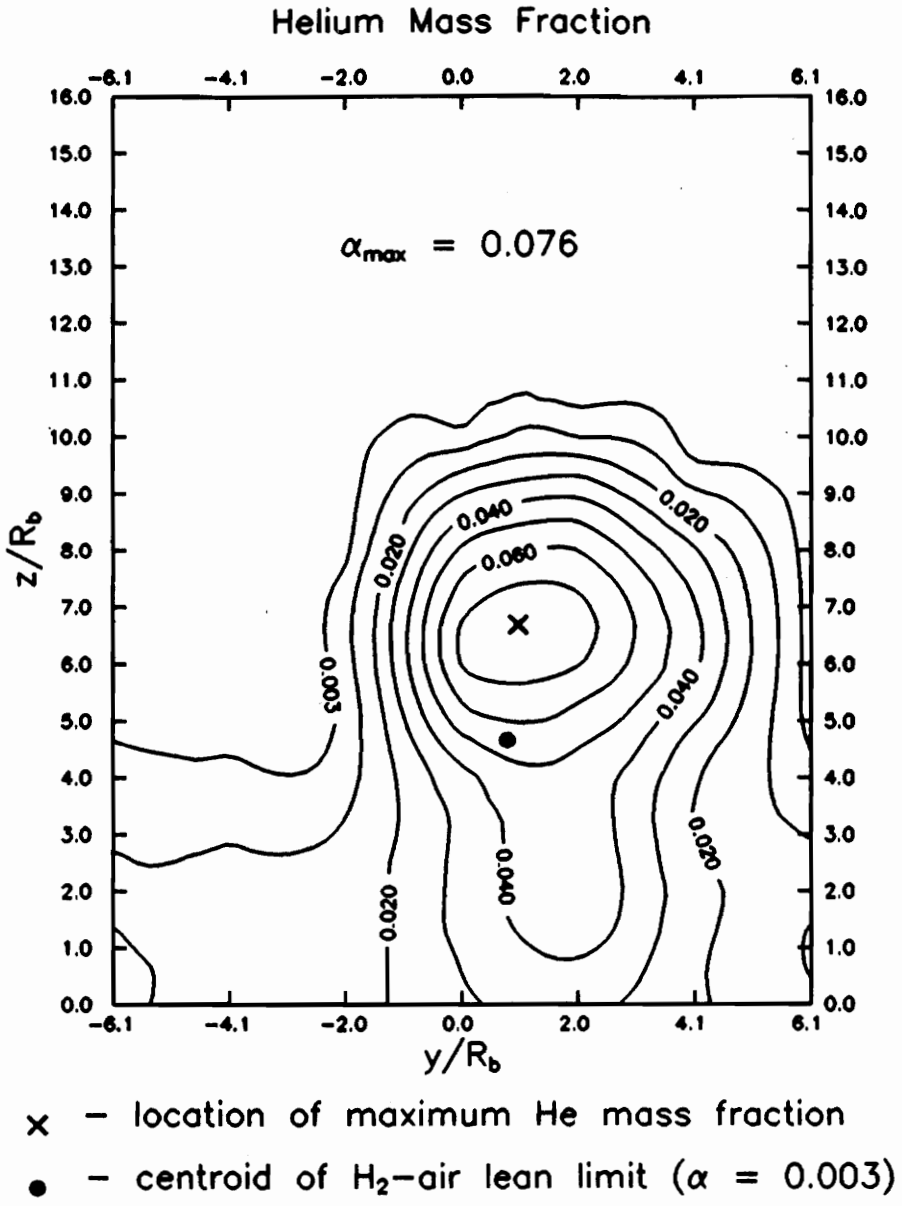

Figure 20. Helium Concentration for the Wedge-shaped Nozzle, $x/R_b=97$.

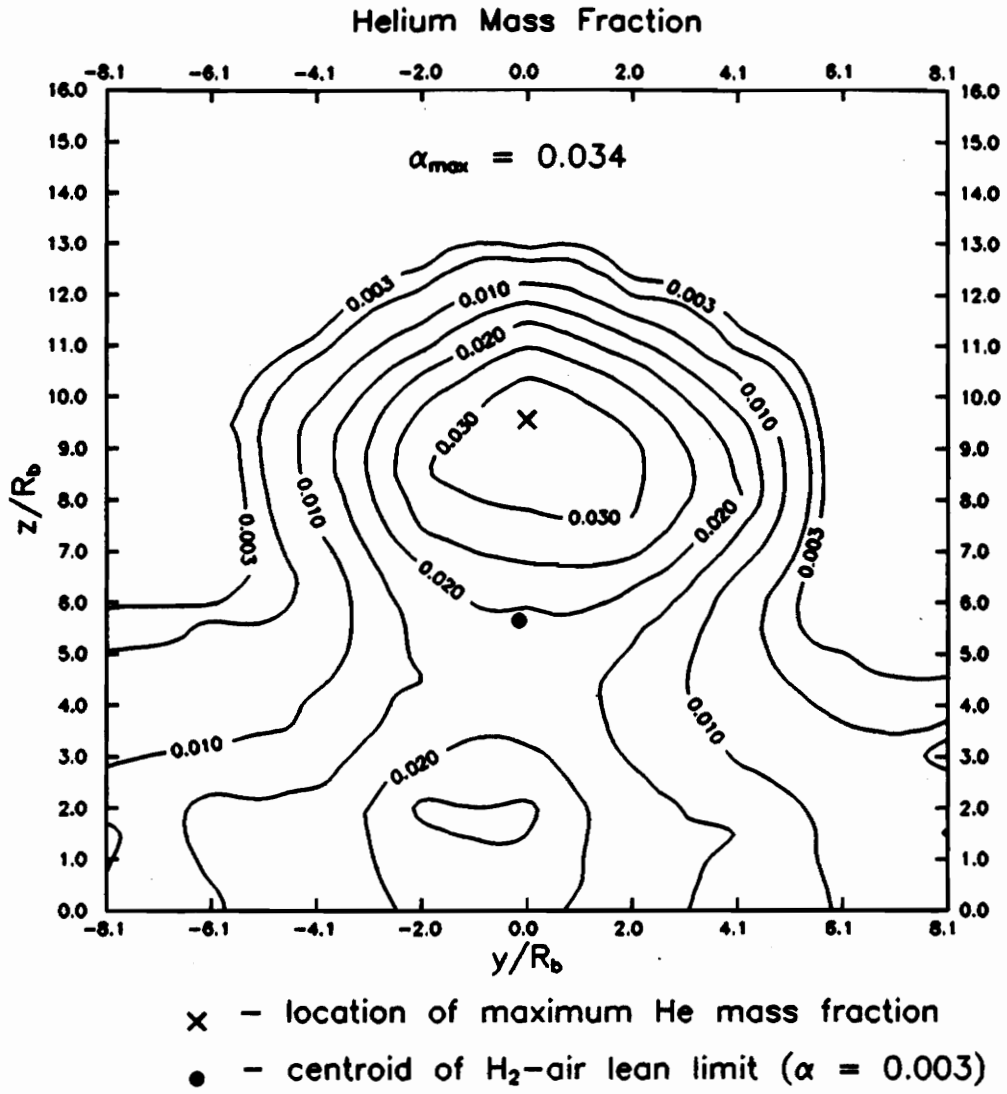

Figure 21. Helium Concentration for the Wedge-shaped Nozzle, x/R_b=201.

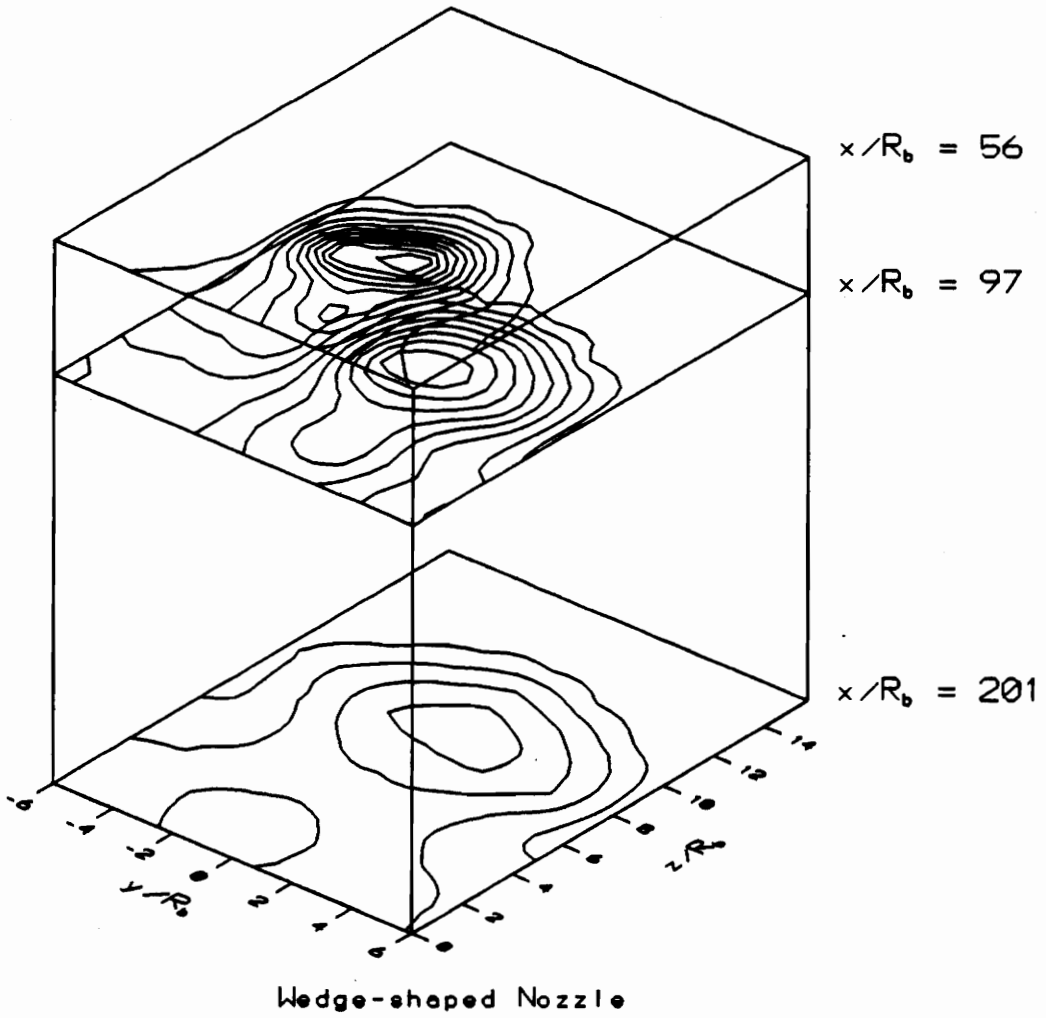

Figure 22. Contour Stack, Wedge-shaped Nozzle.

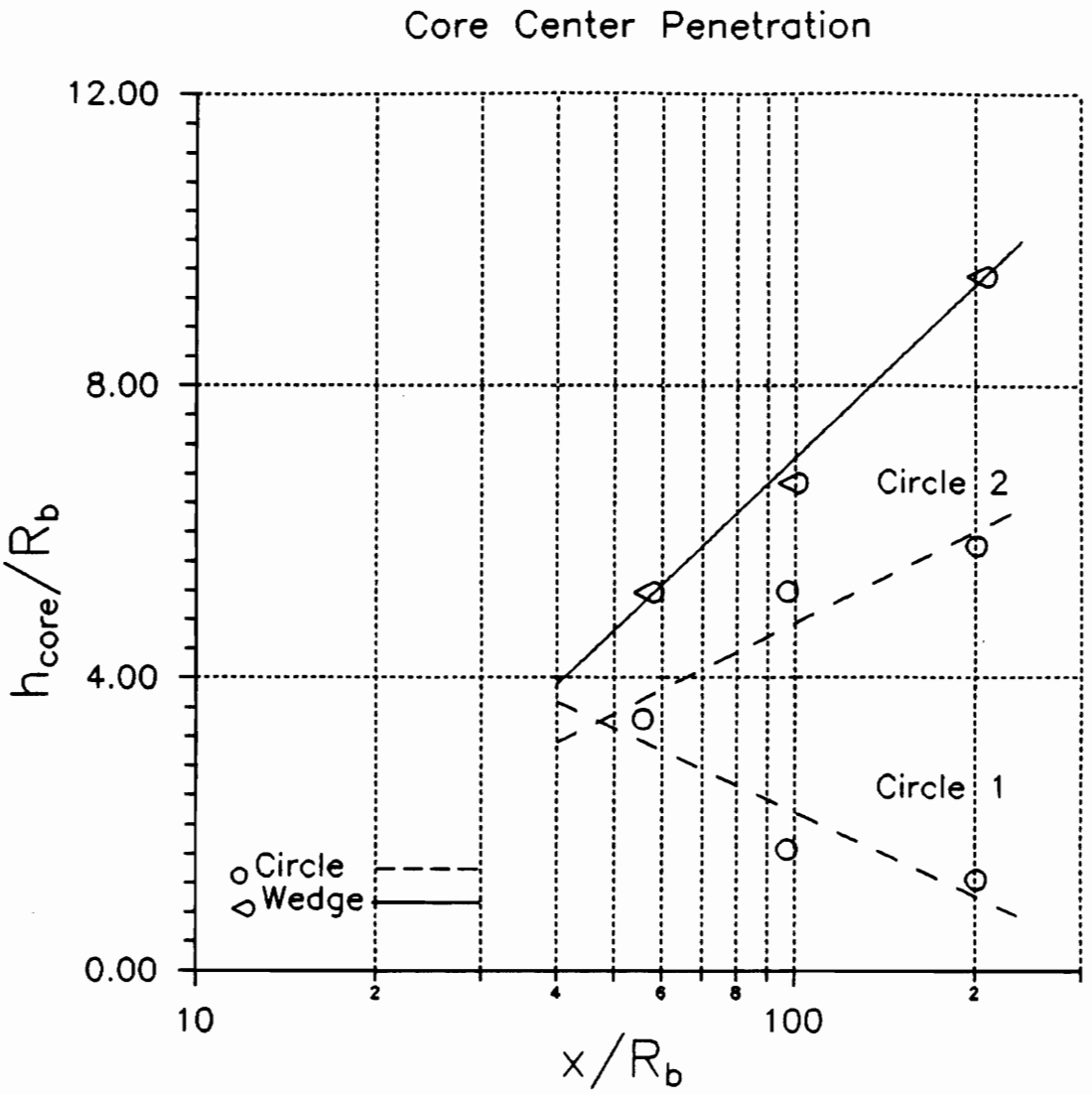

Figure 23. Core Center Penetration.

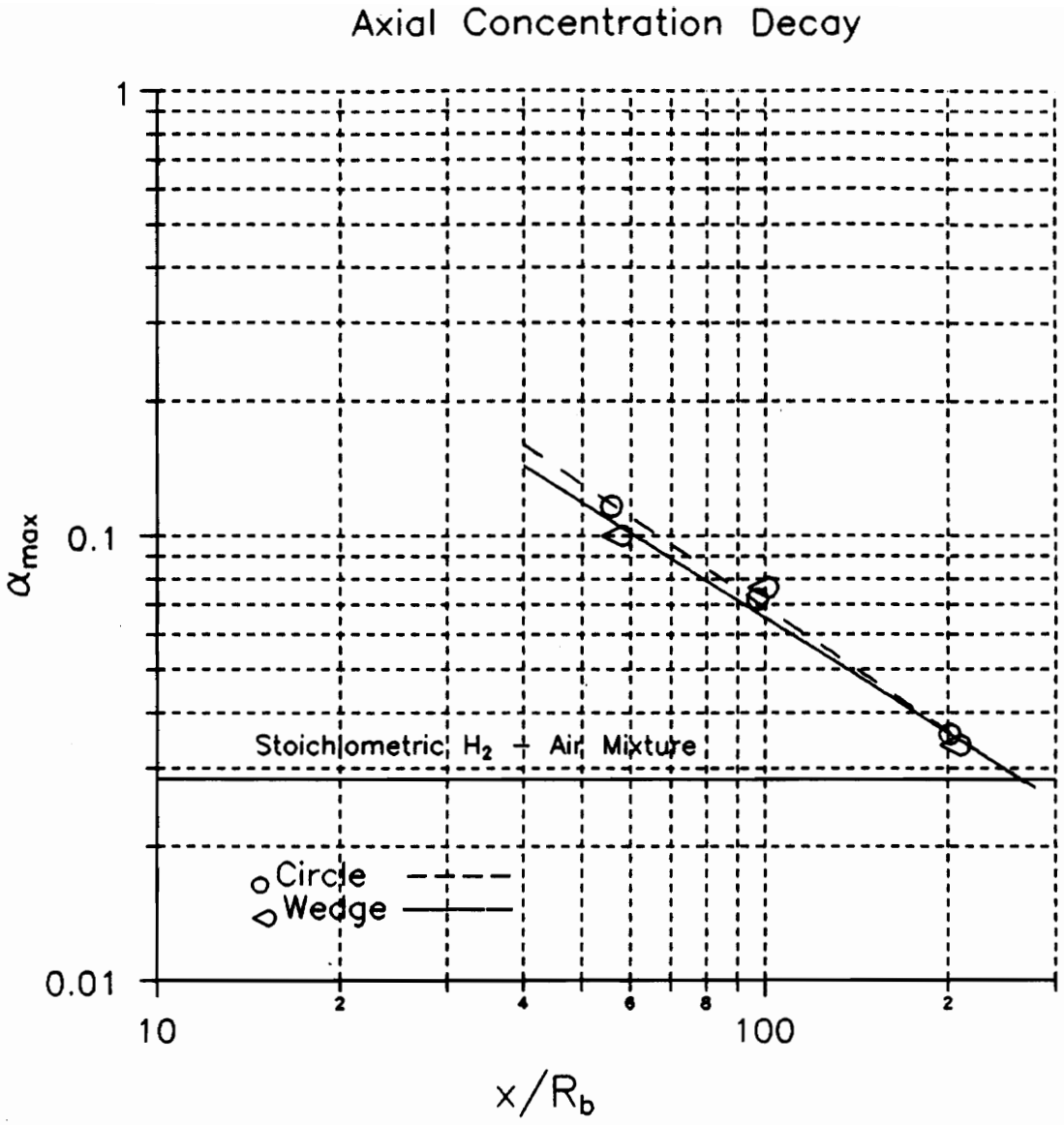

Figure 24. Decay of Maximum Helium Concentration.

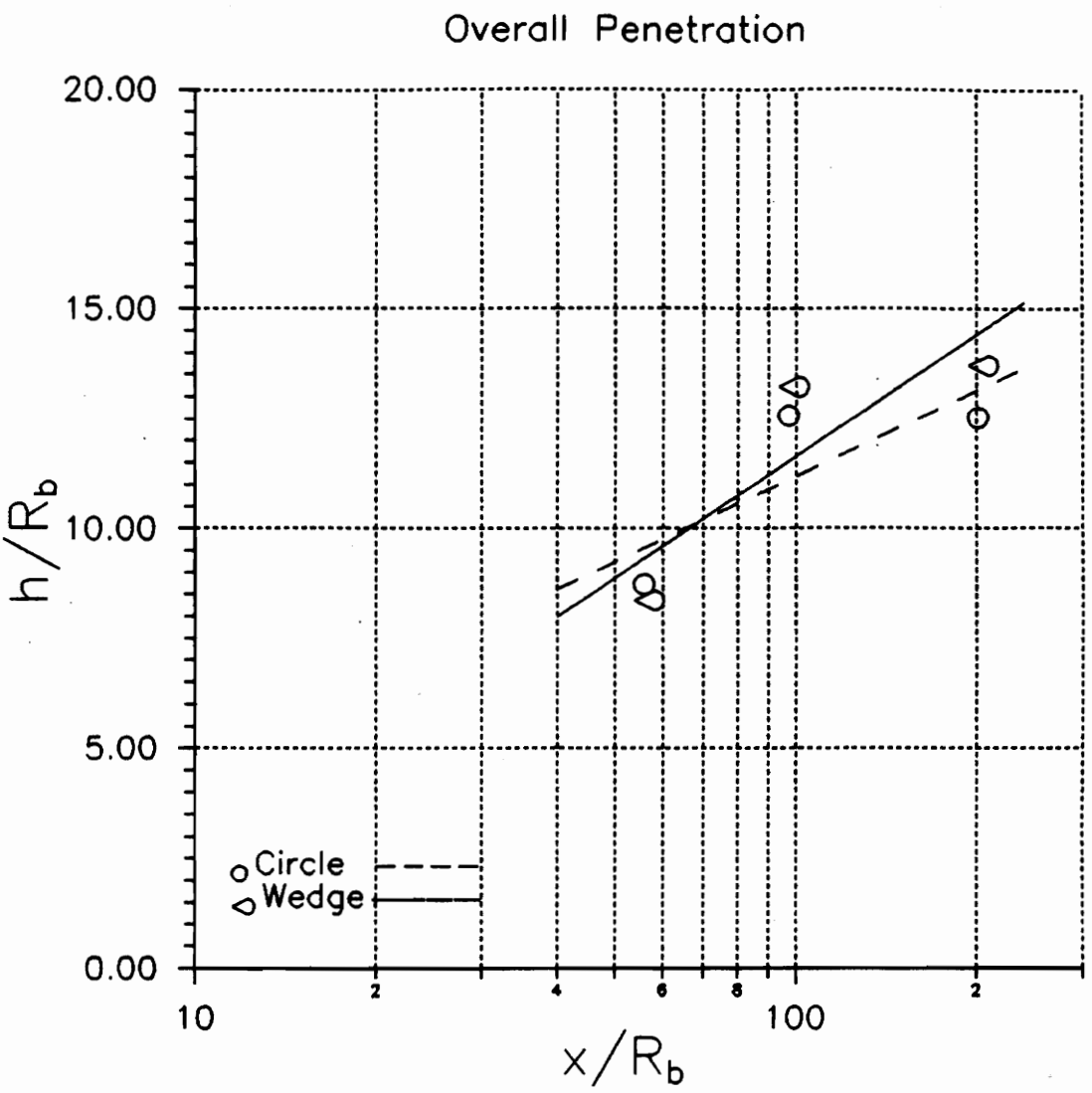

Figure 25. Overall Penetration.

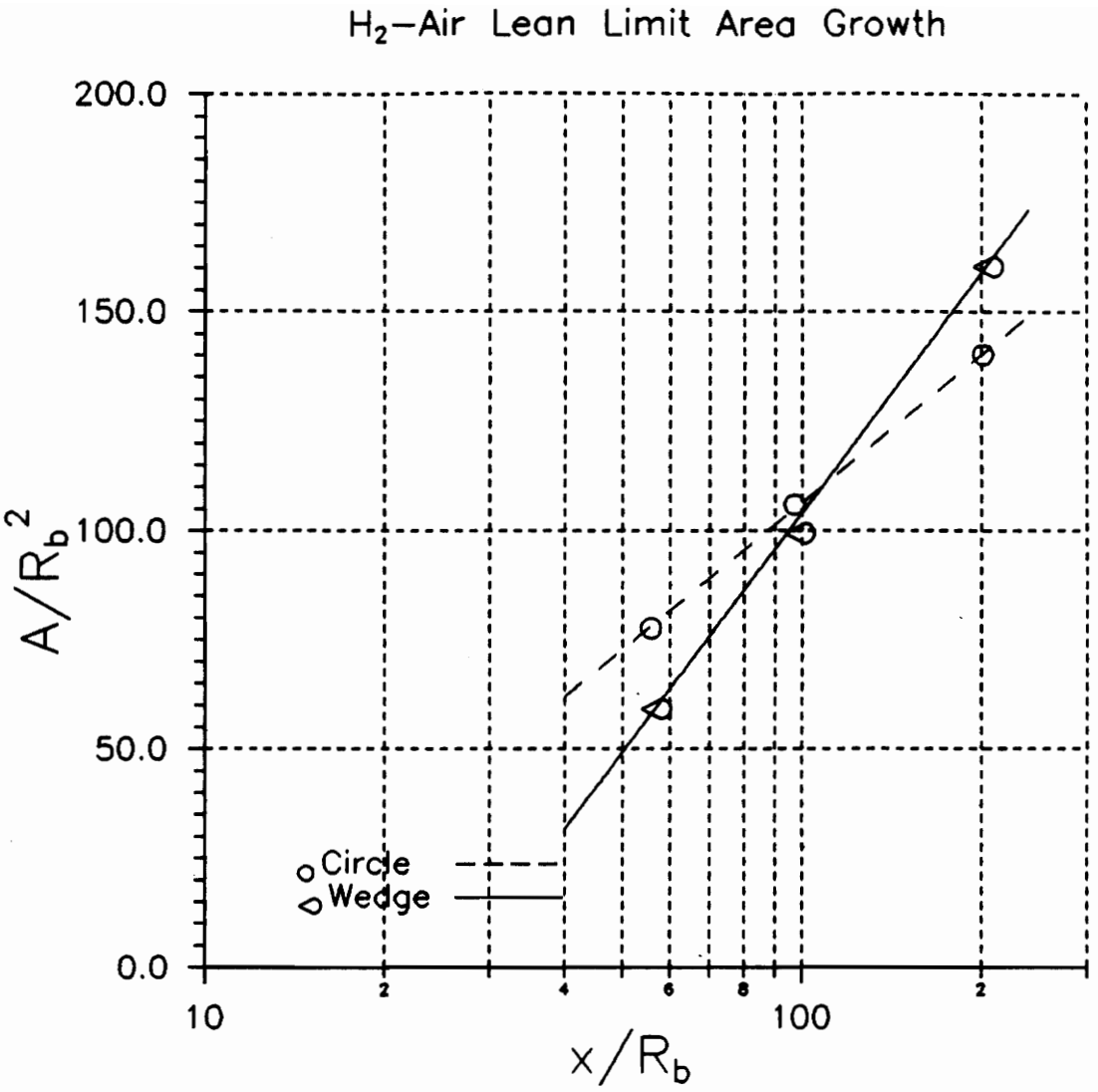

Figure 26. Area Bounded by Lean-Limit Contour.

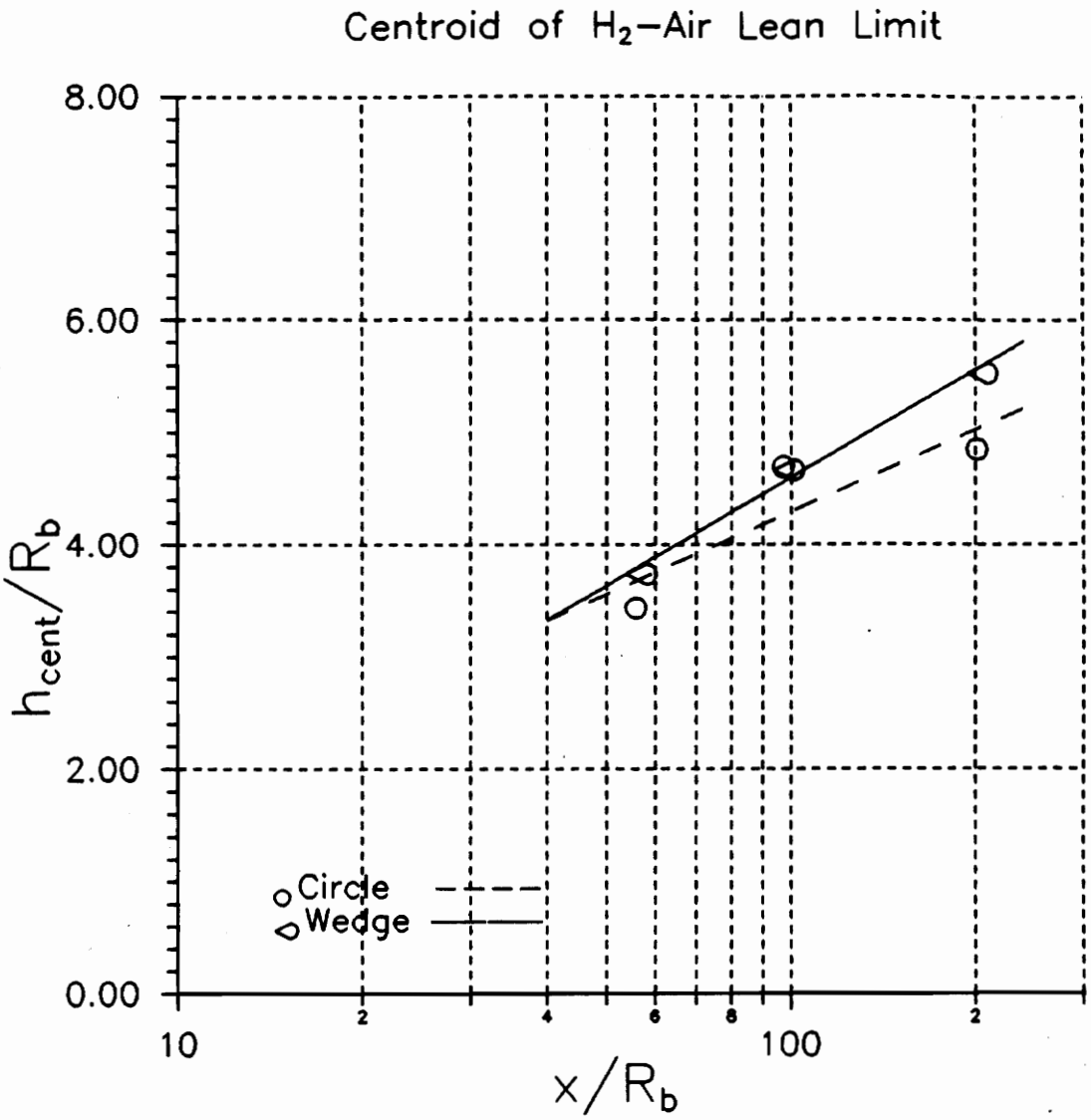

Figure 27. Centroid Penetration.

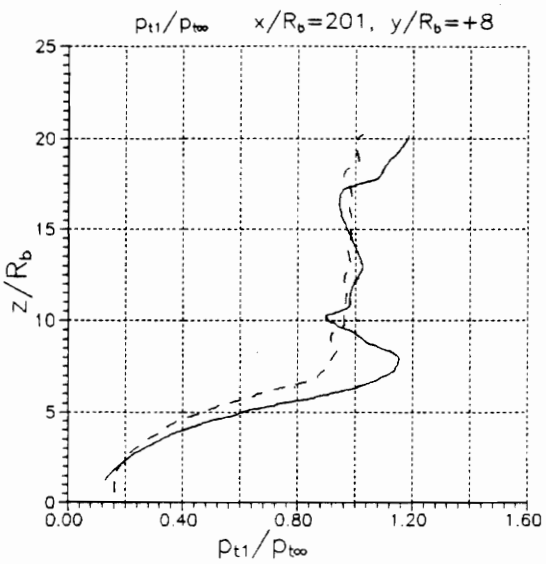

Wedge-shaped Nozzle: Solid Line
Circular Nozzle: Dashed Line

Figure 28. Total Pressure Profile, $y/R_b = +8$.

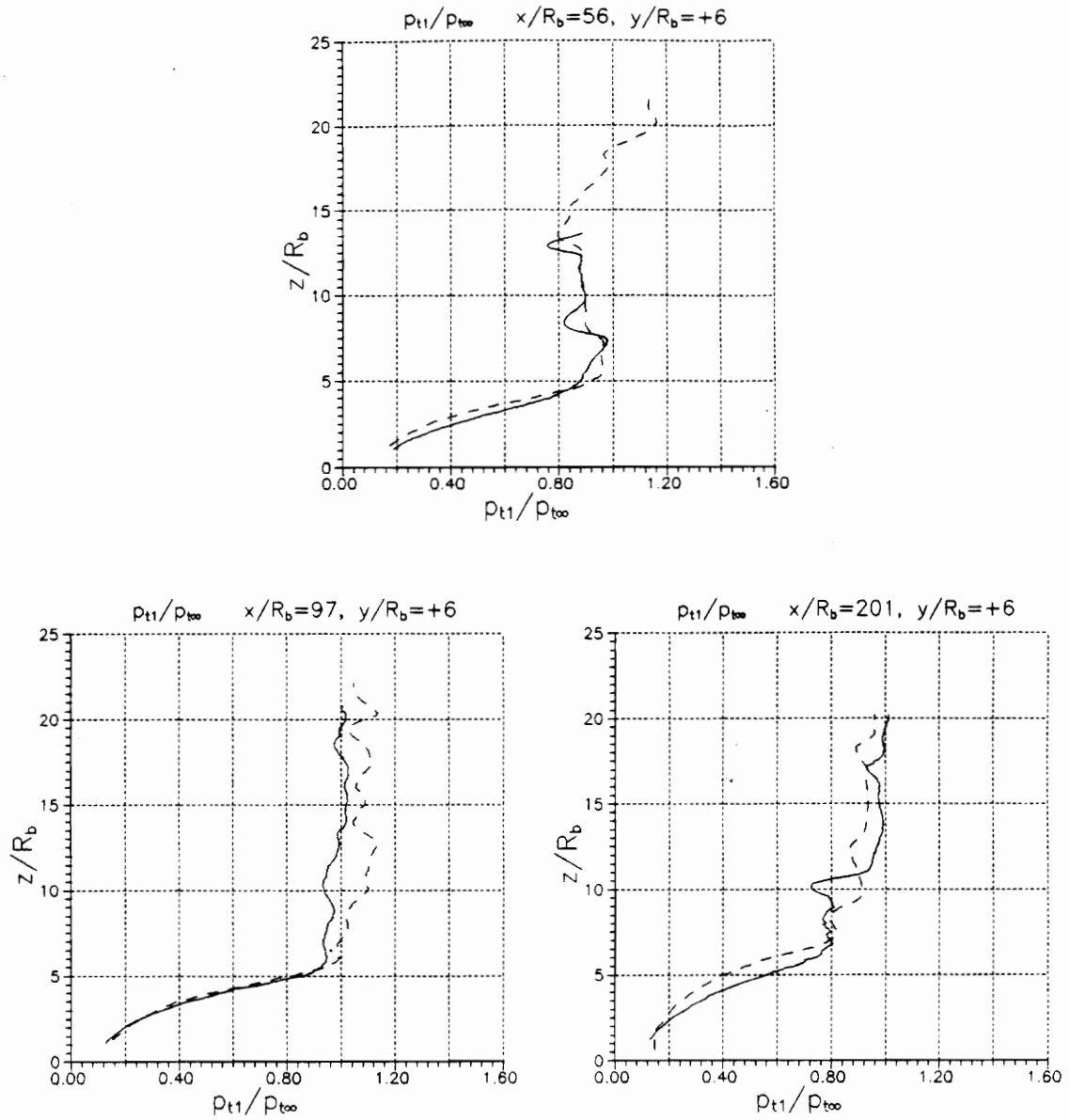

Wedge-shaped Nozzle: Solid Line
Circular Nozzle: Dashed Line

Figure 29. Total Pressure Profiles, $y/R_b=+6$.

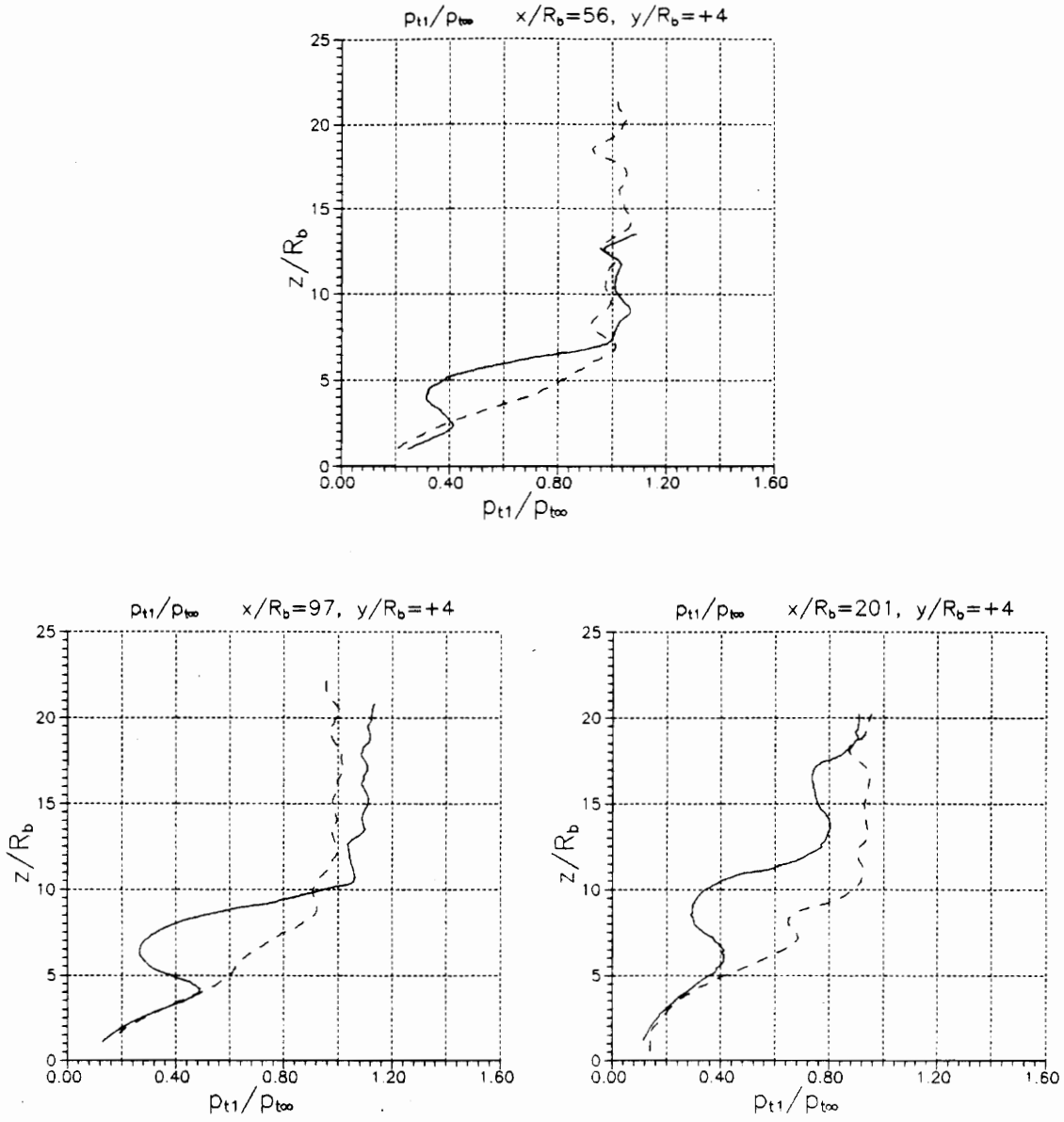

Wedge-shaped Nozzle: Solid Line
Circular Nozzle: Dashed Line

Figure 30. Total Pressure Profiles, $y/R_b=+4$.

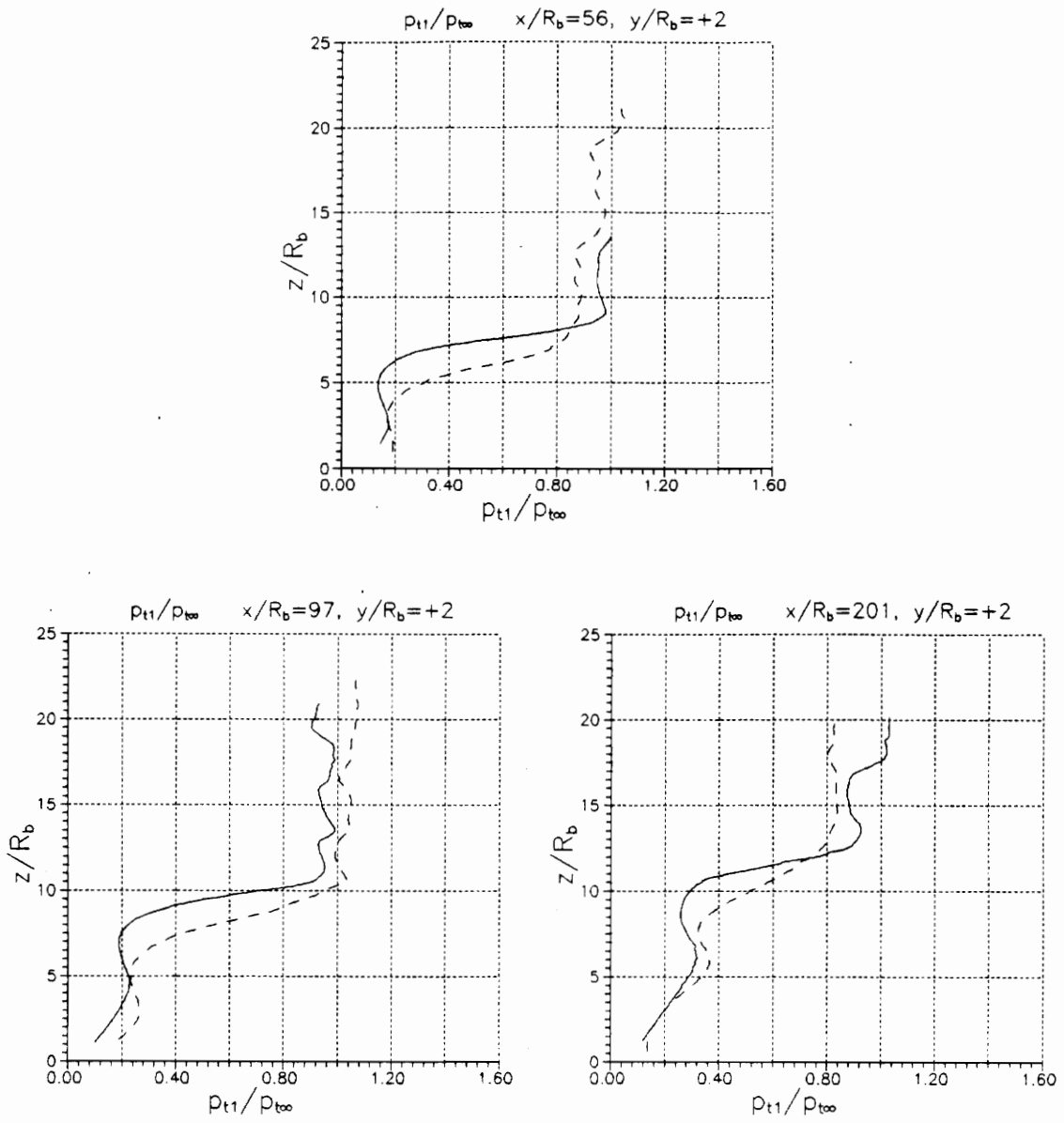

Wedge-shaped Nozzle: Solid Line
Circular Nozzle: Dashed Line

Figure 31. Total Pressure Profiles, $y/R_b=+2$.

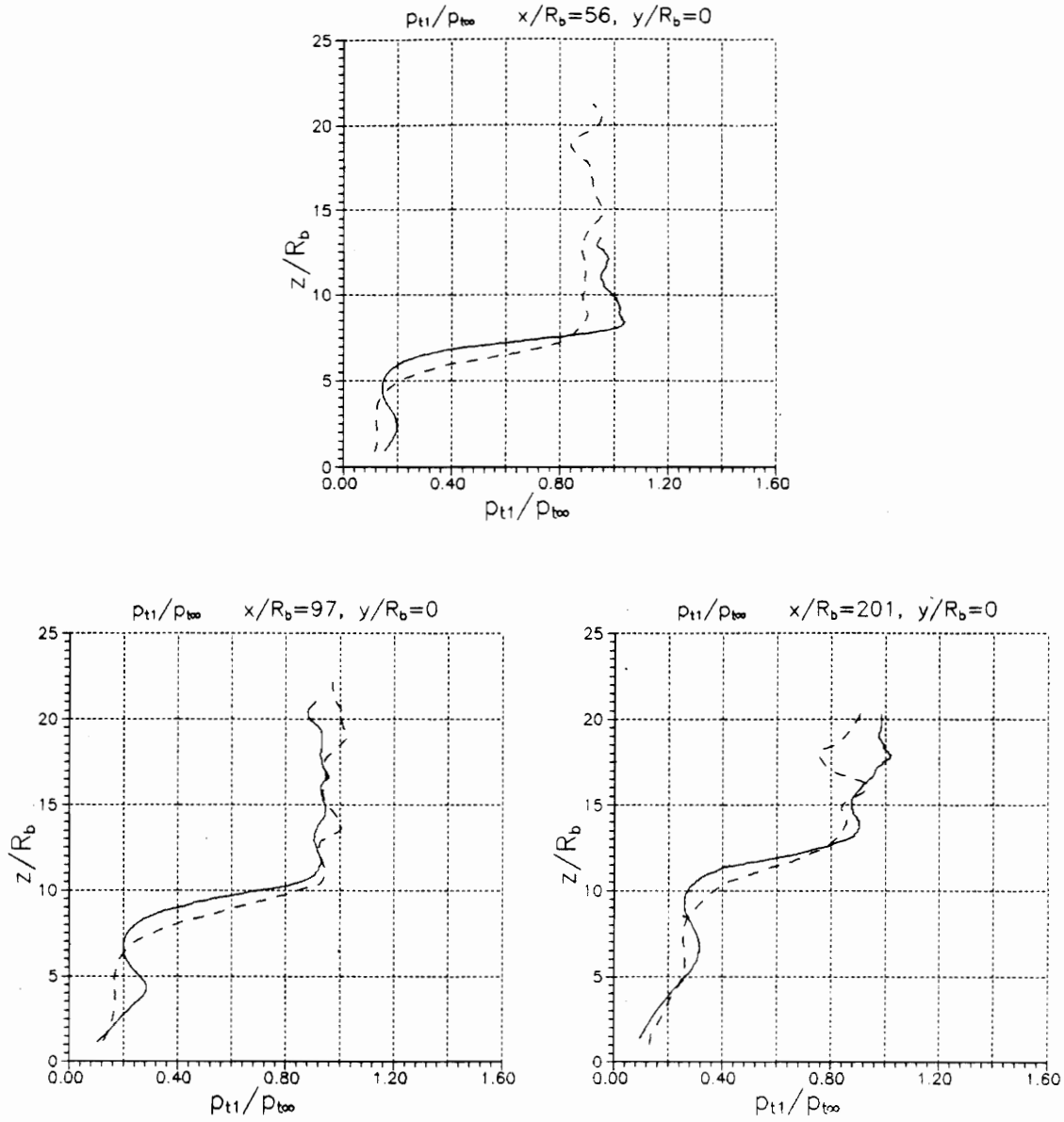

Wedge-shaped Nozzle: Solid Line
Circular Nozzle: Dashed Line

Figure 32. Total Pressure Profiles, $y/R_b=0$.

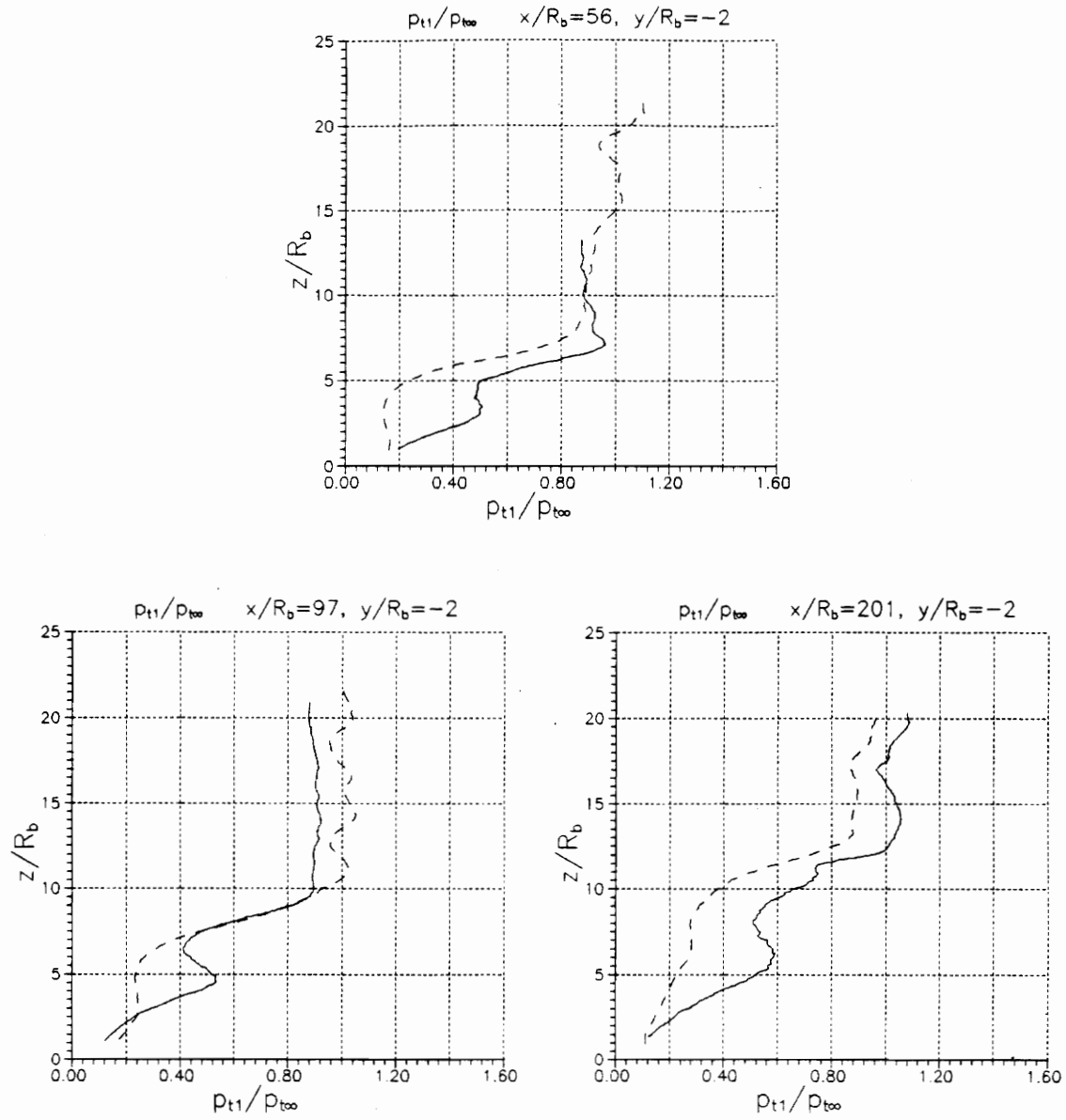

Wedge-shaped Nozzle: Solid Line
Circular Nozzle: Dashed Line

Figure 33. Total Pressure Profiles, y/R_b=-2.

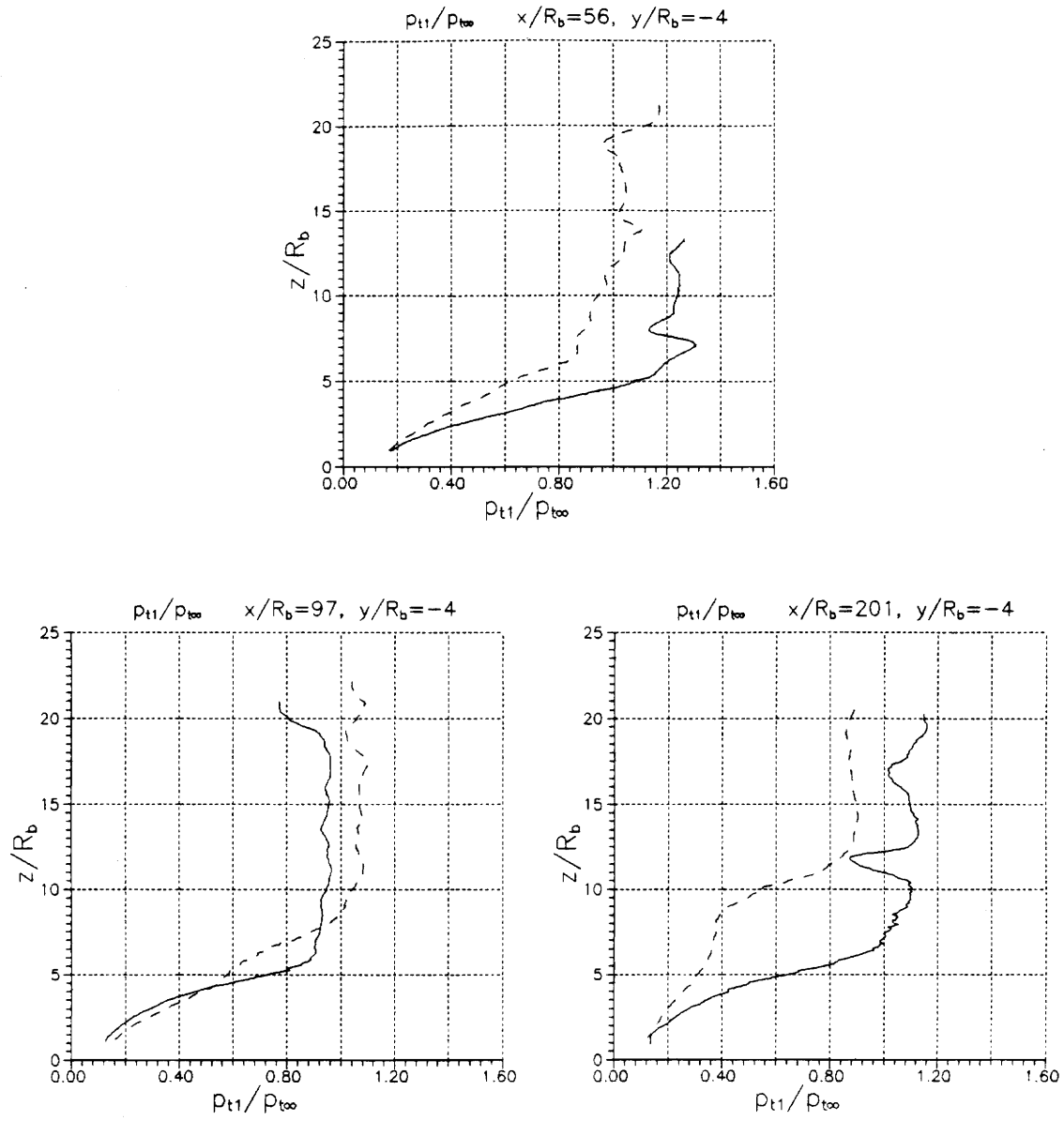

Wedge-shaped Nozzle: Solid Line
Circular Nozzle: Dashed Line

Figure 34. Total Pressure Profiles, $y/R_b=-4$.

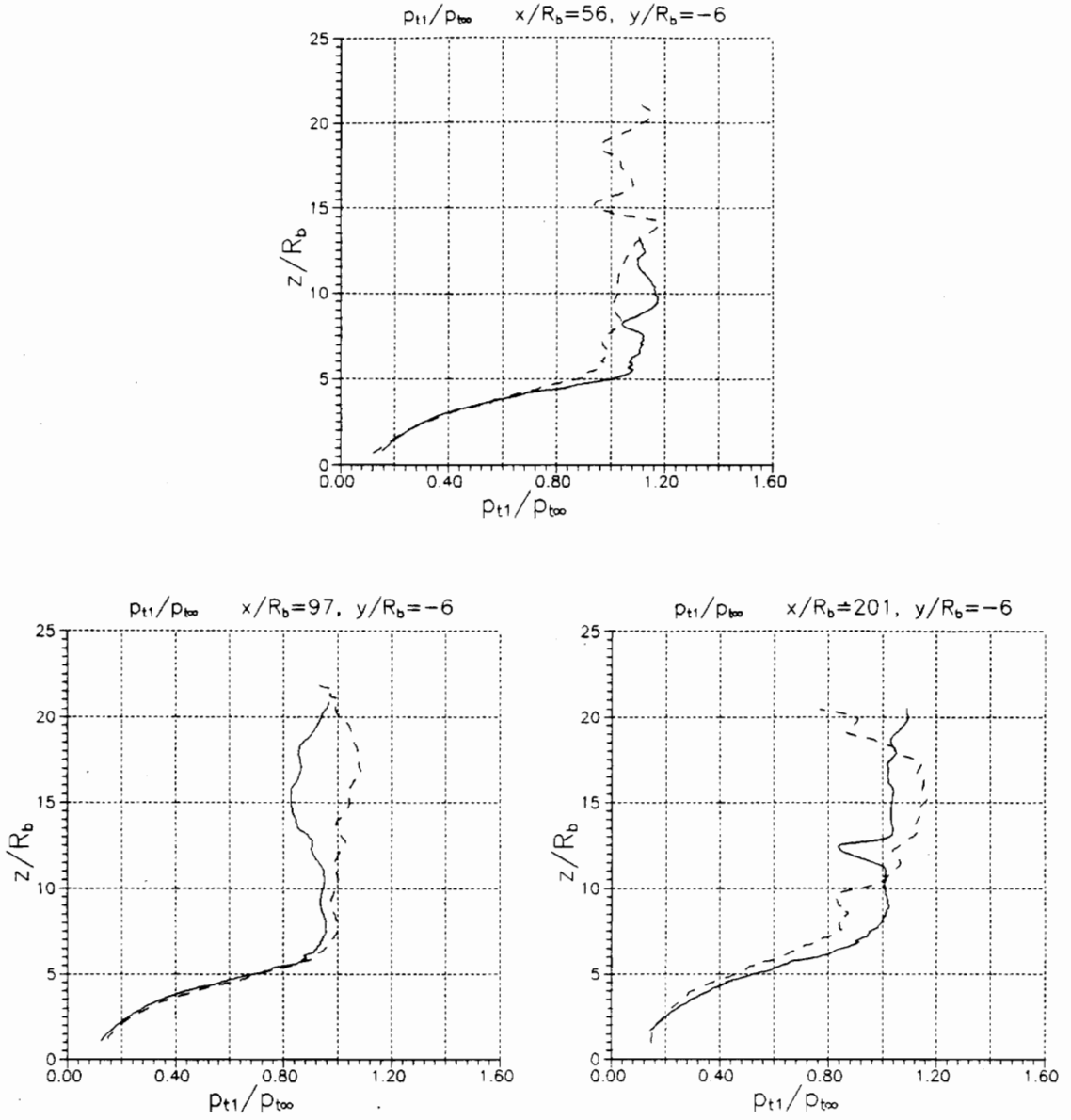

Wedge-shaped Nozzle: Solid Line
Circular Nozzle: Dashed Line

Figure 35. Total Pressure Profiles, $y/R_b=-6$.

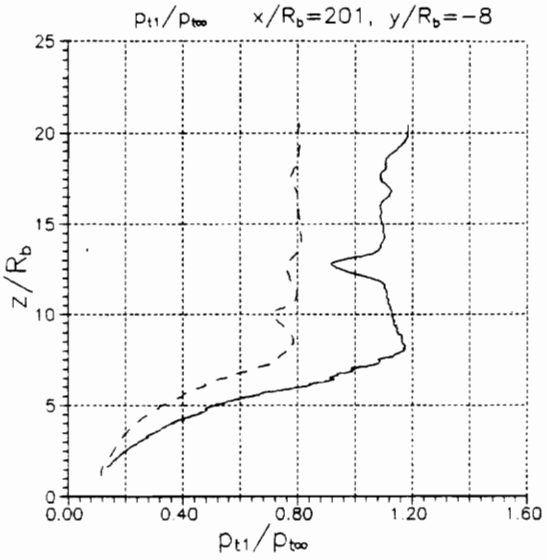

Wedge-shaped Nozzle: Solid Line
Circular Nozzle: Dashed Line

Figure 36. Total Pressure Profiles, $y/R_b=-8$.

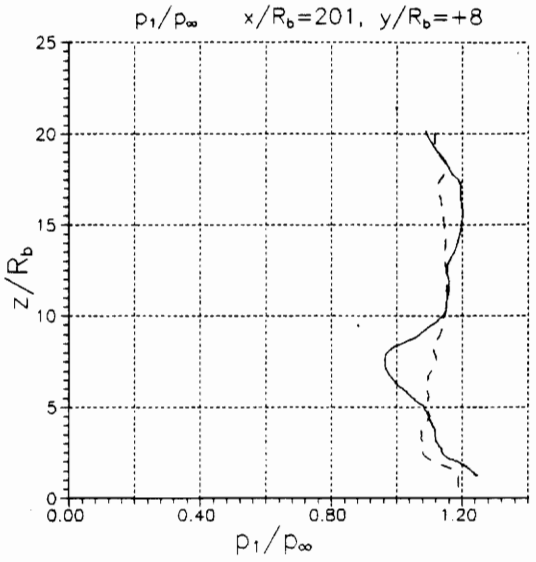

Wedge-shaped Nozzle: Solid Line
Circular Nozzle: Dashed Line

Figure 37. Static Pressure Profiles, $y/R_b = +8$.

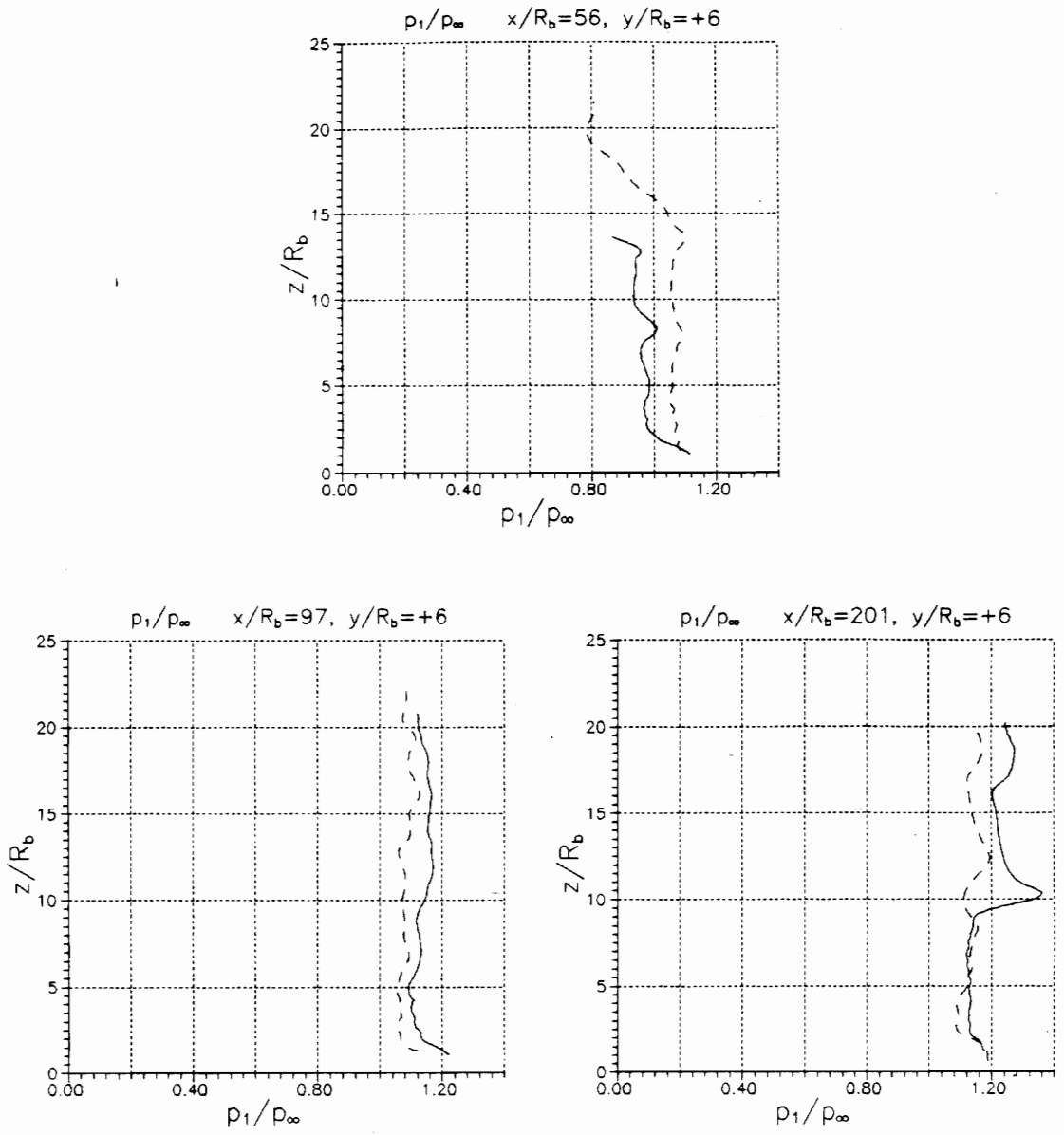

Wedge-shaped Nozzle: Solid Line
Circular Nozzle: Dashed Line

Figure 38. Static Pressure Profiles, $y/R_b = +6$.

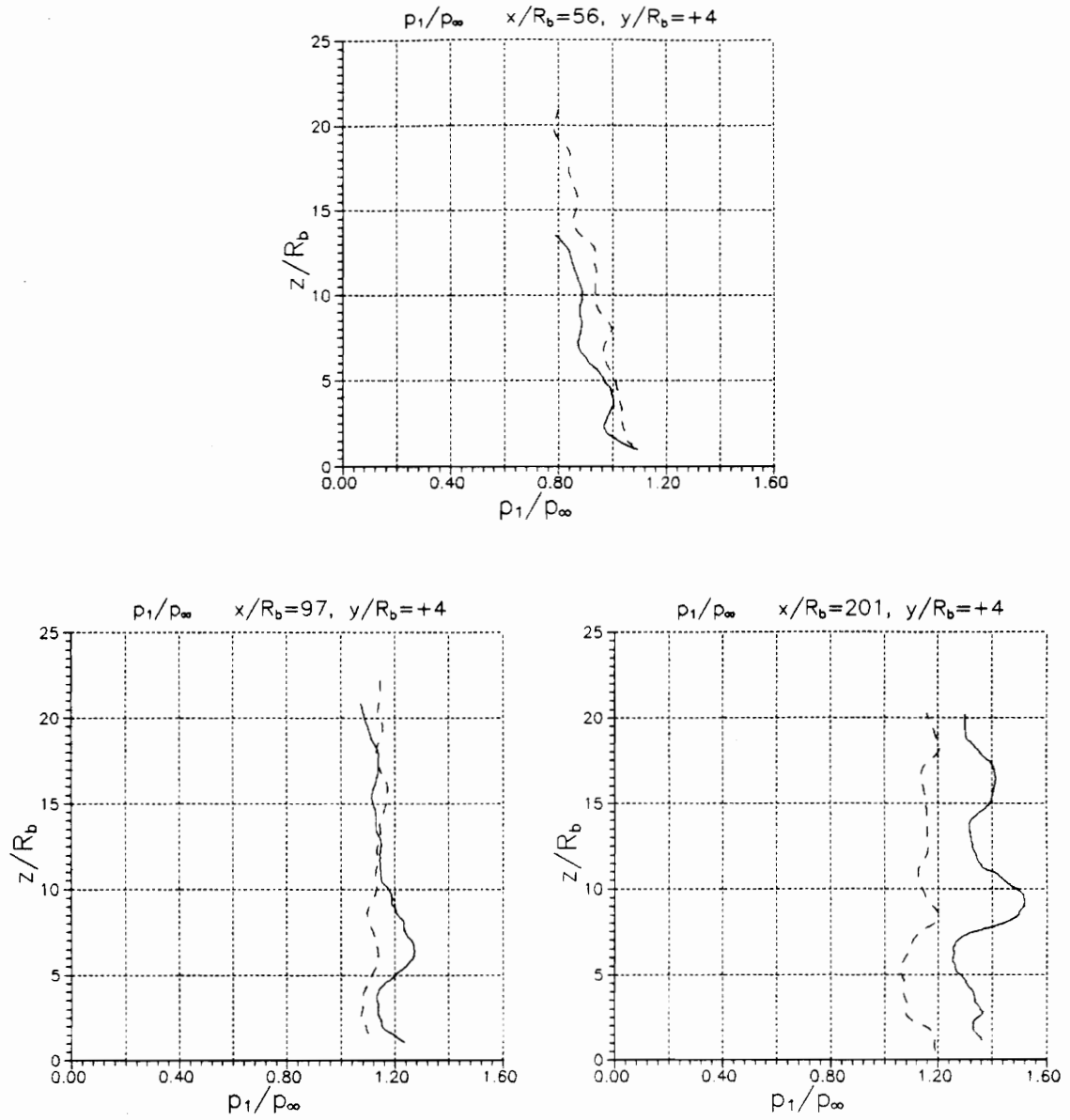

Wedge-shaped Nozzle: Solid Line
Circular Nozzle: Dashed Line

Figure 39. Static Pressure Profiles, $y/R_b = +4$.

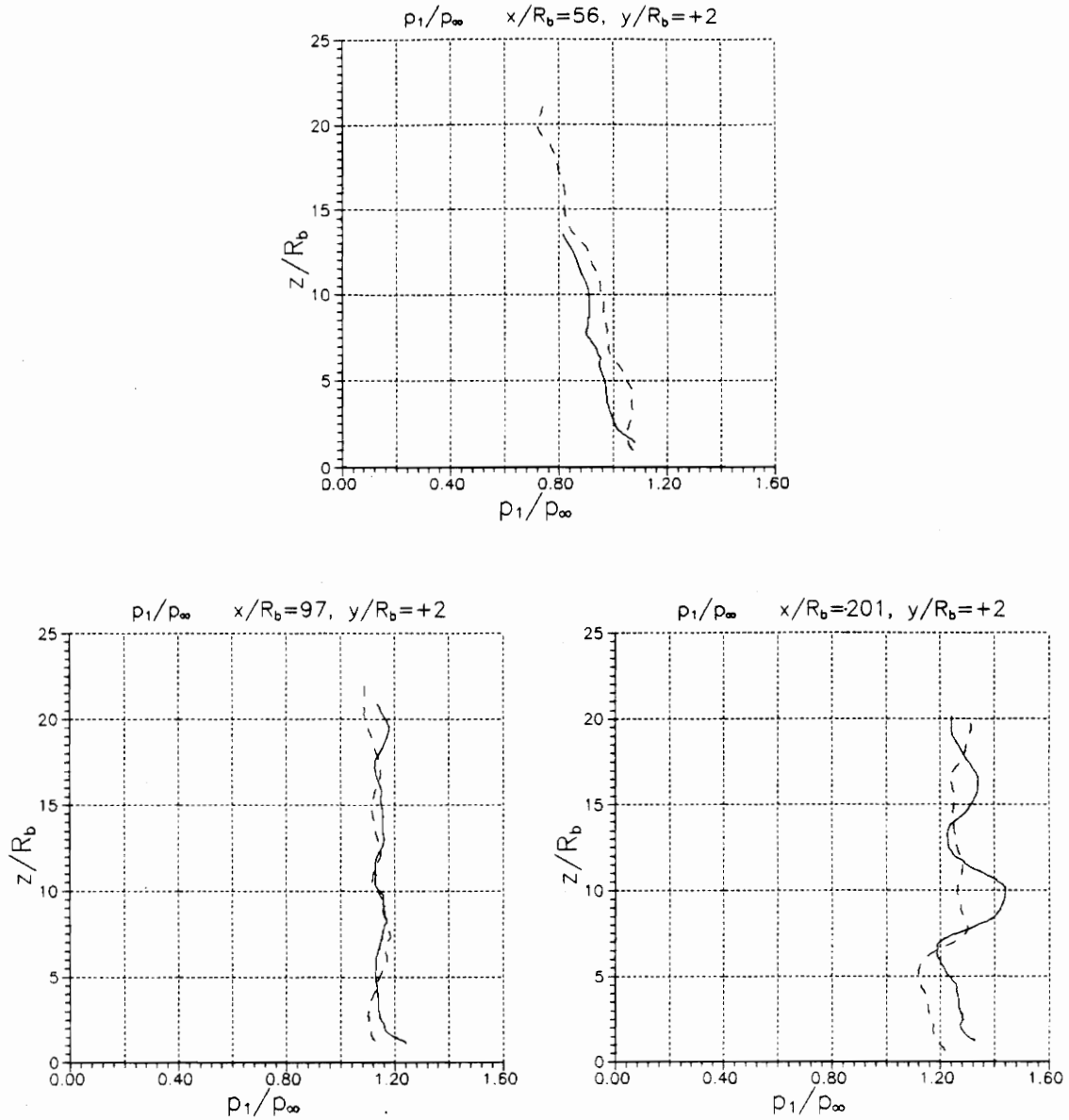

Wedge-shaped Nozzle: Solid Line
Circular Nozzle: Dashed Line

Figure 40. Static Pressure Profiles, $y/R_b = +2$.

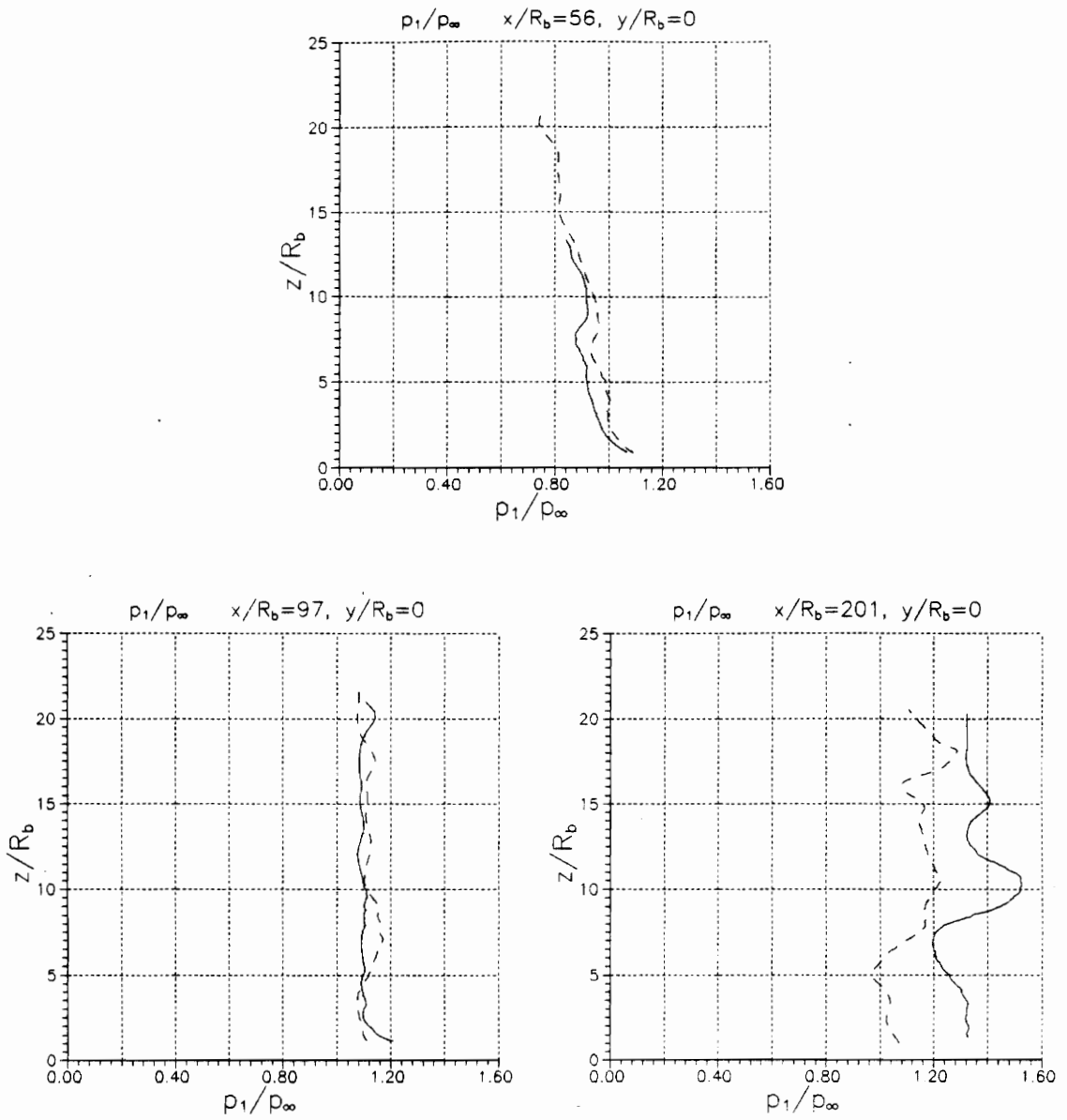

Wedge-shaped Nozzle: Solid Line
Circular Nozzle: Dashed Line

Figure 41. Static Pressure Profiles, $y/R_b=0$.

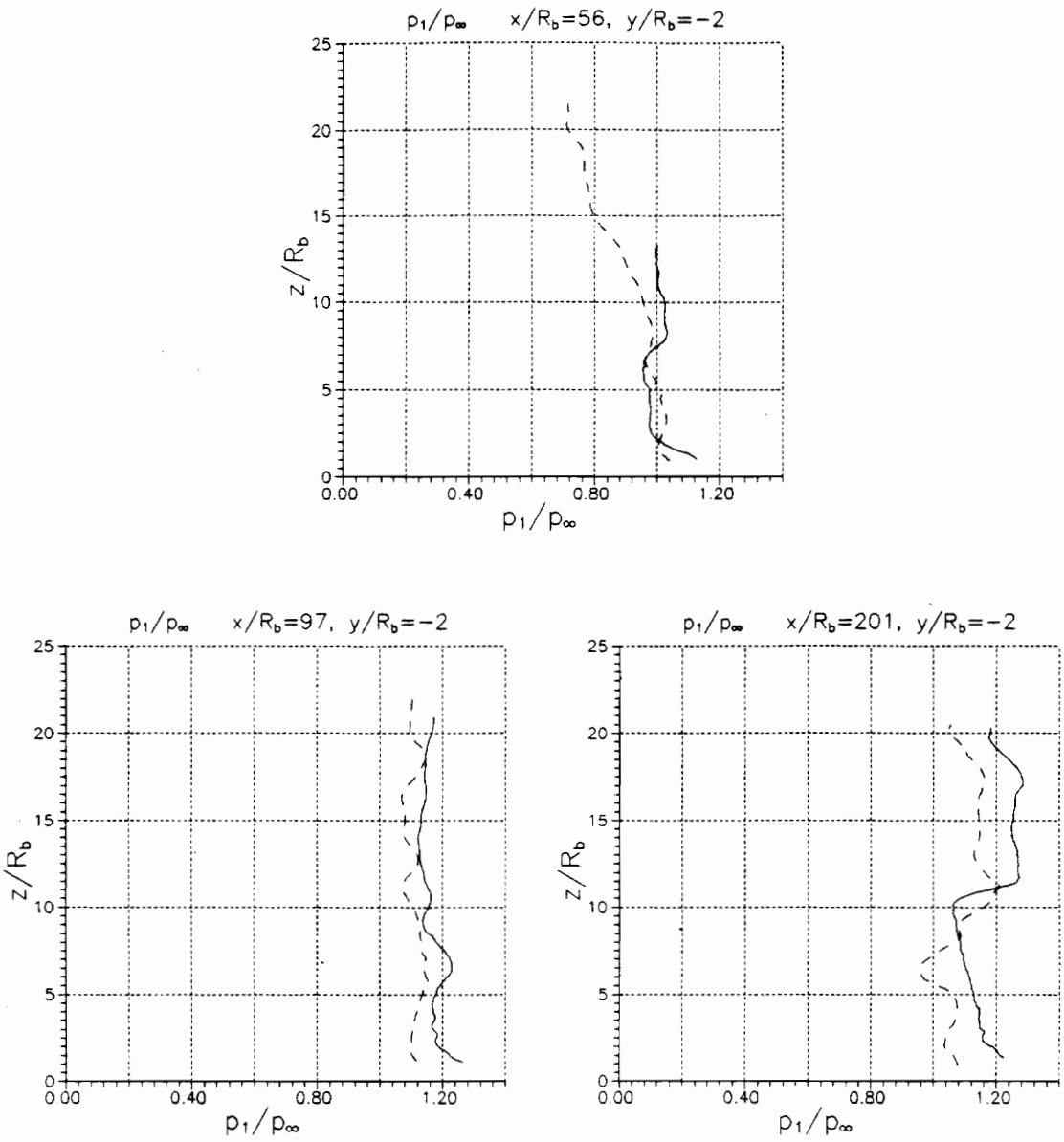

Wedge-shaped Nozzle: Solid Line
Circular Nozzle: Dashed Line

Figure 42. Static Pressure Profiles, y/R_b=-2.

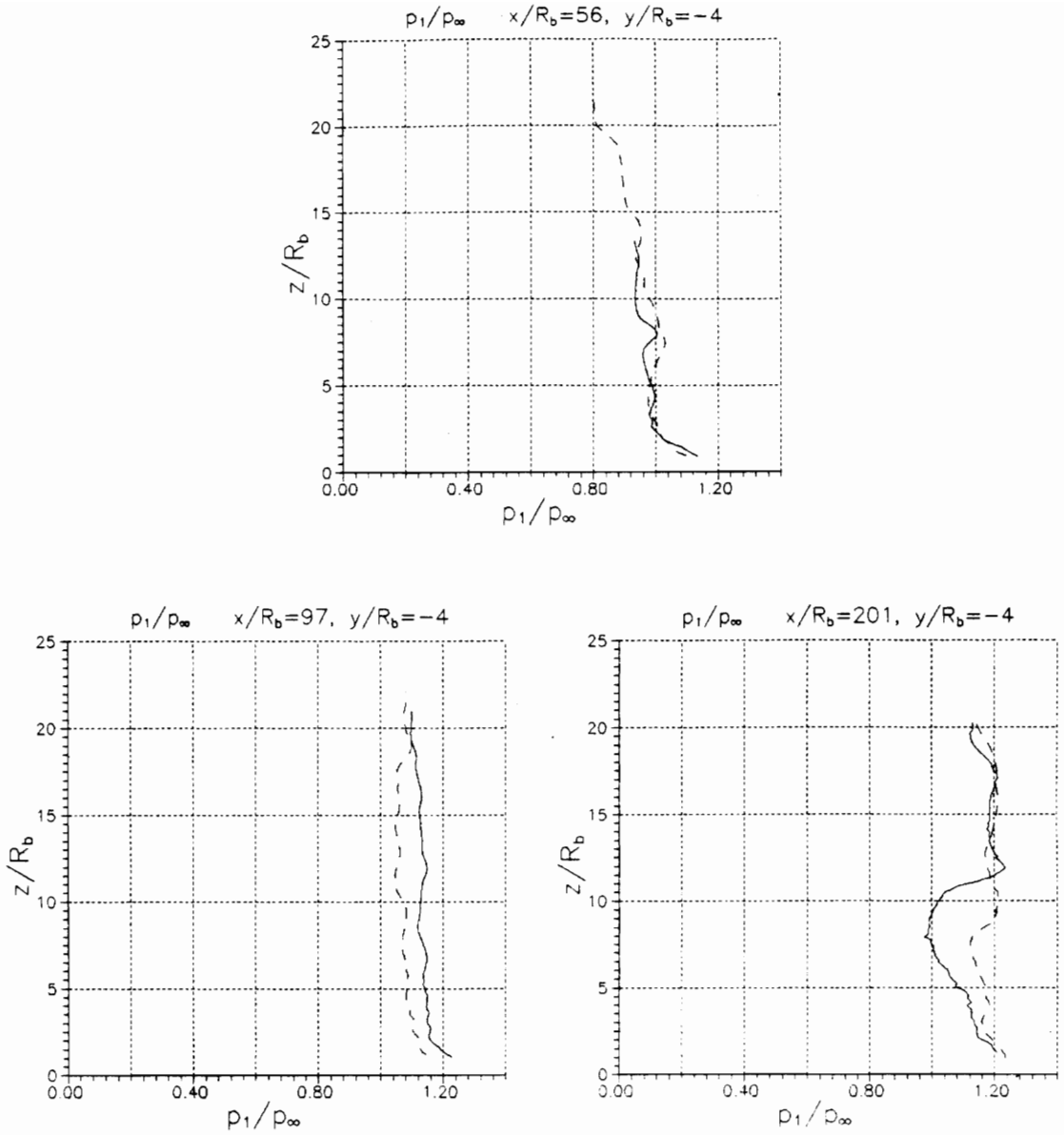

Wedge-shaped Nozzle: Solid Line
Circular Nozzle: Dashed Line

Figure 43. Static Pressure Profiles, y/R_b=-4.

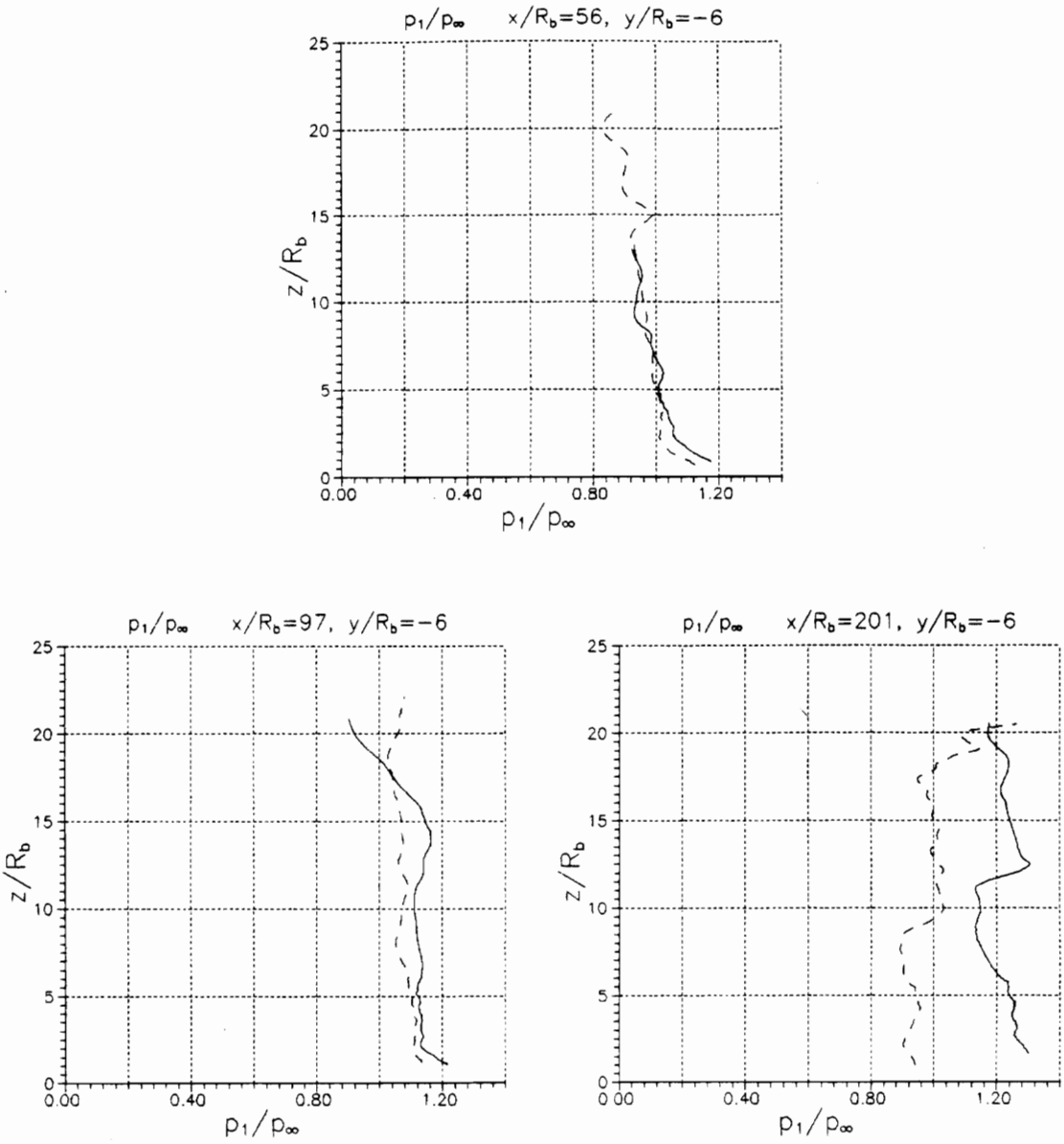

Wedge-shaped Nozzle: Solid Line
Circular Nozzle: Dashed Line

Figure 44. Static Pressure Profiles, $y/R_b=-6$.

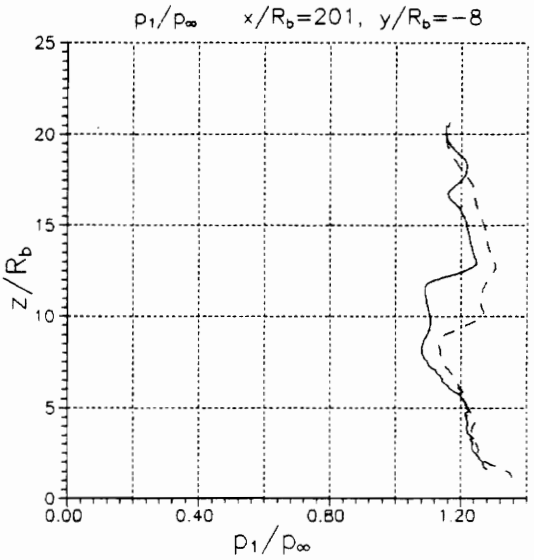

Wedge-shaped Nozzle: Solid Line
Circular Nozzle: Dashed Line

Figure 45. Static Pressure Profiles, $y/R_b=-8$.

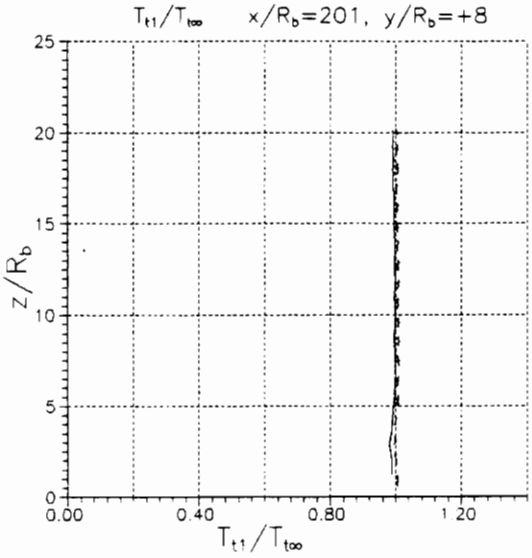

Wedge-shaped Nozzle: Solid Line
Circular Nozzle: Dashed Line

Figure 46. Total Temperature Profiles, $y/R_b = +8$.

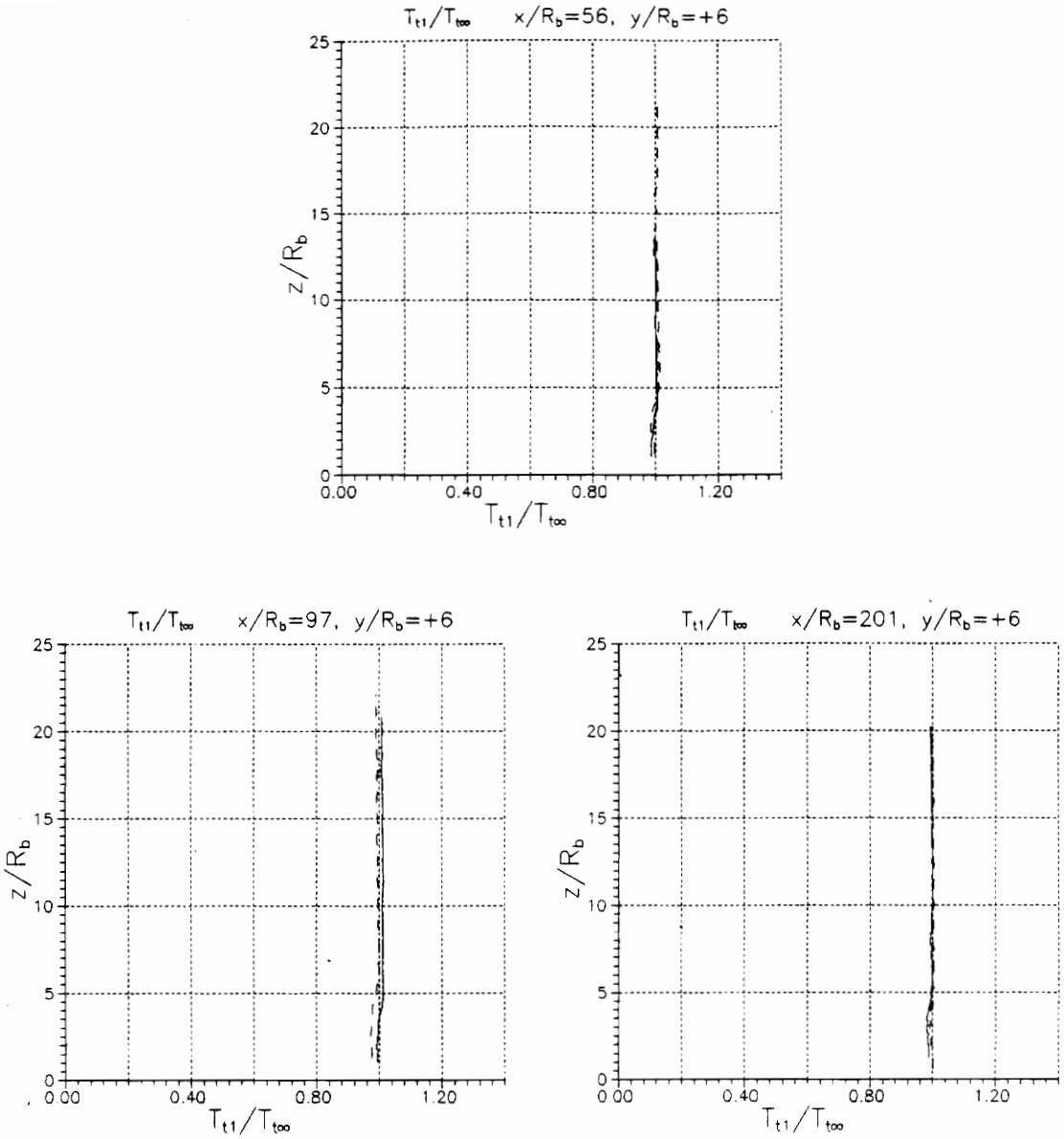

Wedge-shaped Nozzle: Solid Line
Circular Nozzle: Dashed Line

Figure 47. Total Temperature Profiles, $y/R_b = +6$.

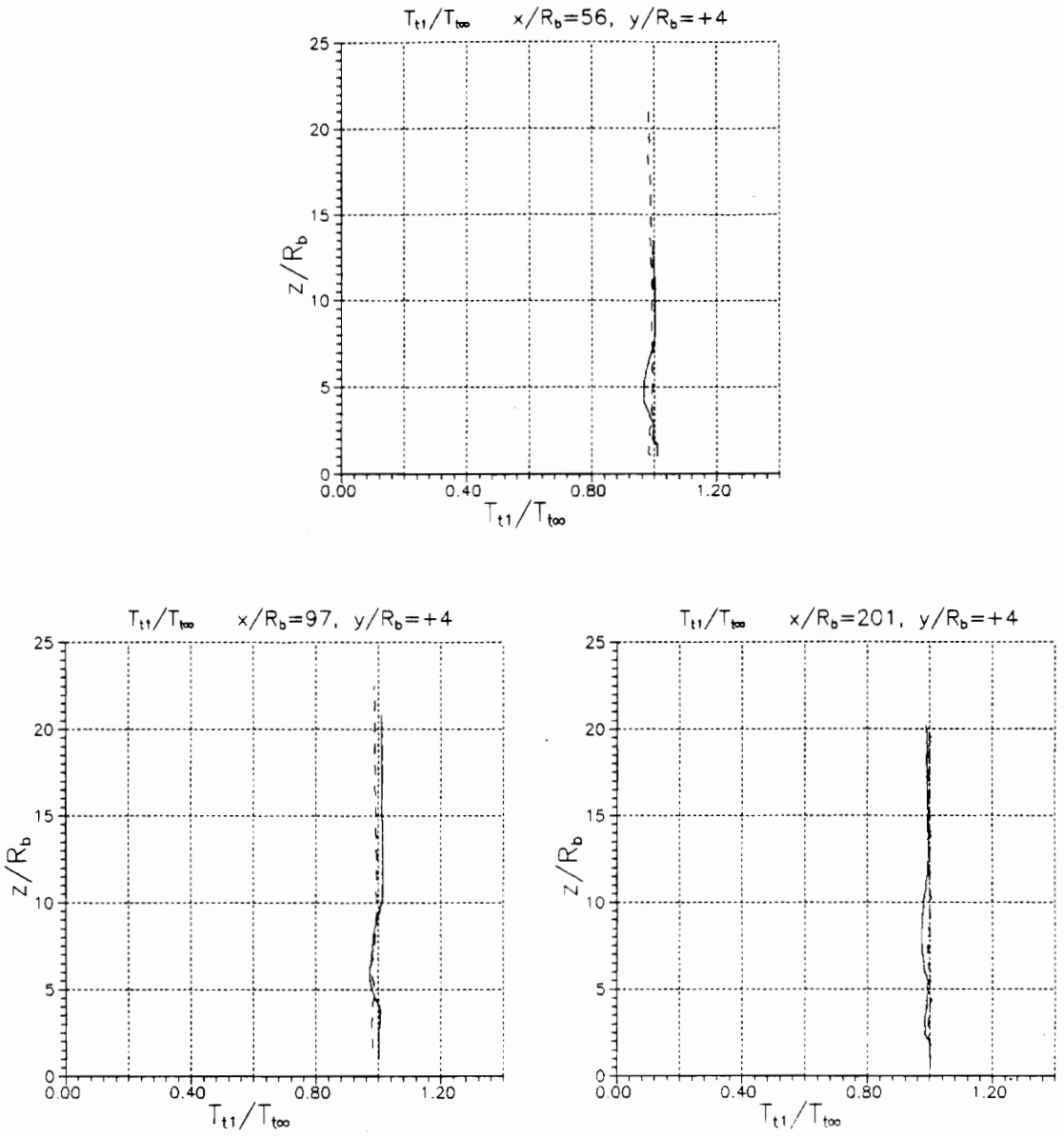

Wedge-shaped Nozzle: Solid Line
Circular Nozzle: Dashed Line

Figure 48. Total Temperature Profiles, $y/R_b=+4$.

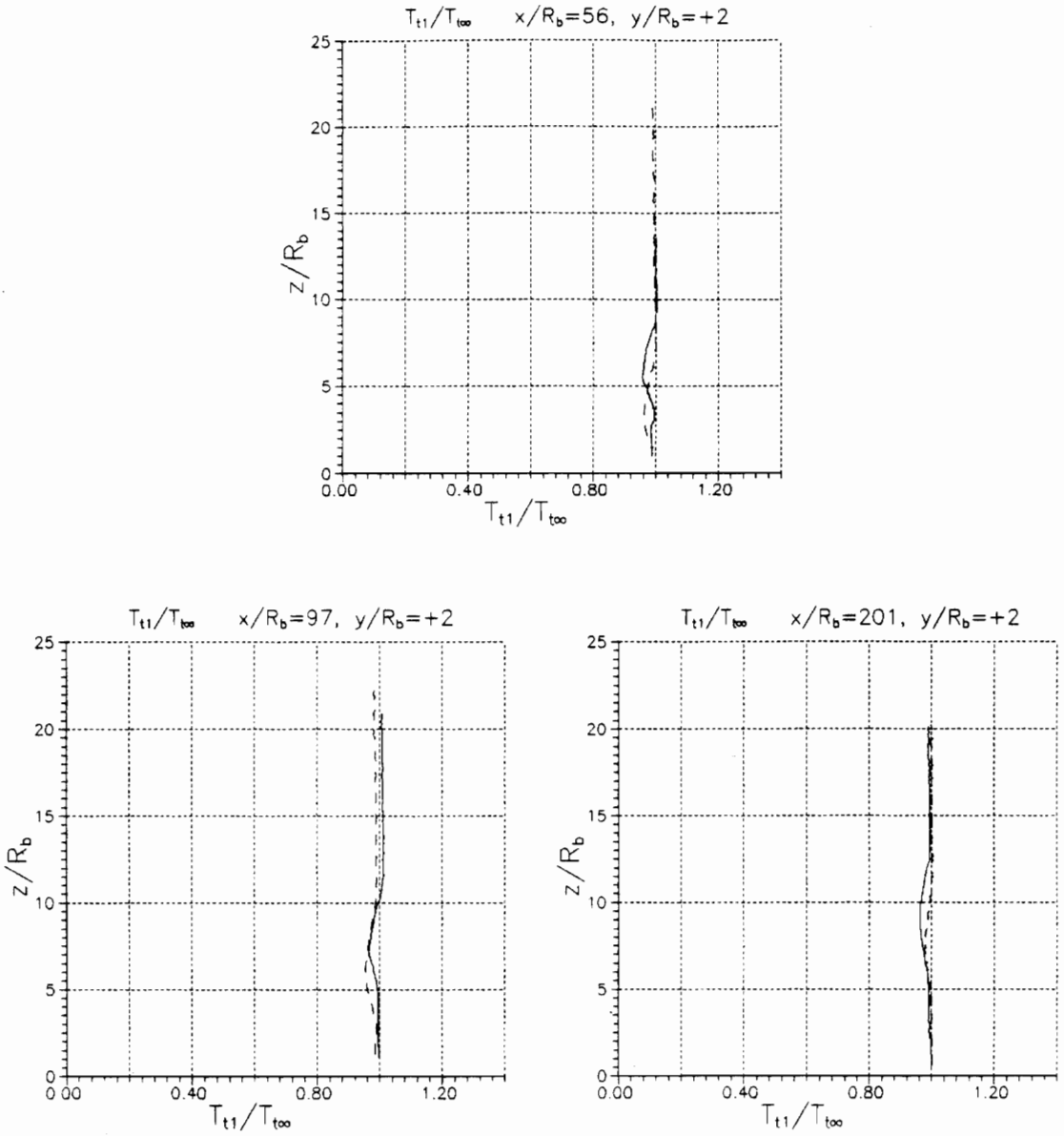

Wedge-shaped Nozzle: Solid Line
Circular Nozzle: Dashed Line

Figure 49. Total Temperature Profiles, $y/R_b = +2$.

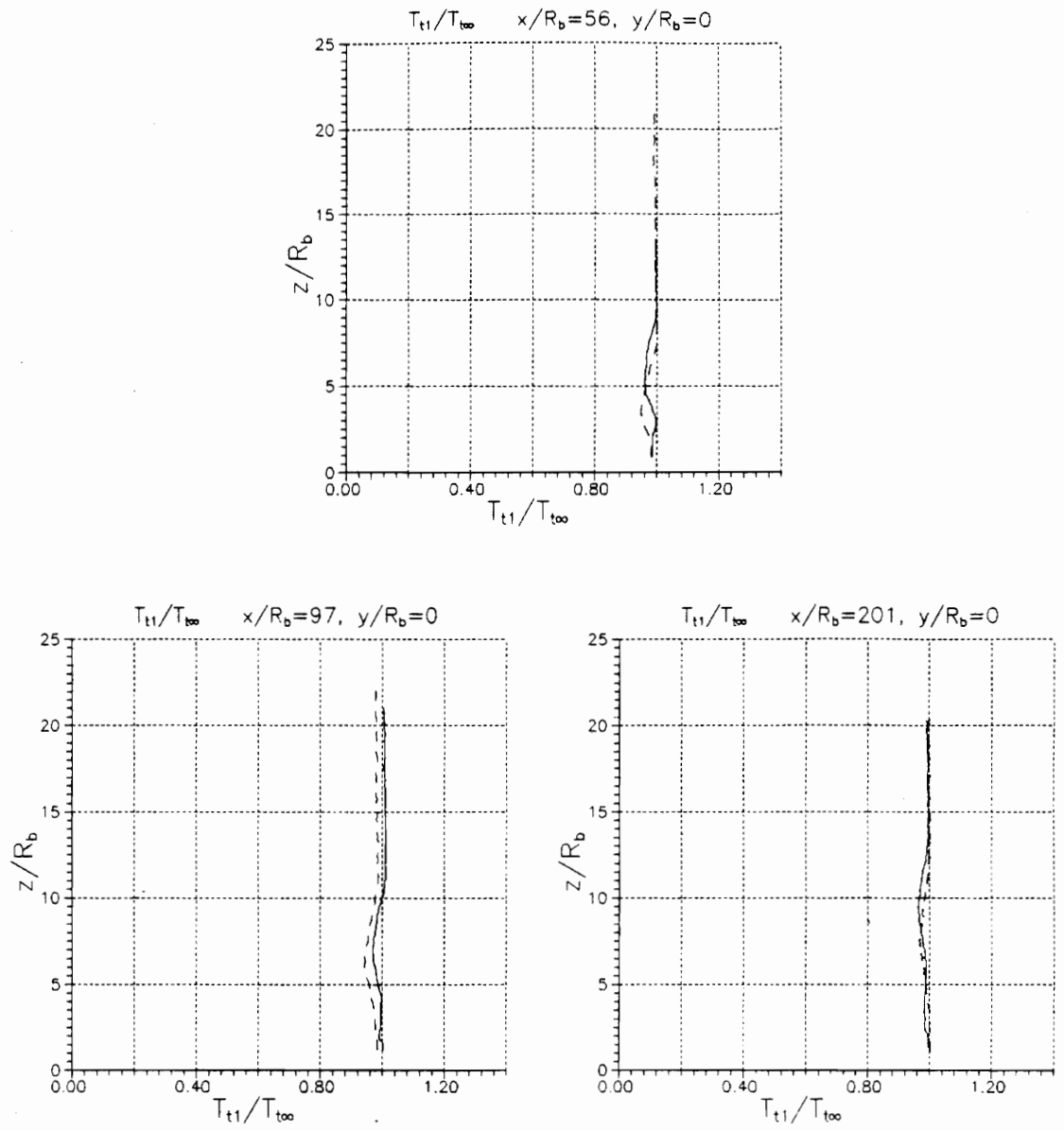

Wedge-shaped Nozzle: Solid Line
Circular Nozzle: Dashed Line

Figure 50. Total Temperature Profiles, $y/R_b=0$.

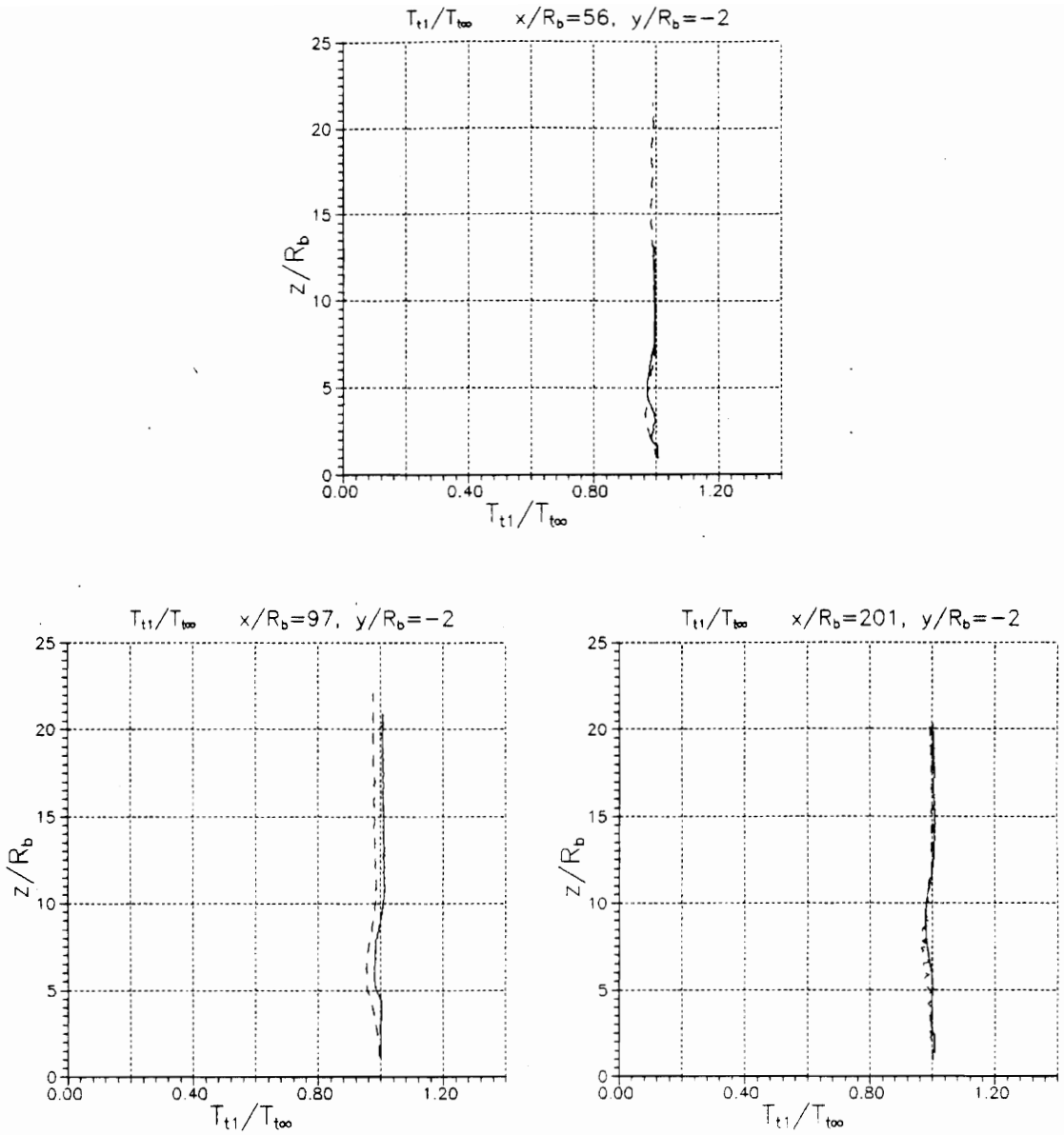

Wedge-shaped Nozzle: Solid Line
Circular Nozzle: Dashed Line

Figure 51. Total Temperature Profiles, $y/R_b=-2$.

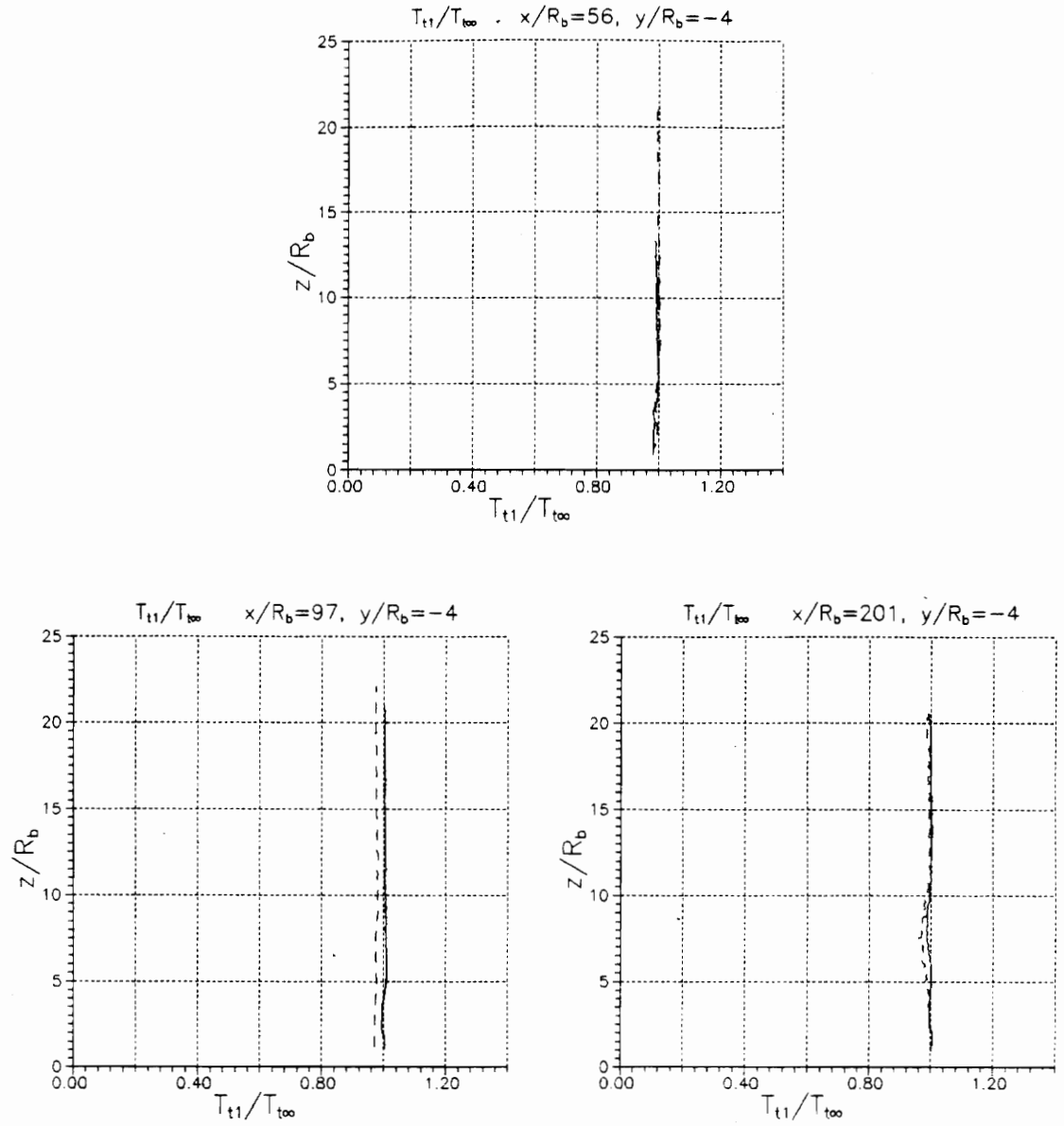

Wedge-shaped Nozzle: Solid Line
Circular Nozzle: Dashed Line

Figure 52. Total Temperature Profiles, $y/R_b=-4$.

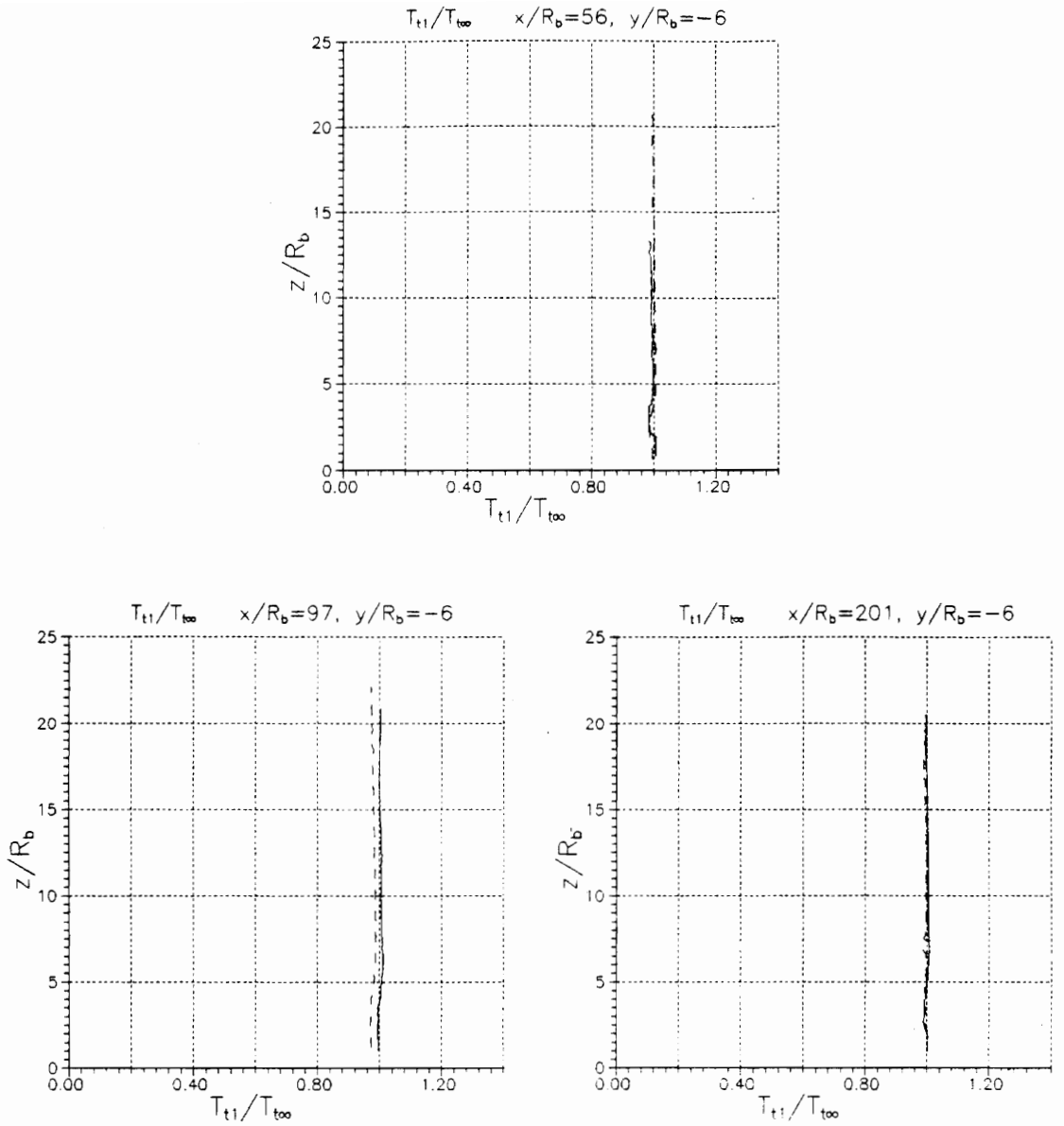

Wedge-shaped Nozzle: Solid Line
Circular Nozzle: Dashed Line

Figure 53. Total Temperature Profiles, $y/R_b=-6$.

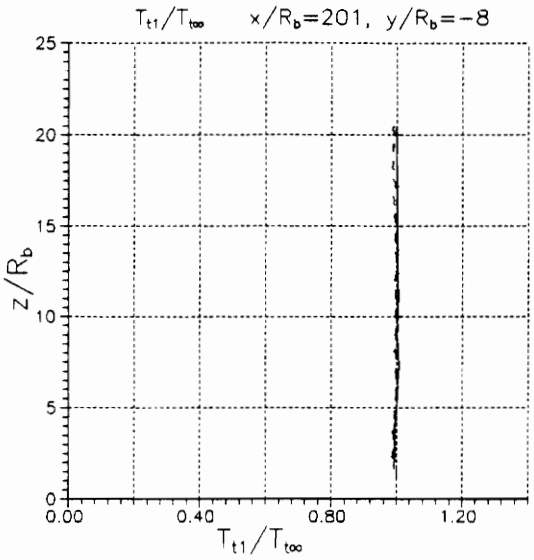

Wedge-shaped Nozzle: Solid Line
Circular Nozzle: Dashed Line

Figure 54. Total Temperature Profiles, $y/R_b=-8$.

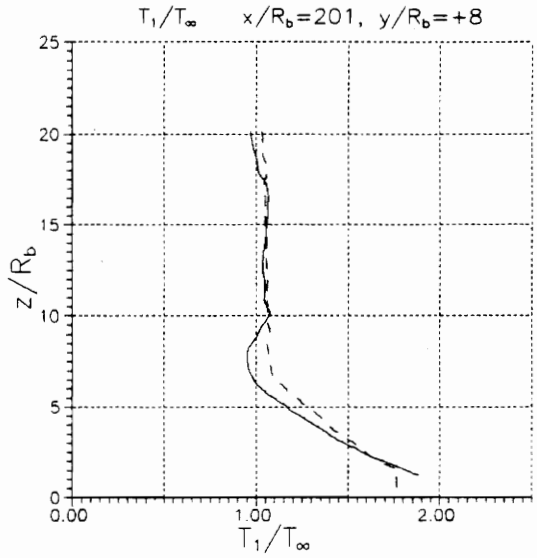

Wedge-shaped Nozzle: Solid Line
Circular Nozzle: Dashed Line

Figure 55. Static Temperature Profiles, $y/R_b = +8$.

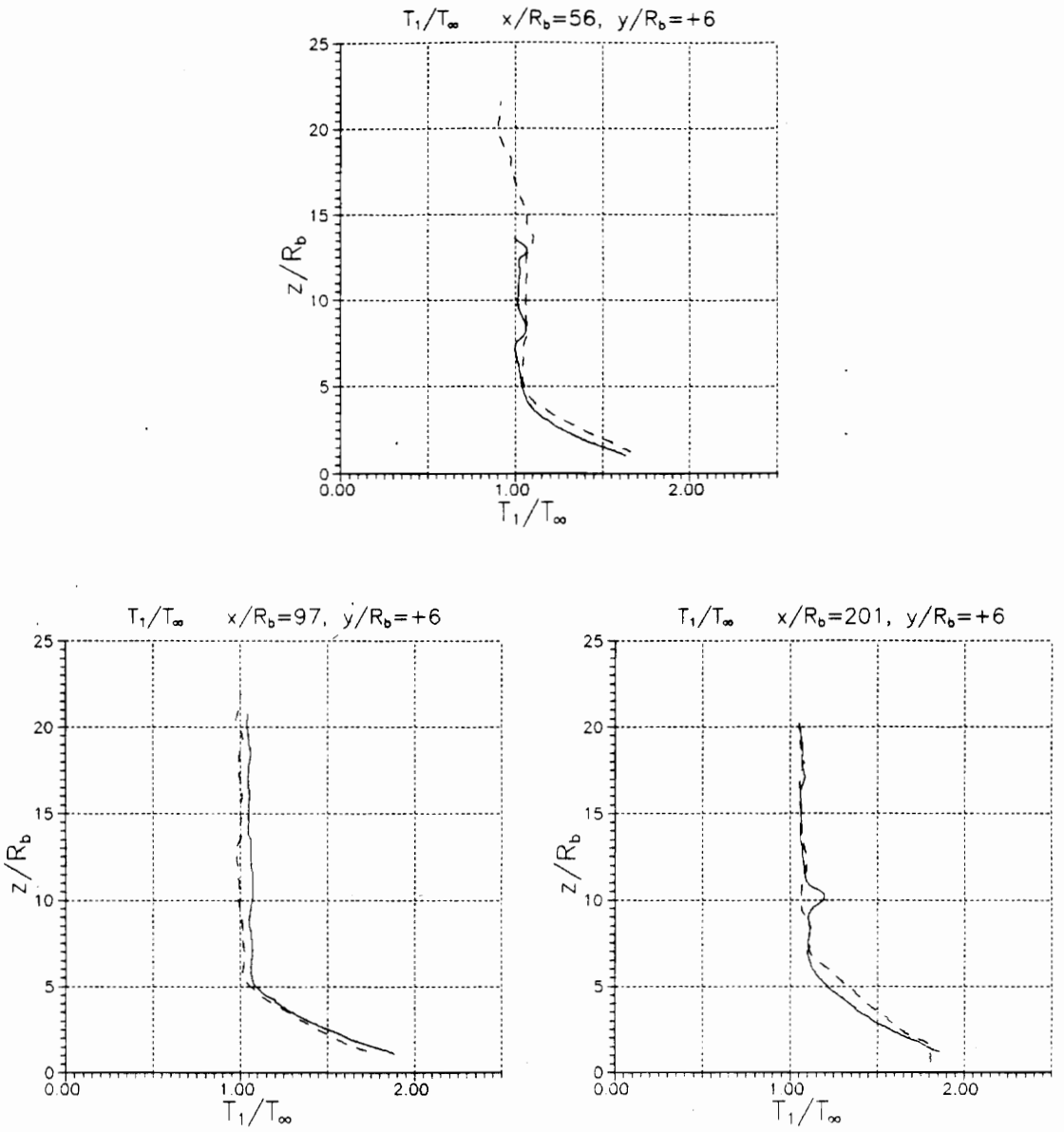

Wedge-shaped Nozzle: Solid Line
Circular Nozzle: Dashed Line

Figure 56. Static Temperature Profiles, $y/R_b = +6$.

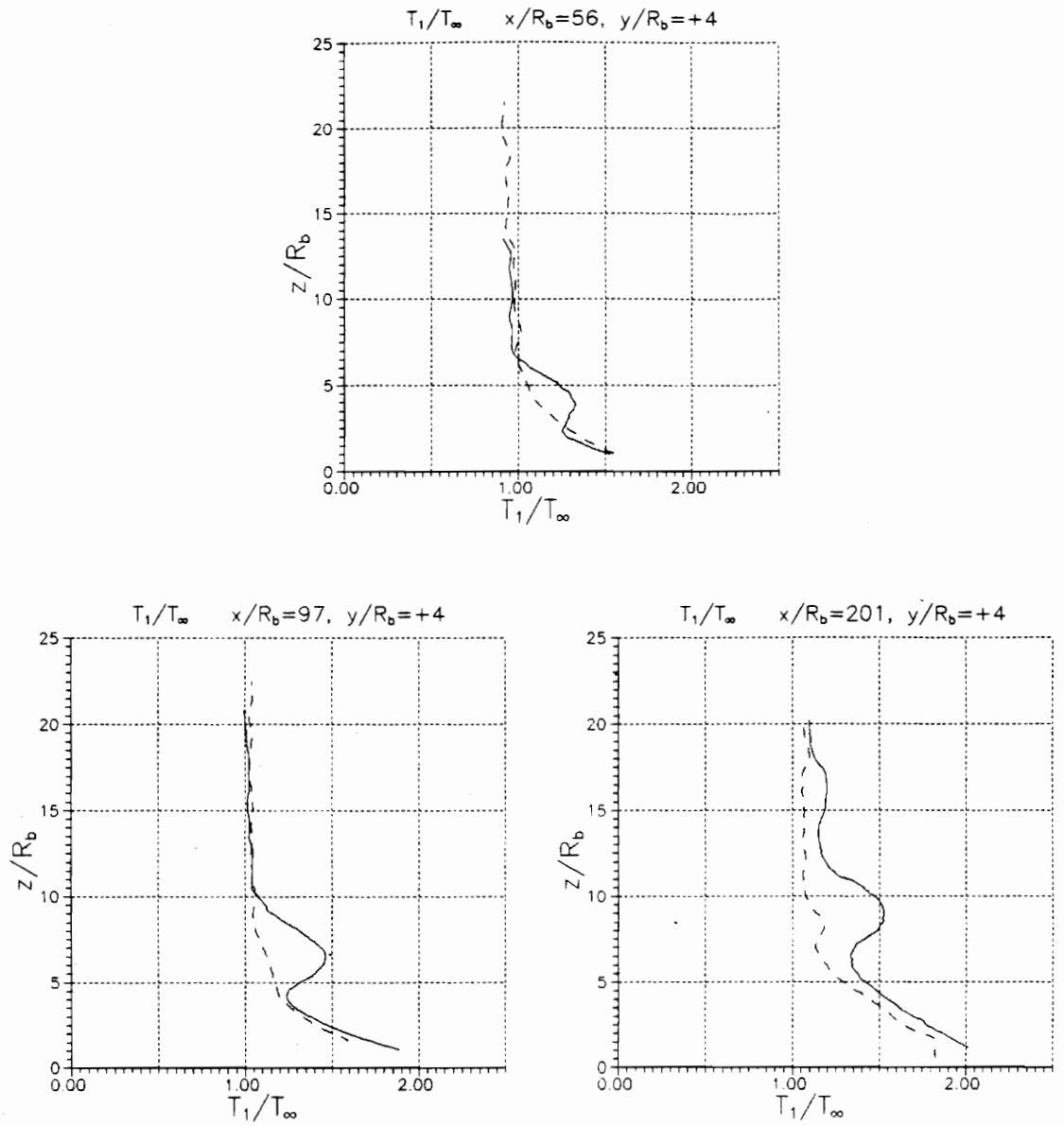

Wedge-shaped Nozzle: Solid Line
Circular Nozzle: Dashed Line

Figure 57. Static Temperature Profiles, $y/R_b = +4$.

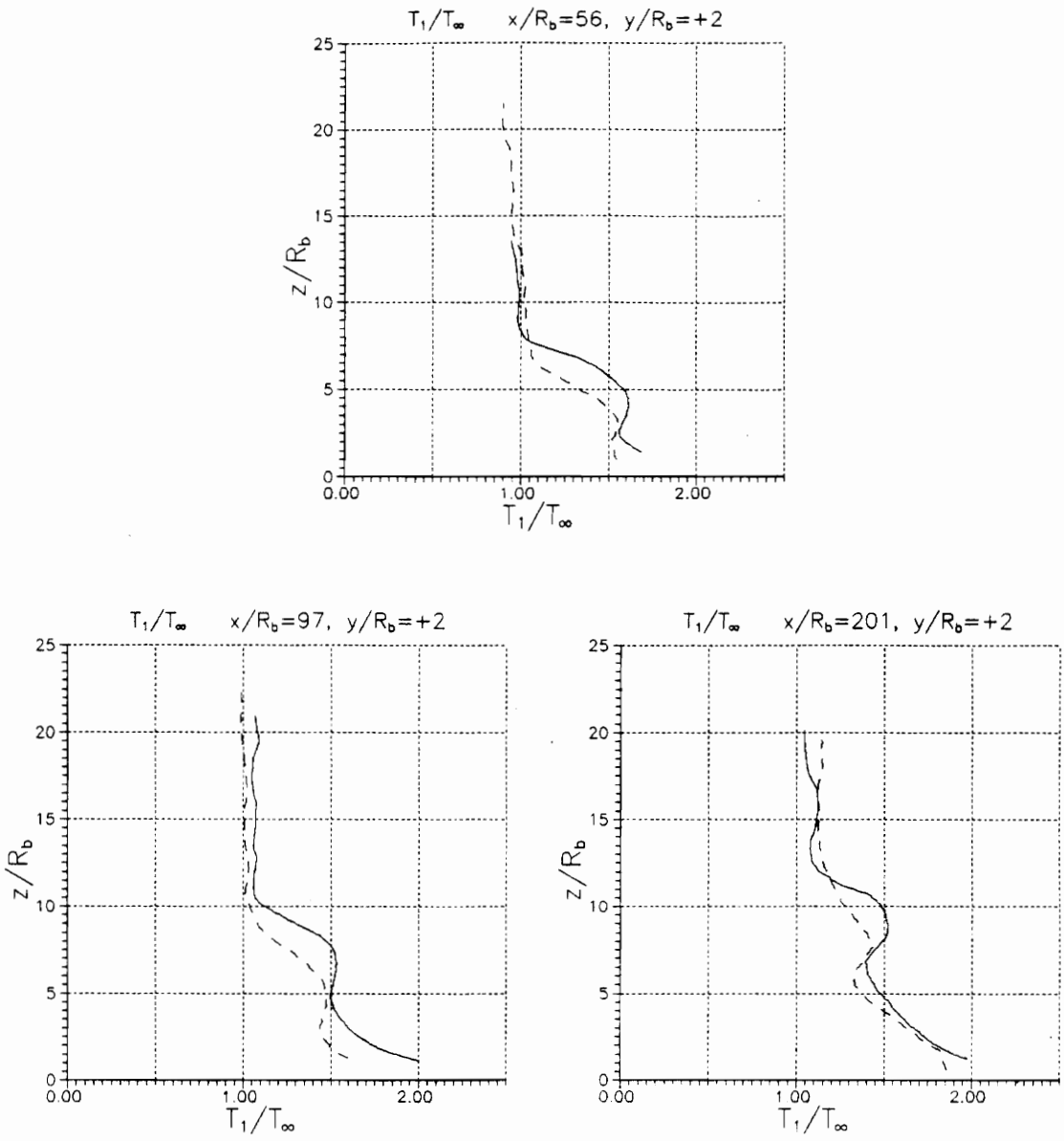

Wedge-shaped Nozzle: Solid Line
Circular Nozzle: Dashed Line

Figure 58. Static Temperature Profiles, $y/R_b = +2$.

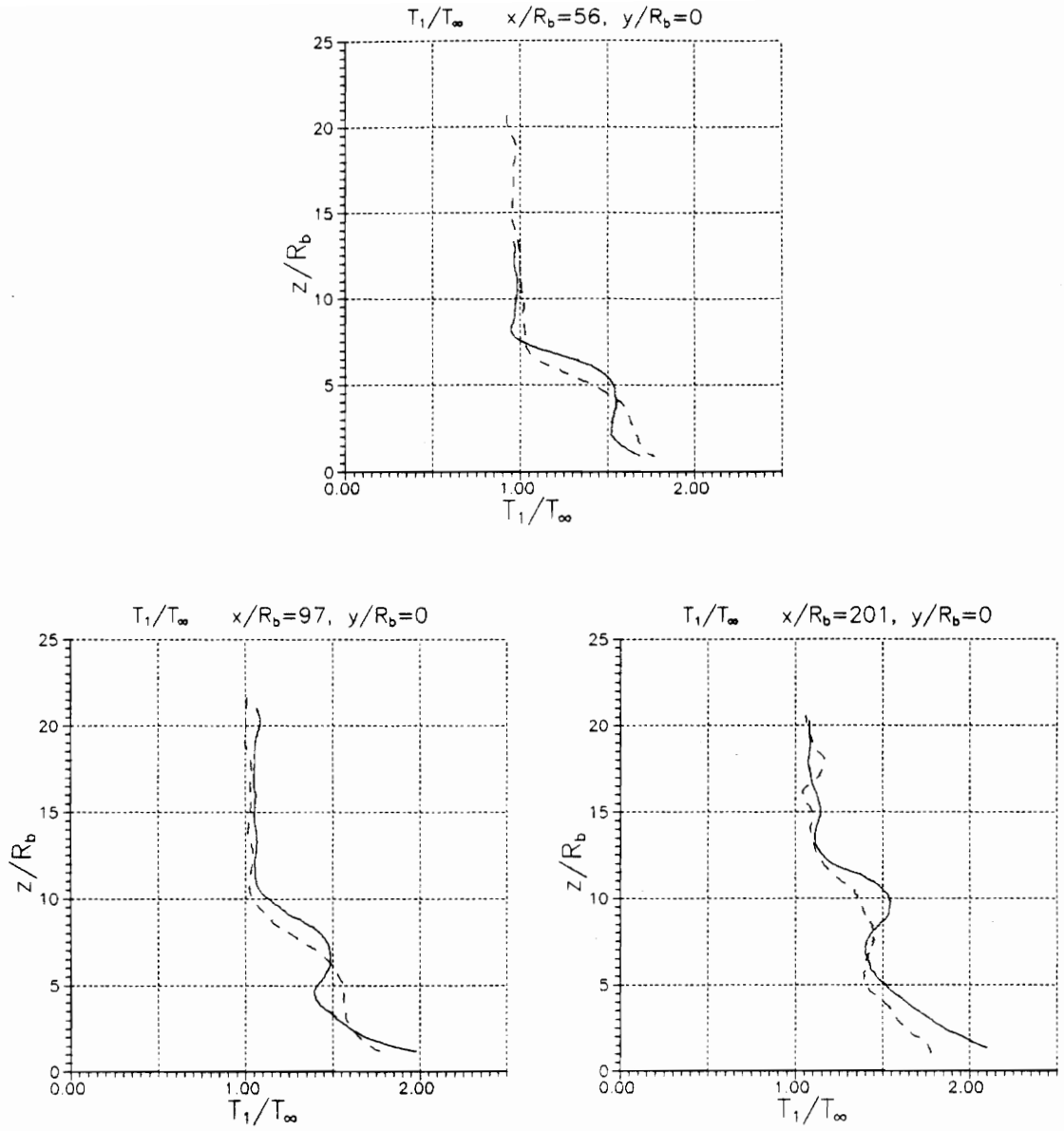

Wedge-shaped Nozzle: Solid Line
Circular Nozzle: Dashed Line

Figure 59. Static Temperature Profiles, $y/R_b=0$.

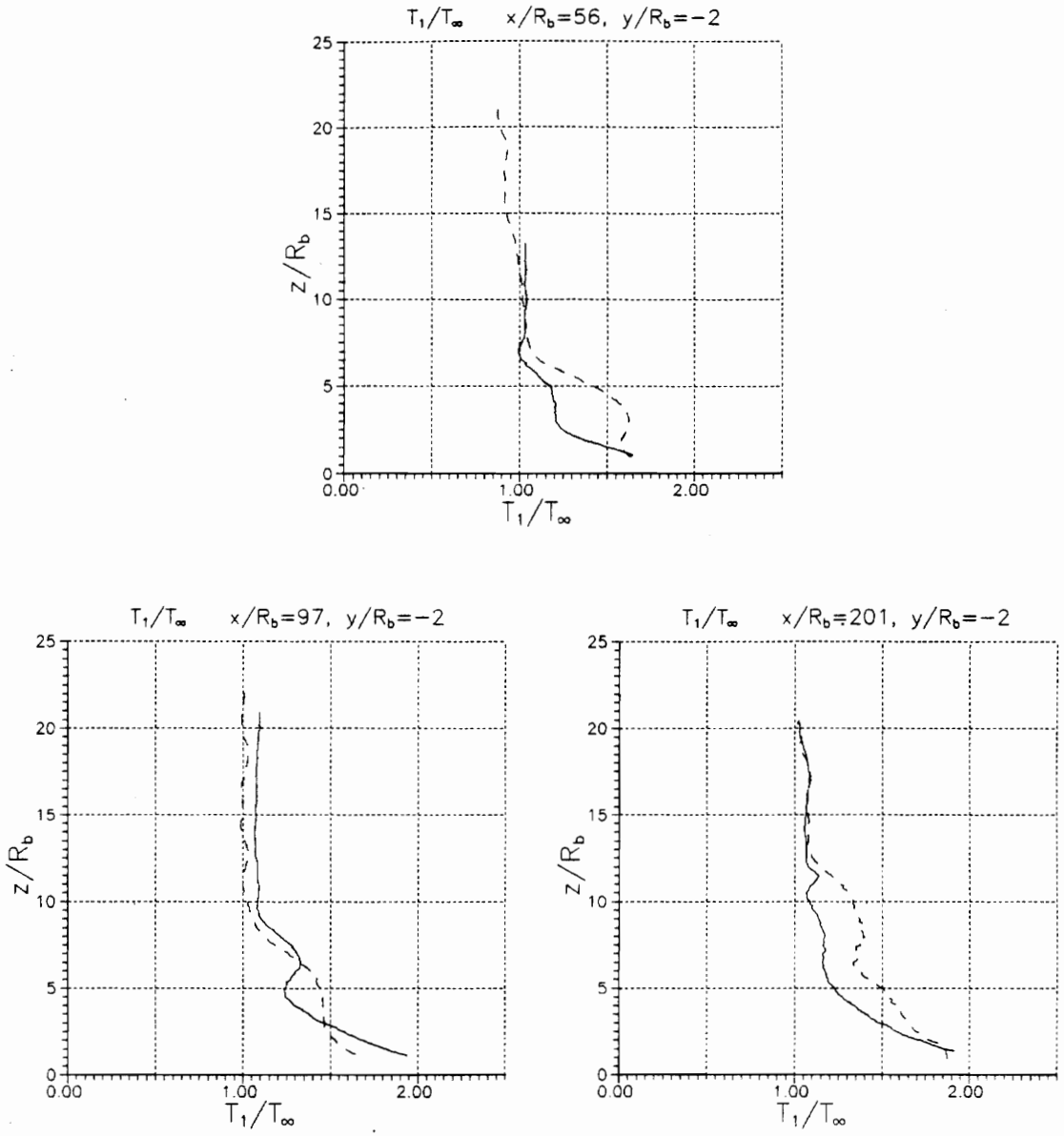

Wedge-shaped Nozzle: Solid Line
Circular Nozzle: Dashed Line

Figure 60. Static Temperature Profiles, y/R_b=-2.

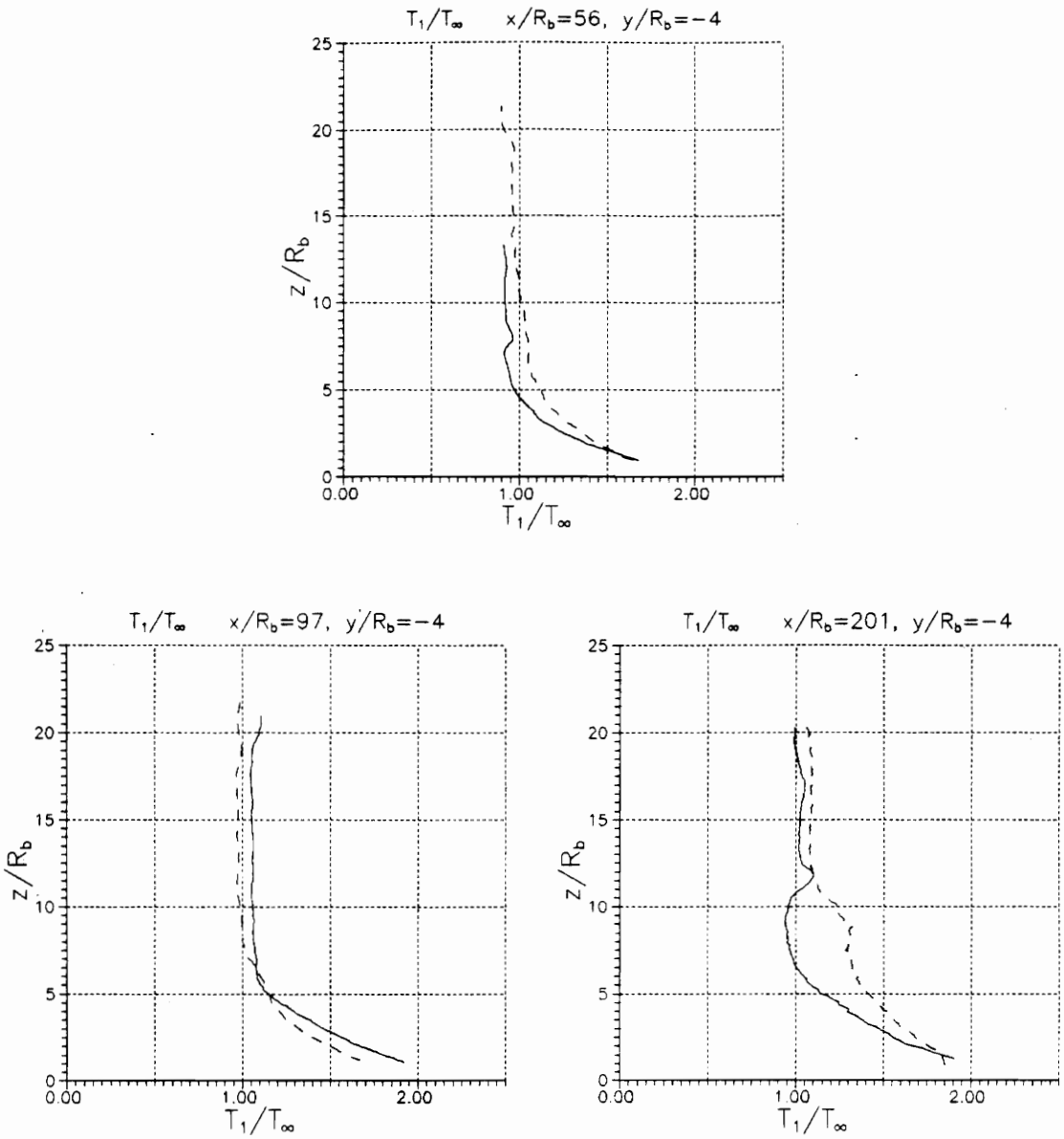

Wedge-shaped Nozzle: Solid Line
Circular Nozzle: Dashed Line

Figure 61. Static Temperature Profiles, $y/R_b=-4$.

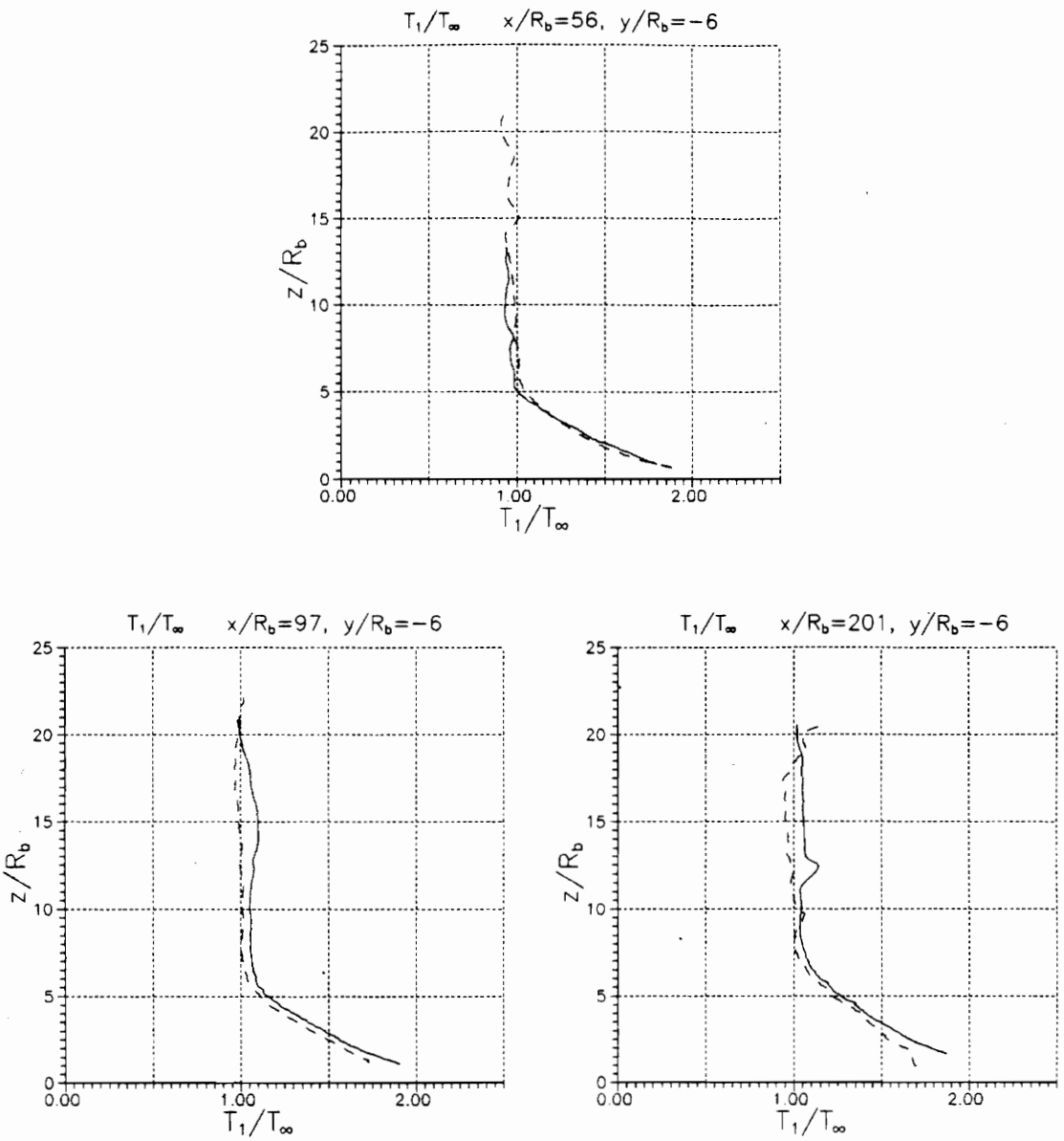

Wedge-shaped Nozzle: Solid Line
Circular Nozzle: Dashed Line

Figure 62. Static Temperature Profiles, $y/R_b=-6$.

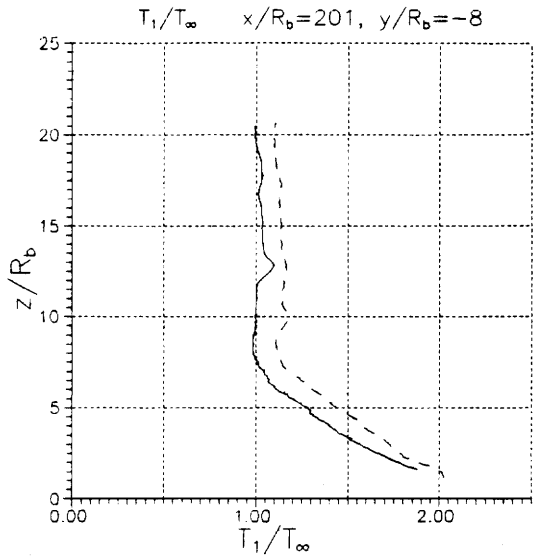

Wedge-shaped Nozzle: Solid Line
Circular Nozzle: Dashed Line

Figure 63. Static Temperature Profiles, $y/R_b=-8$.

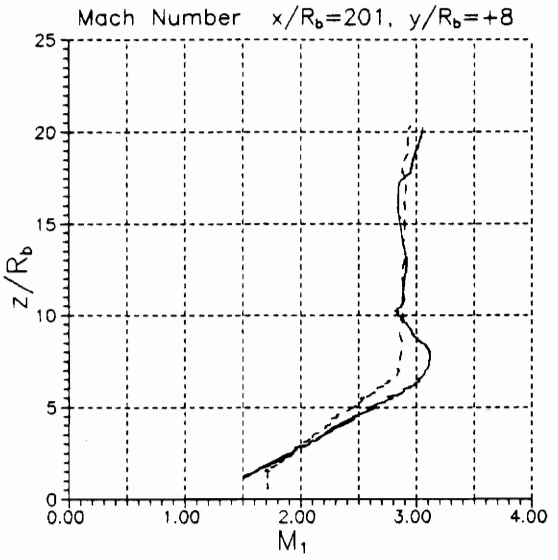

Wedge-shaped Nozzle: Solid Line
Circular Nozzle: Dashed Line

Figure 64. Mach Number Profiles, $y/R_b = +8$.

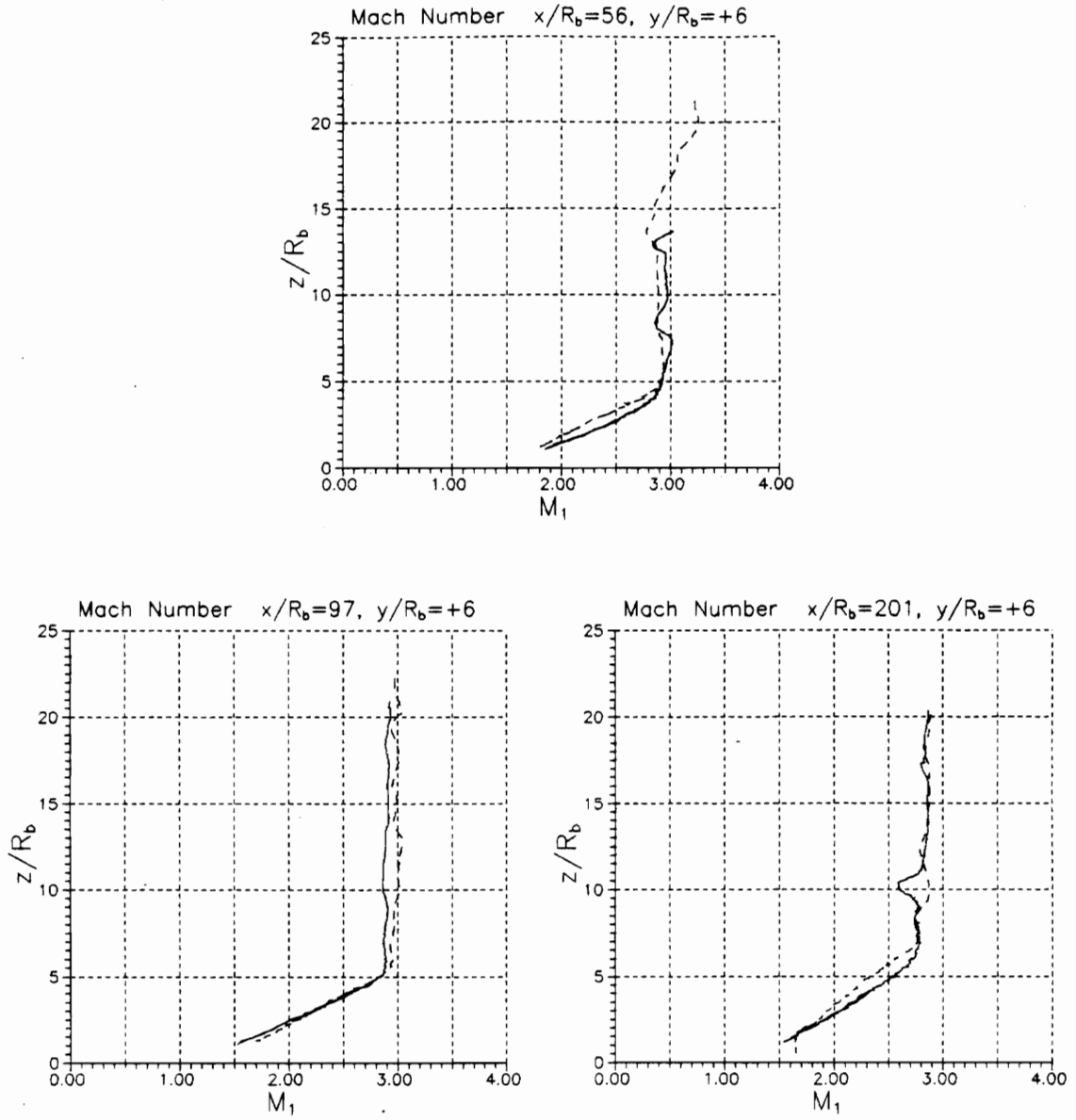

Wedge-shaped Nozzle: Solid Line
Circular Nozzle: Dashed Line

Figure 65. Mach Number Profiles, $y/R_b = +6$.

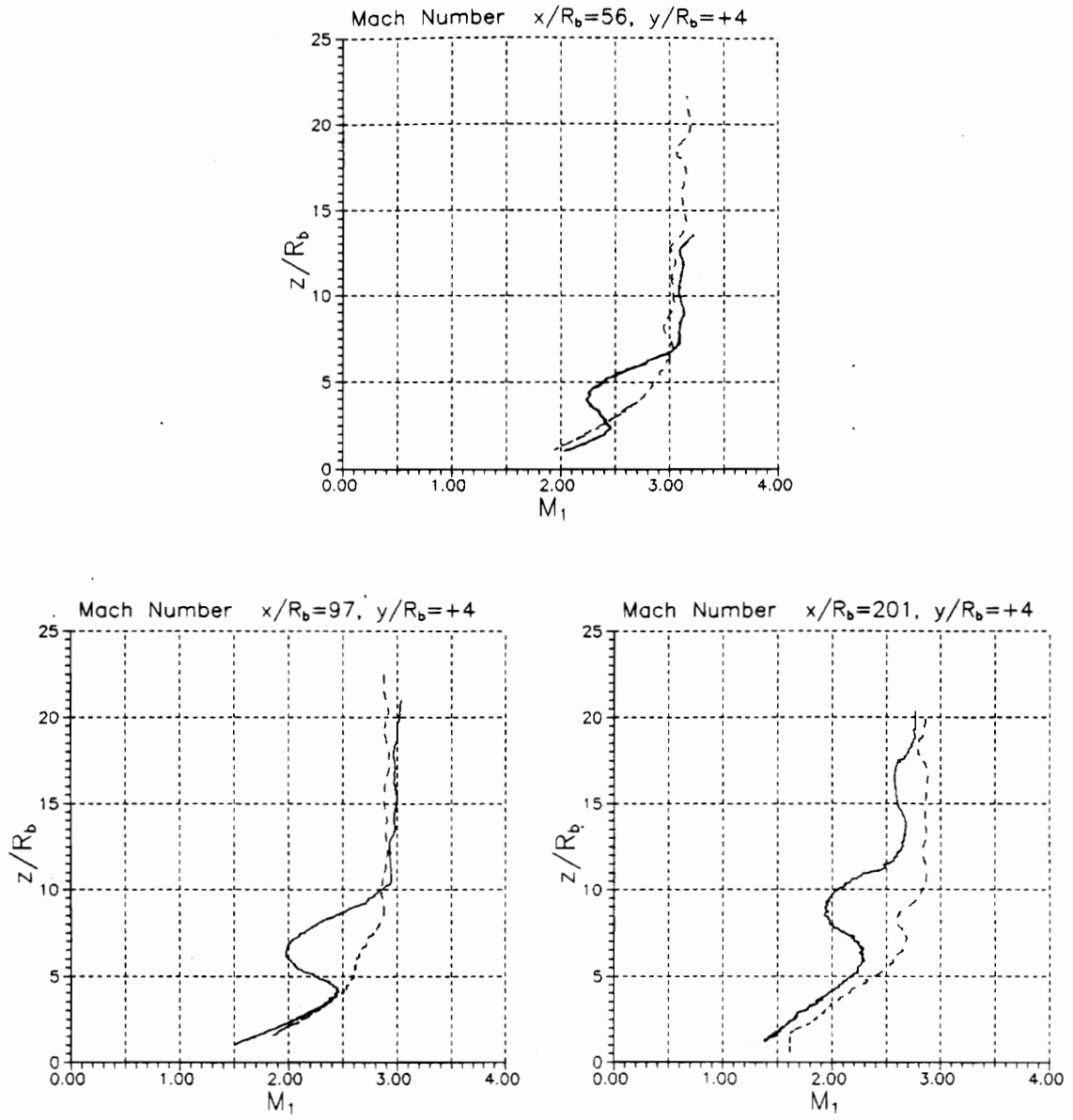

Wedge-shaped Nozzle: Solid Line
Circular Nozzle: Dashed Line

Figure 66. Mach Number Profiles, $y/R_b = +4$.

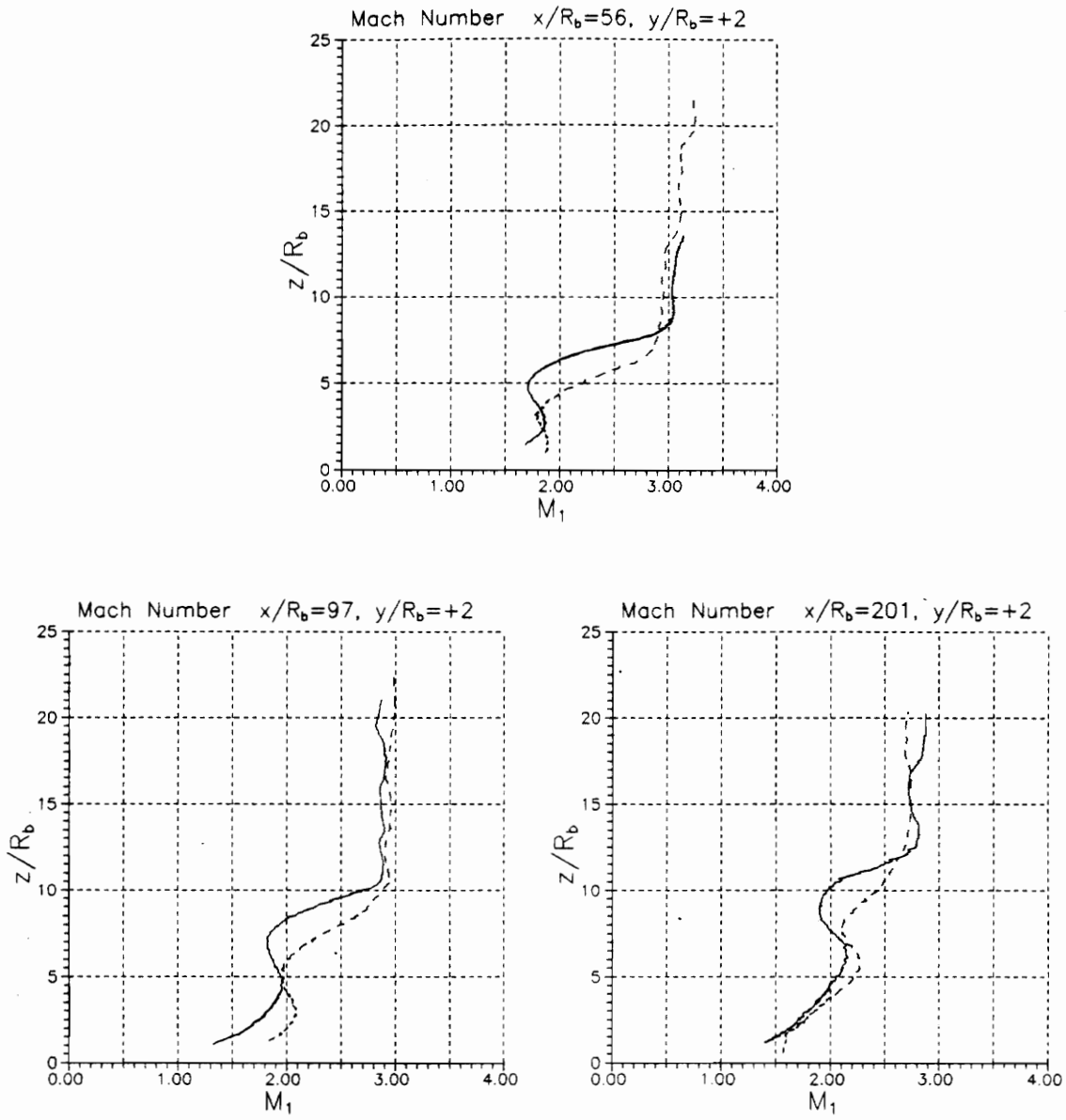

Wedge-shaped Nozzle: Solid Line
Circular Nozzle: Dashed Line

Figure 67. Mach Number Profiles, $y/R_b = +2$.

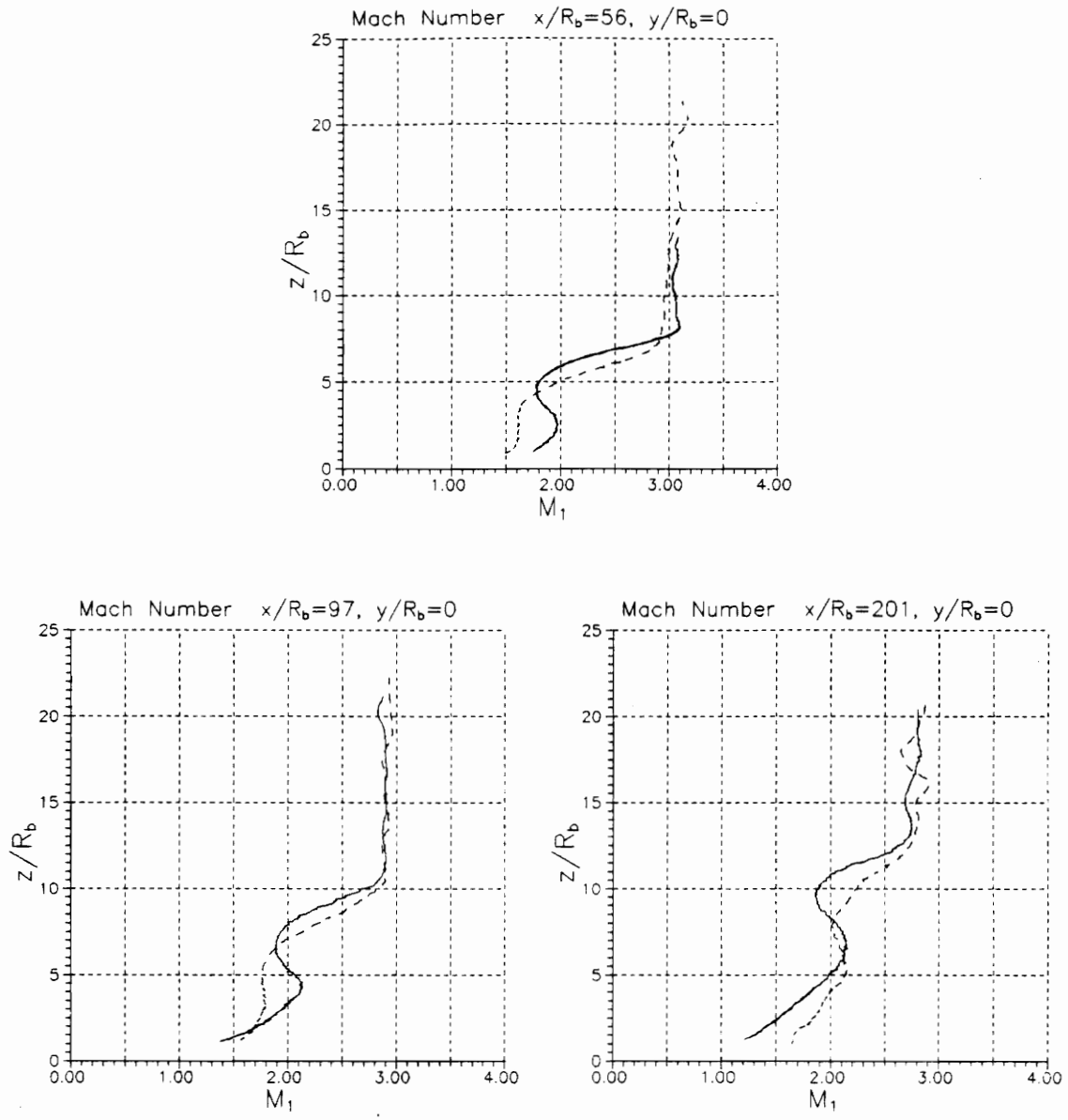

Wedge-shaped Nozzle: Solid Line
Circular Nozzle: Dashed Line

Figure 68. Mach Number Profiles, $y/R_b=0$.

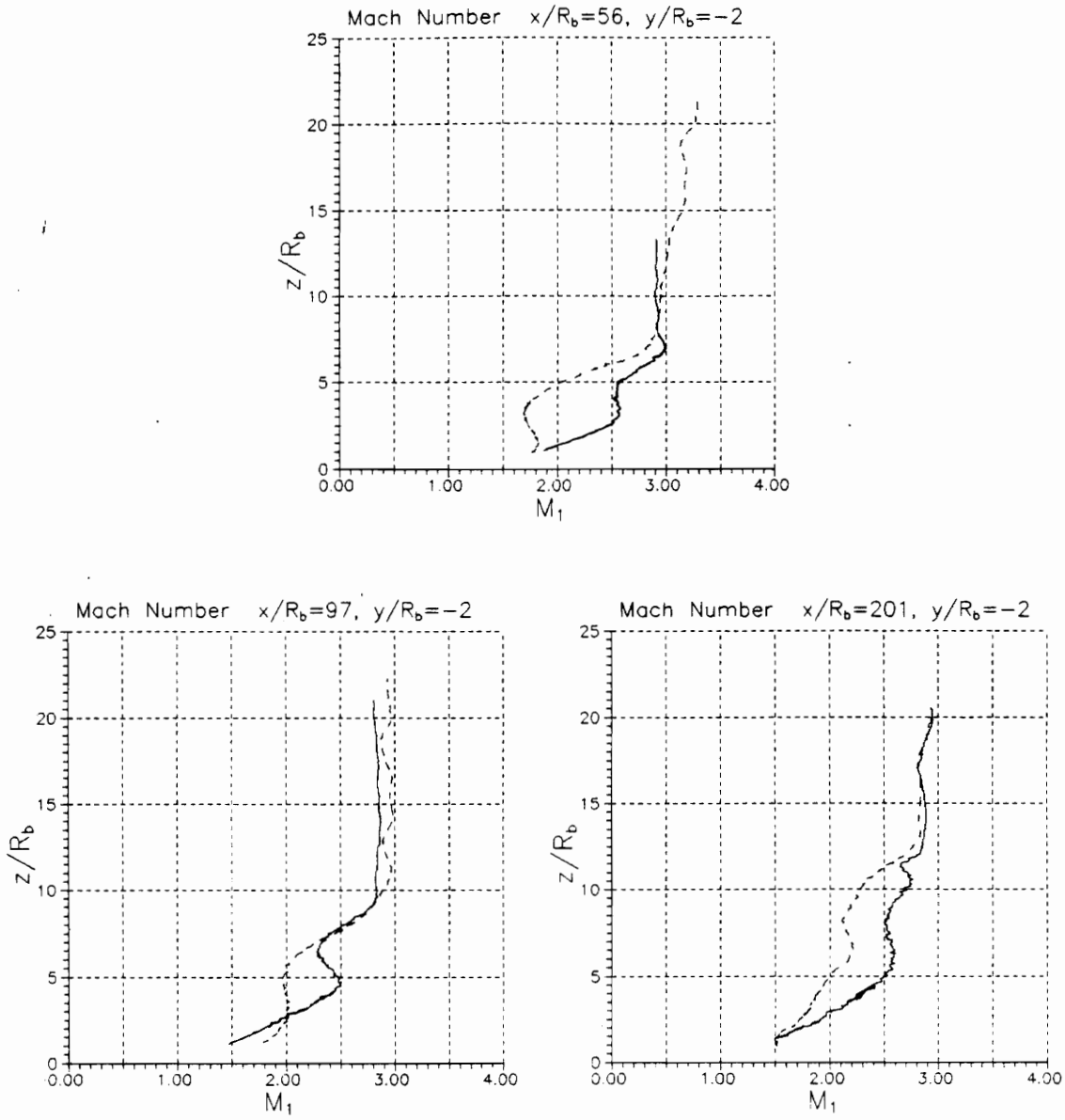

Wedge-shaped Nozzle: Solid Line
Circular Nozzle: Dashed Line

Figure 69. Mach Number Profiles, y/R_b=-2.

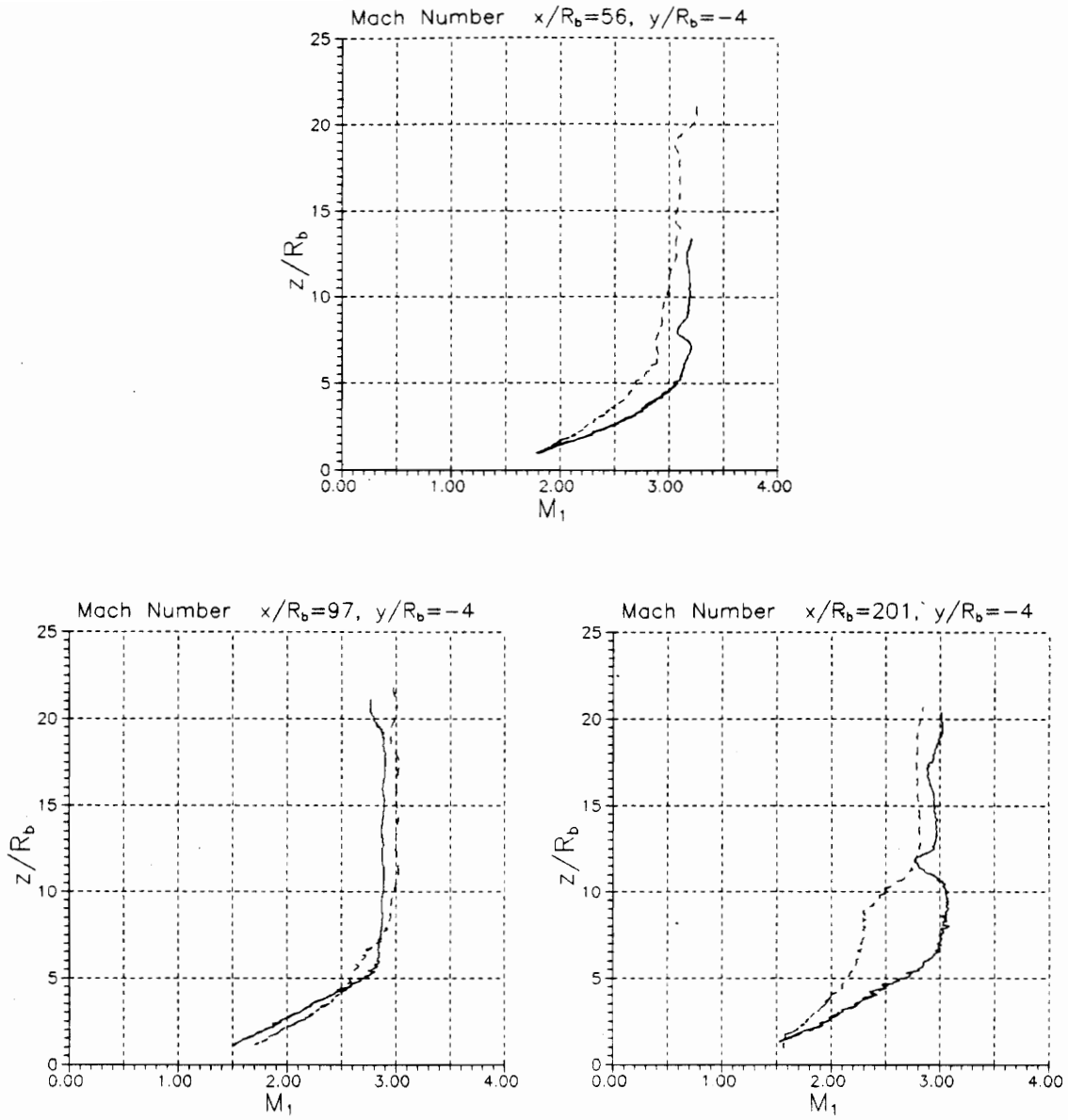

Wedge-shaped Nozzle: Solid Line
Circular Nozzle: Dashed Line

Figure 70. Mach Number Profiles, $y/R_b=-4$.

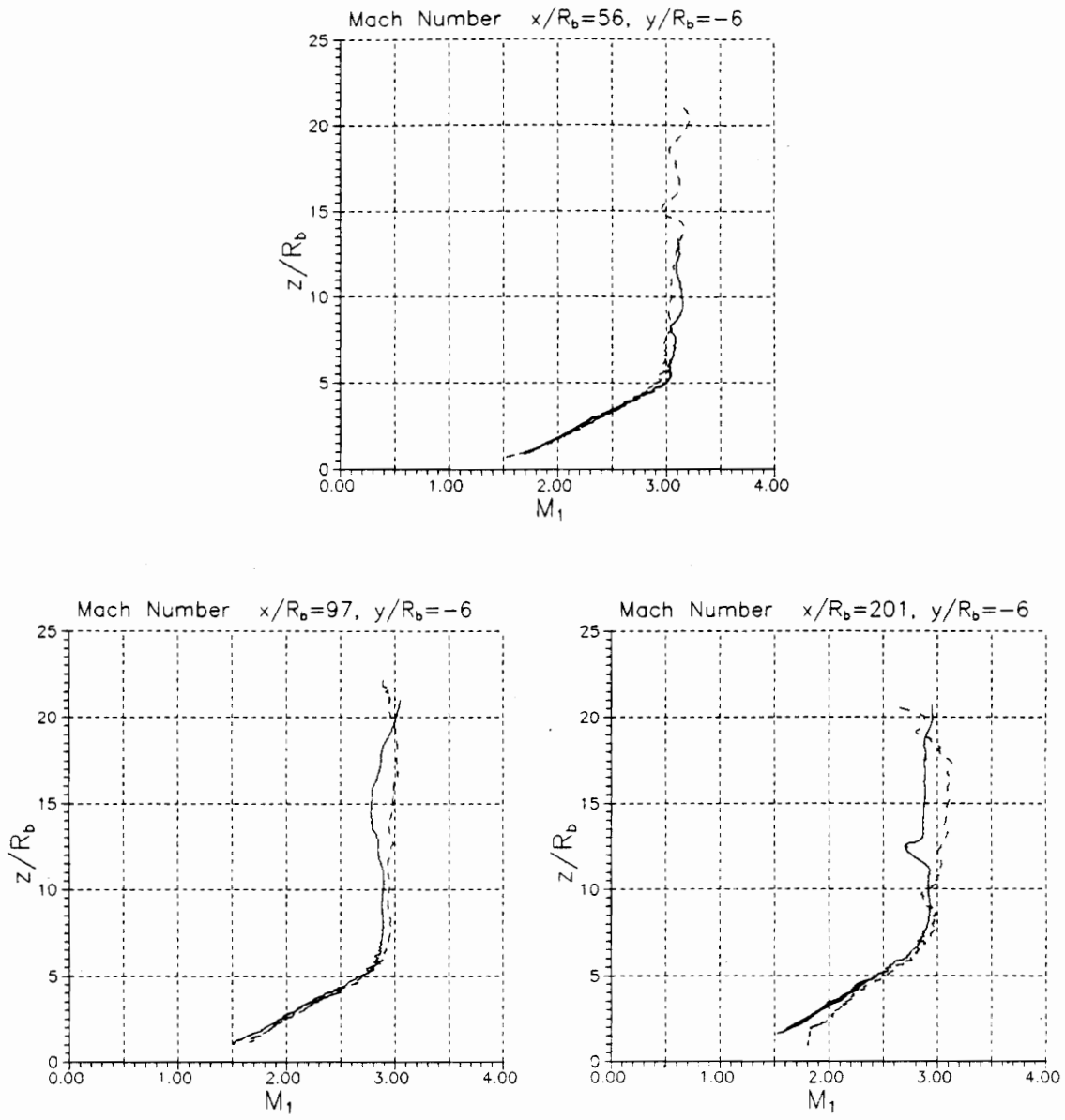

Wedge-shaped Nozzle: Solid Line
Circular Nozzle: Dashed Line

Figure 71. Mach Number Profiles, y/R_b=-6.

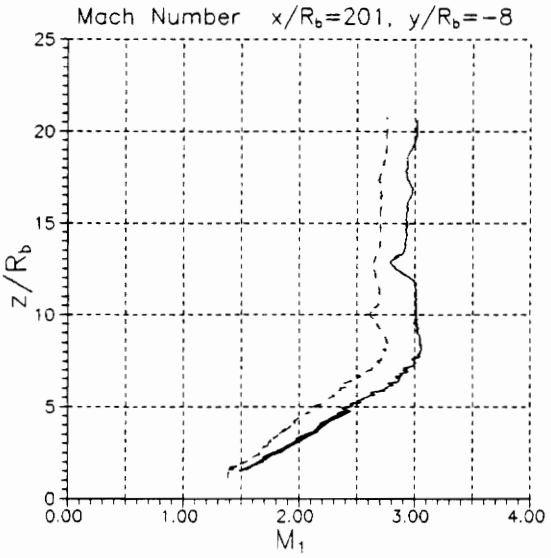

Wedge-shaped Nozzle: Solid Line
Circular Nozzle: Dashed Line

Figure 72. Mach Number Profiles, $y/R_b=-8$.

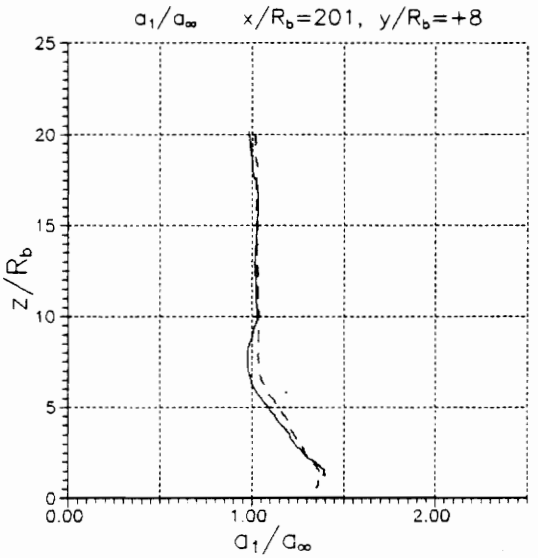

Wedge-shaped Nozzle: Solid Line
Circular Nozzle: Dashed Line

Figure 73. Speed of Sound Profiles, $y/R_b=+8$.

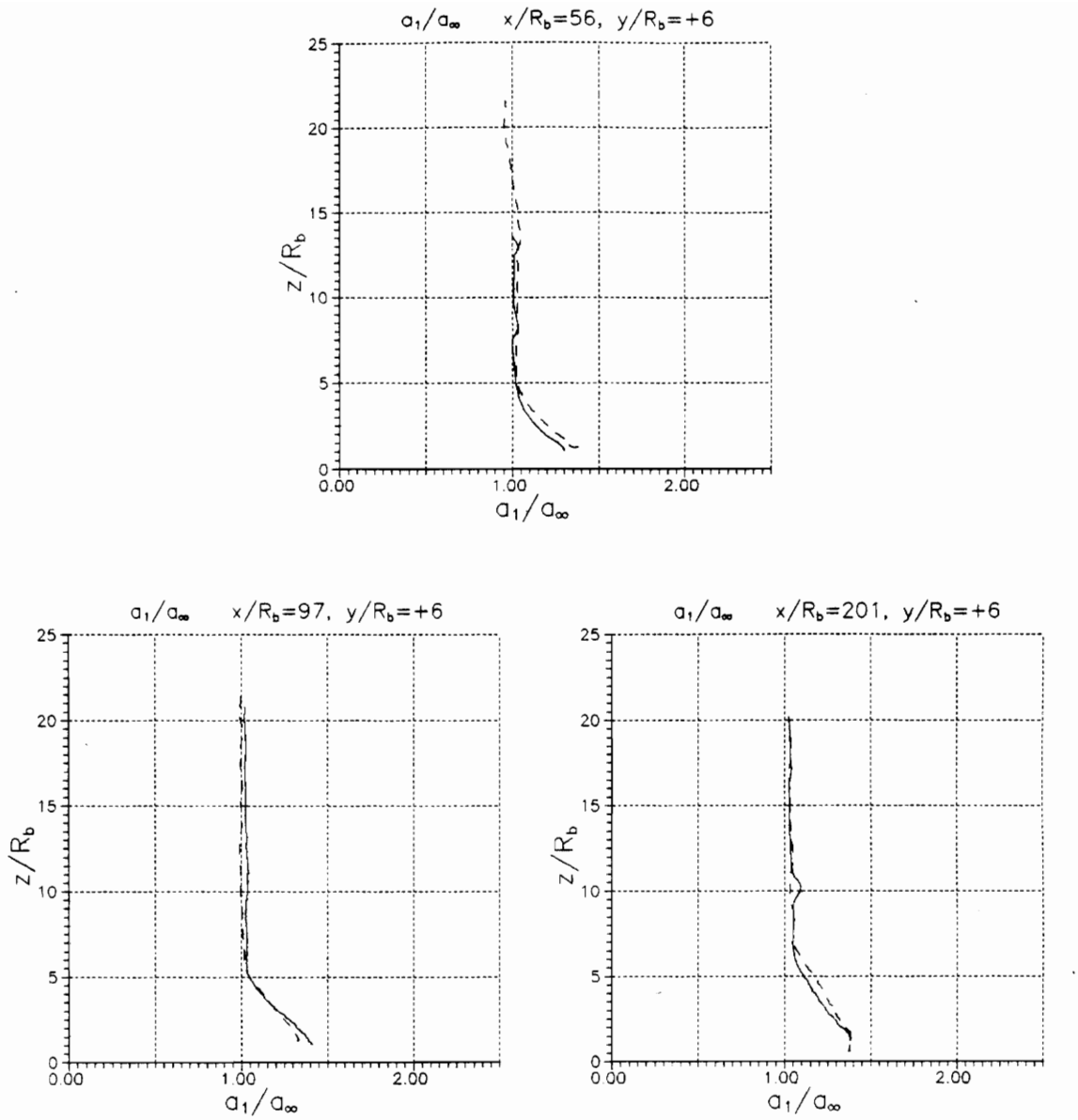

Wedge-shaped Nozzle: Solid Line
Circular Nozzle: Dashed Line

Figure 74. Speed of Sound Profiles, $y/R_b = +6$.

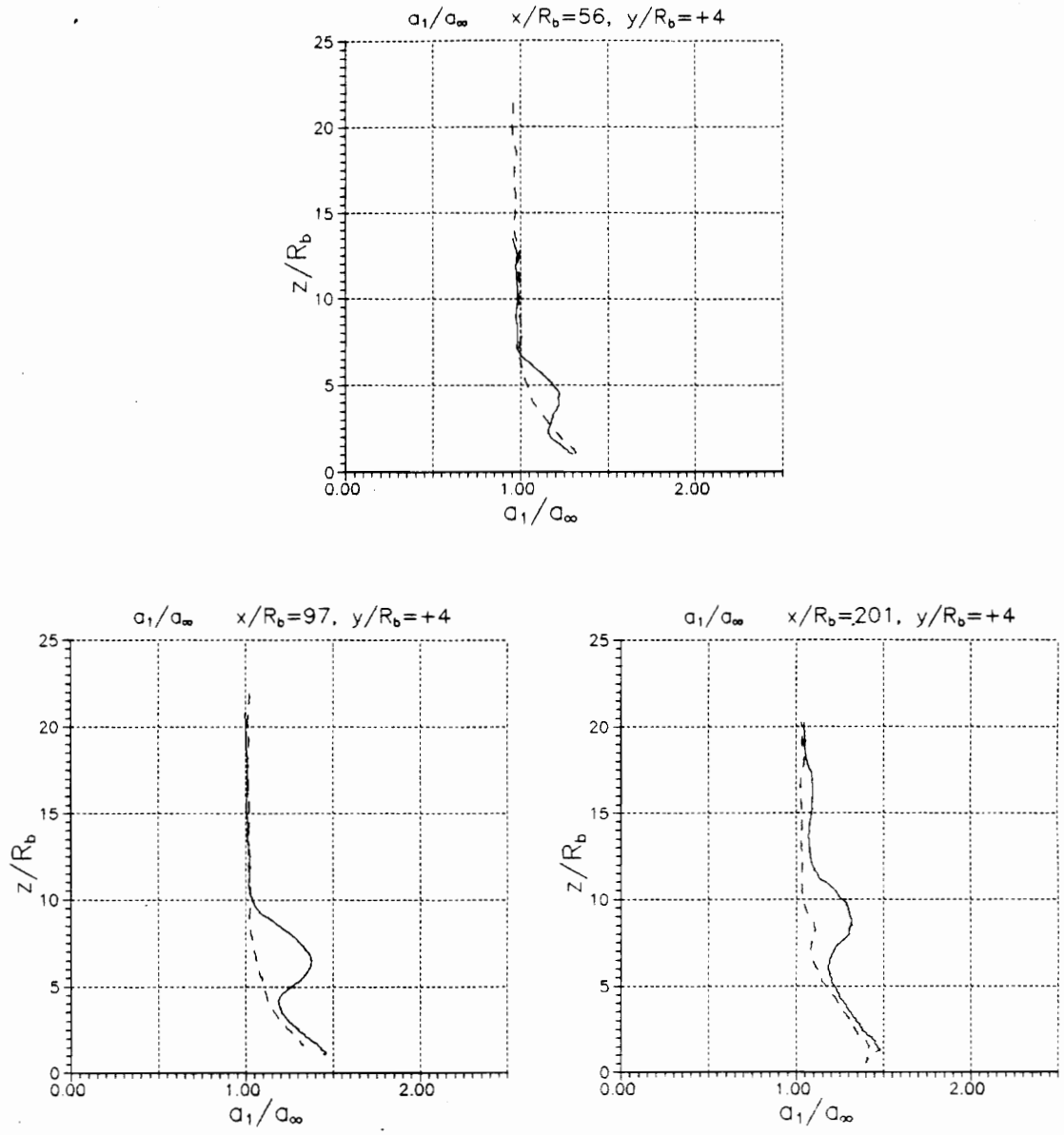

Wedge-shaped Nozzle: Solid Line
Circular Nozzle: Dashed Line

Figure 75. Speed of Sound Profiles, $y/R_b = +4$.

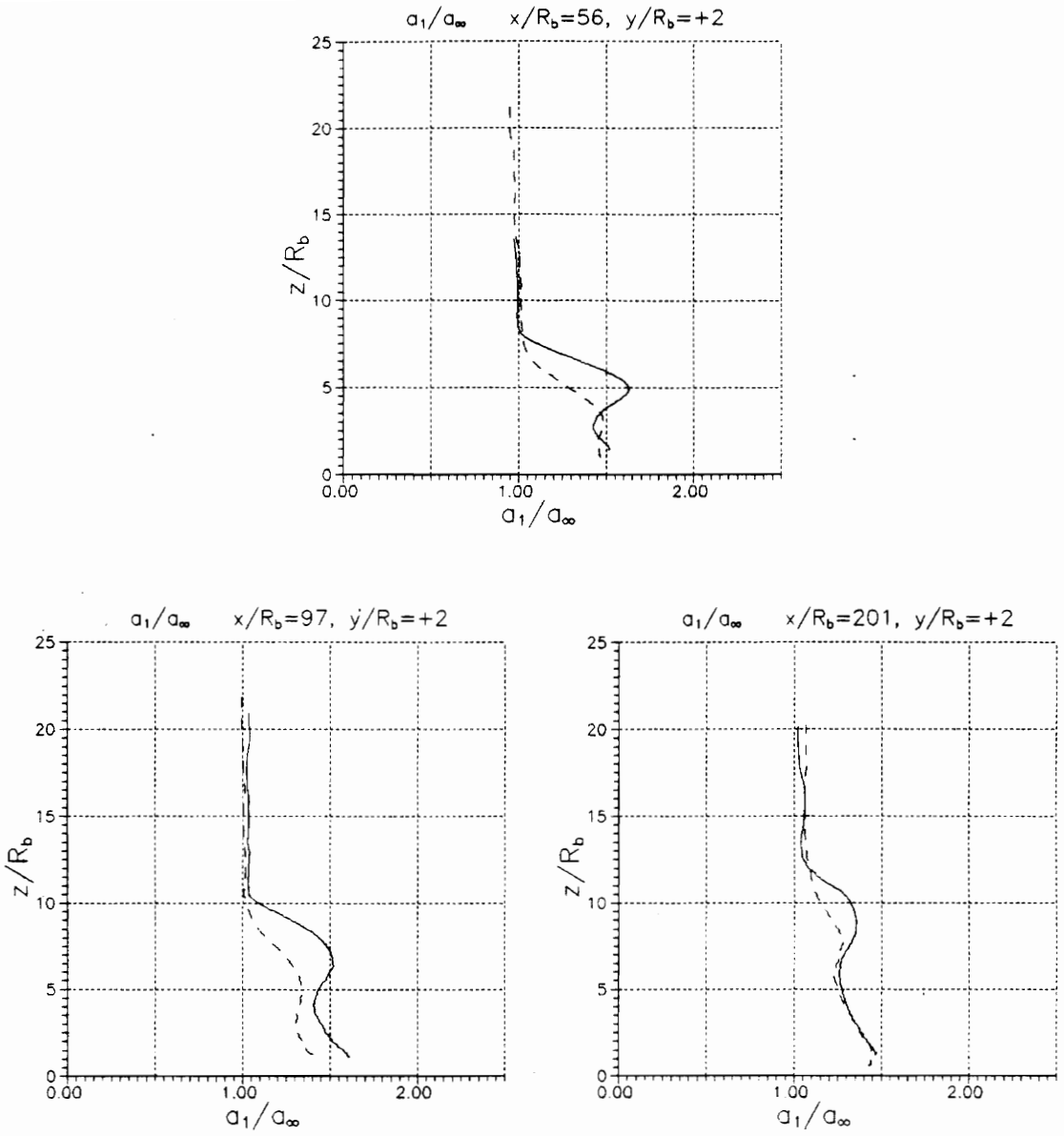

Wedge-shaped Nozzle: Solid Line
Circular Nozzle: Dashed Line

Figure 76. Speed of Sound Profiles, $y/R_b = +2$.

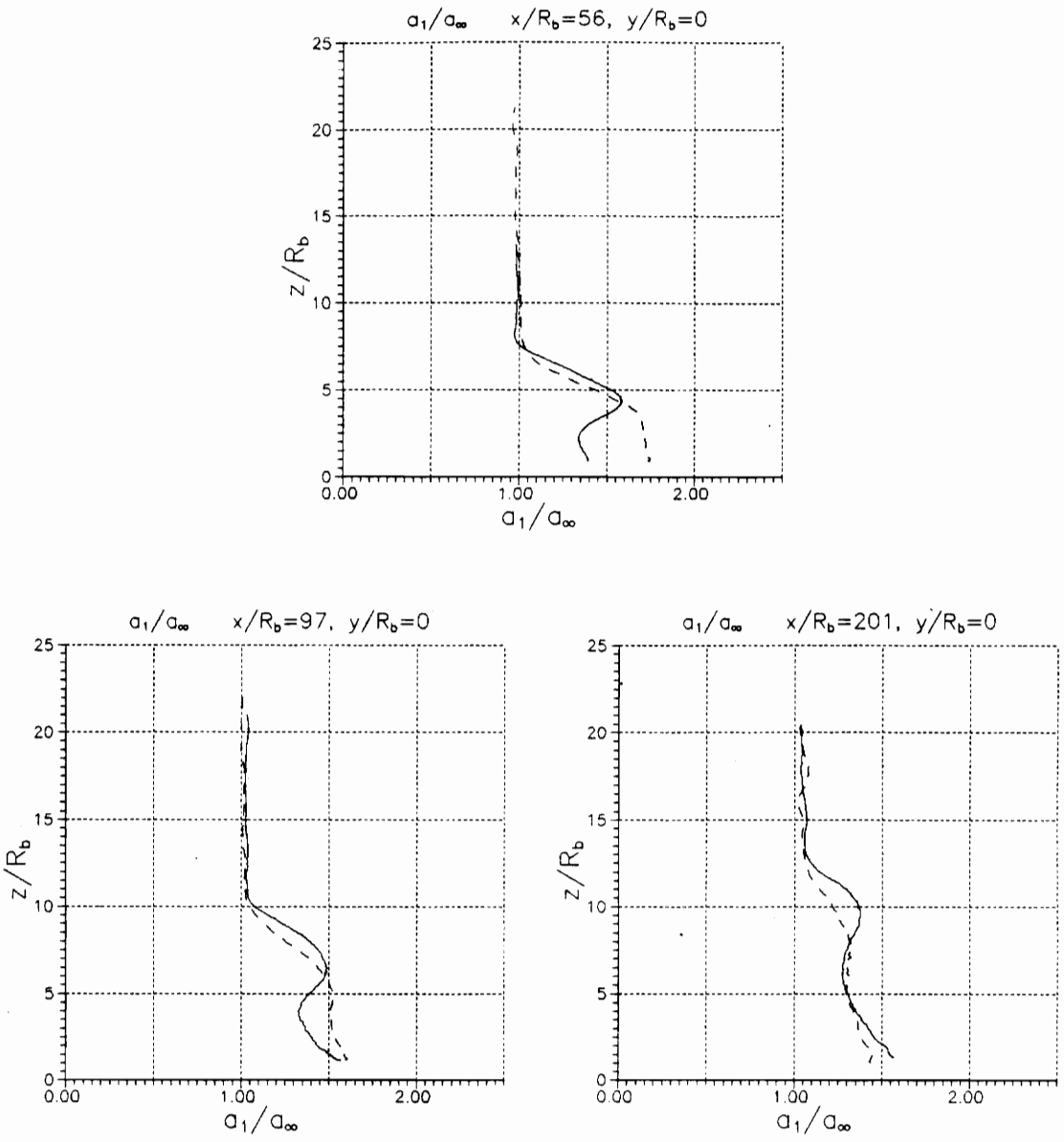

Wedge-shaped Nozzle: Solid Line
Circular Nozzle: Dashed Line

Figure 77. Speed of Sound Profiles, $y/R_b=0$.

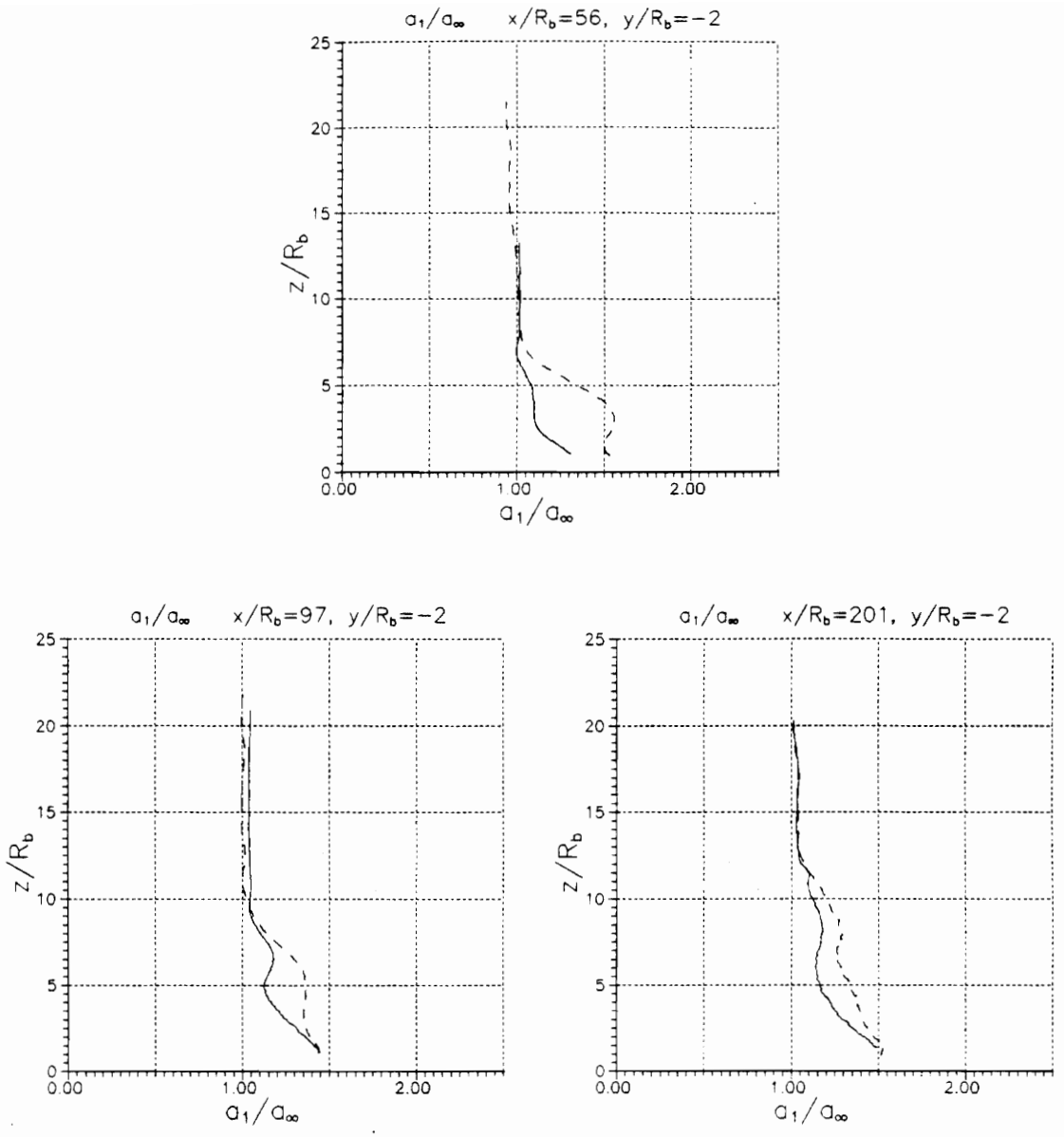

Wedge-shaped Nozzle: Solid Line
Circular Nozzle: Dashed Line

Figure 78. Speed of Sound Profiles, y/R_b=-2.

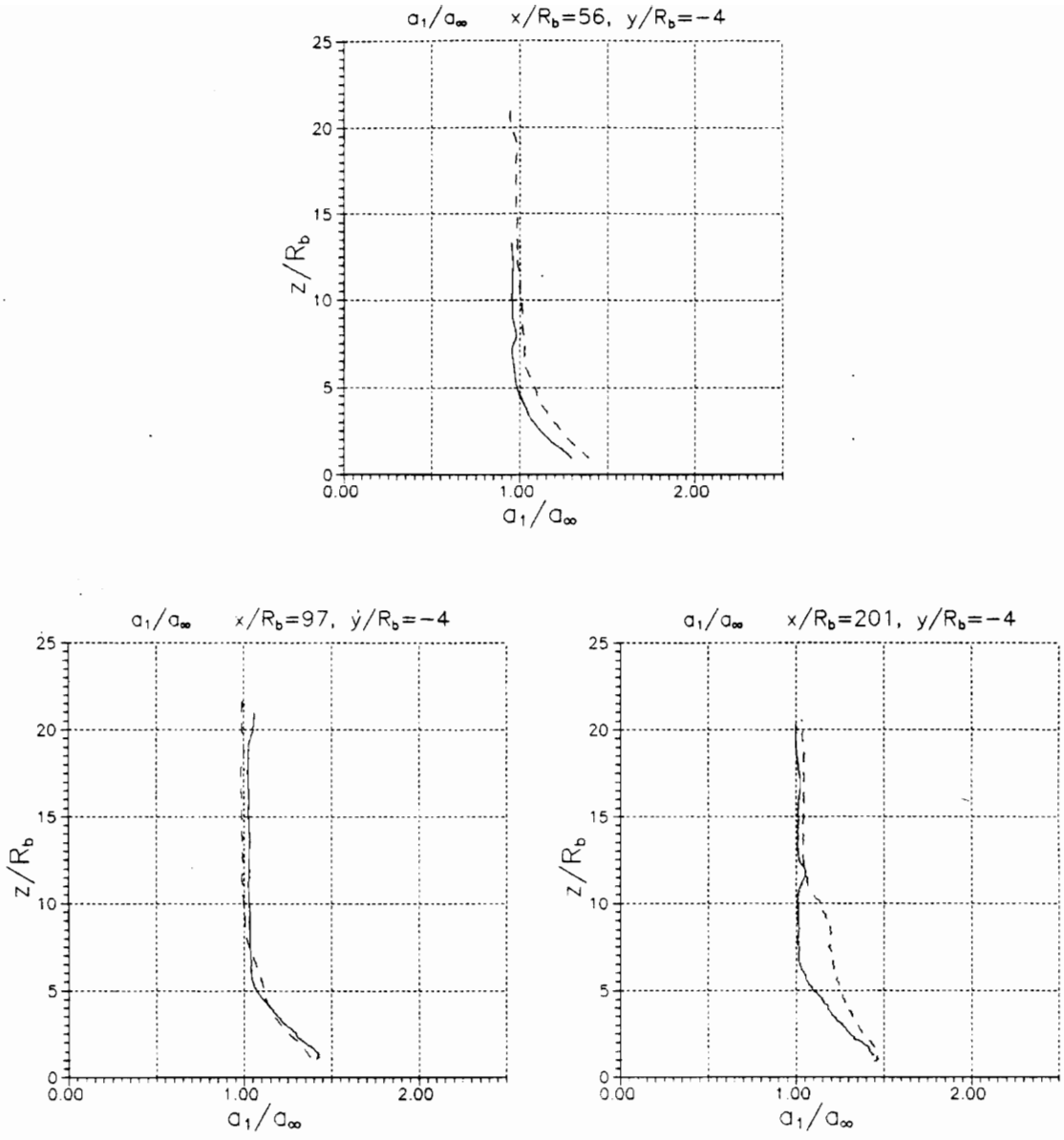

Wedge-shaped Nozzle: Solid Line
Circular Nozzle: Dashed Line

Figure 79. Speed of Sound Profiles, y/R_b=-4.

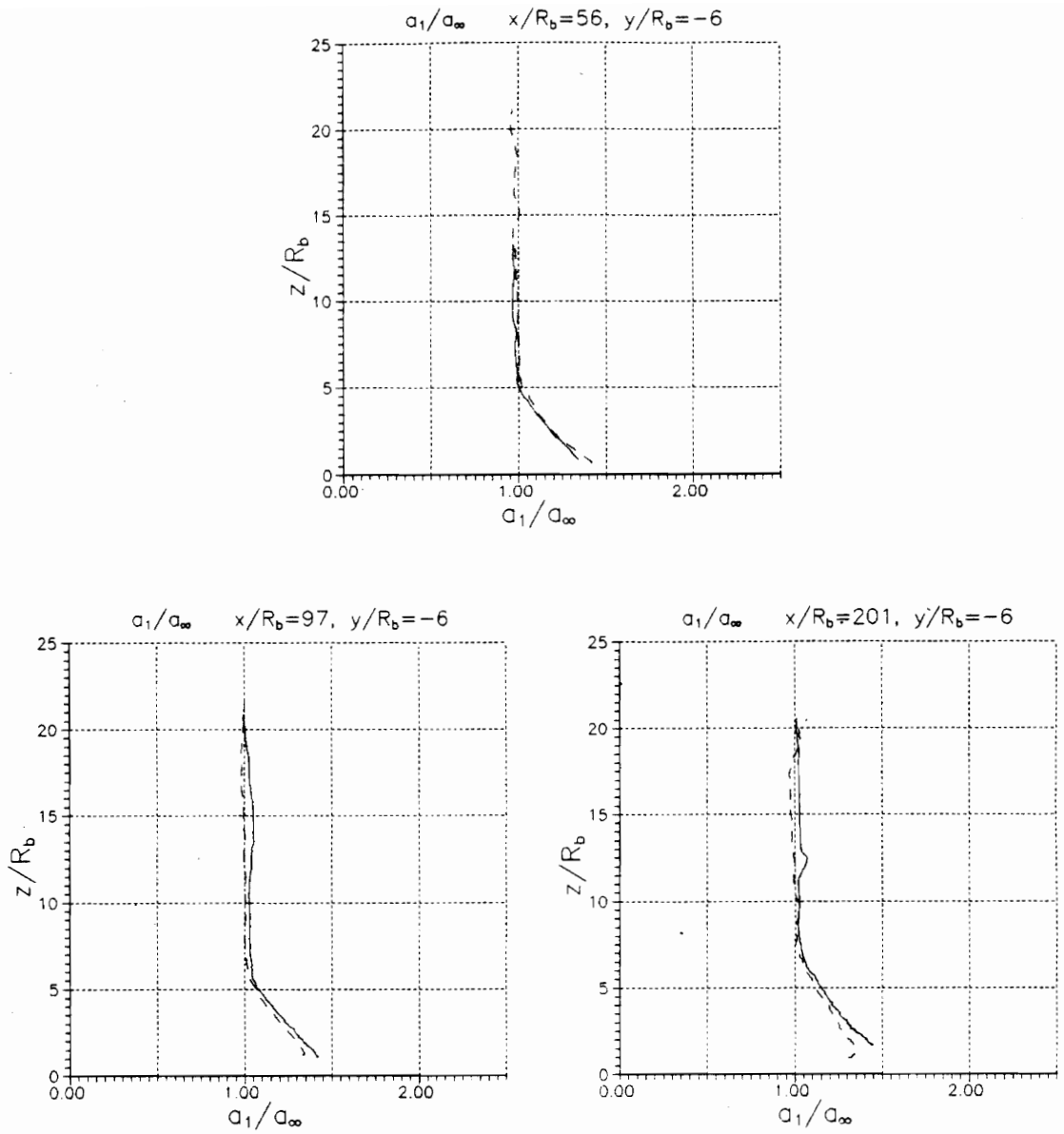

Wedge-shaped Nozzle: Solid Line
Circular Nozzle: Dashed Line

Figure 80. Speed of Sound Profiles, $y/R_b=-6$.

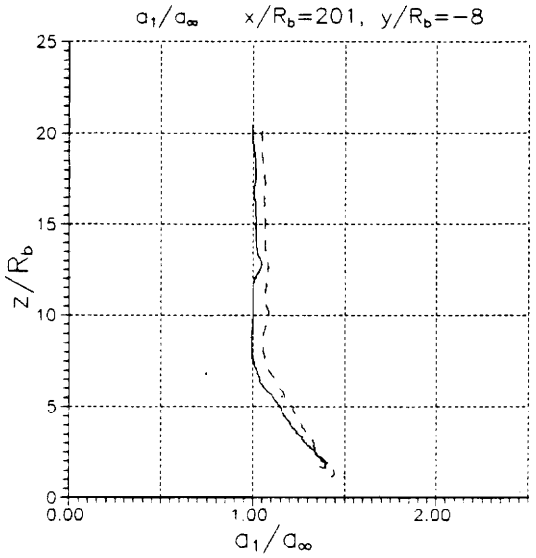

Wedge-shaped Nozzle: Solid Line
Circular Nozzle: Dashed Line

Figure 81. Speed of Sound Profiles, $y/R_b=-8$.

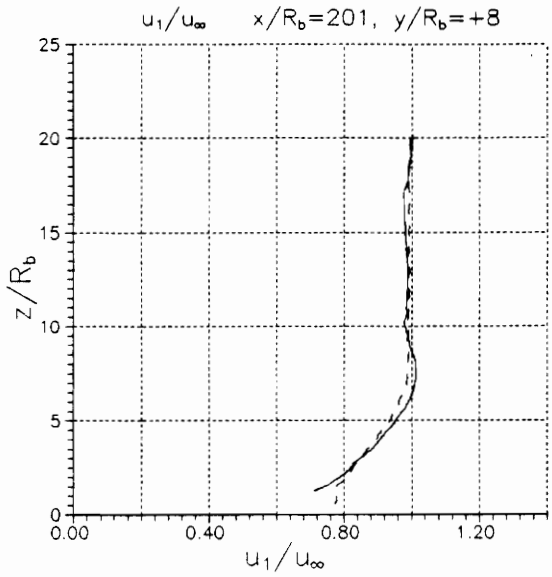

Wedge-shaped Nozzle: Solid Line
Circular Nozzle: Dashed Line

Figure 82. Flow Speed Profiles, $y/R_b = +8$.

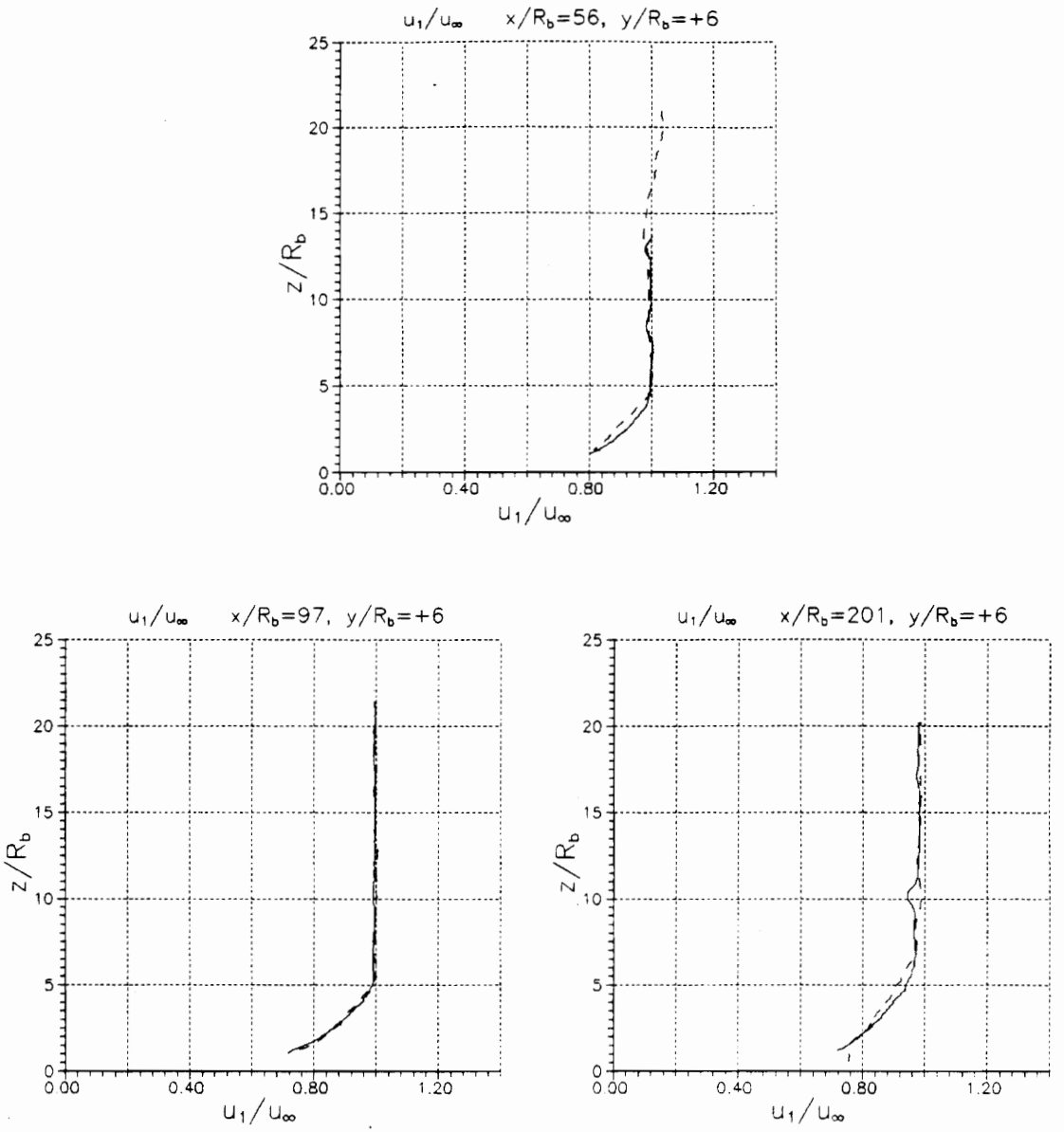

Wedge-shaped Nozzle: Solid Line
Circular Nozzle: Dashed Line

Figure 83. Flow Speed Profiles, $y/R_b = +6$.

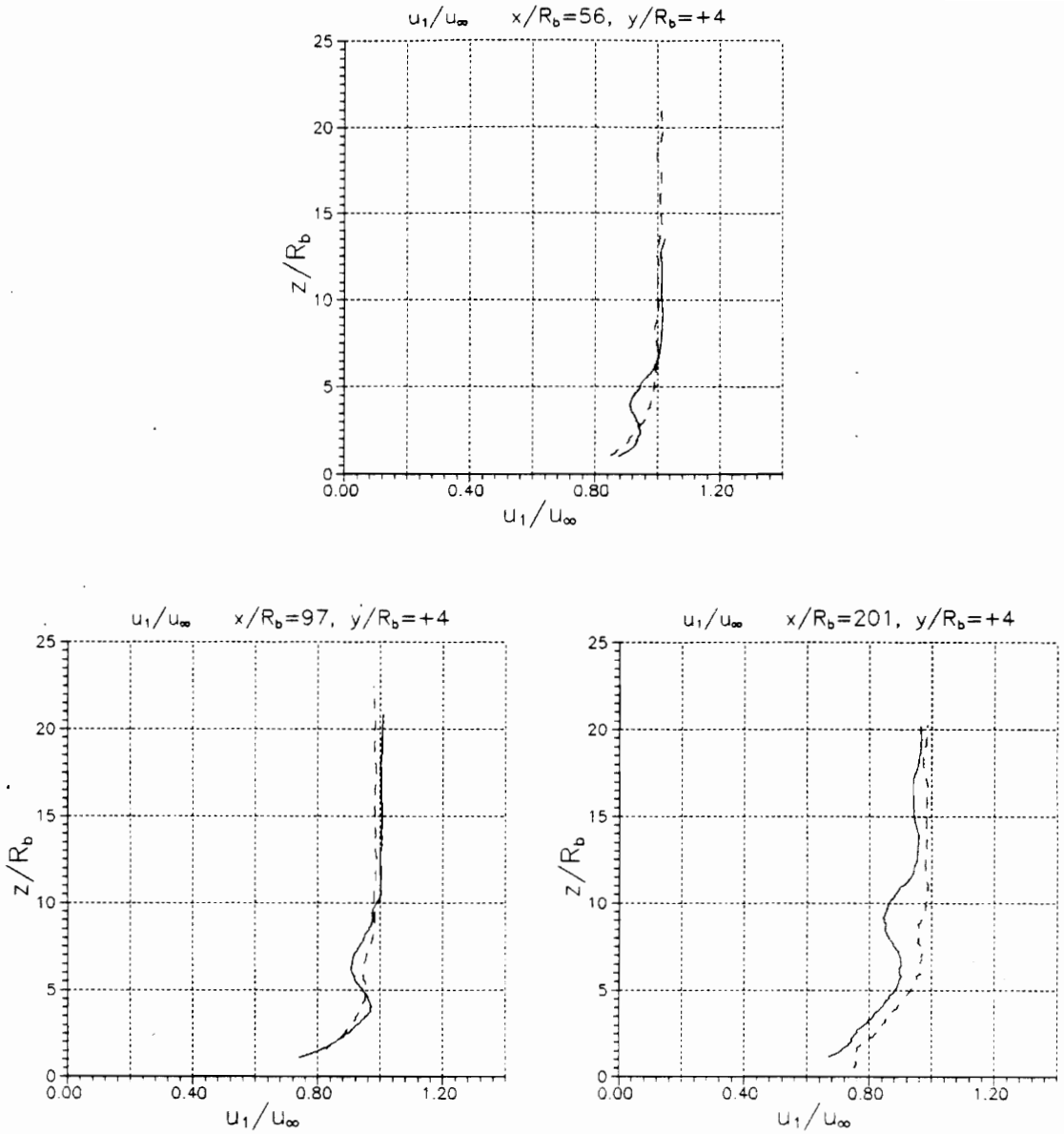

Wedge-shaped Nozzle: Solid Line
Circular Nozzle: Dashed Line

Figure 84. Flow Speed Profiles, $y/R_b = +4$.

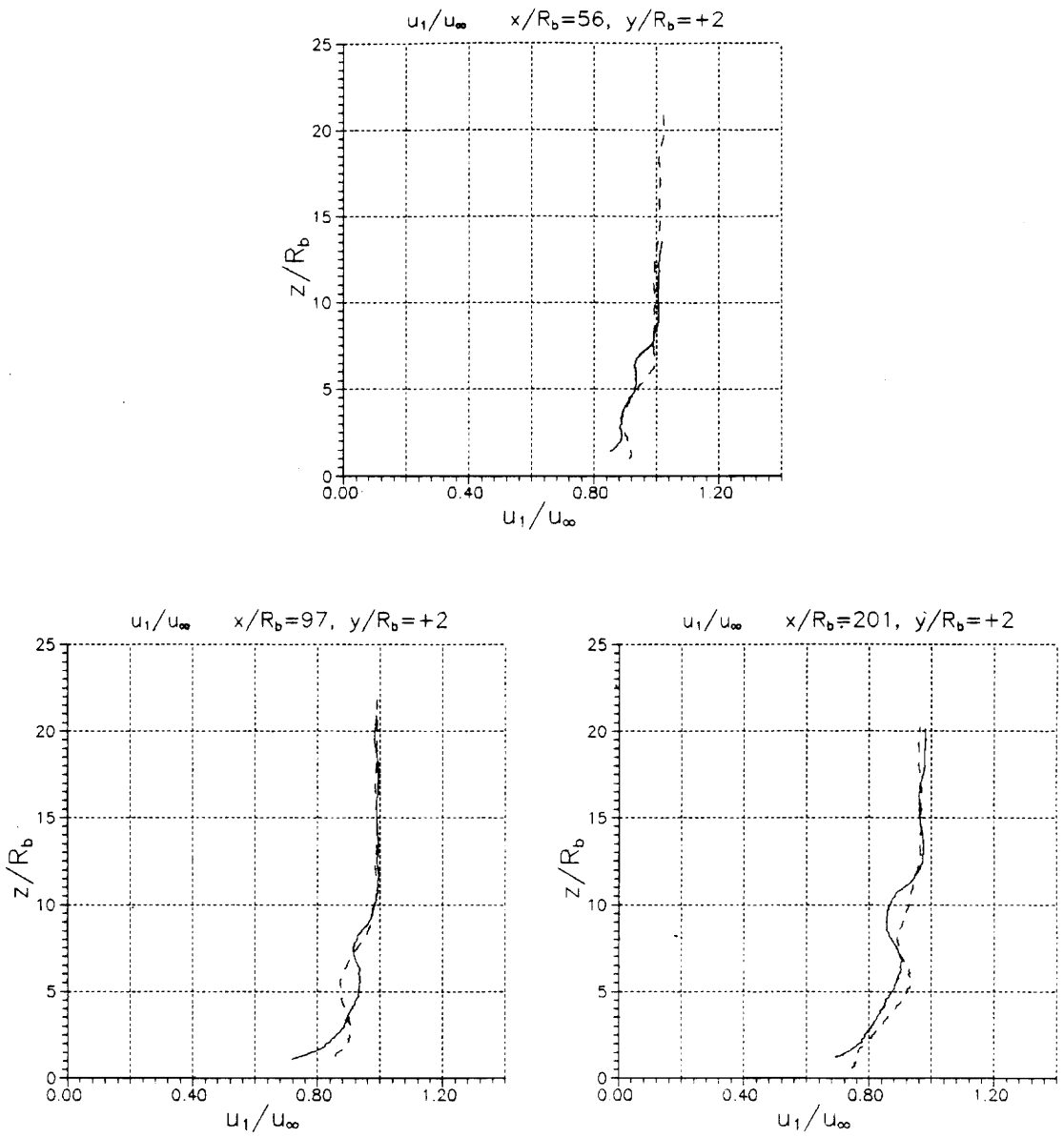

Wedge-shaped Nozzle: Solid Line
Circular Nozzle: Dashed Line

Figure 85. Flow Speed Profiles, $y/R_b = +2$.

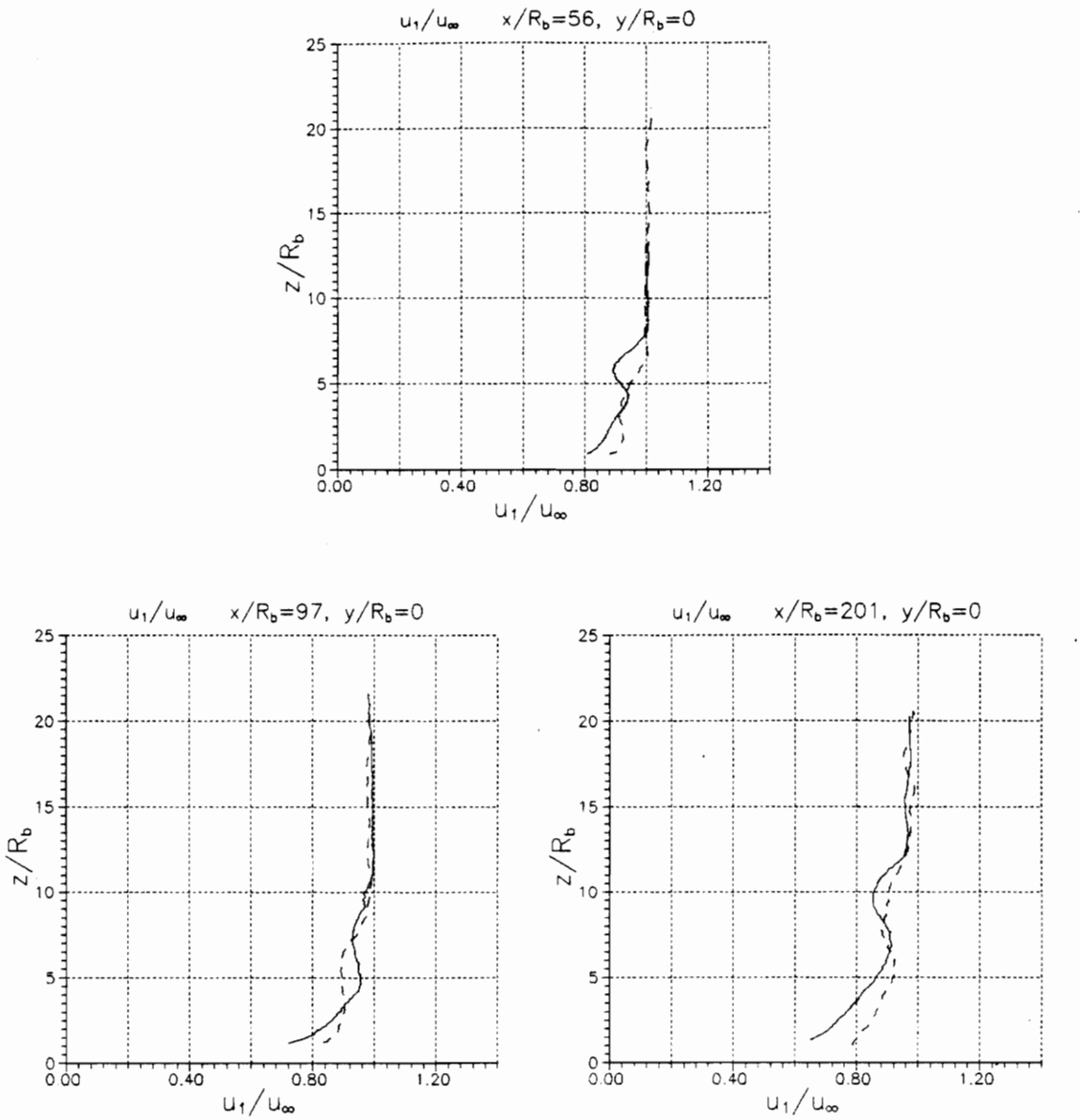

Wedge-shaped Nozzle: Solid Line
Circular Nozzle: Dashed Line

Figure 86. Flow Speed Profiles, $y/R_b=0$.

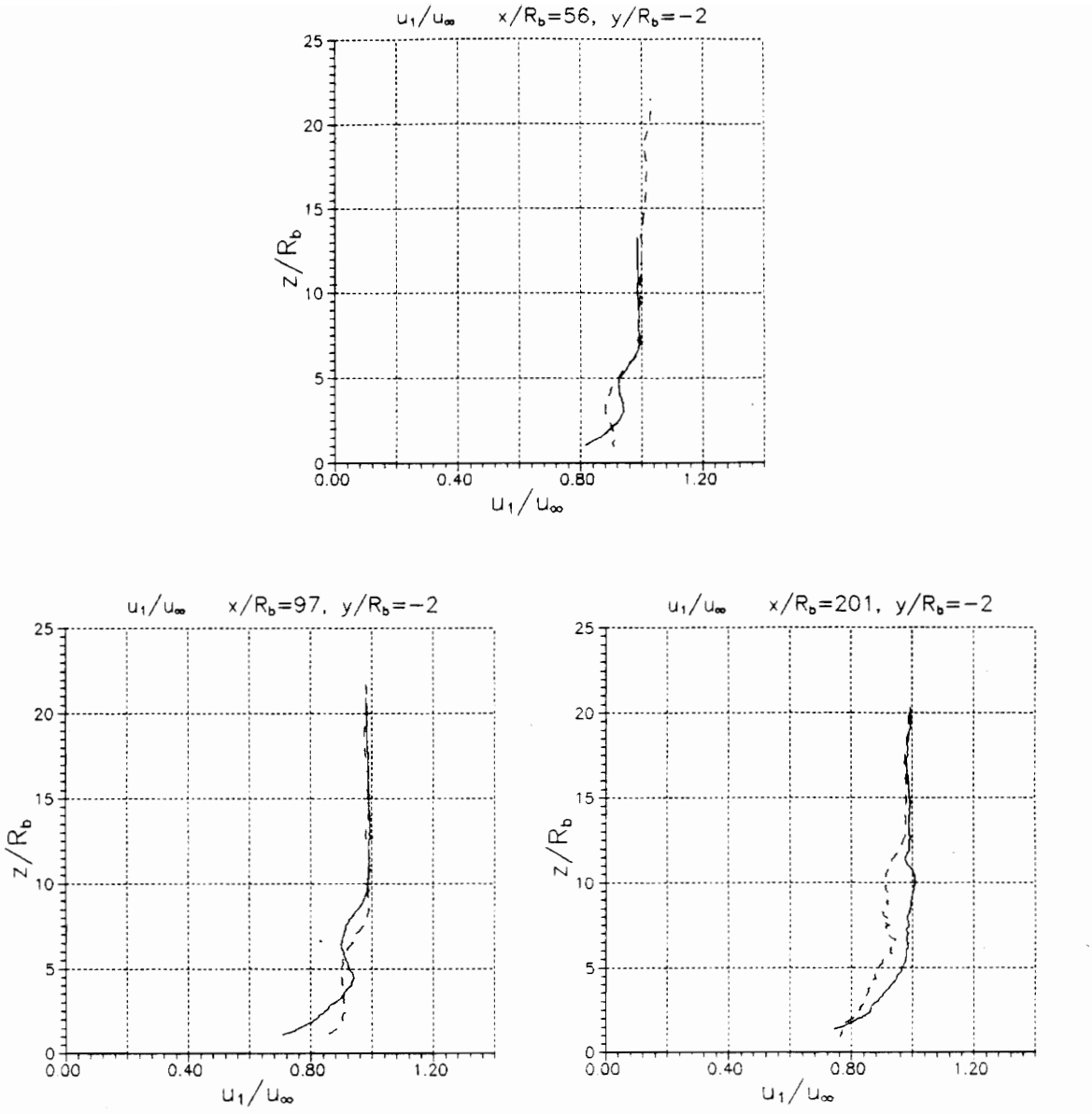

Wedge-shaped Nozzle: Solid Line
Circular Nozzle: Dashed Line

Figure 87. Flow Speed Profiles, $y/R_b=-2$.

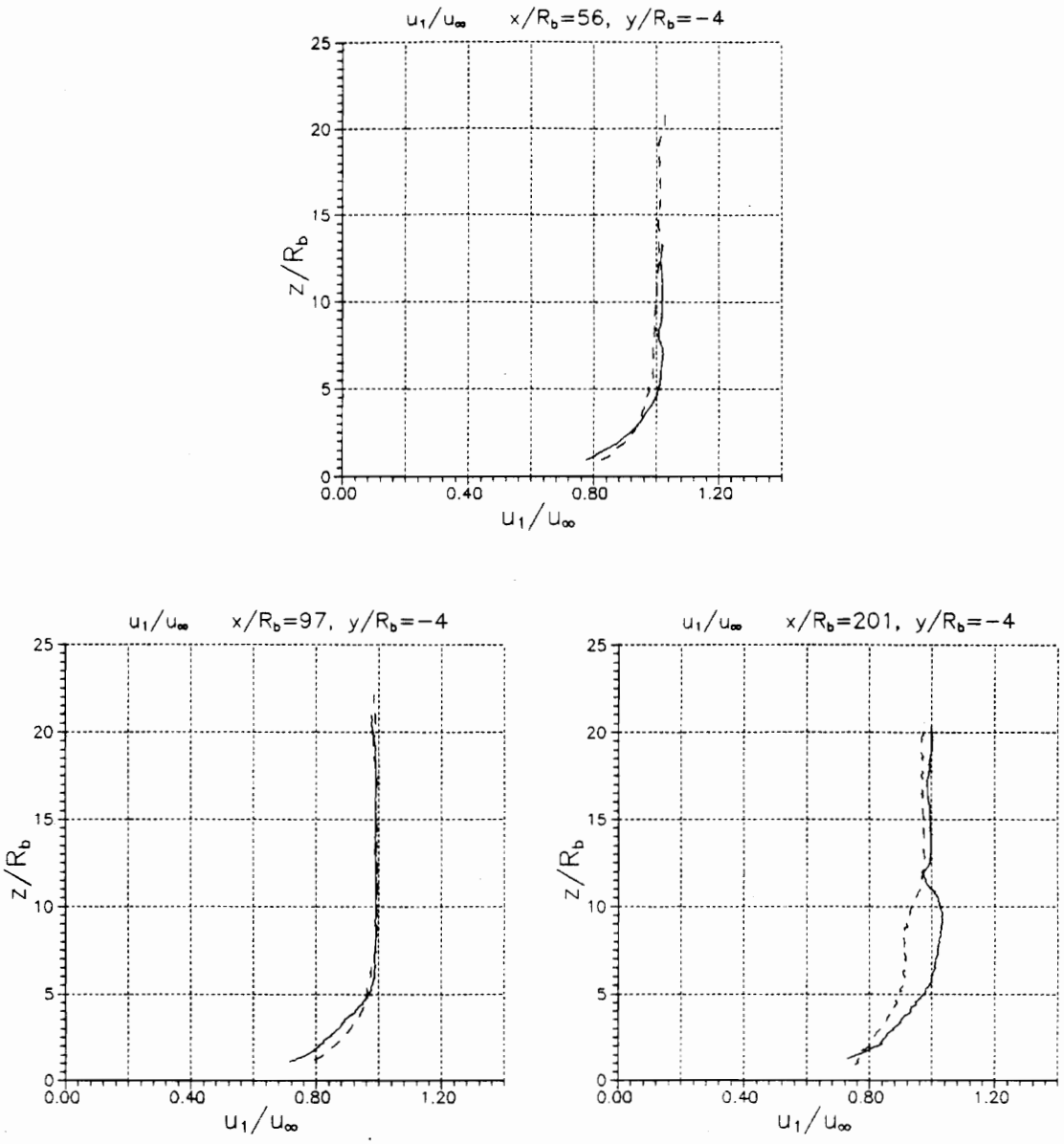

Wedge-shaped Nozzle: Solid Line
Circular Nozzle: Dashed Line

Figure 88. Flow Speed Profiles, $y/R_b=-4$.

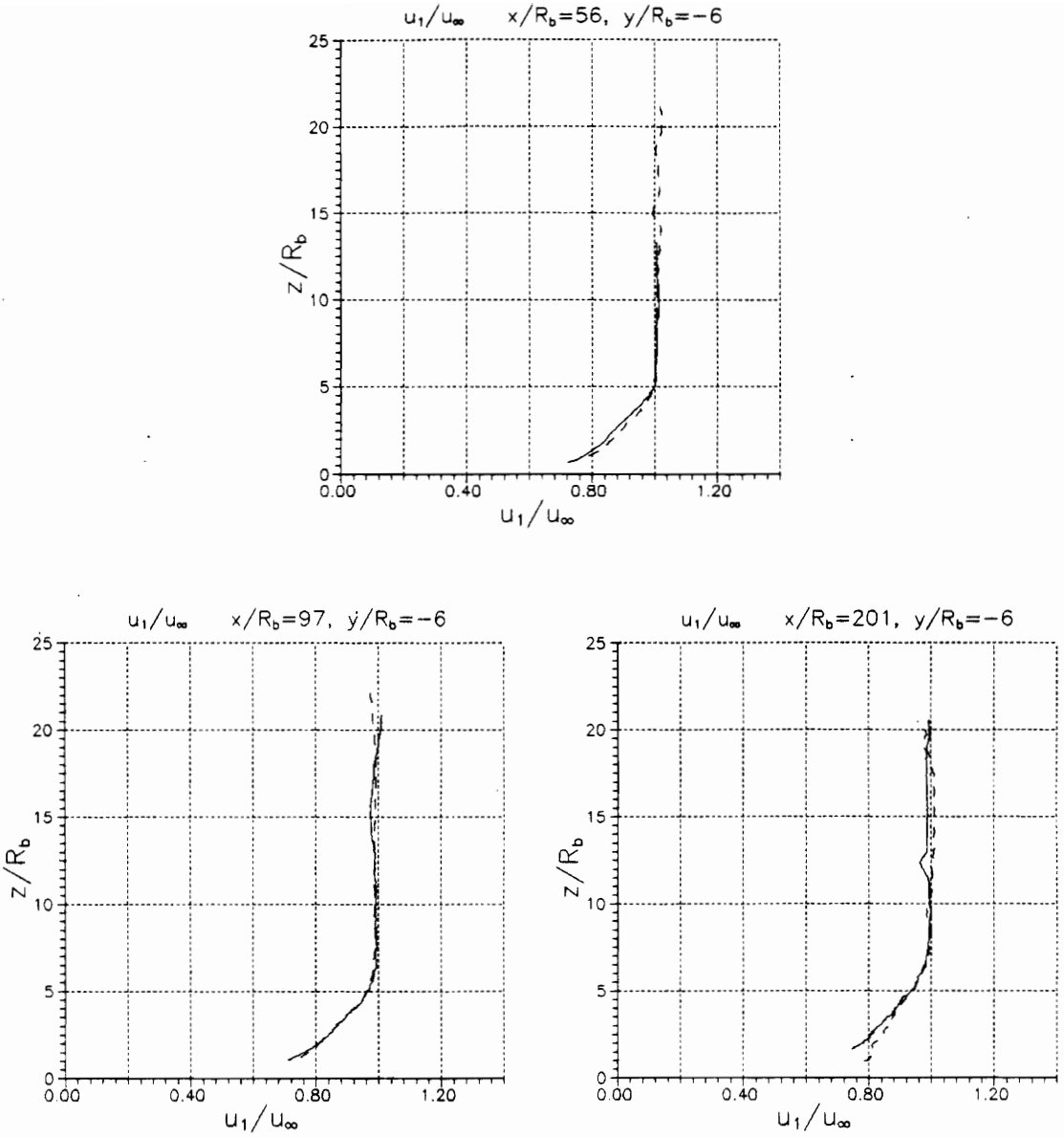

Wedge-shaped Nozzle: Solid Line
Circular Nozzle: Dashed Line

Figure 89. Flow Speed Profiles, $y/R_b=-6$.

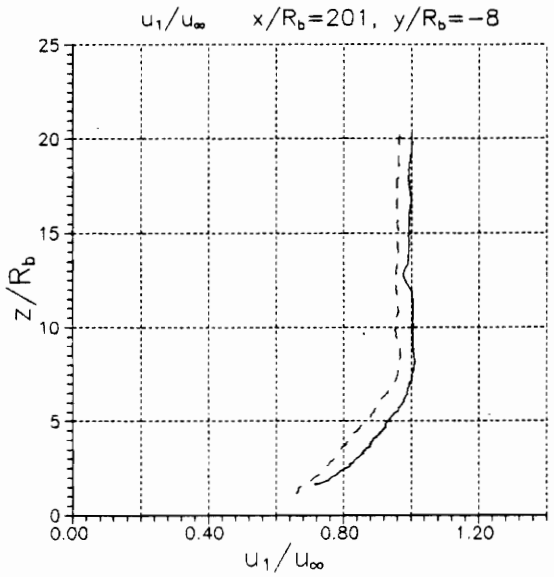

Wedge-shaped Nozzle: Solid Line
Circular Nozzle: Dashed Line

Figure 90. Flow Speed Profiles, $y/R_b=-8$.

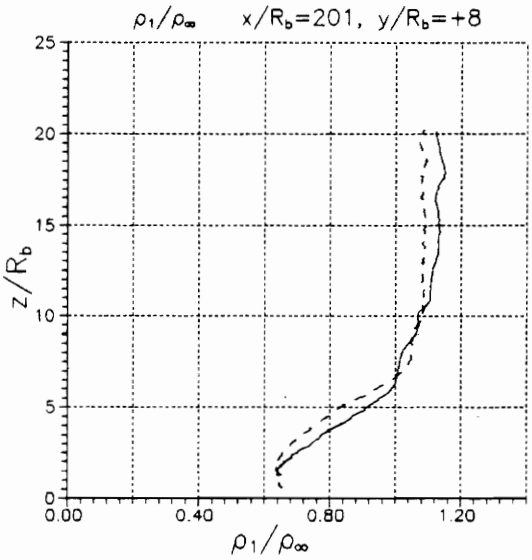

Wedge-shaped Nozzle: Solid Line
Circular Nozzle: Dashed Line

Figure 91. Density Profiles, y/R$_b$ = +8.

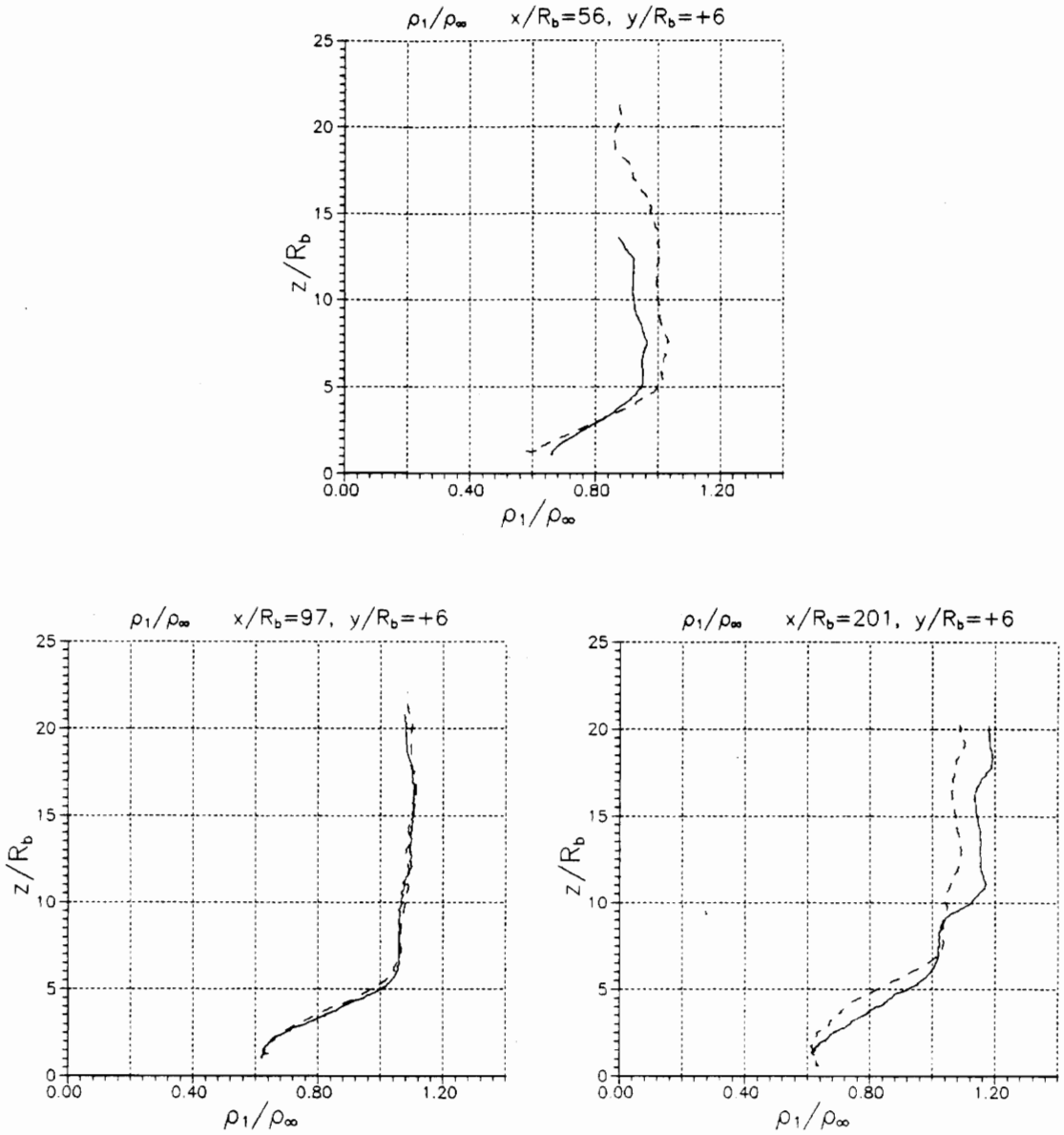

Wedge-shaped Nozzle: Solid Line
Circular Nozzle: Dashed Line

Figure 92. Density Profiles, $y/R_b = +6$.

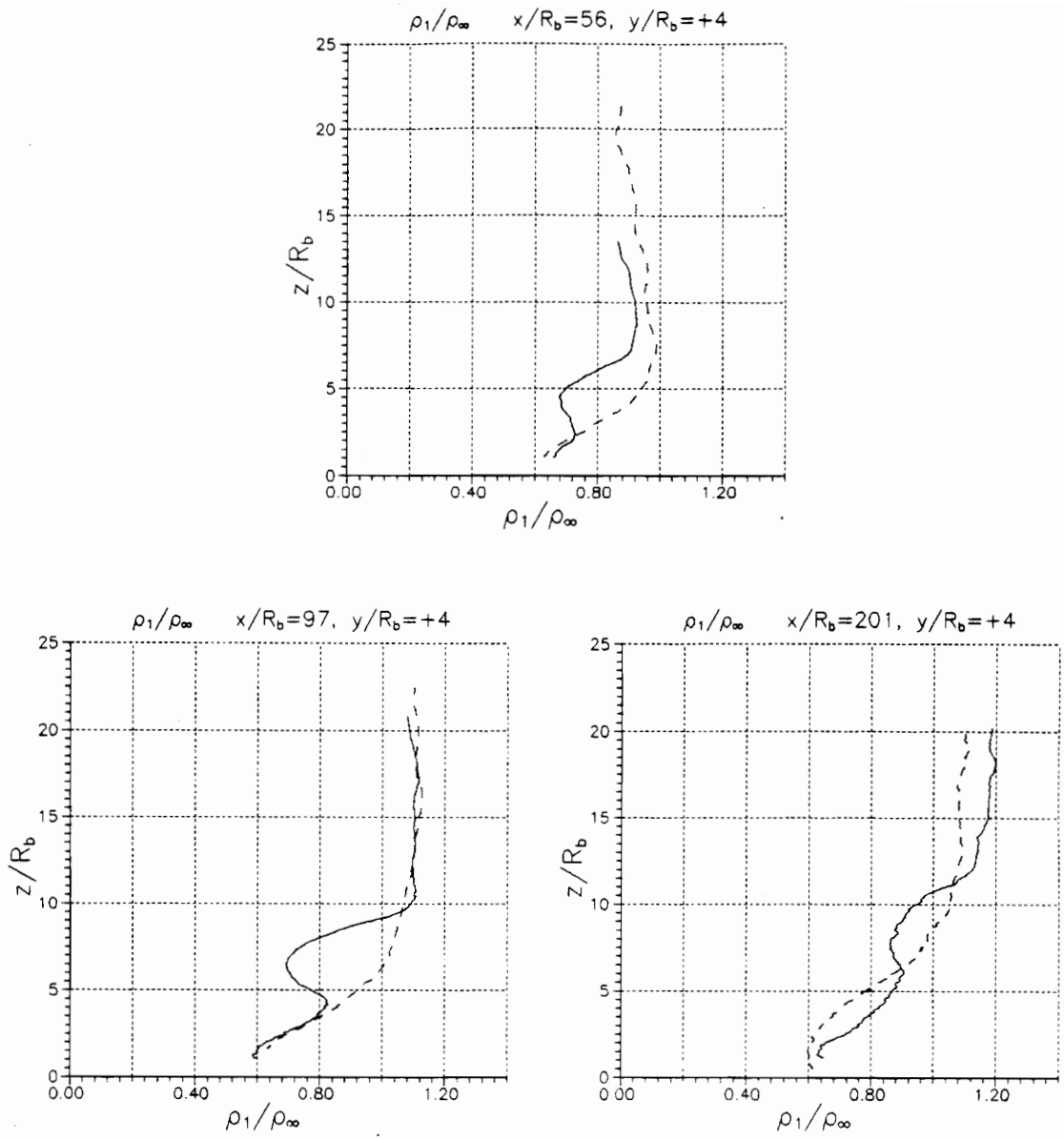

Wedge-shaped Nozzle: Solid Line
Circular Nozzle: Dashed Line

Figure 93. Density Profiles, $y/R_b = +4$.

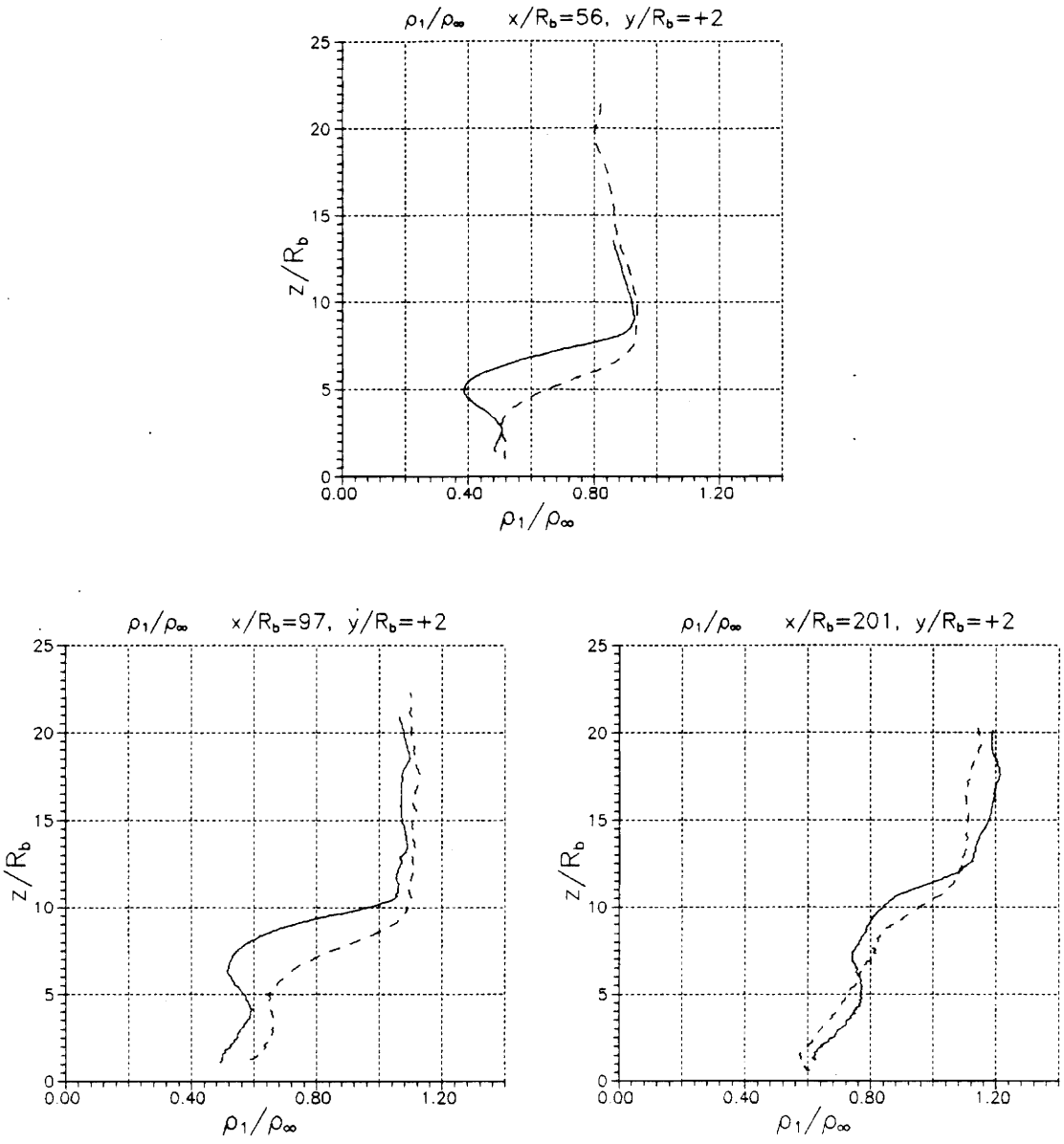

Wedge-shaped Nozzle: Solid Line
Circular Nozzle: Dashed Line

Figure 94. Density Profiles, $y/R_b = +2$.

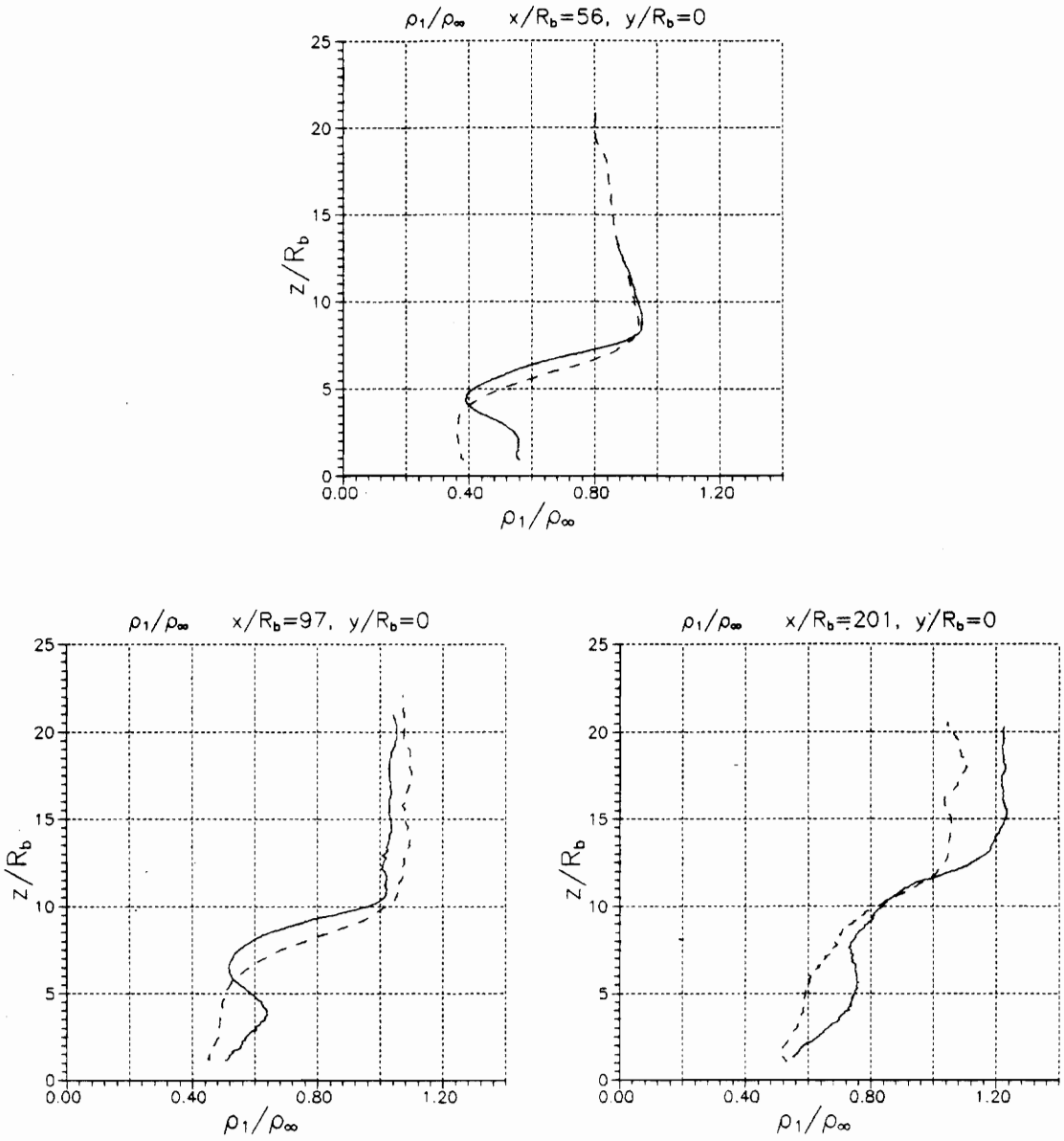

Wedge-shaped Nozzle: Solid Line
Circular Nozzle: Dashed Line

Figure 95. Density Profiles, $y/R_b=0$.

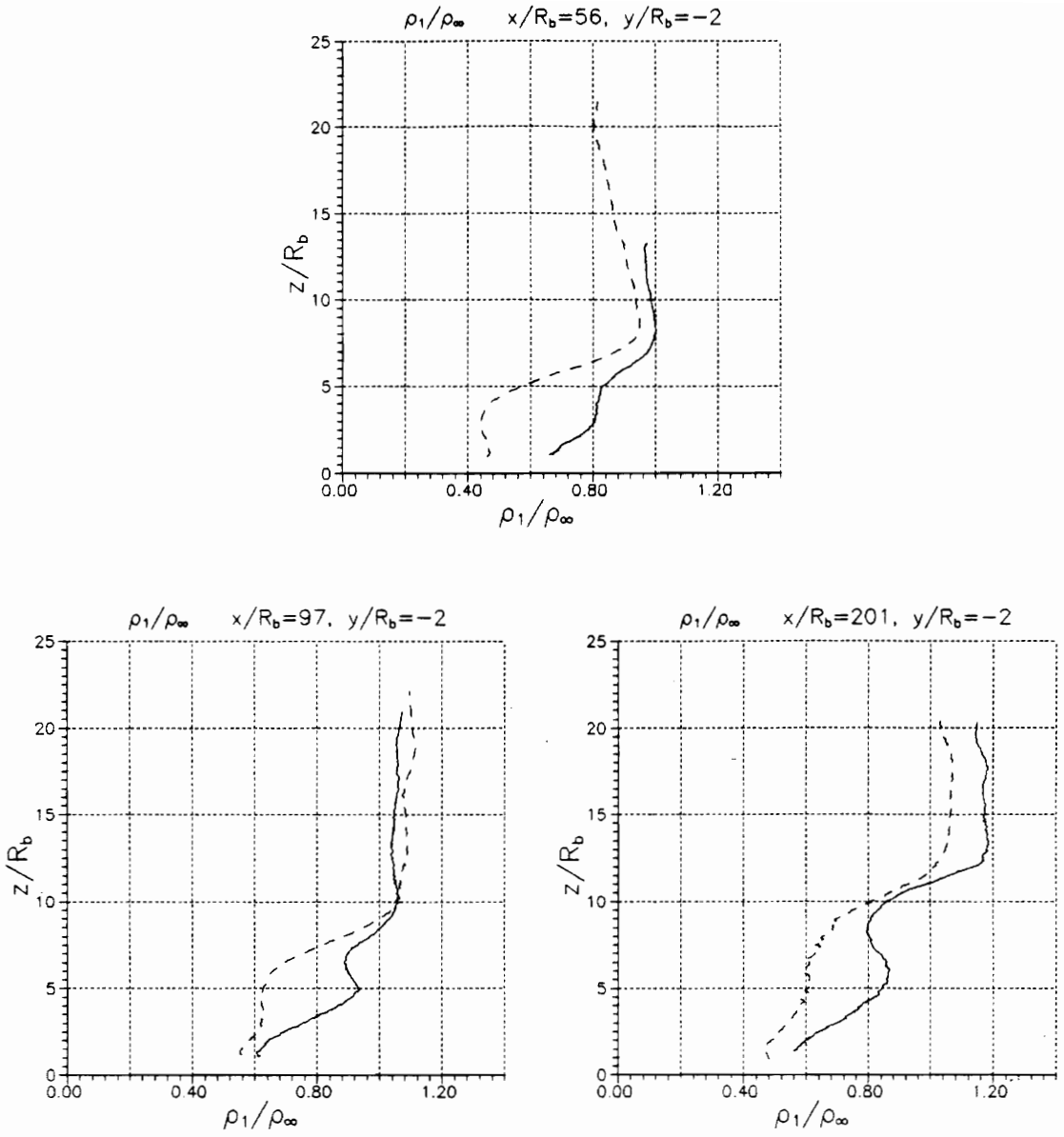

Wedge-shaped Nozzle: Solid Line
Circular Nozzle: Dashed Line

Figure 96. Density Profiles, y/R_b=-2.

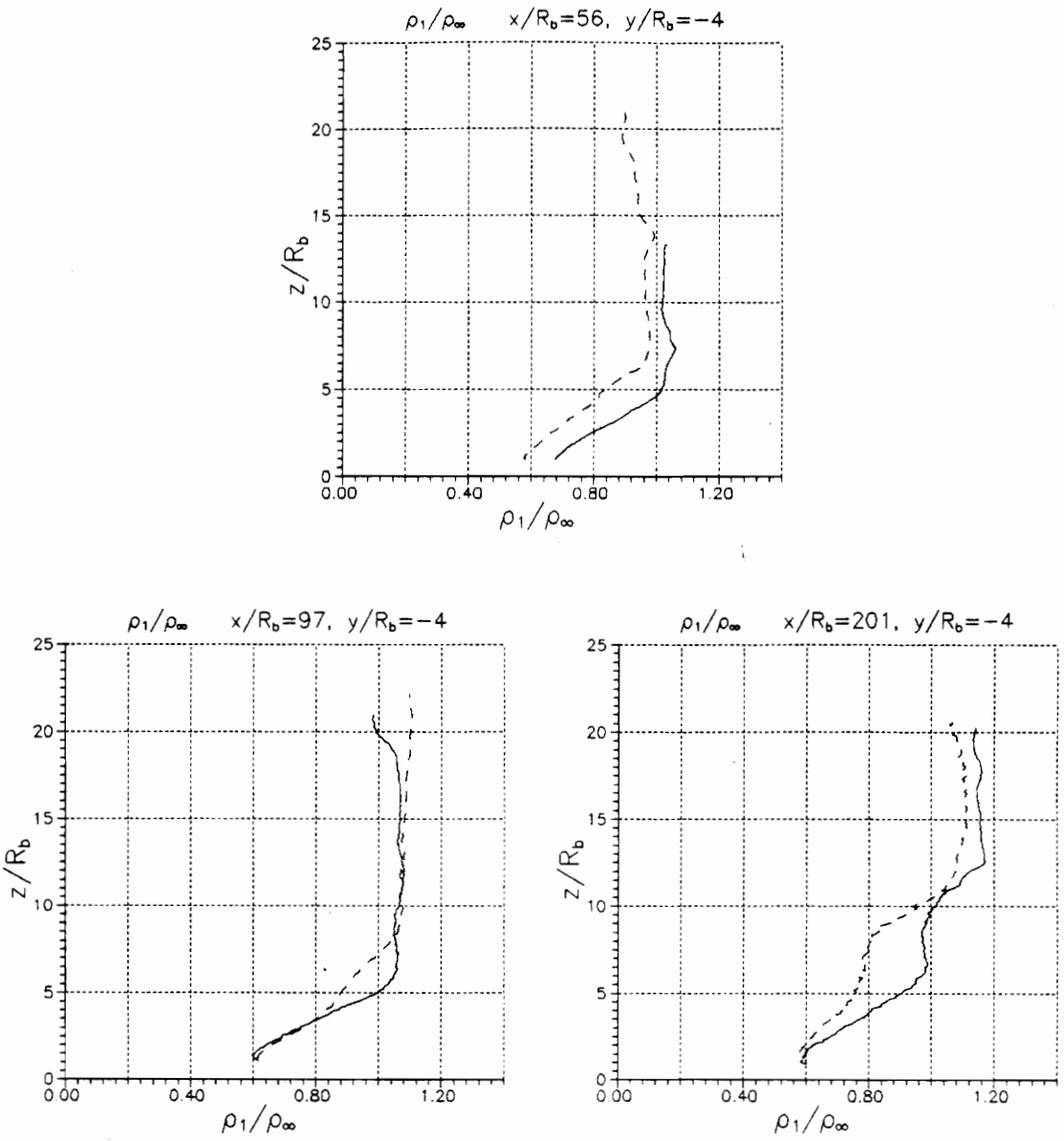

Wedge-shaped Nozzle: Solid Line
Circular Nozzle: Dashed Line

Figure 97. Density Profiles, y/R_b=-4.

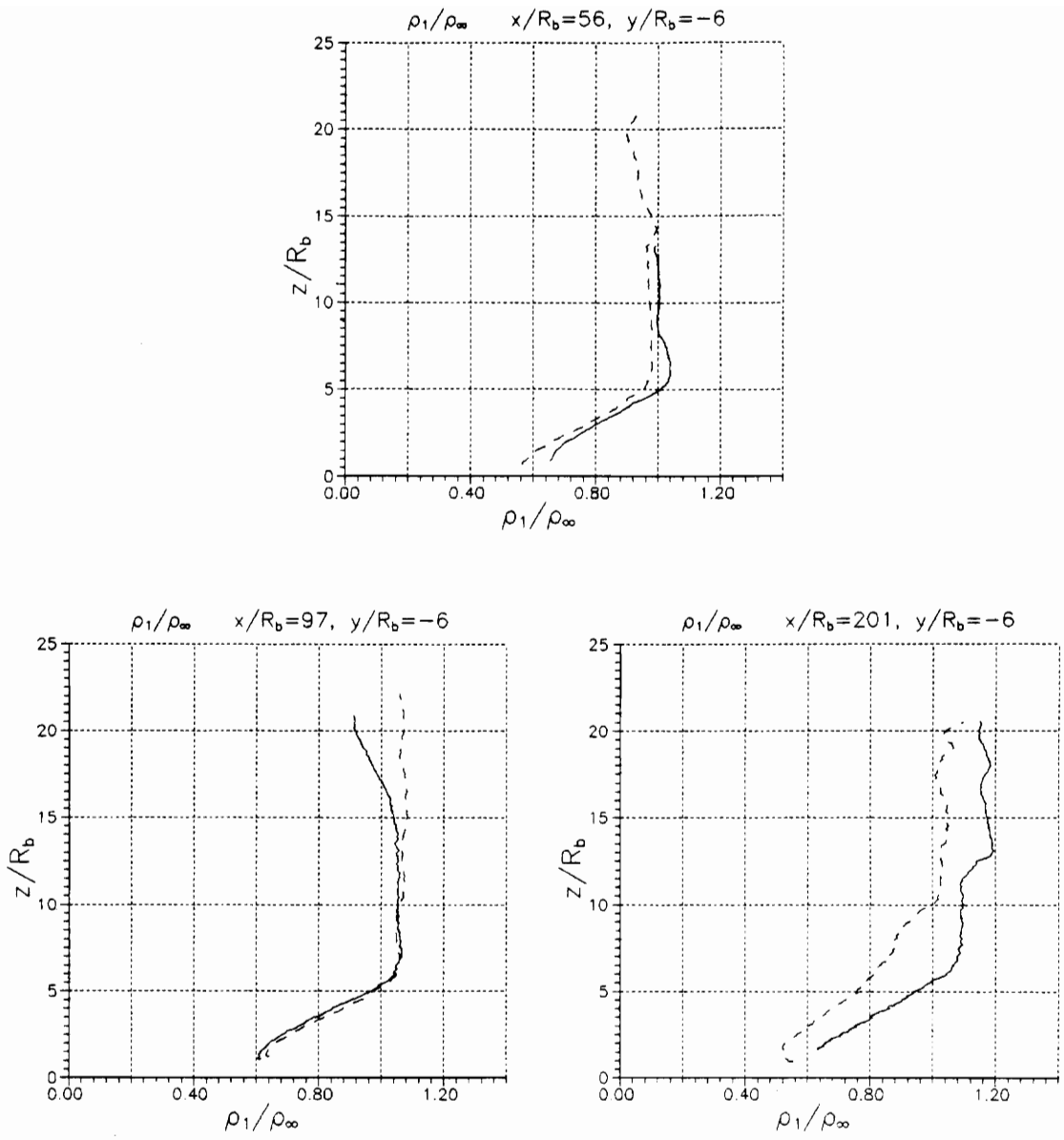

Wedge-shaped Nozzle: Solid Line
Circular Nozzle: Dashed Line

Figure 98. Density Profiles, y/R_b=-6.

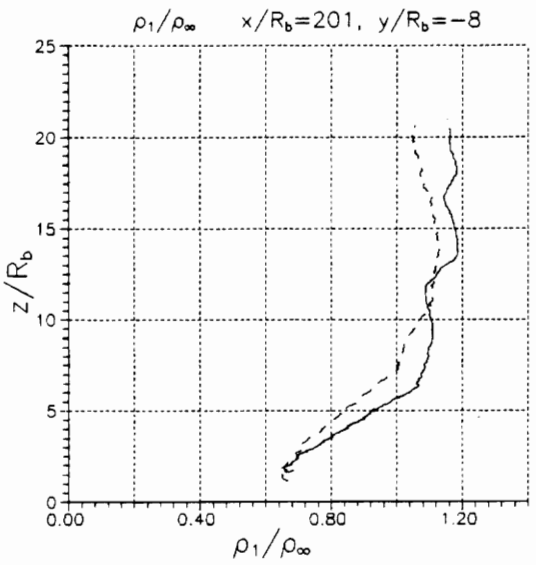

Wedge-shaped Nozzle: Solid Line
Circular Nozzle: Dashed Line

Figure 99. Density Profiles, y/R$_b$=-8.

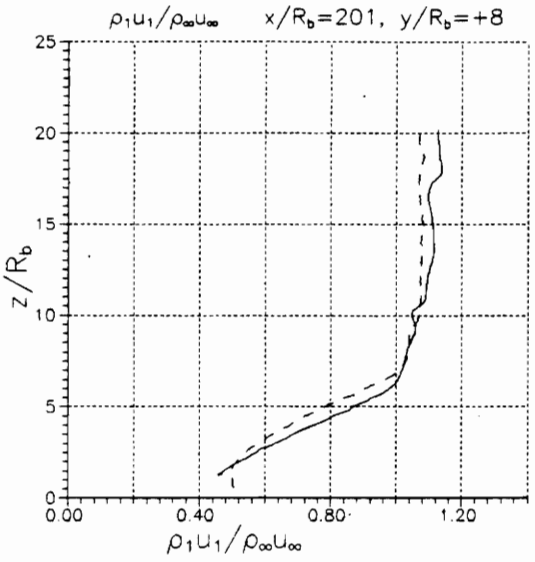

Wedge-shaped Nozzle: Solid Line
Circular Nozzle: Dashed Line

Figure 100. Mass Flux Profiles, $y/R_b = +8$.

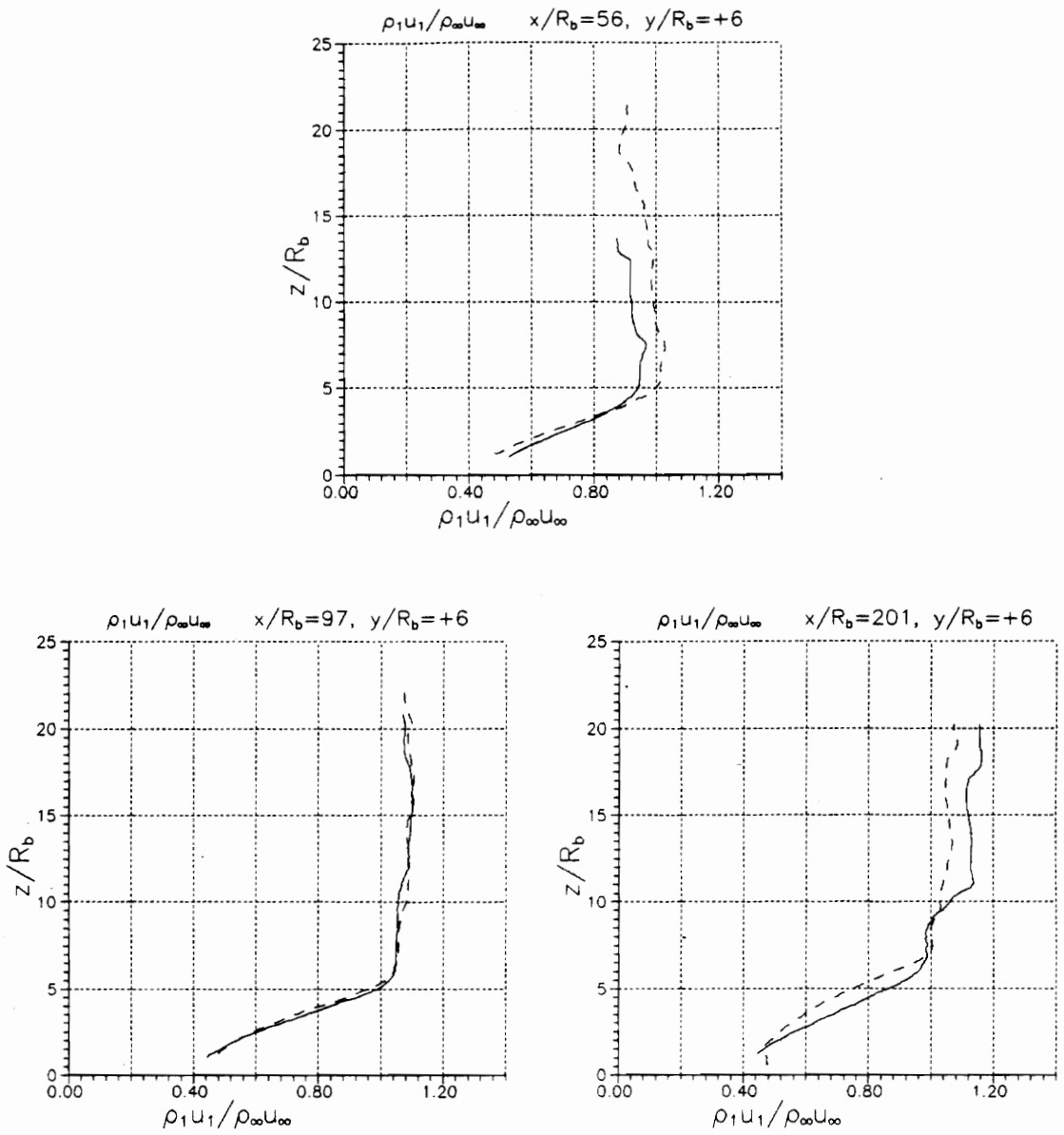

Wedge-shaped Nozzle: Solid Line
Circular Nozzle: Dashed Line

Figure 101. Mass Flux Profiles, y/R$_b$ = +6.

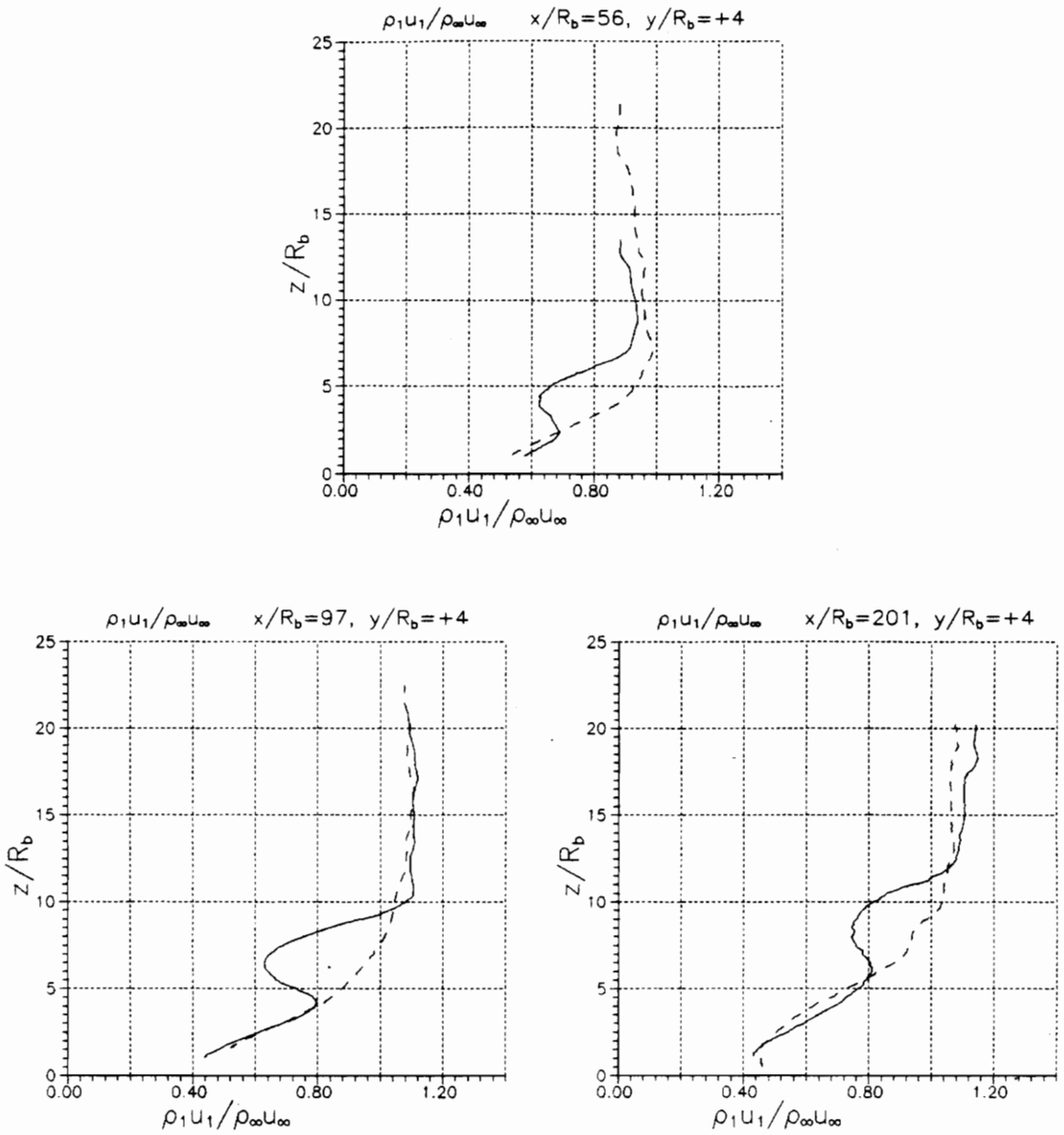

Wedge-shaped Nozzle: Solid Line
Circular Nozzle: Dashed Line

Figure 102. Mass Flux Profiles, $y/R_b=+4$.

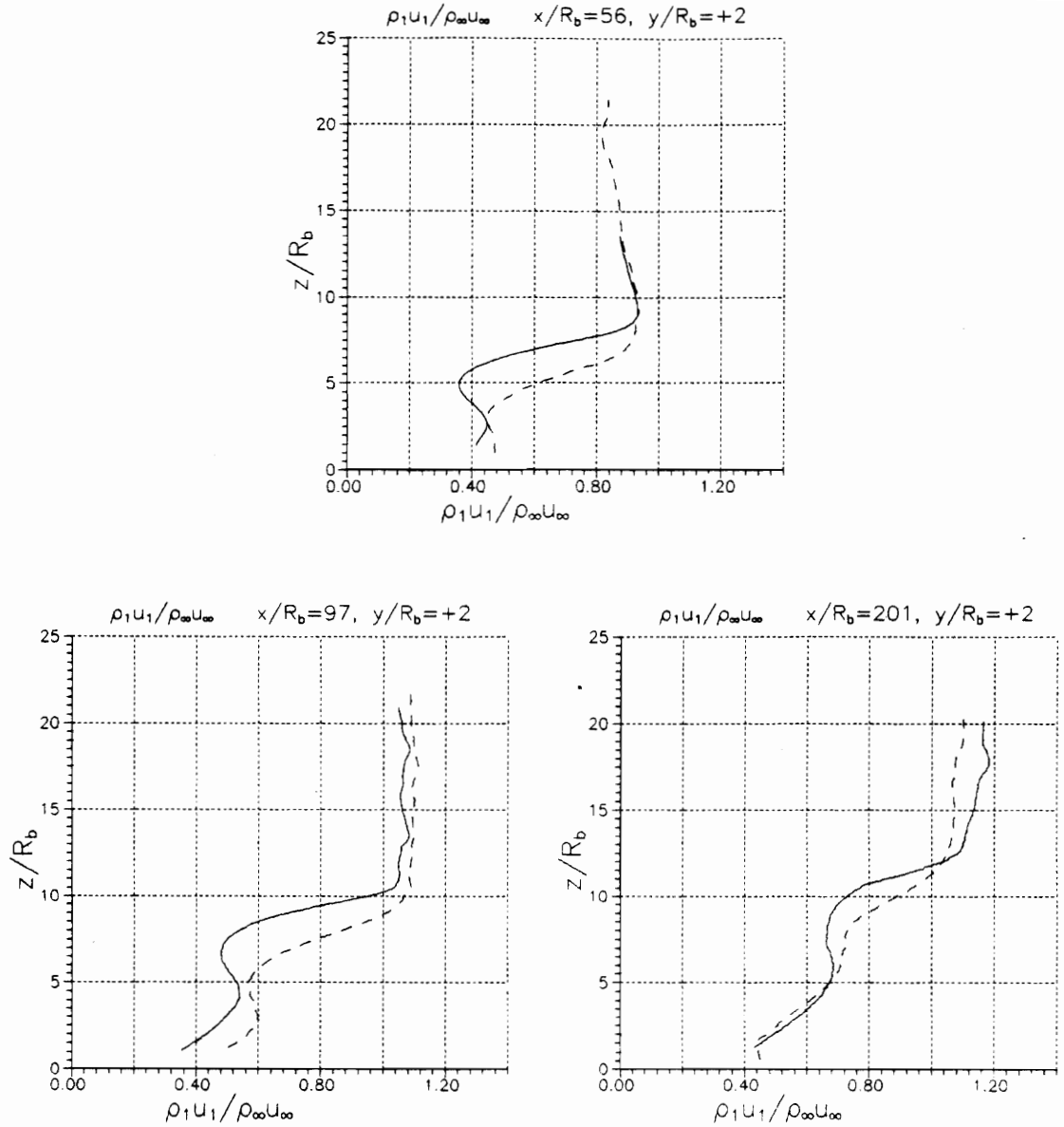

Wedge-shaped Nozzle: Solid Line
Circular Nozzle: Dashed Line

Figure 103. Mass Flux Profiles, y/R$_b$ = +2.

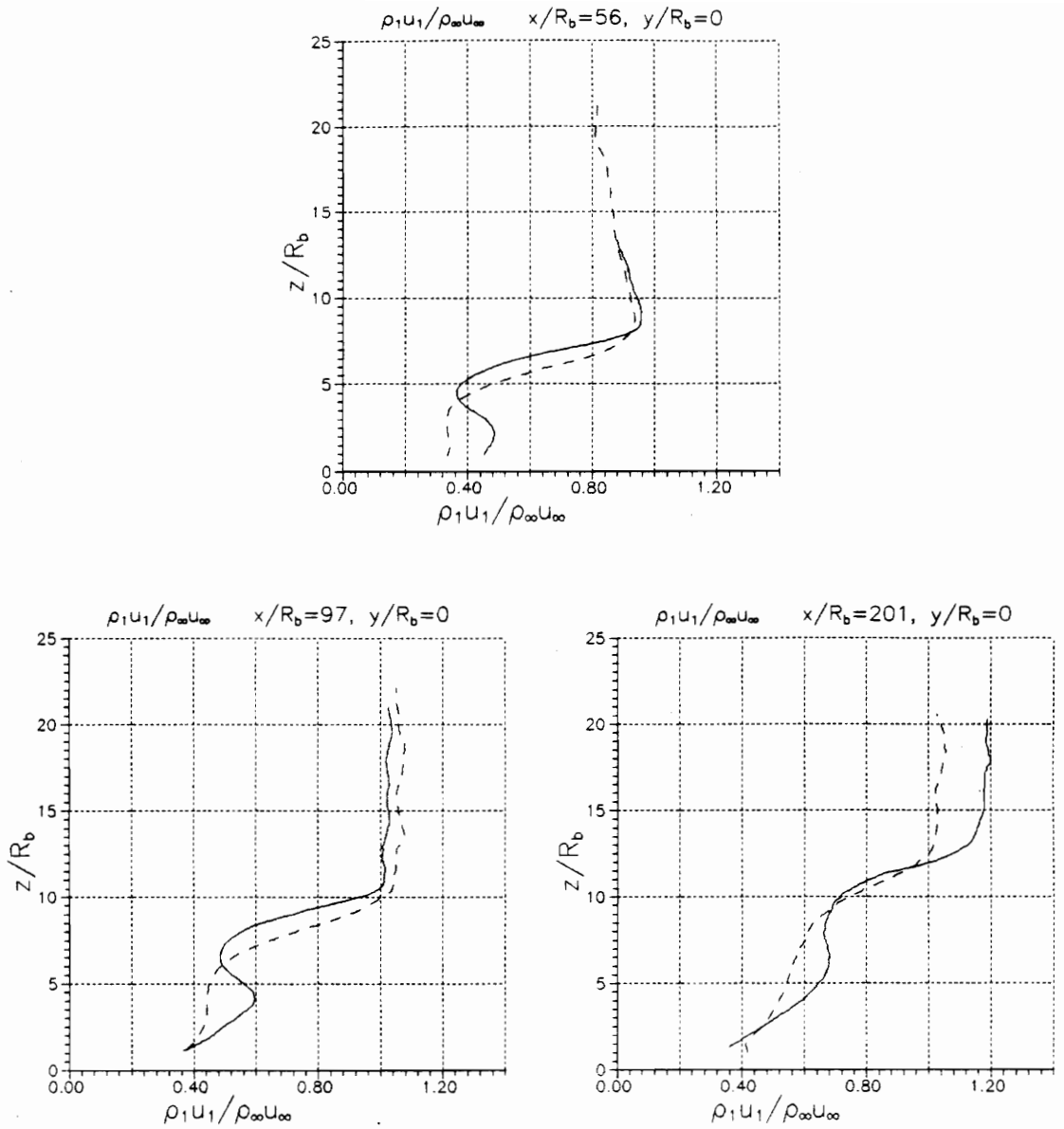

Wedge-shaped Nozzle: Solid Line
Circular Nozzle: Dashed Line

Figure 104. Mass Flux Profiles, $y/R_b=0$.

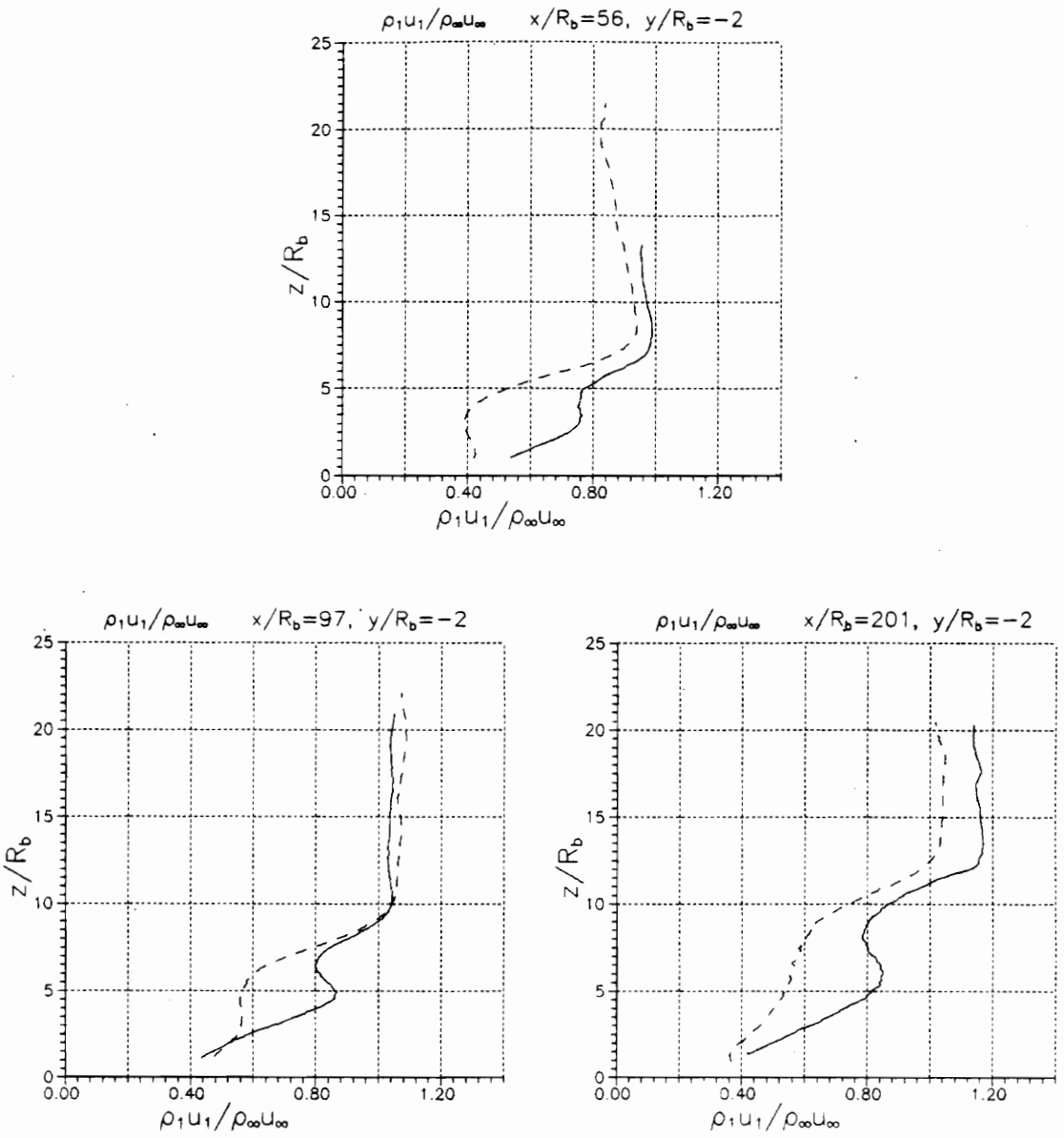

Wedge-shaped Nozzle: Solid Line
Circular Nozzle: Dashed Line

Figure 105. Mass Flux Profiles, y/R_b=-2.

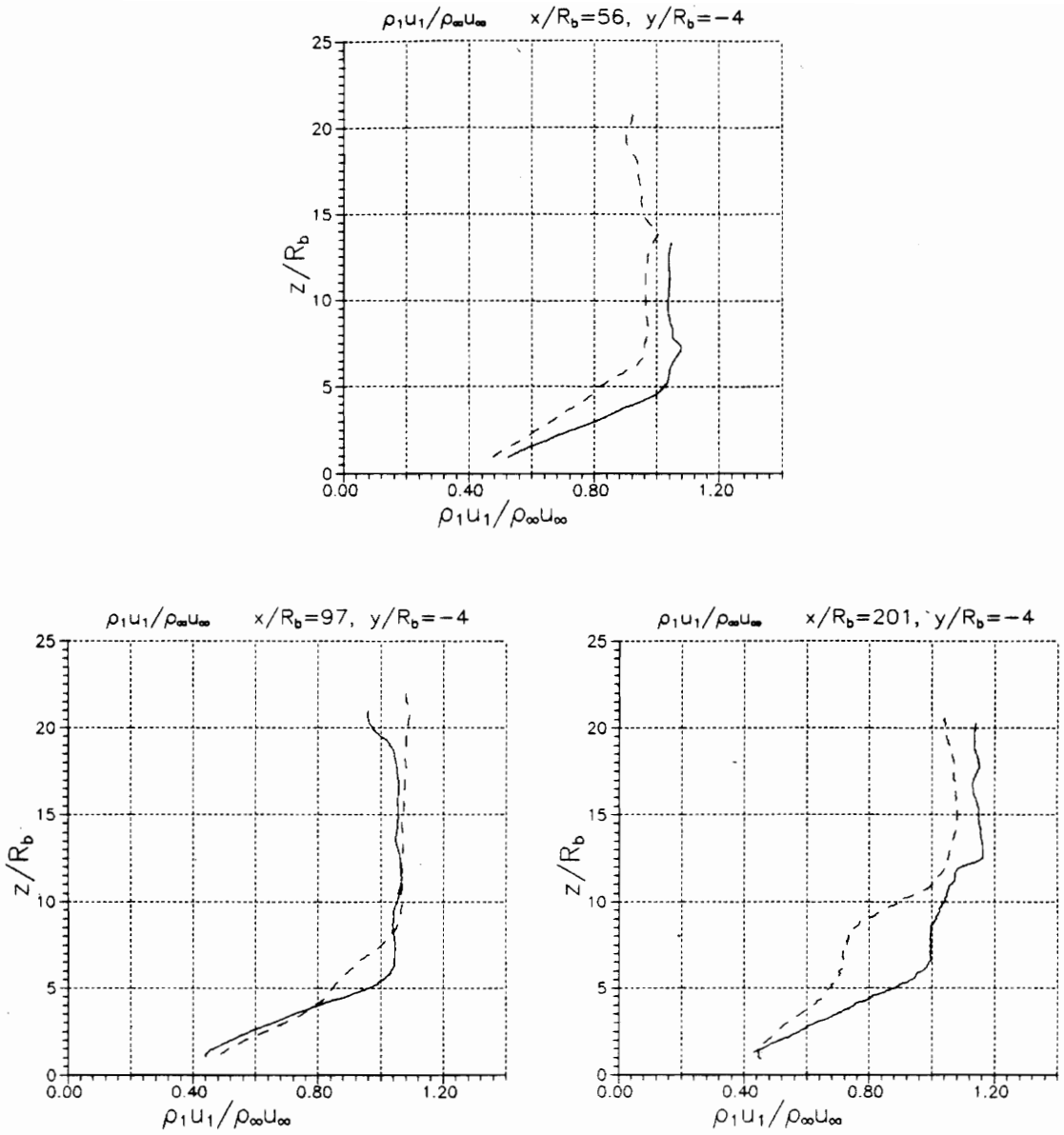

Wedge-shaped Nozzle: Solid Line
Circular Nozzle: Dashed Line

Figure 106. Mass Flux Profiles, y/R_b=-4.

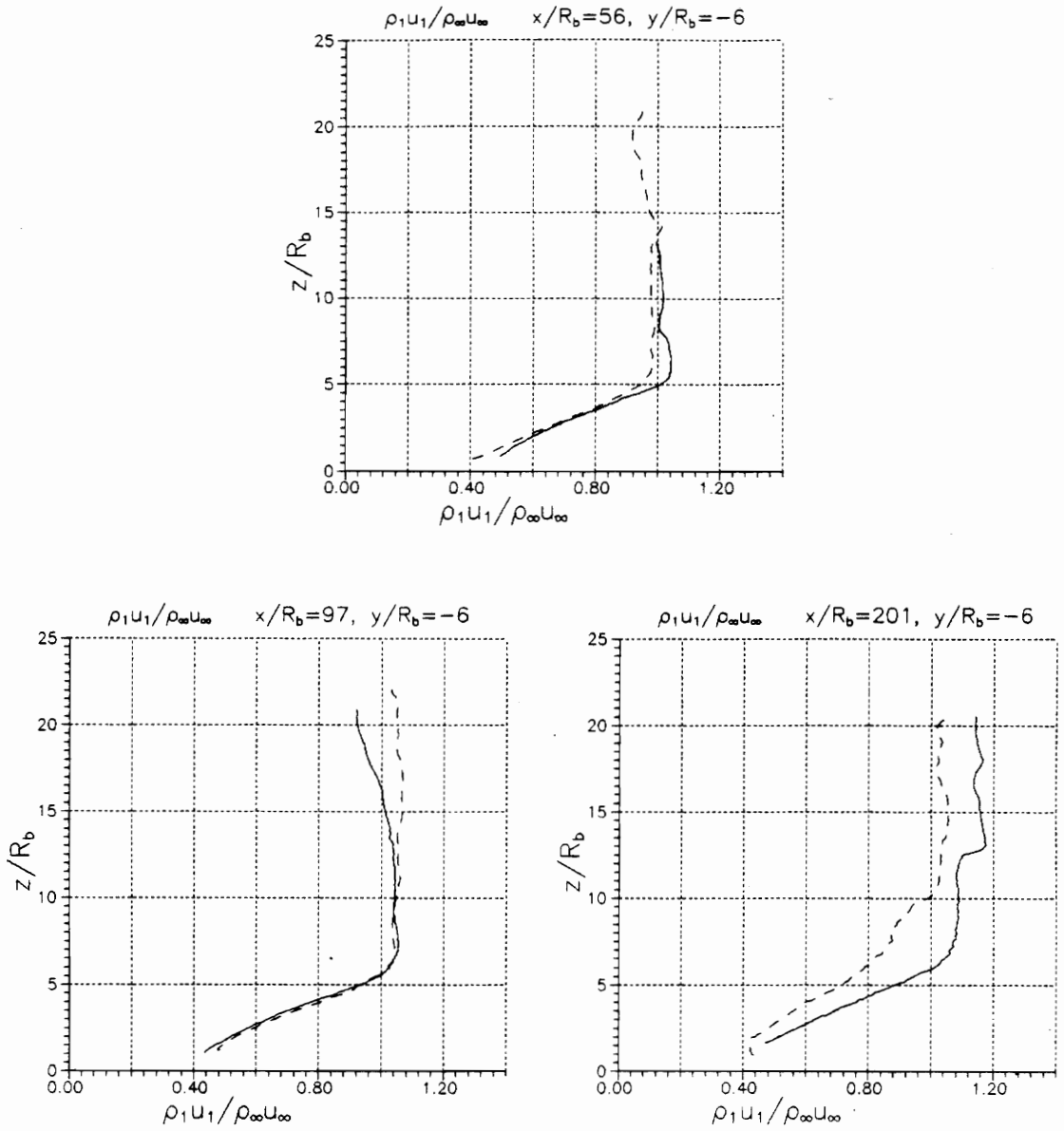

Wedge-shaped Nozzle: Solid Line
Circular Nozzle: Dashed Line

Figure 107. Mass Flux Profiles, y/R$_b$=-6.

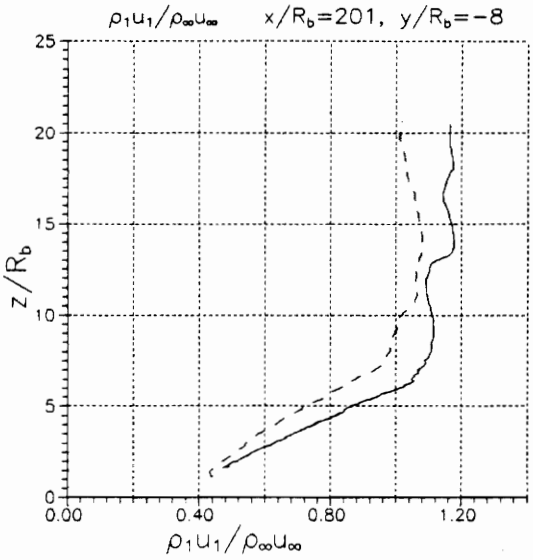

Wedge-shaped Nozzle: Solid Line
Circular Nozzle: Dashed Line

Figure 108. Mass Flux Profiles, $y/R_b=-8$.

Appendix A: Uncertainty Analysis

Possible sources of uncertainties include the tunnel total pressure controller system and the helium injection system, probe characteristics and associated instrumentation, and the vertical position measurement system.

The tunnel total pressure controller circuit maintained the total pressure to within six percent of its desired value. The tunnel total temperature varied by about three percent. The helium supply system allowed less than three percent error in the plenum chamber total pressure and less than two percent error in the plenum chamber total temperature. The error range was determined for all four quantities by finding the maximum and minimum value of each quantity from several data profiles.

The cone-static probe and the Pitot probe measurements contained uncertainties from transducers, transducer calibration curve fits, and probe time response. According to the manufacturers, the pressure transducers were accurate to one percent[5]. The errors from calibration curve fits were less than 0.003 percent and were negligible compared to the other sources of error. The time response of the probes had the effect of vertically shifting the pressure profiles. Since the traverse moved at 3.8 mm/s and the time constant of the cone-static probe was equal to 0.08 seconds, a vertical shift of 0.30 mm was possible. The vertical shift of the Pitot probe was 0.06 mm.

The total temperature measurements had uncertainties caused by insufficient venting of gas through the probe, heat loss through the insulating supports to the

thermocouple wire, and the time response of the thermocouple. The uncertainty from the time response of the thermocouple was negligible because the total temperature variations in this investigation were not large. A vertical shift would not have altered the data significantly. The uncertainty of the total temperature measurements was estimated to be about 2 percent[8].

Concentration measurement uncertainties arose from the calibration curve fit and the interpolation method used in the concentration reduction program. The calibration curve fit had a possible error of 3 percent for the pressure range at which the probe operated. The concentration reduction program linearly interpolated between the calibration curves shown in Figure 11 to determine helium concentration. A careful examination of the curves shows that they are not linearly spaced. The interpolation error was estimated to be about 2 percent.

The overall effects of the uncertainties in probe measurements on the derived flow quantities were investigated using the methods of Kline and McClintock[21] and Moffat[22]. The following estimates for the uncertainties were found:

Mach number	2.9%
Static Pressure	5.0%
Flow Speed	7.8%
Density	12%
Static Temperature	11%
Speed of Sound	7.1%
Mass Flux	15%

The uncertainties in the vertical position measurement system were produced by the cathetometer, the LVDT, and the LVDT calibration curve fit. The vertical position error introduced by the cathetometer was 0.6 percent[5,8]. The error was estimated by taking repeated cathetometer measurements of a point. The LVDT had a 0.5 percent error[19], and the vertical position error introduced by the LVDT calibration curve fit was 0.1 percent. Therefore, the vertical position measurement system introduced a maximum error of 1.2 percent. This corresponds to a 0.4 mm shift in the profiles. However, if the vertical shift caused by the time response of the cone-static probe is included, the profiles could be shifted by as much as 0.7 mm, or 2.1 percent of the full traverse height.

Appendix B: Computer Programs

```
C PROGRAM WTUNNEL
C THIS PROGRAM TAKES DATA EITHER WHILE PROBE IS TRAVERSED OR
C FIXED
C link with libraries: das16for, numer
C
      INTEGER*2 IHOUR0,IHOUR1,IMIN0,IMIN1,ISEC0,ISEC1,IHUND0,
     $             DACN,RTNFLG,DATOUT,DATARRAY(28000),BASEADDR,
     $             STARTC,MODE,ENDCH,NOS,IPAR,DMALEV,CNT1,CNT2,
     $             INTLEV,IHUND1,DAT0(9),DACN0
      REAL MAXPSI,SECS,VOLT,TIME0,TIME1,TIMDIF
      character*14 fname(6), RUN*3
      character*42          pgm(2),pgm1,pgm2,pgm3,pgm4
      character*2 exe1,exe2,exe3,exe4,exe5,exe6,exe7,exe8,exe9,exe10
c       data    pgm1    / 'V400 D200 Z1 R1                          ' /
c       data    pgm2    / 'V400 D200 Z0 R1                          ' /
        data    pgm3    / 'V100 D200 Z1 R1 Z0 R1                      ' /
        data    pgm4    / 'V10 D200 Z1 R1 Z0 R1                       ' /
        data    exe1    / 'Y1' /
        data    exe2    / 'Y2' /
        data    exe3    / 'Y3' /
        data    exe4    / 'Y4' /
        data    exe5    / 'Y5' /
        data    exe6    / 'Y6' /
        data    exe7    / 'Y7' /
        data    exe8    / 'Y8' /
        data    exe9    / 'Y9' /
        data    exe10   / 'xx' /
      DATA DAT0 /4095,3391,2882,2403,2006,1553,988,475,0/

        call cinit


      write(*,*)'INSURE STEPPER POWER IS ON AND STEPPER RESET'
C
C  **  INPUT INITIAL PROGRAM PARAMETERS  **
C
      write(*,*)' input traverse up command'
      read(*,'(A)')pgm(1)
      write(*,*)' input traverse down command'
      read(*,'(A)')pgm(2)

      WRITE(*,*)'INPUT PRESSURE'
      READ(*,*)MAXPSI
      WRITE(*,*)'input calibration constant (around 1.60)'
      read(*,*)fudge
      write(*,*)' input hot-film offset'
```

Program 1. Data Collection Program.

```
      read(*,*)hfoffset
      offset = 0.0

       call outpgm (pgm(1))

      TDEL = 2.0
      TRUP = 6.0
      TDATA = 6.0
      SHUTD = 16.0
      TVAL = 0.00000
C
      DACN = 1
      DACN0 = 0
      BASEADDR = 768
      DMALEV = 3
      INTLEV = 2
      CALL LOCATE(15,2)
      MODE = 18
      RTNFLG = 0

C
C  **  INITIALIZE METRABYTE  **
C
      CALL ADINIT(BASEADDR,DMALEV,INTLEV,RTNFLG)
      IF (RTNFLG.NE.0) GOTO 200
C
       CALL DIGOUT(0)
   10 CALL CLRSCN(7,0)
       CALL LOCATE(5,5)
C
C  **  CHANGE TIME PARAMETERS IF NECESSARY  **
C
      WRITE(*,*)'DEFAULT TIME PARAMETERS ARE AS FOLLOWS:'
      WRITE(*,*)' '
      WRITE(*,*)TDEL,' SECONDS DELAY BEFORE TUNNEL VALVE'
      WRITE(*,*)TVAL,' VALVE OPENS AT T=0'
      WRITE(*,*)TRUP,' SECONDS TRAVERSE UP'
      WRITE(*,*)TDATA,' SECONDS UNTIL DATA STARTS'
      WRITE(*,*)SHUTD,' SECONDS DIGITAL OUTPUTS OFF'
      CALL LOCATE(15,5)
      WRITE(*,*)'WANT TO CHANGE PARAMETERS? ENTER (1) IF YES'
      READ(*,'(F2.0)')CHA
      IF(CHA.NE.1.) GO TO 20
C
      CALL CLRSCN(7,0)
      CALL LOCATE(5,5)
```

Program 1. Data Collection Program.

```
      WRITE(*,*)'TIME IS SET AT ZERO WHEN WIND TUNNEL VALVE OPEN'
      WRITE(*,*)' '
      WRITE(*,*)'ENTER TIME FOR TRAVERSE UP'
      READ(*,*)TRUP
      WRITE(*,*)'ENTER TIME TO START TAKING DATA'
      READ(*,*)TDATA
      WRITE(*,*)'ENTER TIME FOR TUNNEL SHUTDOWN'
      READ(*,*)SHUTD
      WRITE(*,*)'ENTER TIME DELAY BEFORE TIMER IS ENABLED'
      READ(*,*)TDEL
      WRITE(*,*)' '
      WRITE(*,*)'TIMES OK AS ENTERED?  ENTER (2) TO CORRECT.'
      READ(*,'(F2.0)')CORR
      IF(CORR.EQ.2.)GOTO 10
C
C   ** SET UP A/D SAMPLING PARAMETERS **
C
   20 CALL CLRSCN (7,0)
      CALL LOCATE (4,0)
      WRITE(*,'(A\)')' ENTER THE START CHANNEL  = '
      READ(*,'(I2)')STARTC
      WRITE(*,'(A\)')' ENTER THE END CHANNEL    = '
      READ(*,'(I2)')ENDCH
      WRITE(*,*)
      WRITE(*,*)' # OF DATA POINTS PER CHANNEL'
      READ(*,'(I5)')NOS
C
C     ** SET SAMPLE RATE **
C
  250 CALL CLRSCN(7,0)
      CALL LOCATE (0,0)
      WRITE(*,*)' SET SAMPLE RATE.....'
      WRITE(*,*)' '
      WRITE(*,*)' '
      WRITE(*,*)'   RATE IS ESTABLISHED BY DIVIDING THE CLOCK RATE'
      WRITE(*,*)'   (1 MHZ) BY THE PRODUCT OF THE TWO COUNTS.    '
      WRITE(*,*)'   AS AN EXAMPLE:'
      WRITE(*,*)' '
      WRITE(*,*)'   HIGH COUNT = 10, LOW COUNT = 10 '
      WRITE(*,*)'   SAMPLE RATE = (1000000/(10*10)) = 10000 '
      WRITE(*,*)'         SAMPLES PER SECOND PER CHANNEL'
      WRITE(*,*)' '
      WRITE(*,'(A\)')' ENTER THE LOW COUNT   = '
      READ(*,'(I6)')CNT1
      WRITE(*,'(A\)')' ENTER THE HIGH COUNT  = '
      READ(*,'(I6)')CNT2
```

Program 1. Data Collection Program.

```
      DELTA = 1000000./FLOAT(CNT1*CNT2)
      SECS = NOS/DELTA
      ISECS = INT(SECS*100.)
      WRITE(*,*)
      WRITE(*,*)' THE COUNT SELECTION AS ENTERED WILL PROVIDE...'
      WRITE(*,*)'  '
      WRITE(*,*)'    ',DELTA,' SAMPLES PER SECOND PER CHANNEL'
      WRITE(*,*)'FOR '
      WRITE(*,*)'    ',SECS,' SECONDS'
      WRITE(*,*)' '
      WRITE(*,*)' IF PARAMETERS OK, PRESS RETURN.  IF NO, ENTER 1'
      READ(*,'(I2)')IPAR
      IF(IPAR.EQ.1)GOTO 250
  666 CALL CNTMO1 (2,CNT1)
      CALL CNTMO2 (2,CNT2)
C
      WRITE(*,*)'ENTER (1) WHEN READY TO BEGIN COUNTDOWN'
      READ(*,'(F1.0)')BEGIN
      IF(BEGIN.NE.1.)GOTO 10
      CALL GTIME(IHOUR0,IMIN0,ISEC0,IHUND0)
      TIME0 = IHOUR0*3600.+IMIN0*60.+ISEC0+IHUND0/100.
   51 CALL GTIME(IHOUR1,IMIN1,ISEC1,IHUND1)
      TIME1 = IHOUR1*3600.+IMIN1*60.+ISEC1+IHUND1/100.
      TIMDIF = TIME1 - TIME0
      IF(TIMDIF.LT.TDEL)GOTO 51
      CALL CLRSCN(7,0)
      CALL LOCATE(10,10)
      IHOUR0=0
      IMIN0=0
      ISEC0=0
      IHUND0=0
      IHOUR1=0
      IMIN1=0
      ISEC1=0
      IHUND1=0
      TIME0=0
      TIME1=0
C
      WRITE(*,*)' *******  TIMER ENABLED  *******'
C
      CALL GTIME(IHOUR0,IMIN0,ISEC0,IHUND0)
      TIME0 = IHOUR0*3600.+IMIN0*60.+ISEC0+IHUND0/100.
      VOLT = MAXPSI / (10. * fudge)
      DATOUT = INT(VOLT/2.96E-3)
      CALL DAOUT(DACN,DATOUT,RTNFLG)
```

Program 1. Data Collection Program.

```
      WRITE(*,*)'VALVE ON'
      CALL DIGOUT(1)
   39 CALL GTIME(IHOUR1,IMIN1,ISEC1,IHUND1)
      TIME1 = IHOUR1*3600.+IMIN1*60.+ISEC1+IHUND1/100.
      TIMDIF = TIME1 - TIME0
      IF(TIMDIF.LT.TRUP)GOTO 39
      if (iflag.eq.0) then
        write(*,*) '** Initial Traverse Up **'
          call outexe(exe1)
          call outexe(exe10)
  944     call gtime(ihour1,imin1,isec1,ihund1)
          time1=ihour1*3600.+imin1*60.+isec1+ihund1/100.
          timdif=time1-time0
          if (timdif.lt.trup+1.0)go to 944
          call outpgm(pgm(1))
      end if

      WRITE(*,*)'TRAVERSE UP'
      WRITE(*,*)

         call outexe (exe1)
         call outexe (exe10)

      CALL DIGOUT(11)
   159  CALL GTIME(IHOUR1,IMIN1,ISEC1,IHUND1)
      TIME1 = IHOUR1*3600.+IMIN1*60.+ISEC1+IHUND1/100.
      TIMDIF = TIME1 - TIME0
      IF(TIMDIF.LT.TDATA)GOTO 159

C
      NCONV = NOS * (ENDCH - STARTC + 1)
           CALL ADCONV(MODE,STARTC,ENDCH,NOS,DATARRAY(1),RTNFLG)
           IF(RTNFLG.NE.0) GO TO 200
C
         call outpgm (pgm(2))
      WRITE(*,*)
      WRITE(*,*)'TRAVERSE DOWN'
         call outexe (exe1)
         call outexe (exe10)
      CALL DIGOUT(5)
   29 CALL GTIME(IHOUR1,IMIN1,ISEC1,IHUND1)
      TIME1 = IHOUR1*3600.+IMIN1*60.+ISEC1+IHUND1/100.
      TIMDIF = TIME1 - TIME0
      IF(TIMDIF.LT.SHUTD)GOTO 29
      CALL DIGOUT(0)
      WRITE(*,*)'ALL DIGITAL OUTPUTS OFF'
```

Program 1. Data Collection Program.

```
      WRITE(*,*)
C
C  **  WRITE TO FILES  **
C
      NSTEPS = 1
      write(*,*)'WRITING TO FILES . . .'
      nch = endch - startc + 1
      fname(1) = 'b:hfs.run'
      fname(2) = 'b:lvdts.run'
      fname(3) = 'b:p1s.run'
      fname(4) = 'b:p2s.run'
      fname(5) = 'b:pt1s.run'
      fname(6) = 'b:tt1s.run'
      do 23 j =1, nch
        open(j,file=fname(j),status='new', form ='FORMATTED')
          in2 = j
        write(j,'(I3)')j-1
          write(j,*)delta
          if(j.eq.1)then
            write(j,*)hfoffset
          else
            write(j,*)offset
          end if
        write(j,'(i5)') nos
          do 13 i = 1,nos*nsteps
            write(j,'(i5)') datarray(in2)
              in2 = in2 + nch
 13       continue
          close (j)

 23   continue
      GO TO 188
C
 200  CALL CLRSCN(7,0)
      CALL DIGOUT(0)
      CALL LOCATE(2,2)
      WRITE(*,*)'** THERE HAS BEEN AN ERROR NUMBER ',RTNFLG
      WRITE(*,*)
      WRITE(*,'(A\)')' HIT <ENTER> TO RETURN TO MAIN MENU '
      READ(*,'(I2)')IERR
  188 CONTINUE
          END
```

Program 1. Data Collection Program.

```
C --- outpgm
      subroutine      outpgm (pgm)
      character*42    pgm
        do 100 i = 1,42
          call cout (pgm(i:i))
100     continue
        call cout (13)
        return
      end

C --- outexe
      subroutine      outexe (exe)
      character*2     exe
        do 100 i = 1,2
          call cout (exe(i:i))
100     continue
        call cout (13)
        return
      end
```

Program 1. Data Collection Program.

```
$DEBUG
C*************************************************************
C
c  This program computes concentration profiles from
c  hot film voltage, pressure P1, and total temperature.
c
c
c
C*************************************************************
C
      DIMENSION TT(2000),PT(2000),AP1(2000),XHE(2000),YLVDT(2000)
      DIMENSION VISA(16,2),CONA(16,2),VISHE(16,2),CONHE(16,2)
      DIMENSION CC1(10) , XN1(10)
      character*15 runin,runout,limit
C
C  VOLTAGE VS. TOTAL TEMPERATURE AND PRESSURE DATA
C    TT(K), PT(PSI),XHE(MOLE FRACTION)
C  L=NUMBER OF DATA VALUES FOR CALIBRATION
      OPEN(5,FILE='CALIB.IN',STATUS='OLD',FORM='FORMATTED')
      open(1,file='hfrun.num',status='old')
      read(1,*)numrun

c
c Big loop for each run.###
c
     do 9999 jrun=1,numrun
     read(1,19)runin,runout,limit,sh
  19  format(3a15,f5.2)
     write(*,19)runin,runout,limit,sh
      OPEN(6,FILE=RUNIN,STATUS='OLD',FORM='FORMATTED')
      OPEN(7,FILE=RUNOUT,STATUS='NEW',FORM='FORMATTED')
      OPEN(8,FILE=LIMIT,STATUS='NEW',FORM='FORMATTED')
      READ(5,*) NR,L,TRT,RCAB,RRT,RSET1,D,TOL,NCONST,DELX
      WRITE(*,*)NR,L,TRT,RCAB,RRT,RSET1,D,TOL,-TOL,NCONST,DELX
      WRITE(*,*)
C  *** INPUT  XHE = 0.0  TO  XHE = 1.0  ***
      DO 252 I = 1 , NCONST
        READ(5,*) CC1(I) , XN1(I)
         WRITE(*,*) CC1(I) , XN1(I)
  252  CONTINUE
      WRITE(*,*)' LOADING DATA VALUES . . .'
      DO 10 I=1,L
      READ(6,*) YLVDT(I),AP1(I),PT(I),TT(I)
   10  CONTINUE
C
C  VISCOSITY FOR AIR IN KG/M*S OR N*S/M**2
```

Program 2. Concentration Data Reduction Program.

```
      DATA VISA/140.,150.,160.,180.,200.,220.,240.,260.,280.,
     1      290.,300.,310.,320.,330.,340.,350.,
     1   .96112E-5,1.0283E-5,1.08842E-5,1.20866E-5,1.3289E-5,
     1   1.43694E-5,1.54498E-5,1.64844E-5,1.74732E-5,1.79676E-5,
     1   1.8462E-5,1.89196E-5,1.93772E-5,1.9834E-5,2.02924E-5,
     1    2.075E-5/
C
C  THERMAL CONDUCTIVITY FOR AIR IN W/M*K
      DATA CONA/140.,150.,160.,180.,200.,220.,240.,260.,280.,
     1      290.,300.,310.,320.,330.,340.,350.,
     1   .0128372,.013735,.014606,.016348,.01809,.019762,
     1   .021434,.023064,.024652,.025446,.02624,.026998,
     1    .027756,.028514,.029272,.03003/
C
C VISCOSITY FOR HELIUM IN KG/M*S
      DATA VISHE/140.,150.,160.,180.,200.,220.,240.,260.,280.,
     1    290.,300.,310.,320.,330.,340.,350.,
     1    1.22E-5,1.288E-5,1.344E-5,1.455E-5,1.566E-5,
     1    1.657E-5,1.749E-5,1.839E-5,1.927E-5,1.971E-5,2.015E-5,
     1   2.059E-5,2.103E-5,2.147E-5,2.191E-5,2.235E-5/
C
C THERMAL CONDUCTIVITY FOR HELIUM IN W/M*K
      DATA CONHE/140.,150.,160.,180.,200.,220.,240.,260.,280.,
     1    290.,300.,310.,320.,330.,340.,350.,
     2    9.07E-2,9.5E-2,9.92E-2,1.072E-1,1.151E-1,
     3   1.228E-1,1.304E-1,1.374E-1,1.447E-1,1.484E-1,1.52E-1,
     4    1.555E-1,1.591E-1,1.626E-1,1.662E-1,1.697E-1/
C
     A = 0.
     R = 0.
C
C*************************************************************
C
C  RS=SERIES RESISTANCE (OHMS)
      RS= 50.0
C  RCAB=CABLE RESISTANCE(OHMS)
C  RSET1=ANEMOMETER RESISTANCE SETTING(OHMS)
C  RWIRE=HOT WIRE RESISTANCE AT THE OPERATING TEMP.
      RWIRE1=RSET1-RCAB
C  RRT=HOT WIRE RESISTANCE AT ROOM TEMPERATURE(OHMS)
C  TRT=STANDARD ROOM TEMP (K)
C  Y=THERMAL COEEFICIENT OF RESISTIVITY FOR HOT-FILM (1/K)
      Y=0.0024
C  RWIRE=RRT(1+Y(TWIRE-TRT)
      TWIRE1=TRT+(RWIRE1/RRT-1.0)/Y
C  XL=WIRE LENGTH (INCHES CONVERTED TO METERS)
```

Program 2. Concentration Data Reduction Program.

```
      XL=0.040*0.0254
C  XD=WIRE DIAMETER (INCHES CONVERTED TO METERS)
      XD=0.002*0.0254
C  B=RATIO OF THROAT AREA TO WIRE PLANE AREA
      B=0.214515
C  D=RATIO OF STATIC TO TOTAL TEMP FOR ISENTROPIC CHOKE
C     D=0.9725
C  A=RATIO OF SPECIFIC HEATS
      PI=3.141593
C  R=GAS CONSTANT (KJ/KG*K) CONVERT TO J/KG*K
C*****************************************************************
C
      V = 0.0
      C = 0.0
      G = 0.0
       WRITE(*,*)' INPUT SHIFT VALUE IN VOLTS (EXP-CALC)'
c      READ(*,*) SH
       WRITE(8,*) SH
       WRITE(*,*) SH
C
      NCOUNT = 0
      NC0 = 0
      NC1 = 0
      DO 1000 I=1,L
       T=D*TT(I)
       PT(I)=PT(I)*6894.757
       DO 50 J=1,15
       IF((T.GE.VISA(J,1)).AND.(T.LE.VISA(J+1,1))) GO TO 55
  50  CONTINUE
  55  CONTINUE
C
      XLOW = 0.0
      XUP = DELX
      DO 253 ILIMS = 1 , NCONST-1
       CALL MIXTURE(VISA,CONA,VISHE,CONHE,A,R,J,XLOW,T,V,C,G)
C
       VLOW =((RS+RWIRE1+RCAB)**2/RWIRE1*PI*XL*C*CC1(ILIMS)*(TWIRE1-
     1    T)*(XD/V*B*G*PT(I)*(A/(R*TT(I)))**0.5)**XN1(ILIMS))**0.5
     2      + SH
C
C
       CALL MIXTURE(VISA,CONA,VISHE,CONHE,A,R,J,XUP,T,V,C,G)
C
      VUP=((RS+RWIRE1+RCAB)**2/RWIRE1*PI*XL*C*CC1(ILIMS+1)*(TWIRE1-
     1  T)*(XD/V*B*G*PT(I)*(A/(R*TT(I)))**0.5)**XN1(ILIMS+1))**0.5
     2      + SH
```

Program 2. Concentration Data Reduction Program.

```
      IF(ILIMS.EQ.1.AND.AP1(I).LT.VLOW)THEN
        XHE(I) = 0.0
        NC0 = NC0 + 1
        WRITE(8,*) I,XHE(I),AP1(I)-VLOW
        GO TO 1600
      ELSE IF(ILIMS.EQ.NCONST-1.AND.AP1(I).GT.VUP)THEN
        XHE(I) = 1.0
        NC1 = NC1 + 1
        WRITE(8,*) I,XHE(I),AP1(I)-VUP
        GO TO 1600
      END IF
C
      IF(AP1(I).EQ.VLOW)THEN
        XHE(I) = XLOW
         GO TO 1600
      ELSE IF(AP1(I).EQ.VUP)THEN
        XHE(I) = XUP
        GO TO 1600
      ELSE IF(AP1(I).GT.VLOW.AND.AP1(I).LT.VUP) THEN
        XM = (XUP - XLOW) / (VUP - VLOW)
        XHE(I) = XM * (AP1(I) - VLOW) + XLOW
        GO TO 1600
      END IF
      XLOW = XUP
      XUP = XLOW + DELX
  253 CONTINUE
 1600 WRITE(7,*) XHE(I),YLVDT(I)
      NCOUNT = NCOUNT + 1
C
C     WRITE(*,*)I
 1000 CONTINUE
      WRITE(*,*)' Number of pts used = ',NCOUNT,' out of ',L
      WRITE(*,*)
      WRITE(*,*)' Number of pts. forced to 1.0 = ',NC1
      WRITE(*,*)
      WRITE(*,*)' Number of pts. forced to 0.0 = ',NC0
      rewind(5)
      CLOSE(6)
      CLOSE(7)
      CLOSE(8)
 9999 continue
      STOP
      END
C
```

Program 2. Concentration Data Reduction Program.

```
      SUBROUTINE MIXTURE(VISA,CONA,VISHE,CONHE,A,R,J,TT,T,V,C,G)

      DIMENSION VIS(16,2),CON(16,2),VISA(16,2),CONA(16,2),
     1          VISHE(16,2),CONHE(16,2)
      REAL MHE,MA,M,MUA,MUHE,KHE,KA
C
C  HELIUM PROPERTIES
      XHE = TT
      MHE = 4.00260
      RHE = 8317./MHE
      CPHE = 5200.
C
C  AIR PROPERTIES
      XA = 1. - XHE
      MA = 29.
      RA = 8317./MA
      CPA = 1005.7
C
C  MIXTURE PROPERTIES
      M = XHE * MHE + XA * MA
      CP = ( XHE * CPHE * MHE + XA * CPA * MA ) / M
      R = 8317./M
      CV = CP - R
      A = CP / CV
C
      IXHE = NINT(100. * XHE)
      DO 10 I = J , J+1
        VIS(I,1) = VISHE(I,1)
        CON(I,1) = CONHE(I,1)
      IF(IXHE.EQ.100)THEN
        VIS(I,2) = VISHE(I,2)
        CON(I,2) = CONHE(I,2)
      ELSE IF(IXHE.EQ.0)THEN
        VIS(I,2) = VISA(I,2)
        CON(I,2) = CONA(I,2)
      ELSE
        MUA = VISA(I,2)/(1+XHE/XA*(1+SQRT(VISA(I,2)/VISHE(I,2))
     1        *(MHE/MA)**.25)**2/(2.82843*SQRT(1+MA/MHE)))
        MUHE = VISHE(I,2)/(1+XA/XHE*(1+SQRT(VISHE(I,2)/
     1          VISA(I,2))*(MA/MHE)**.25)**2/(2.82843*
     2          SQRT(1+MHE/MA)))
        VIS(I,2) = MUA + MUHE
        KA = CONA(I,2)/(1+XHE/XA*(1+SQRT(CONA(I,2)/CONHE(I,2))
     1       *(MHE/MA)**.25)**2/(2.82843*SQRT(1+MA/MHE)))
        KHE = CONHE(I,2)/(1+XA/XHE*(1+SQRT(CONHE(I,2)/CONA(I,2)
     1        )*(MA/MHE)**.25)**2/(2.82843*SQRT(1+MHE/MA)))
```

Program 2. Concentration Data Reduction Program.

```
      CON(I,2) = KA + KHE
    END IF
 10 CONTINUE
C
    G=(2.0/(A+1.0))**((A+1.0)/(2.0*(A-1.0)))
C
    VIS1=VIS(J,2)
    VIS2=VIS(J+1,2)
    CON1=CON(J,2)
    CON2=CON(J+1,2)
    TEMP1=VIS(J,1)
    TEMP2=VIS(J+1,1)
    V=VIS1+(VIS2-VIS1)*(T-TEMP1)/(TEMP2-TEMP1)
    C=CON1+(CON2-CON1)*(T-TEMP1)/(TEMP2-TEMP1)
C
C    WRITE(*,*) V , C
C
    RETURN
    END
```

Program 2. Concentration Data Reduction Program.

```
$debug
$large
C
c   Program : MEAN.F
c
c   This program reduces mean-flow variables from
c        given concentration, Pitot, cone-static, and
c        total temperature profiles.
c
c   m1.dat (file #1) is a reference file containing Pc/Pt2
c        values versus Mach numbers and gamma, as defined by
c        the Rayleigh Pitot Formula and the Cone Flow
c        equation.
c
c                Written :       Fei T. Kwok      9/1/89
c                Revised :       Eric J. Fuller   4/4/90
c               modified :       Matthew Barber   9/1/90
c-------------------------------------------------------------
c
c   Dimension all needed variables
c
      REAL  G(20) , M1(20,20) , PCPT2C(20,20) , PT2(800) , PC(800) ,
     1      TT2(800) , XHE(800) , LVDT(800) , M(800) , P1(800) ,
     2      GS(800) , RS(800) , T1(800) , A1(800) , RHO1(800) ,
     3      U1(800), pt1calc(800)
c
      INTEGER  NP1(200) , CH ,numrun
      character*10 concin,pt2in,pcin,tt2in,m1out,p1out,u1out,rho1out
      character*10 t1out,a1out,r1u1out,gout,rout,calpt1
c
      npts=800
c
c   Open file HFRUN.NUM and read total number of runs to reduce
c
      open (20,file='hfrun.num',status='old')
      read(20,*)numrun
c
c   Loop to reduce each run number
c
      do 1 jrun = 1,numrun
        read (20,993) concin,pt2in,pcin,tt2in,m1out,p1out,u1out
        read(20,993)rho1out,t1out,a1out,r1u1out,gout,rout,calpt1
        write (*,993) concin,pt2in,pcin,tt2in,m1out,p1out,u1out
        write(*,993)rho1out,t1out,a1out,r1u1out,gout,rout,calpt1
 993  format(7a10)
```

Program 3. Program to Calculate Other Mean Flow Values.

```
C
C  Open input files
C
      OPEN(1,FILE='m1.dat',STATUS='OLD',FORM='FORMATTED')
      OPEN(2,FILE=concin,STATUS='OLD',FORM='FORMATTED')
      OPEN(3,FILE=pt2in,STATUS='OLD',FORM='FORMATTED')
      OPEN(4,FILE=pcin,STATUS='OLD',FORM='FORMATTED')
      OPEN(5,FILE=tt2in,STATUS='OLD',FORM='FORMATTED')
C
C  Open output files
C
      OPEN(15,FILE=m1out,STATUS='NEW',FORM='FORMATTED')
      OPEN(7,FILE=p1out,STATUS='NEW',FORM='FORMATTED')
      OPEN(8,FILE=u1out,STATUS='NEW',FORM='FORMATTED')
      OPEN(9,FILE=rho1out,STATUS='NEW',FORM='FORMATTED')
      OPEN(11,FILE=t1out,STATUS='NEW',FORM='FORMATTED')
      OPEN(12,FILE=a1out,STATUS='NEW',FORM='FORMATTED')
      OPEN(13,FILE=r1u1out,STATUS='NEW',FORM='FORMATTED')
      OPEN(14,FILE=gout,STATUS='NEW',FORM='FORMATTED')
      OPEN(16,FILE=rout,STATUS='NEW',FORM='FORMATTED')
      OPEN(17,FILE=calpt1,STATUS='NEW',FORM='FORMATTED')
C
C
C
c  Read input files (xhe, lvdt, pt2, pc, tt2)
c
      DO 2 I = 1 , npts
        READ(2,*) xhe(i) , lvdt(i)
        READ(3,*) PT2(I), ztrash
        READ(4,*) PC(I), ztrash
        READ(5,*) TT2(I), ztrash
    2 CONTINUE
C
c  Read M1.DAT reference file
c
      READ(1,*) NG , NP
      DO 3 IG = 1 , NG
        READ(1,*) G(IG)
        DO 3 IP = 1 , NP
          READ(1,*) M1(IG,IP) , PCPT2C(IG,IP)
    3 CONTINUE
C
c  Loop using gas mixture properties and Pc/Pt2 ratio to
c     determine Mach number and P1
c
      NMC = 0
```

Program 3. Program to Calculate Other Mean Flow Values.

```
      DO 4 I = 1 , NPTS
c
c   From concentration, determine gamma and R values
c
        CALL MIXTURE( XHE(I) , GAM , RS(I) )
c
        GS(I) = GAM
        PCPT2 = PC(I) / PT2(I)
C
c   From gamma, Pc/Pt2 and reference values from M1.DAT,
c      determine Mach numbers
c
        CALL MACH1( GAM,PCPT2,NG,NP,G,M1,PCPT2C,M(I),NMC,I,NP1 )
C
        GAMM1 = GAM - 1.
        GAMP1 = GAM + 1.
c
c   If Mach number is reasonable, find P1 from Ray. Pitot Equ.
c
      write(*,*)I,M(i)
        IF( M(I).GT.-0.1) P1(I) = (2.*GAM/GAMP1*M(I)**2 - GAMM1/
     1      GAMP1)**(1./GAMM1) / (GAMP1/2.*M(I)**2)**(GAM/GAMM1) *
     2      PT2(I)
    4 CONTINUE
C
C   Loop to find any remaining values of P1 not found previously
c      because of M = -1.0 (used to mark values where Cone flow
c      Equation does not apply
c
      IF(NMC.NE.0) THEN
        NI = 1
   10   IFLAG = 0
        DO 5 I = NI , NMC
          IF( NP1(I+1).NE.NP1(I)+1 ) THEN
            IF(IFLAG.EQ.0)THEN
              N1 = NP1(I)
              N2 = NP1(I)
            END IF
            GO TO 6
          ELSE
            IF(IFLAG.EQ.0) N1 = NP1(I)
            N2 = NP1(I+1)
            IFLAG = 1
          END IF
    5   CONTINUE
```

Program 3. Program to Calculate Other Mean Flow Values.

```
C
c  Interpolate for remaining P1's
c
   6   IF(N1.EQ.1) THEN
         DO 7 I2 = NI , I
           P1(NP1(I2)) = P1(N2+1)
   7     CONTINUE
       ELSE IF( N2.EQ.NPTS ) THEN
         DO 8 I2 = I , NI , -1
           P1(NP1(I2)) = P1(N1-1)
   8     CONTINUE
       ELSE
         DO 9 I2 = NI , I
           CALL INTERP( LVDT(N2+1),LVDT(N1-1),LVDT(NP1(I2)),
    1                   P1(N2+1),P1(N1-1),P1(NP1(I2)) )
   9     CONTINUE
       END IF
C
       NI = I + 1
       IF( I.LT.NMC ) GO TO 10
     END IF
C
c  Loop to find remaining M's with interpolated P1's from above
c
     DO 11 I = 1 , NMC
       N = NP1(I)
c
C  with gamma, Pt2, and new P1, find M
c
       CALL MACH2( GS(N) , P1(N) , PT2(N) , M(N) )
     write(*,*)n,M(n)
  11 CONTINUE
C
c  Loop to determine other variables from standard
c     isentropic flow equations and ideal gas equ.
c
     DO 12 I = 1 , NPTS
       T1(I) = TT2(I) / (1.+(GS(I)-1.)/2.*M(I)**2)
       A1(I) = SQRT( GS(I)*RS(I)*T1(I) )
       U1(I) = M(I) * A1(I)
       RHO1(I) = P1(I)*6894.757 / (RS(I)*T1(I))
       pt1calc(i) = p1(i)*(1.+(gs(i)-1.)/2.*m(i)**2)**(gs(i)/
    1             (gs(i)-1.))
  12 CONTINUE
C
```

Program 3. Program to Calculate Other Mean Flow Values.

```
c  Loop to write to output files:
c     -- lvdt
c     -- P1, Pt1 . psia
c     -- U1, A1  . m/sec
c     -- rho1  . . kg/m^3
c     -- T1  . . . deg Kelvin
c     -- Xhe . . . mole fraction of helium
c     -- R . . . . J/(kg*deg K)
C
      DO 13 I = 1 , NPTS
        YL = LVDT(I)
        WRITE(15,*)  M(I) , YL
        WRITE(7,*)  P1(I) , YL
        WRITE(8,*)  U1(I) , YL
        WRITE(9,*)  RHO1(I) , YL
        WRITE(11,*) T1(I) , YL
        WRITE(12,*) A1(I) , YL
        WRITE(13,*) RHO1(I) * U1(I) , YL
        write (14,*) gs(i), yl
        write (16,*) rs(i), yl
        write (17,*) pt1calc(i), yl
  13  CONTINUE
C
C   close all the files
C
       DO 1000 I = 1 , 17
         if (i.ne.6) CLOSE(I)
 1000   CONTINUE
c
    1   continue
c
      STOP
      END
C
c-------------------------------------------------------------
C
c   Subroutine MIXTURE :
c
c       determines gamma and R
c
      SUBROUTINE MIXTURE(XHE,G,R)
      REAL M , MHE , MA
c
c   Molecular weight (kg/kmole) and Cp (J/kg/Kelvin) of
c      Helium and air
```

Program 3. Program to Calculate Other Mean Flow Values.

```
c
      MHE = 4.0026
      CPHE = 5200.
      MA = 29.0
      CPA = 1005.7
C
c   calculate mixture molecular weight from mole fraction helium
c         and then retrieve R and gamma
c
      XA = 1. - XHE
      M = XHE * MHE + XA * MA
      CP = ( XHE * CPHE * MHE + XA * CPA * MA ) / M
      R = 8317. / M
      CV = CP - R
      G = CP / CV
      RETURN
      END
C
C-------------------------------------------------------------
c
c   Subroutine :  MACH1
c
c   determines Mach number over profile, if applicable
c
      SUBROUTINE MACH1(GAM,PCPT2,NG,NP,G,M1,PCPT2C,M,NMC,I,NP1)
      REAL  G(20) , M1(20,20) , PCPT2C(20,20) , M , PCPT2L(20) ,
     1      ML(20)
      INTEGER  NP1(200)
C
c   Loop to find proper interval of gamma as compared to
c      values in M1.DAT
c
      DO 1 IG = 1 , NG-1
        IF(GAM.GE.G(IG).AND.GAM.LE.G(IG+1)) GO TO 2
    1 CONTINUE
    2 GIG = G(IG)
      GIG1 = G(IG+1)
C
c   Interpolate for proper interval of Pc/Pt2 references
c
      CALL INTERP(GIG,GIG1,GAM,PCPT2C(IG,1),PCPT2C(IG+1,1),PCPT2L(1))
c
c   Loop to check experimental Pc/Pt2 against critical Pc/Pt2
c      from M1.DAT to determine if Cone Flow applies
c
```

Program 3. Program to Calculate Other Mean Flow Values.

```
      IF(PCPT2.GT.PCPT2L(1)) THEN
        M = -1.0
        NMC = NMC + 1
        NP1(NMC) = I
        write(*,*)i,M
        RETURN
      END IF
c
c   Loop to determine Pc/Pt2 and Mach number intervals
c
      DO 3 IP = 1 , NP
        CALL INTERP(GIG,GIG1,GAM,PCPT2C(IG,IP),PCPT2C(IG+1,IP),
     1              PCPT2L(IP))
        CALL INTERP(GIG,GIG1,GAM,M1(IG,IP),M1(IG+1,IP),ML(IP))
    3 CONTINUE
c
c   Loop to find final Mach number value according to
c     corresponding Pc/Pt2 ratio
c
      DO 4 IP = 1 , NP-1
        IF(PCPT2.LE.PCPT2L(IP).AND.PCPT2.GE.PCPT2L(IP+1)) THEN
          CALL INTERP(PCPT2L(IP),PCPT2L(IP+1),PCPT2,ML(IP),
     1                ML(IP+1),M)
          RETURN
        END IF
    4 CONTINUE
c
      RETURN
      END
C
c-------------------------------------------------------------
c
c   Subroutine : MACH2
c
c   determine remaining unknouwn Mach numbers
c
      SUBROUTINE MACH2( G , P1 , PT2 , M )
      REAL  M , M1 , M2
      GM1 = G - 1.
      GP1 = G + 1.
      P1PT2 = P1 / PT2
      sonic = (2.*g/gp1-gm1/gp1)**(1./gm1) / (gp1/2.)**(g/gm1)
c
c   Loop to see if flow is subsonic, supersonic or sonic, then
c     determine Mach number accordingly
```

Program 3. Program to Calculate Other Mean Flow Values.

```
c
      IF(P1PT2.GT.sonic) THEN
c
c  If subsonic, then M from isentropic flow
c
        IF(P1PT2.GT.1.0) P1PT2 = 1.0
        M = SQRT( 2./(G-1.)*(P1PT2**((1.-G)/G)-1.))
        RETURN
      ELSE
c
c  If supersonic, then M iterated from Ray. Pitot Equ.
c
        M1 = 2.0
c
c     Use shooting method to iterate for M
c
        DO 1 I = 2 , 4
          DELM = 10. * 0.1**I
    2     M2 = M1 - DELM
          PM1 = (2.*G/GP1*M1*M1 - GM1/GP1)**(1./GM1) /
     1          (GP1/2.*M1*M1)**(G/GM1)
          PM2 = (2.*G/GP1*M2*M2 - GM1/GP1)**(1./GM1) /
     1          (GP1/2.*M2*M2)**(G/GM1)
          DM1 = PM1 - P1PT2
          DM2 = PM2 - P1PT2
          IF(ABS(DM1).LE.1E-3) THEN
            M = M1
            GO TO 3
          ELSE IF(ABS(DM2).LE.1E-3) THEN
            M = M2
            GO TO 3
          END IF
          IF((DM1*DM2).LT.0.0) GO TO 1
          M1 = M2
          GO TO 2
    1   CONTINUE
        IF(ABS(DM1).LE.ABS(DM2)) THEN
          M = M1
        ELSE
          M = M2
        END IF
      END IF
    3 IF( M.GT.1.12) M = 1.10
      RETURN
      END
```

Program 3. Program to Calculate Other Mean Flow Values.

```
C
c-------------------------------------------------------------
c
c   Subroutine : INTERP
c
c   interpolation routine
c
      SUBROUTINE INTERP(X2,X1,X,Y2,Y1,Y)
      SM = (Y2-Y1) / (X2-X1)
      Y = SM * (X-X1) + Y1
      RETURN
      END
```

Program 3. Program to Calculate Other Mean Flow Values.

```
$debug
c
c     Program:  INTEGRATE.FOR
c
c     This Program integrates in two dimensions to find
c        the mass flow of Helium.
c     It does this by performing a Reimann Sum up a profile
c        and 1/3 Simpson's rule across the test section.
c
c
c                        Eric J. Fuller      4/6/90
c               modified:  Matthew J. Barber   10/25/90
c-------------------------------------------------------------
      Character*15 rhou,massf
      dimension rsum(15),ru(900),alpha(900),walpha(900),wru(900)
      double precision rsum,ru,alpha,z,zmin,zmax,delz,b,a,pn
      double precision hemf,hemfr,RUAH,XT
c
c   open file containing run numbers and read number of runs
c
      open (9,file='helmf')
      write (9,19)
 19   format (//3x,'***   Integrate in the Y - direction   ***'/)
      open (1,file='hmfrun.num',status='old')
      read (1,*) numrun,b,a,pn
c
c   Loop to do each profile
c
      do 1 jrun = 1,numrun
c
c   Set rsum(jrun) = 0.
c
        rsum(jrun) = 0.D0
c
c   Read run # and open files for that run number
c
        read (1,1000) rhou,massf
        write (*,1000) rhou,massf
 1000   format (2a15)
        open (3,file=rhou,status='old')
        open (4,file=massf,status='old')
c
c   Read Lvdt to get zmax and zmin
c
        zmax = 0.D0
        zmin = 100.D0
```

Program 4. Mass Rate of Flow Integration Program.

```
      do 10 i = 1,800
        read (3,*) ru(i),z
        read (4,*) alpha(i),z
        if (z.lt.zmin) zmin = z
        if (z.gt.zmax) zmax = z
   10   continue
c
c   Calculate delta z and convert to meters
c
      delz = 0.0254D0*(zmax - zmin)/799.0D0
      write(*,*)'zmax = ',zmax,' zmin =',zmin
      write (*,*) ' delz = ',delz
c
c   Perform Reimann sum  (using average value)
c
      do 20 i = 2,800

c
c   set alpha = 0. if it is less than .07%
c
        if (alpha(i).lt.0.0007D0) alpha(i) = 0.D0
c
c   calculate ru*alpha*dely and add it to sum
c
        ruah = (ru(i)*alpha(i)+ru(i-1)*alpha(i-1))*delz/2D0

        rsum(jrun) = rsum(jrun) + ruah


   20   continue
c
      do 30 kfile = 3,4
        close (kfile)
   30   continue
      write (*,*) ' Rsum = ',rsum(jrun)
      write (9,20) rhou,rsum(jrun)
   20   format (/5x,'Reimann Sum for ',a15,
     b' = ',f10.5,' kg/(m-sec)'/)
c
    1 continue
c
c   Now do the horizontal integration
c
     hemf = 0.D0
c
     do 40 i = 1,numrun
```

Program 4. Mass Rate of Flow Integration Program.

```
      if (i.eq.1.or.i.eq.numrun) then
        xt = rsum(i)
      else if (i/2*2.eq.i) then
        xt = 4.D0*rsum(i)
      else
        xt = 2.D0*rsum(i)
      end if
c
      hemf = hemf + xt
   40 continue
c
c   calculate Helium mass flow (kg/sec)
c
      hemfr = ((b-a)/(3D0*pn))*hemf


c
      close (1)
c
c   Write out the Helium mass flow
c
      write (9,21) hemfr
   21 format (/,2x,'***  After Horizontal integration ***'/
     b/5x,'The Helium mass flow = ',f15.7,' kg/sec'/)
c
      stop
      end
```

Program 4. Mass Rate of Flow Integration Program.

Appendix C: Helium Mass Fraction Profiles

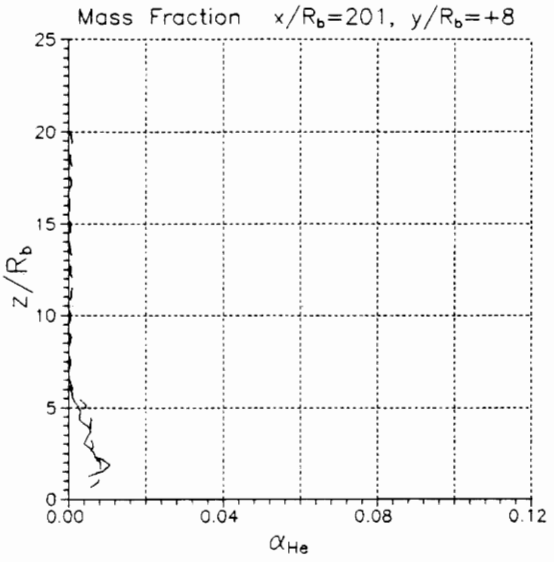

Helium Mass Fraction
Wedge-shaped Nozzle: Solid Line
Circular Nozzle: Dashed Line

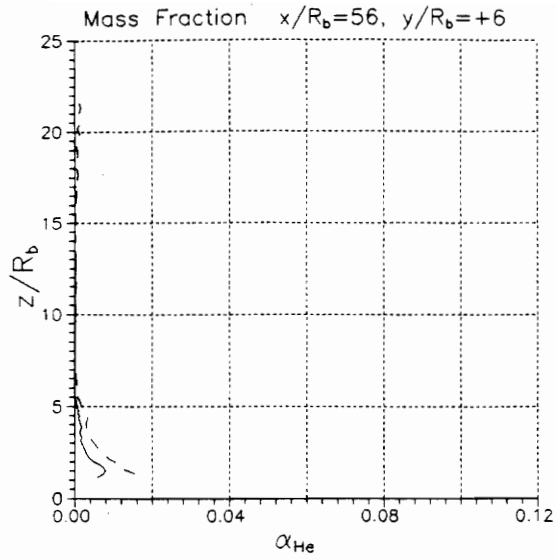

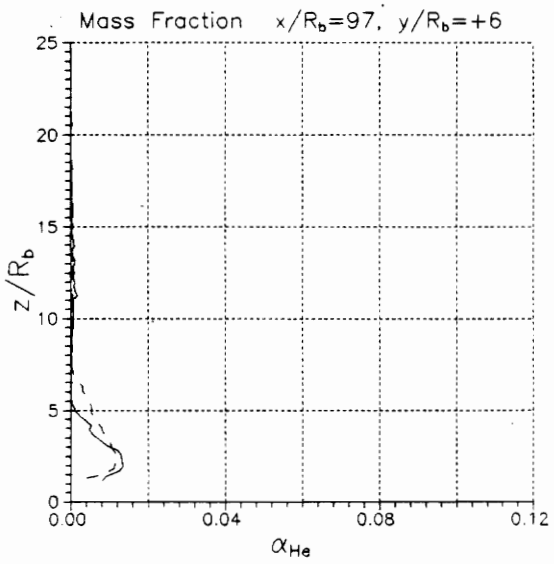

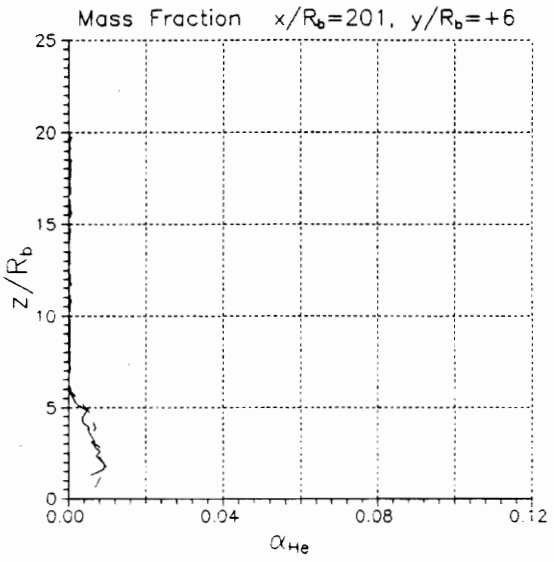

Helium Mass Fraction
Wedge-shaped Nozzle: Solid Line
Circular Nozzle: Dashed Line

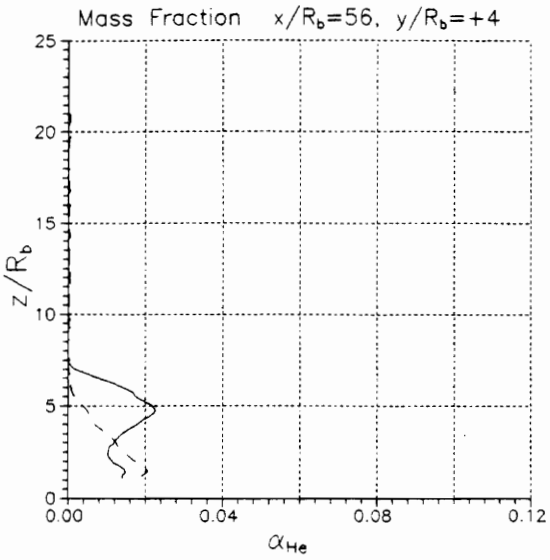

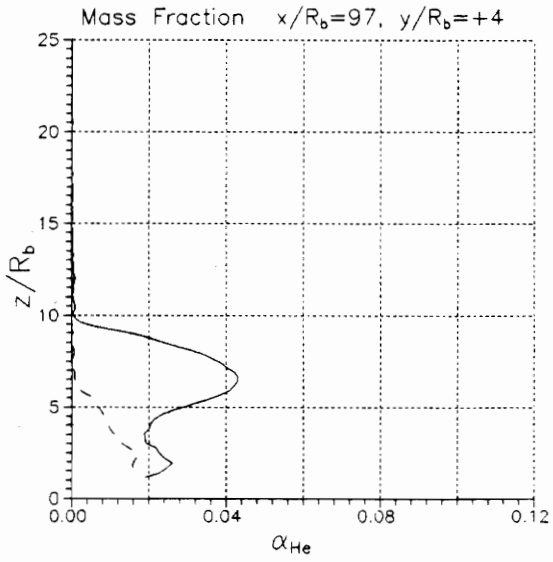

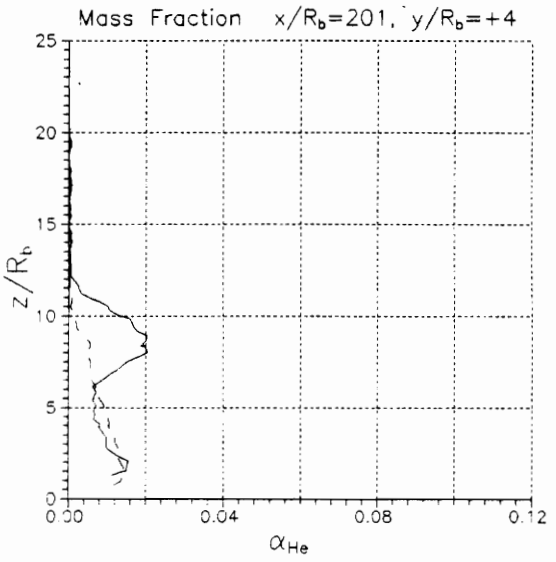

Helium Mass Fraction
Wedge-shaped Nozzle: Solid Line
Circular Nozzle: Dashed Line

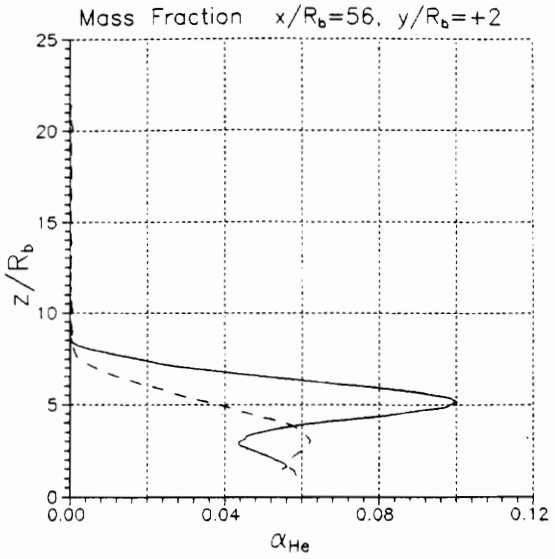

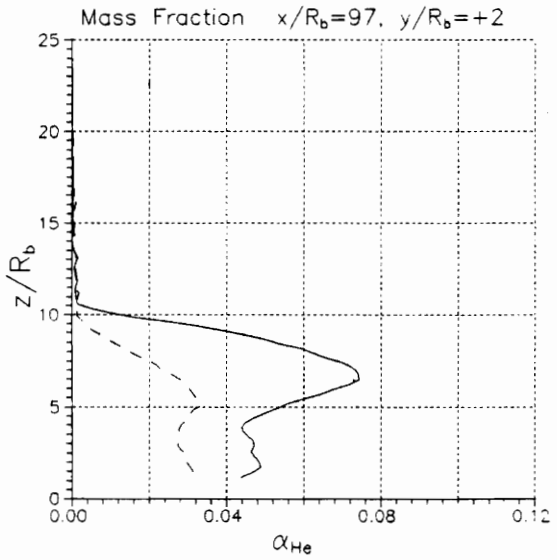

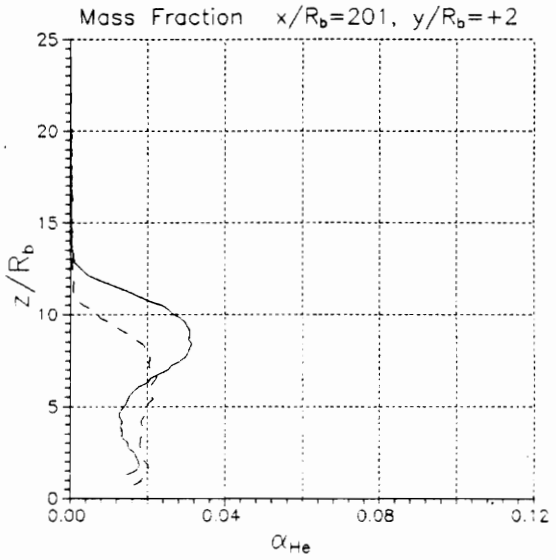

Helium Mass Fraction
Wedge-shaped Nozzle: Solid Line
Circular Nozzle: Dashed Line

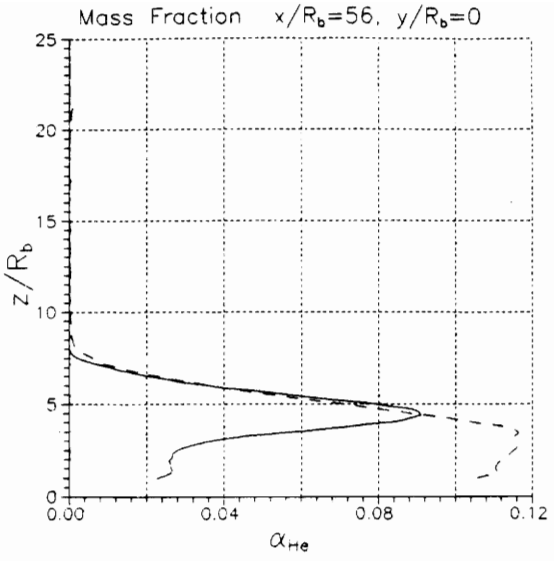

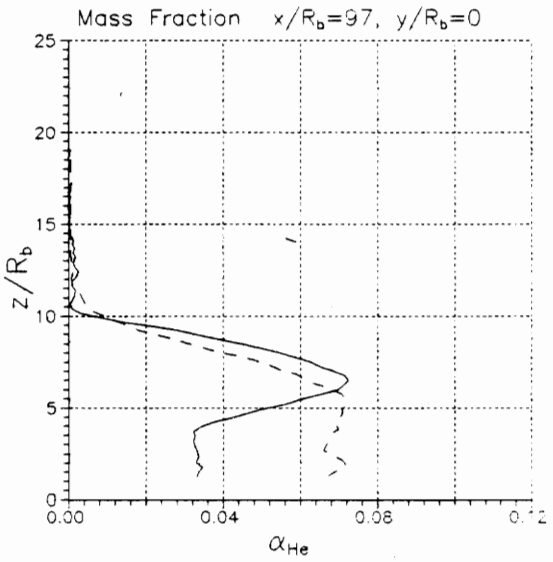

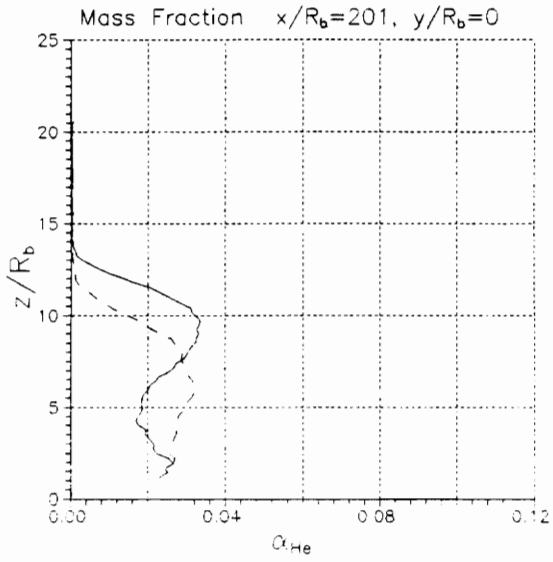

Helium Mass Fraction
Wedge-shaped Nozzle: Solid Line
Circular Nozzle: Dashed Line

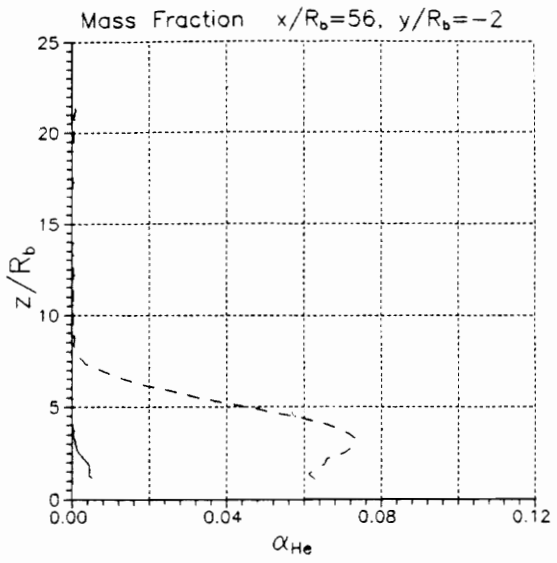

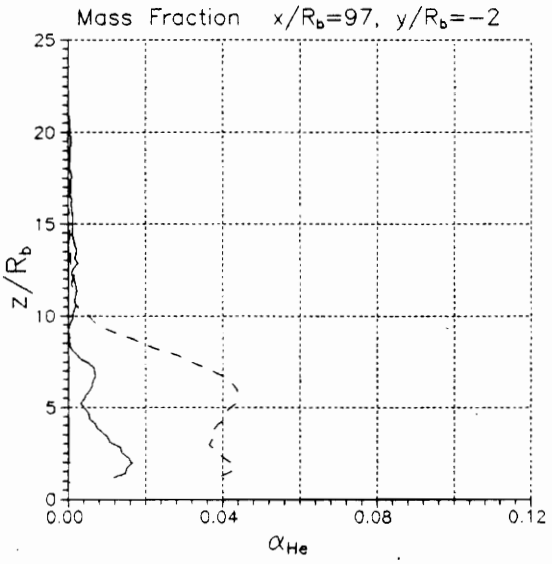

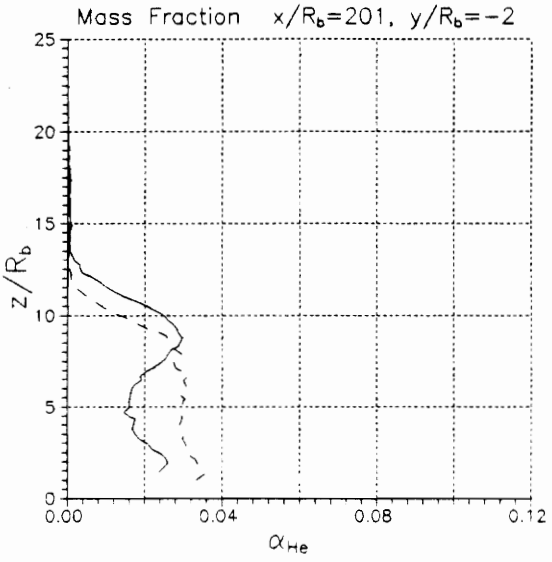

Helium Mass Fraction
Wedge-shaped Nozzle: Solid Line
Circular Nozzle: Dashed Line

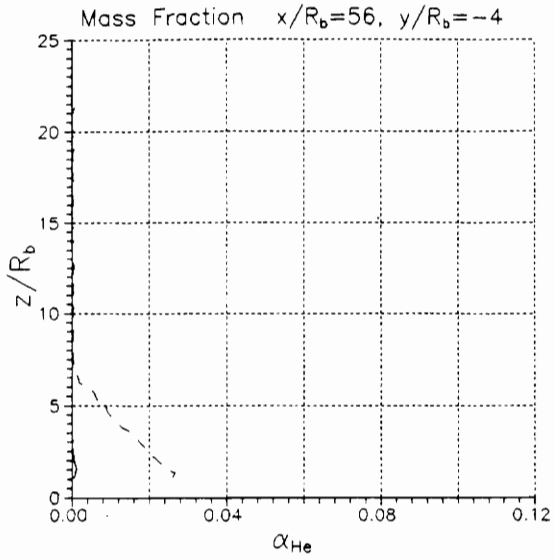

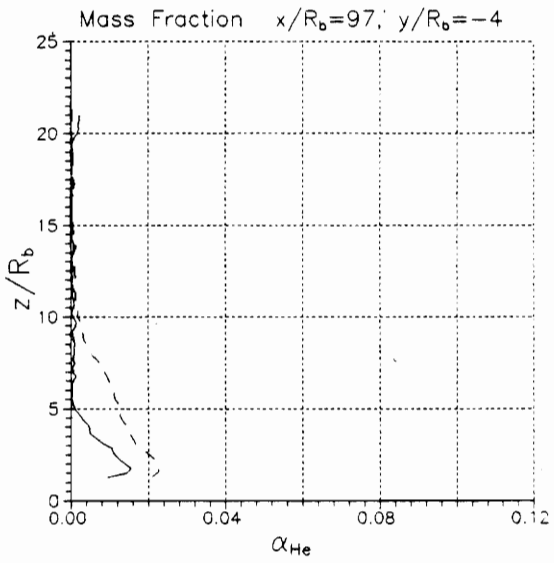

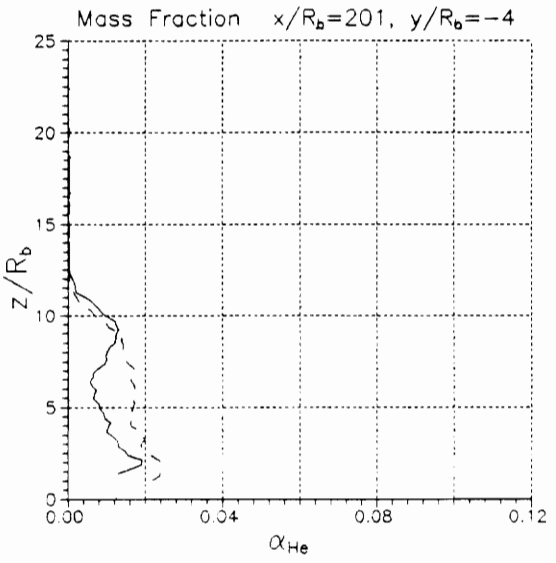

Helium Mass Fraction
Wedge-shaped Nozzle: Solid Line
Circular Nozzle: Dashed Line

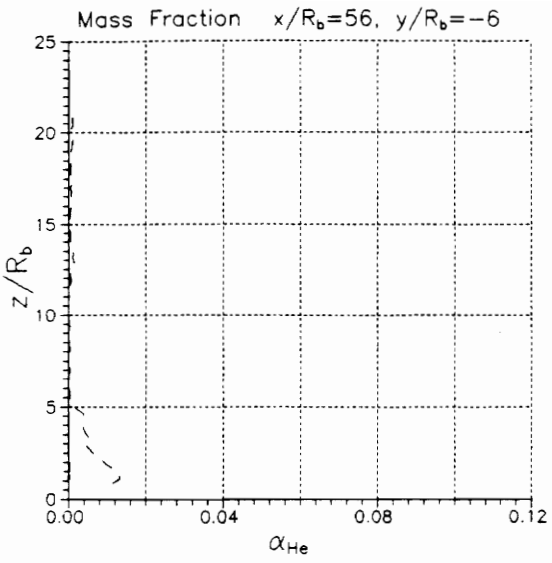

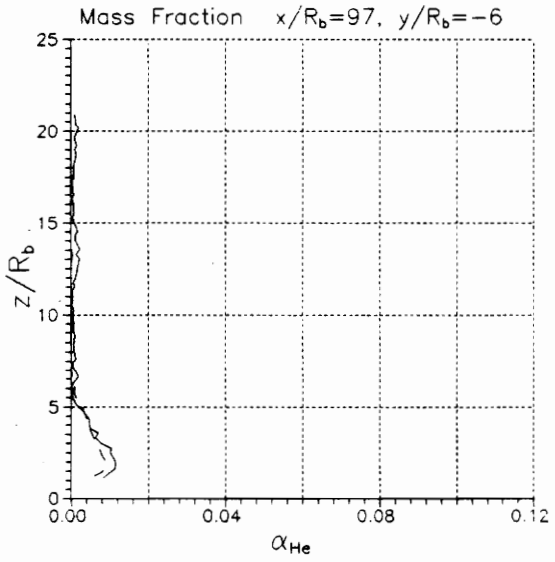

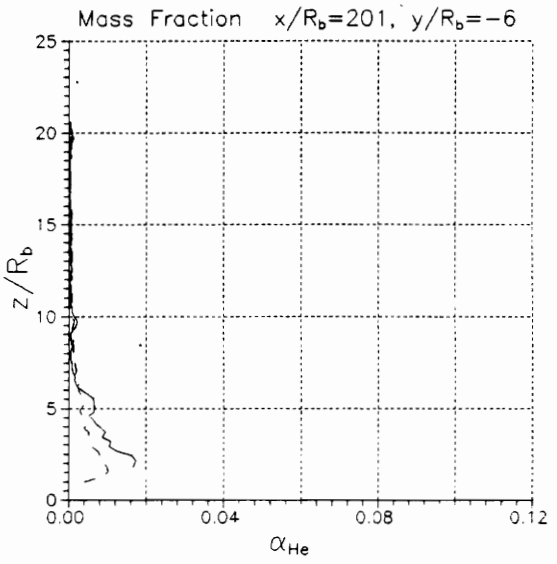

Helium Mass Fraction
Wedge-shaped Nozzle: Solid Line
Circular Nozzle: Dashed Line

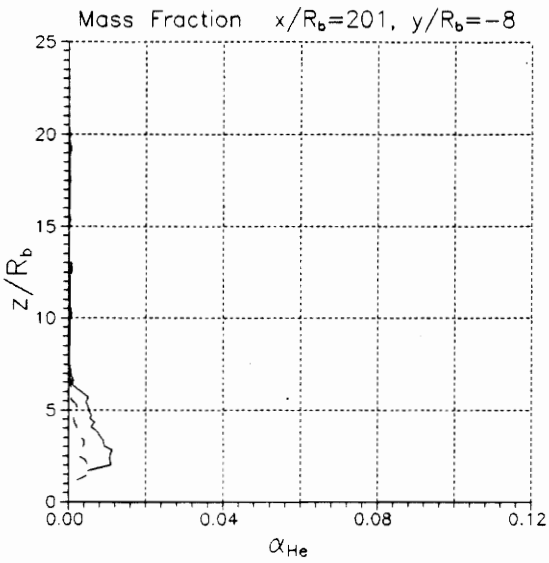

Helium Mass Fraction
Wedge-shaped Nozzle: Solid Line
Circular Nozzle: Dashed Line

Vita

Matthew James Barber was born on May 26, 1966 in South Charleston, West Virginia. He graduated from Winfield High School in June 1984 and enrolled at Virginia Polytechnic Institute and State University in September 1984. He worked as a cooperative engineer at Comdial Business Communications in Charlottesville, Virginia where he conducted research and development of thermoplastic elastomer keypads for telephones. He received a Bachelor of Science degree in Mechanical Engineering in May 1989 and stayed at VPI&SU to pursue graduate studies in Mechanical Engineering.